Homogenization Approach to Filtration Combustion of Reactive Porous Materials-Modeling,Simulation and Analysis-

明治大学大学院先端数理科学研究科

2013 年度

博士学位請求論文

Homogenization Approach to Filtration Combustion of Reactive Porous Materials: Modeling, Simulation and Analysis

多孔質媒体の濾過燃焼に対する均質化法によるアプローチ：

モデリング，シミュレーションおよび解析

学位請求者　現象数理学専攻

IJIOMA　EKEOMA　ROWLAND

Homogenization Approach to Filtration Combustion of Reactive Porous Materials: Modeling, Simulation and Analysis

Ekeoma Rowland Ijioma

Abstract

This thesis is concerned with the modeling of filtration combustion of thin reactive porous media, with an intended application on the consequence of material property on a controlled experimentally observed fingering instability in reverse smoldering combustion. The challenges usually encountered with such modeling of porous media are the absence of a complete description of the microstructure of complex materials and of distributed local chemical reactions.

At the pore scale level, we use the forms of existing combustion type equations describing two competing transport mechanisms-the transport of heat and the transport of reactants. Also we provide a complete description of the intended material of interest, which we assume to consist of periodic arrangement of solid inclusions embedded in a matrix of a gaseous phase. Due to the difficulty in dealing with the distributed nature of the localized chemical reactions at surfaces of the solid inclusions and the highly oscillating coefficients in the governing conservation laws, we apply the homogenization method in order to derive distinct and tractable functional forms of macroscopic limit problems, which allow for treatment of different problem scenarios.

Furthermore, we rely on the derived macroscopic equation structures to investigate the emergence of two-dimensional fingering states. Based on the derived homogenization limits with effective diffusion tensors and on the mechanism of thermal-diffusion instability, we discuss the consequence of material property on the behavior of the fingering instability. Also, we investigate anisotropy effect on the fingering patterns, and treat numerically the disparity of the derived macroscopic models since two distinct forms of the models are derived-the *one-temperature* equilibrium model and the *distributed-temperature* nonequilibrium model.

Finally, we show the well-posedness of the microscopic model and justify its rigorous convergence to the homogenization limit, using both mathematical and numerical tools. We further compared the values of the homogenized effective tensors with some known theoretical bounds, and show some of the factors that may influence the effective diffusion tensors such as volume fraction of inclusion and geometric form of the inclusion.

Preface

During my Master's program at Eindhoven University of Technology, I was privileged to work under the supervision of Professor Adrian Muntean, who first introduced me to multiscale modeling via the homogenization method, during an introductory homogenization course. It was his idea to use homogenization method to develop filtration combustion models that inspired the content of this thesis. The idea was to develop an idealized description of the porous material and of the physics of the phenomenon at the microscopic level, which was missing from previous efforts. I was motivated in this area by the results detailed in the works of Ikeda and Mimura (2008); Fasano et al. (2009) on mathematical modeling of smoldering combustion in microgravity. This guided my research interest to pursuing a Ph.D. position at the Meiji Institute for Advanced Study of Mathematical Sciences.

Thus, this thesis is devoted to the application of the homogenization technique to a smoldering combustion problem under microgravity conditions. In view of the problem of interest, this study attempts to provide answers, from a new point of view based on the homogenization theory, to some questions in smoldering combustion pertaining to those reported experimentally in Zik and Moses (1999); Olson et al. (1998). These questions concern the relation of the homogenization theory approach to previous efforts on a smoldering combustion problem. It is often difficult to distinguish most models derived by homogenization from other macroscopic models that exist in the literature (see Fasano et al., 2009; Kagan and Sivashinsky, 2008, e.g.), since the two approaches rely on macroscopic descriptions that seem functionally identical. However, the models derived (in Chapter 3) through the homogenization method arise as limit problem from a pore scale description (representative of a simplified adiabatic model (Chapter 2)), and hence reflect the macroscopic behavior of this description. Unlike in other macroscopic models, the effective diffusion tensors (see Chapter 5) from homogenization are determined by the solutions of a so-called cell problems, which describe the influence of geometry. In most scenarios, the geometry effects induce anisotropy in the system (Chapter 8), which introduces a new perspective to the studied combustion models. Also, the effective tensors can be used to study the homogenized models in order to verify the contribution of the homogenization approach to the phenomenon of interest (see Chapters 7 and 8). This aspect is treated under fingering patterns of the first kind. In a slightly different consideration similar to most previous efforts (see Kagan and Sivashinsky, 1996; Yuan and Lu, 2013; Chen et al., 1992; Kim

et al., 1996), the effective tensors are replaced by dimensionless free parameters, leading to thermal-diffusion instability in the system. This is treated under fingering patterns of the second kind. Other significance of the homogenization approach as applied in this thesis include to provide answers to the following mathematical questions (Chapters 4 and 5):

(i) How close is the solution of the homogenized problem from the solution of the pore scale description of the problem?

(ii) How good are the derived effective tensors, and the corrector estimates in approximating oscillations of the heterogeneous medium?

It is more difficult to provide answers to these questions by using existing mathematical models, which are specifically more useful when analyzing the problem from the viewpoint of pattern formation (see Ikeda and Mimura, 2008; Fasano et al., 2009; Lu et al., 2006, e.g.). Thus, the scope of this thesis is basically on the derivation of macroscopic models from a pore scale description, verification of the derived models with effective diffusion tensors using mathematical and numerical tools, and application of the derived models to a problem of reverse smoldering combustion.

Acknowledgements

For the successful completion of this thesis, I acknowledge the guidance of my supervisor, Professor Toshiyuki Ogawa for entrusting me with this research study, and for all his patience and insightful contributions during our discussion sessions. I also appreciate his encouragements and supports in other matters related to life in Japan.

My research study in Japan is not coincidental, but one inspired by interests and motivation. I am most indebted to the man that made it all happen, Professor Masayasu Mimura. I am thankful to him for motivating my research study through his research contributions, and for encouraging me to undertake a research work at MIMS under his co-supervision. The completion of this work is also due to two personalities, based on their contributions during the mathematical aspects of the research. For this, I thank Professor Kota Ikeda for all the insightful discussions and for the critical assessment of different aspects of this research work. I am also indebted to Professor Adrian Muntean. As a mentor, he introduced me to homogenization theory. Also, I appreciate the collaborative work we were able to accomplish during the period of this study, and for the stimulating discussions in current trends related to the application of the homogenization theory.

Special moments in life may not happen without the mentioning of friends in it. My life in Japan has been meaningful and at a balance because of friends who provided such exciting moments; I appreciate the friendship of my fellow international MIMS students. The

likes of Dr. Amy Poh Ai Ling, Gani O. Mohammad, Lukito Adi Nugroho, and Tommaso Scotti. Also, I would have been lost in so many ways in Japan without the assistance of Dr. Kikkawa Mitsuru, Yamaguchi Masahiro, Ohya Yoshito, Mayuko Iwamoto, etc. I am grateful for all your kind assistance. For most people, family comes first, but in my opinion family is everything. I am grateful to my family for the unconditional and spiritual support they provided throughout the periods of my absence for academic pursuits.

Furthermore, I am grateful to the members of staff, Graduate School of Advanced Mathematical Sciences, who have supported me in one way or the other, and specifically to Professor N.J. Suematsu, for the opportunity of discussion of the experimentally related part of my work and for extending the courtesy of providing the microscopic snapshots used in this study. I am also indebted to the administrative officers-Miss Takahashi Sayako, Mr. Kimura Makoto, Mr. Egashira Yosuke, and Miss Tokita Kanako-at GCOE and AMS for providing substantial support and clarifications in administrative matters.

I also appreciate the effort of the member of my thesis committee for their active involvement in my Dissertation. Finally, to the joint sponsors of this project work-the GCOE and Japanese Government (MONBUKAGAKUSHO: MEXT), I am most thankful for their financial support. This work would not have been accomplished without the supports.

Ekeoma Rowland Ijioma. Nakano. February, 2013.

Contents

Chapter 1

Introduction

1.1 Background

The modeling of reactive flows in reactive porous materials has been a subject of interest over the years. Specifically, in the theory of flame propagation, combustion reactors and filtration combustion, reactive flows cover a broad range of areas of phenomenological importance. An example is in the case of *filtration combustion* process in which a self-sustaining heterogeneous exothermic reaction front propagates through a porous material that reacts with a gaseous (liquid) oxidizer infiltrating the pores of the solid matrix.

In this framework, the characteristics of filtration combustion waves can be determined by a number of factors; the kinetics of chemical reaction of the solid-gaseous reactants, the thermal and filtration properties of the physical system, the existence of heat losses, as well as the direction of oxidizer transport to the reaction zone. Based on the direction of flow of the inlet oxidizer and the direction of propagation of thermal and reaction fronts, filtration combustion can be classified as reverse (counterflow), forward (coflow) and two-sided filtration regimes (see Figure 1.1). It is classified as reverse (forward) filtration regime when the reaction zone propagates in the opposite (same) direction to the direction of flow of the inlet oxidizer. The two-sided filtration combustion occurs when the oxidizer gas flows both from the inlet and outlet. Figure 1.2 depicts a schematic of a reverse filtration combustion regime in a porous solid. In this regime, the material is ignited at the outlet; an oxidizer gas infiltrates the pore of the solid matrix from the inlet; reaction occurs at surfaces presented by the solid, and a reaction front propagates opposite to the direction of flow of the oxidizer gas. Filtration combustion has been studied extensively in the literature (see Wahle et al., 2003; Oliveira and Kaviany, 2001; Rein, 2005; Henneke and Ellzey, 1999, e.g.) and its significance is not limited to such important processes as smoldering and self-sustaining high temperature synthesis (SHS) of materials, etc. In particular, *smoldering* describes a slow, low temperature, and flameless form of burning porous materials. It is considered a potential fire hazard because the process of smoldering is difficult to detect, involves the release of toxic gaseous fumes and may transit into flaming, making it a precursor of

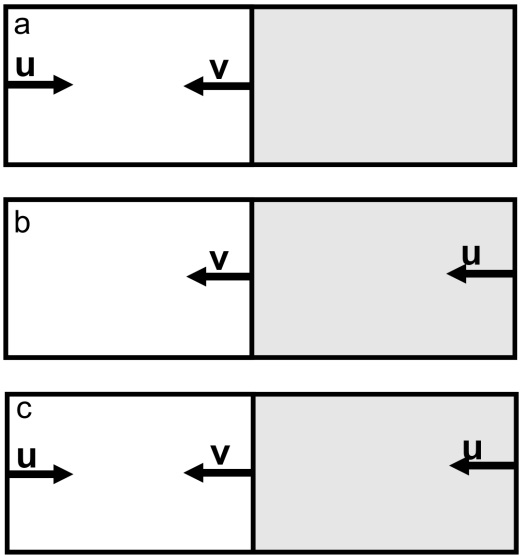

Figure 1.1: Schemes of filtration regimes. (a) counterflow (reverse) (b) concurrent (forward) (c) two-sided filtration regime; u and v are the filtration and reaction flux velocities; the shaded region indicates the burnt fuel and the line demarcating the two regions is the reaction front.

accidental fires.

Inspite of its disadvantages, smoldering has some important features; specifically, the smoldering combustion of biomass has a positive environmental impact on lowering the CO_2 presence in the atmosphere. SHS, on the other hand, employs high-temperature combustion waves to synthesize materials. While the process of smoldering and SHS may be different in their applications, the underlying mechanisms are similar, thus allowing for a description of the processes with the same mathematical model. For a detailed discussion on the theory of filtration combustion, we refer to Wahle et al. (2003). An importance aspect

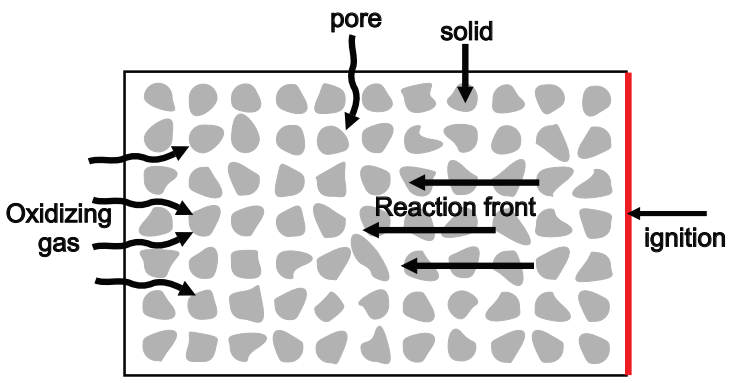

Figure 1.2: Typical scenario of flow in a reverse (counterflow) filtration combustion of a solid porous material

in the formulation of mathematical models of filtration combustion involves the role of thermal and filtration properties related to the inherent nature of micro-structural distribution of materials. Although existing filtration combustion models have been successfully used in the study of filtration combustion problems (Fatehi and Kaviany, 1994; Di Blasi, 1995; Buckmaster, 1985; Yarin et al., 2004), it is desirable in most cases to understand the influence of processes taking place at distinct observation scales. While most combustion phenomena are observed at scales much larger than the scale of heterogeneities, it may turn out to be insightful if the influence of local structure and processes can be integrated into the study of filtration combustion. A formidable challenge in this direction is the absence of a complete description of microstructure of materials for practical applications, and hence an explicit representation of local heterogeneity may not be possible. This necessitates the design of mathematical models capable of approximating the heterogeneous medium by a homogeneous medium described by some averaged parameters. Furthermore, such equivalent descriptions, if they exist, should take into account the influence of the heterogeneities at the local (microscopic) scale.

According to the presentation in Wahle et al. (2003), filtration combustion waves can be investigated under a one-temperature or two-temperature description based on the strength of the gas flux infiltrating the porous material. One-temperature models are appropriate for describing slowly propagating coflow filtration combustion waves in which the time of contact between the solid particles and the gas is sufficiently large for rapid thermal equilibrium to occur. However, for a relatively large gas flux, convectively driven coflow filtration combustion waves depend on the presence of a distinctive temperature difference between the gaseous and solid phases, and thus can only be described by a two-temperature model.

On the other hand, in counterflow filtration waves, the solid fuel at the vicinity of the reaction zone loses heat to the cool infiltrating gas. This means that such filtration waves are necessarily driven by *conduction* because the convective mechanism depends on the ability of the gas to deliver heat to the unburned solid fuel. However, the infiltrating gas absorbs heat from the unburned solid fuel, and hence driving the combustion process towards its extinction. Schult et al. (1995); Decker and Schult (2004) reported an analysis of a one-temperature model in which extinction of steady traveling waves occur when the gas influx is sufficiently large. Under such sufficiently large gas flux, the gas and solid phases may not have a sufficient time to equilibrate, in which case a two-temperature model suffices.

In the counterflow regime, the transport of an infiltrating gas opposite to the direction of propagation of the reaction front suppresses combustion. This is because the solid near the reaction zone loses heat to the cool infiltrating gas, thus decreasing the combustion temperature and hence the reaction rate. It is also known that in counterflow configuration under a *smoldering regime*, the propagating reaction front exhibits characteristic combustion instability in form of fingering patterns. This instability is known to be driven by the destabilizing effect of oxidizer deficiency (Zik and Moses, 1999; Zik et al., 1998; Olson

et al., 1998). In addition to the influence of filtration properties, namely the porosity of the material, it is also important to take into account, in a counterflow regime, the effect of the conductivity contrast that exists between the interacting gaseous and solid phases as well as the effect of a *forced suppression*[1] of the reaction rate. In the present study, we focus on the consequence of these effects on the behavior of a counterflow smoldering combustion wave.

1.2 Experimental overview of the problem of counterflow smoldering combustion

In their fundamental experiment, Zik and Moses (1999) showed that a thin solid material, in a counterflow smoldering regime, develops a steady fingering state. The instability emerged in a well-defined regime of Rayleigh Ra, and Peclet Pe, numbers, in which the effect of natural convection is suppressed, with molecular diffusion dominating in the horizontal plane. The studied system combines a two-dimensional Hele-Shaw geometry with smoldering combustion, in which a uniform flow of oxygen interacts with a thin porous reagent to produce char, gaseous product and heat that drives the process. The details of the experimental set-up can be found in Zik and Moses (1998, 1999). The destabilizing effect of reactant transport, which plays the same role as the thermal diffusion instability, is enhanced under a countercurrent configuration.

The emerging front exhibits directional fingering instability along the direction of flow, with two decoupled length scales-the finger width and the spacing between the fingers. These length scales correspond to two transport mechanisms: transport of heat and transport of reactants. The transport of reactants, which is controlled by the Pe, determines the front velocity and the spacing d between fingers, whereas the characteristic finger width w depends on the ability of the front to release heat. The design of their experiment emphasizes uniformity on the following quantities:

(i) flow of the oxidizer,

(ii) sample fuel (e.g., Whatman grade no. 2),

(iii) ignition at one end of the fuel.

In the absence of uniformity in any of the mentioned quantities, the emerging fingering patterns exhibit nonuniformity. Specifically, in a highly anisotropic porous sample, the uniformity and reproducibility of the patterns is reduced, otherwise distinct regimes of the fingering patterns can be observed. The nonuniformity is such that the fingering patterns are directed towards a lateral side of the sample, and may also propagate along the lateral boundaries. The experiments capture three basic and distinct fingering states-connected front, tip-splitting fingers, and sparse fingers as shown in Figure 1.3. The fingering patterns

[1]Forced suppression means that the reaction rate of the chemical reaction is appropriately tuned prior to the onset of the combustion process.

(a) Connected front (b) Tip-splitting fingers (c) Sparse fingers

Figure 1.3: Spatial profiles of two-dimensional fingering (char) patterns of a filter paper sample, observed experimentally in a Hele-Shaw cell; The char propagation is from bottom to top; Ignition is initiated at the bottom and oxidizer gas is passed from the top, in a typical counterflow configuration. The char is identified by the dark finger-like patterns, and the light shades are the quenched part of the flame, which separates regions of burned parts from unburned parts. (a) connected front which manifests at high flux velocity; the fingers are connected. (b) Tip-splitting regime marked by splitting of sole fingers at the tips; it is observed at a moderate flux velocity. (c) Sparse fingers, which manifest at a relatively low flux velocity; the fingers are more distinct from each other and the tips do not split. The snapshots are courtesy of Professor Elisha Moses (Weizmann Institute of Science).

depicted in Figure 1.3 are obtained under uniform conditions as mentioned above. However, there are other forms of patterns which are observed under nonuniform conditions. Furthermore, it was also shown that the role of the small gap (see experimental setup in Zik and Moses, 1999) between the plates of the Hele Shaw cell is to inhibit natural convection- an inexpensive alternative to turning off gravity. This implies that increasing the width of the gap enhances the strength of natural convection. This induces some characteristic behavior on the fingering pattern, e.g. thickening of the finger width and the emergence of nonuniform patterns in most cases. It was shown that the finger width w is linearly dependent on the gap size h. This quantitative dependence is consistent with a qualitative observation, which show that the finger width is determined by the ability of the front to release heat. For a full description of the experiment and other forms of pattern behavior, we refer the interested reader to Zik and Moses (1998); Zik et al. (1998); Zik and Moses (1999); Olson et al. (1998).

1.3 Mathematical treatment of filtration combustion

There is a vast number of filtration combustion models in the literature, which has been used to investigate filtration combustion processes. Here, we describe a couple of the models which are related to the discussions in the present study. We begin with the form of filtration combustion model presented in Yarin et al. (2004). To describe filtration combustion, they used the mass, momentum (in form of Darcy's law) and energy equations.

One-temperature filtration combustion model (Yarin et al. (2004))

$$\frac{\partial \rho_{\mathrm{g}}}{\partial t} + \frac{\partial \rho_{\mathrm{g}}}{\partial t} = -\sigma W, \tag{1.1}$$

$$\rho_{\mathrm{m},0}\frac{\partial \eta}{\partial t} = W, \tag{1.2}$$

$$\frac{dP}{dx} = -\frac{\mu_{\mathrm{f}}}{k_{\mathrm{f}}}, \tag{1.3}$$

$$\frac{\partial}{\partial t}\Big\{\Big(c_{\mathrm{g}}\rho_{\mathrm{g}} + c_{\mathrm{m}}\rho_{\mathrm{m}} + c_{\mathrm{p}}\rho_{\mathrm{p}})T\Big\} + c_{\mathrm{g}}\frac{\partial}{\partial x}(\rho_{\mathrm{g}}u_{\mathrm{f}}T) = \lambda\frac{\partial^2 T}{\partial x^2} + qW, \tag{1.4}$$

where ρ, P and T are the density, pressure and temperature, respectively. W is the chemical reaction rate; $\eta = (\rho_{\mathrm{m},0} - \rho_{\mathrm{m}})/\rho_{\mathrm{m},0}$ is the completeness of conversion of the solid reagent; c_{m} and c_{p} are the specific heat of the solid reagent and product, c_{g} is the isochoric specific heat of the gaseous oxidizer, q is the heat released by the reaction, k_{f} is the filtration coefficient equal to the permeability of the porous matrix divided by the gas viscosity, λ is the thermal conductivity. The subscripts g, m and p refer to gaseous phase, solid reagent and combustion product, respectively. The system of Eqs. (1.4)–(1.4) is supplemented by the equation of state of the gaseous phase assumed to be an ideal gas

$$mP = \rho_{\mathrm{g}}R_{\mathrm{g}}T, \tag{1.5}$$

where R_{g} is the gas constant, m is the medium porosity. The chemical reaction rate is given by

$$W = zP^{\nu}f(\eta)exp\Big(-\frac{E}{RT}\Big), \tag{1.6}$$

The specific heats and densities have the following relations

$$c_{\mathrm{m}} + \sigma c_{\mathrm{g}} = (1+\sigma)c_{\mathrm{p}} \tag{1.7}$$

$$\rho_{\mathrm{m}} = \rho_{\mathrm{m},0}(1-\eta) \tag{1.8}$$

$$\rho_{\mathrm{p}} = (1+\sigma)\rho_{m,0}\eta. \tag{1.9}$$

In (1.6), the burn-out function is given by

$$f(\eta) = (1-\eta),$$

where z and ν are kinetic constants, E is the activation energy, R is the universal gas constant. Most filtration combustion models in the literature generally have the macroscopic form given by (1.2)–(1.4). Such equations are particularly useful, in view of their simple forms, when dealing with problems related to analysis of thermal structures of combustion waves as well as stability of filtration combustion models.

Two-temperature (non-adiabatic) filtration combustion model (Fasano et al. (2009))

The previous model only accounts for a one-temperature equation for the gas-solid combustion system. Also, the process of heat transfer between the system and the environment is not taken into account, and hence placing it in the class of adiabatic models. Presently, we introduce another type of filtration combustion model, in which heat transport is accounted in the solid and gaseous phases. It also takes into consideration different heat transfer mechanism; heat exchange between the solid and gas, and between the solid and the environment. The model is presented by Fasano et al. (2009) in an attempt to describe the experimentally studied smoldering phenomena under microgravity conditions. Their model emphasizes the significance of heat losses in the observed combustion instability. In addition, the characteristics of the model is such that both counterflow and coflow combustion waves can be successively treated. Thus, the prediction of the model coincides with the experimental work reported by Olson et al. (1998). For a detailed presentation of the model, we refer the interested reader to Fasano et al. (2009).

Other relevant models treating the smoldering combustion under microgravity includes the one-temperature model of (see Ijioma et al., 2013; Kagan and Sivashinsky, 2008; Ikeda and Mimura, 2008, e.g.). Using a pore-network, two-temperature filtration combustion model, Lu and Yortsos (2005a); Lu et al. (2006) analyzed the distinct fingering regimes of the experimentally observed fingering instability under adiabatic and non-adiabatic conditions. There are also other related studies on the development of fingering instability reported in the literature Yuan and Lu (2013).

In the present study, the method of homogenization is applied for the first time in order to investigate the consequence of material property such as the intrinsic geometric form of the microstructure, the thermal and filtration properties, etc. on a developed fingering state in counterflow smoldering combustion of thin porous materials. The microscopic description is inspired from a previous attempt (Kagan and Sivashinsky, 2008), in which the pertinent system of equations was reduced to an interface problem that analyzes regimes of the traveling reaction front. Most other problems of interest reported so far in the literature have been focussed on the analysis of the pattern-forming system in terms of verifying the distinct fingering states Ikeda and Mimura (2008); Lu and Yortsos (2005a), the the spread rate of the reaction front Fasano et al. (2009); Kagan and Sivashinsky (2008), as well as the effect of heat losses (Yuan and Lu, 2013; Lu and Yortsos, 2005a). However, our primary interest is to analyze the problem from a new point of view that is based on the homogenization theory. First, we develop a model that takes into consideration the microstructure of the material, the interplay between components of the medium, and the influence of microstructure on the structure formation. The latter entails investigating anisotropy effects on the fingering patterns. This generalizes the upscaled models developed previously for isotropic porous media (Ijioma et al., 2013), and also allows for discussion of various anisotropic situations. In addition to analyzing the fingering patterns in isotropic

porous media, the role of anisotropy on the behavior of the fingering patterns is a major contribution in this thesis.

Furthermore, the starting point of the modeling is to assume, at the pore scale, a material with uniformly repeating cells, embedded in a matrix of a gaseous phase. This implies that a single cell consists of a solid part (made of cellulosic fiber in this case) and a gaseous part (the air filled part). The cells are allowed to cover the entire material, thus providing a complete description of the material. At this level, the cells can be of any simplified geometric forms in two or three-dimensions; even more complex geometries are also possible. The balance laws at the pore scale are based on the two competing transport processes-the transport of heat and the transport of mass of reactants-which are defined on the constructed periodic medium. The problem of this description (see Figure 1.4) is that the

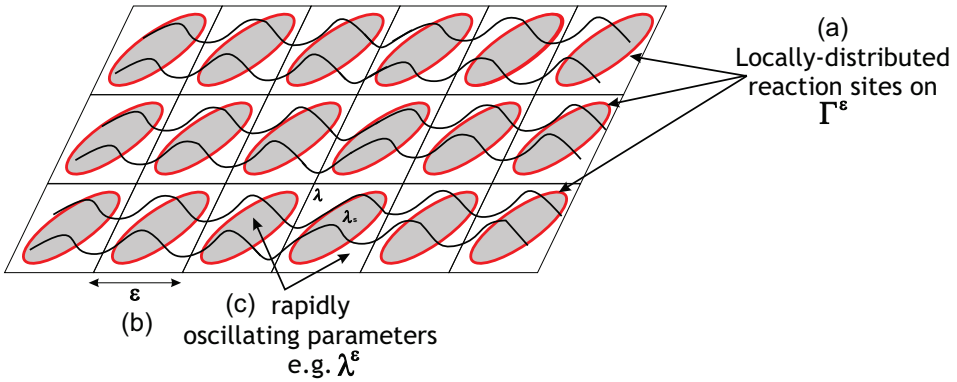

Figure 1.4: The scheme of the periodic domain indicating some of the challenges at the pore scale description; (a) the reactions are locally distributed on the surfaces $\Gamma^{\epsilon,i}$, which makes the reaction front less tractable for combustion applications; (b) the domain dependence on a scale parameter, ϵ which increasingly becomes small; (c) the parameters of the domain are rapidly oscillating, as indicated by the oscillating curve;

physical quantities in the governing laws are rapidly oscillating between the phases. Also, the chemical reactions assume a distributed nature on surfaces $\Gamma^{\epsilon,i}$ of the solid inclusions, and the periodic medium depends on a small scale parameter ϵ. Thus, for tractability of the method for applications, we need a method of overcoming the challenges encountered by working on the periodic heterogeneous medium. The method should preserve the relevant properties of the medium and the phenomenon of interest. An exemplary method that provides us with the desirable approximation technique for the pore scale description is the homogenization method, which is presently used in this study.

The consequence of approximating the pore scale description by a homogenized (averaged) description raises further mathematical questions on the efficiency of the homogenization process. It turns out that we are immediately faced with two distinct problems: at the large (observation) scale, the homogenized problems determine the macroscopic limit behavior of the pore scale description. They are also viable for the verification of physical phenomenon

of interest. At the pore scale level, we deal with the problem of establishing convergence to the homogenization problem. This process require some mathematical rigor, in which we will approach through the notion of two-scale convergence and corrector results (see Allaire, 1992; Nguestseng, 1989; Neuss-Radu, 1996; Fatima and Muntean, 2014, for instance).

In order to show qualitatively the efficiency of the homogenization process through the design of multiscale numerical methods, we require the construction of correctors, at least of the first order with respect to a scale parameter ϵ. Then, the homogenized solutions may be "corrected" as depicted in Figure 1.5, thus recovering the original pore scale description, in this case, at the first order of approximation. We point out that additional correctors may also be relevant as long as the scale parameter entering the computation is not significantly small. In Figure 1.5, we illustrate the scheme of the multiscale reconstruction of microscopic solution by using the first two terms of the asymptotic expansion:

$$C^{\epsilon}(t,x) \approx C^{0}(t,x) + \epsilon C^{1}(t,x,\frac{x}{\epsilon})$$

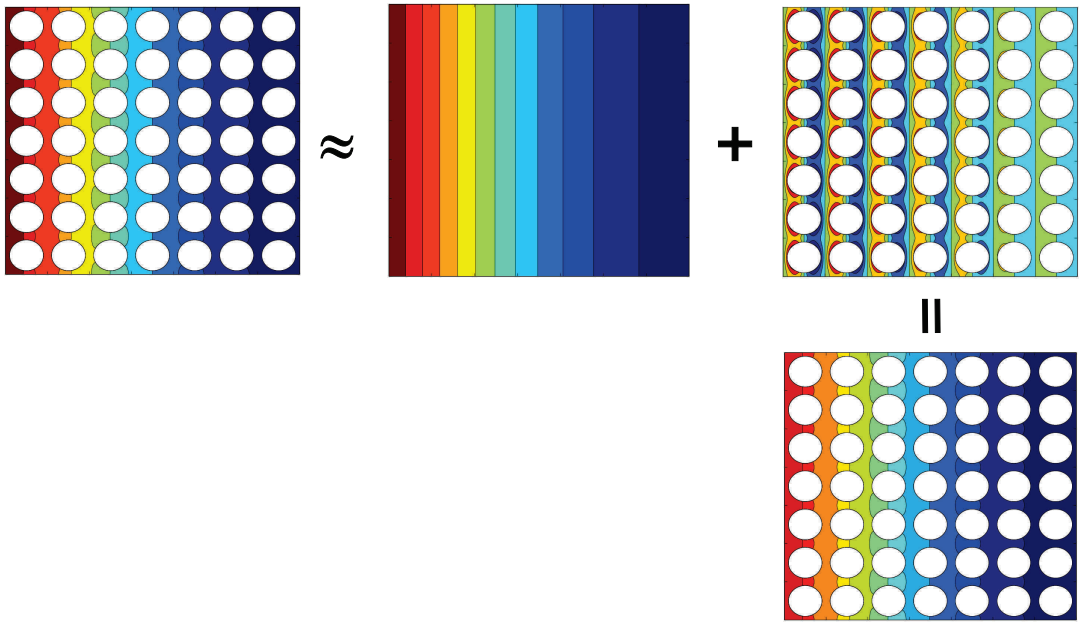

Figure 1.5: Scheme of the multiscale numerical algorithm; the term on the left is the solution of the microscopic (pore) problem, $C^{\epsilon}(t,x)$; on the right is the homogenized solution $C^{0}(t,x)$ and the corrector $C^{1}(t,x,\frac{x}{\epsilon})$; the sum of the two terms equals the reconstructed solution, $C^{0}(t,x) + \epsilon C^{1}(t,x,\frac{x}{\epsilon})$.

1.4 Outline of this thesis

This thesis is concerned with the modeling, analysis and simulation of filtration combustion of reactive porous materials, with an intended objective of analyzing the development of fingering instability in reverse smoldering combustion of heterogeneous porous materials. The structure of this thesis is divided into Chapters, which end with a brief summary of the results, and further open questions that may be of interest for future research consideration.

In Chapter 2, we describe the mathematical modeling of the filtration combustion process at the pore level. We also give a brief introduction to the homogenization method. At this level, the description of the geometry, the transport processes and chemical reaction are also presented based on the physical process of interest.

Chapter 3 presents the derivation of the macroscopic models for filtration combustion by the asymptotic homogenization method. By scaling relations in ϵ, three distinct materials are analyzed based on thermal conductivity contrast: material with moderately conductive inclusions, highly conductive inclusions and weakly conductive inclusions embedded in a gaseous matrix such that the inclusions remain distinct from each other. The homogenization method allows us to derive formulas for calculating the effective transport coefficients, which are different for each of the considered models. Two of the derived macroscopic models have the form a one-temperature equilibrium model of filtration combustion, whereas the third model is a class of two-scale combustion model, which has not yet gained popularity in the framework of combustion problems in literature.

In Chapter 4, the rigorous upscaling of the pore scale description presented in Chapter 2 is examined using the two-scale convergence method due to Allaire (1992) and Nguetseng (1989). We recovered a class of two-scale homogenization limit problems, the effective diffusion formulas and the correctors. Also, the strong convergence of the homogenization process was proven using the notion of two-scale convergence.

In Chapter 5, we present the calculation of the effective thermal conductivity tensor for the derived macroscopic models. We examine some of the important factors influencing the effective thermal conductivity such as the volume fraction of inclusions, and geometric form of the inclusion. The numerical values of the effective thermal conductivity obtained from homogenization are compared with some known theoretical bounds for effective thermal conductivity.

Chapter 6 presents a reconstruction procedure to recover the solution of the pore scale description through corrections to the homogenized solutions. We investigate the convergence rates of the homogenization process presented in Chapter 3. The relative error estimates between original problem and the reconstructed solution are compared with theoretical estimates derived in Chapter 4.

In Chapter 7, the derived macroscopic models are analyzed for the development of fingering instability in reverse filtration combustion of an isotropic porous material. We examine two different problems: first we verify the implication of the limit homogenized problems on the behavior of the fingering patterns, and secondly, we analyze the pattern behavior based on the mechanism of thermal diffusion instability, which is well studied in combustion literature (see Kagan and Sivashinsky, 1996, e.g.). This is one of the main chapters of this thesis.

Chapter 8 is a consequence of the results presented in Chapter 7. We examine the behavior of the finger-like patterns in an anisotropic porous medium. The pattern behavior in various anisotropic geometries is analyzed in terms of distinct anisotropic matrices. We also verified that even in the case of highly anisotropic media, distinct fingering regimes are captured, except for a change in the uniformity of the patterns. This observation is consistent with the experimental work of Zik and Moses (1999).

Finally, the results of the previous chapters are summarized in Chapter 9. This chapter underlies the significant results of the present study and gives further insights on prospective areas for future research.

1.5 Statement of originality

Contrary to previous efforts toward the analysis of fingering instability of thin porous samples, we approach the problem from a new point of view based on the periodic homogenization theory. This allows for the incorporation of microstructures of materials into the modeling. This is relevant when dealing with the influence of microstructure on structure formation. Previous efforts have been restricted to macroscopic descriptions, which are usually introduced directly at the macroscopic level; In Lu and Yortsos (2005a), an attempt is made using a pore network simulator, which does not present a complete description of the material.

While the behavior of fingering patterns have been reported experimentally in the literature Zik and Moses (1999) for highly anisotropic media, it has not yet been shown through mathematical modeling. Thus, we analyze the fingering instability from the perspective of anisotropic porous media. In the present study, the behavior of patterns resulting from distinct types of anisotropic tensors is examined. We attempt to analyzing the structure of patterns in anisotropic porous media via a fixed geometry consideration. The analysis based on fixed geometries revealed how anisotropy can be induced into the conservation laws through the effective diffusion tensors. The latter shows a degree of consistency between the orientations of the microstructure geometry with directional fingering of the patterns.

It is evident from literature that different types of materials can exhibit fingering patterns, which explains why the phenomenon is seems to be fuel independent. However, it is unclear

how conductivity contrast can influence the pattern behavior. We analyze the problem of conductivity contrast based on the homogenization theory. This allows considering general porous samples with distinct conductivity contrast. The motivation behind here is that in the regime of reverse filtration combustion, heat conductivity is an important mode of heat transfer besides the radiative heat mechanism. This aspect of structure formation has also not gained much insight. Until now, the effect of conductivity contrast on the behavior of emerging fingering patterns has not been studied. We analyze in this framework different factors determining the contribution of conductivity contrast in a particular combustion scenario: heat conductivity, fuel conversion within fingers, ability of fingers to tip-split, as well as the time for onset of ignition.

Chapter 2

Upscaling strategy and formulation of the local scale problem

2.1 The homogenization strategy

In this section, we describe the method of homogenization[1] which we plan to use in the present study. The method is based on formal asymptotic expansion and was developed by Bensoussan et al. (1978) and (Sanchez-Palencia, 1980; Zhikov et al., 1994; Bakhvalov and Panasenko, 1989, etc.). It is usually referred to as the homogenization of periodic structures (HPS), because the method is built upon the assumption of working with a heterogeneous structure, and of periodic fields and parameters describing processes in such media. The HPS method (Bakhvalov and Panasenko, 1989; Hornung, 1997; Auriault et al., 2009; Persson et al., 1993; Sanchez-Palencia and Zaoui, 1985; Sanchez-Palencia, 1980; Bensoussan et al., 1978; Cioranescu and Paulin, 1998) has been successfully used in capturing the effective behavior of porous media having complex interconnected parts with properties, which are presumably rapidly oscillating. The effective behavior of such systems is known in the limit of the homogenization process and allows to study not only the macroscopic behavior of a pore scale description, but also to adapt the macroscopic equations for other applications.

While it is evident that the real life structure of most materials are not periodic, the HPS method provides a mathematically complete description of the structure of complex materials in such a way as to allow tractability to practical problems posed on complex structures and to their rigorous mathematical treatments. For any choice of periodic structure, the micro-macro transition process gives an equivalent macroscopic description, intrinsic to the material and to the phenomenon of interest (Auriault et al., 2009).

Contrary to most other methods e.g., volume averaging method (see Whitaker, 1999, e.g.),

[1] Homogenization is simply a collection of methods that approximates a heterogeneous medium by a homogeneous medium with constant parameters.

HPS does not rely on any assumption on the physics of the model at the macroscopic level in order to ensure the quality of the result. For instance, in the derivation of conservation laws for energy, there is usually, in most cases, the use of the assumption of thermodynamic equilibrium in order to pass to a macroscopic one-temperature model. Such an assumption is not a requirement in the HPS method. The structure of the derived macroscopic models are sometimes quite different from the structures of the corresponding microscopic model. This fact arises due to estimations of physical parameters governing the process of interest, and it will be made clearer in Chapter 3, when we discuss *distributed microstructure*[2] combustion models.

The periodicity assumption, which is based on a translational invariance, implies the existence of a unit cell, or put differently, a representative elementary volume (REV) at the scale of the heterogeneity. The invariance property ensures that the REV remains fixed on its translation to cover the entire structure of interest. However, in recent years, attention has been given to *locally-periodic*[3] structures (see Chechkin and Piatnitski, 1999; Fatima et al., 2011, e.g.). In addition to the locally-periodic treatment, there are problems (see Meier, 2008), specifically in the framework of reactive flows in porous media, in which the REV is assumed to evolve in time. Such homogenization problems are usually treated under the assumption of an *evolving microstructure*. Another aspect concerns the REV used in stochastic homogenization. It has been shown that the results obtained for periodic media upscaling is equivalent to the results obtained for a large class of stochastically random media (Auriault et al., 2009). Thus, this justifies that the periodic assumption on the media is not too restrictive.

The validity of the HPS method is based on the existence of separation of length scales, i.e. the following condition is satisfied:

$$\epsilon = \frac{l}{L} \ll 1, \tag{2.1}$$

where l is the characteristic length of the periodic cell (heterogeneity) and L is the characteristic length of the domain or observation at the macroscopic level. The condition (2.1) provides a small scale parameter ϵ which, through a normalization procedure, allows for a discussion of distinct problems based on some phenomenon of interest. In subsequent sections and in Chapter 3, the following general homogenization procedure as outlined in Auriault (1991):

1. Description of the geometry of the microstructure, and hence the periodic medium of the physical system of interest. The condition of separation of scales allows us

[2]This relates to the continuous distribution of cells at the homogenization limit, where each macroscopic point is associated with a representative model cell. (see Hornung and Showalter, 1990; Hornung, 1997, e.g.).

[3]Locally-periodic means here, very much in the spirit of Bensoussan et al. (1978), that the REV is x-dependent.

to introduce two distinct length scales, which are dimensionless with respect to the normalization of the dimensional variable $\tilde{x} = (x_1, x_2, x_3)$ with the length scales at the REV level and the macroscopic level, i.e.

- macroscopic variable $x = \tilde{x}/L$,
- microscopic variable $y = \tilde{x}/l$,

where x and y are related via the small scale parameter by

$$x = \epsilon y \tag{2.2}$$

$$y = \frac{x}{\epsilon}. \tag{2.3}$$

(2.2) refers to the microscopic viewpoint and (2.3) to the macroscopic viewpoint. In the present study, we consider the macroscopic viewpoint, although the two viewpoints result to the same homogenization limit.

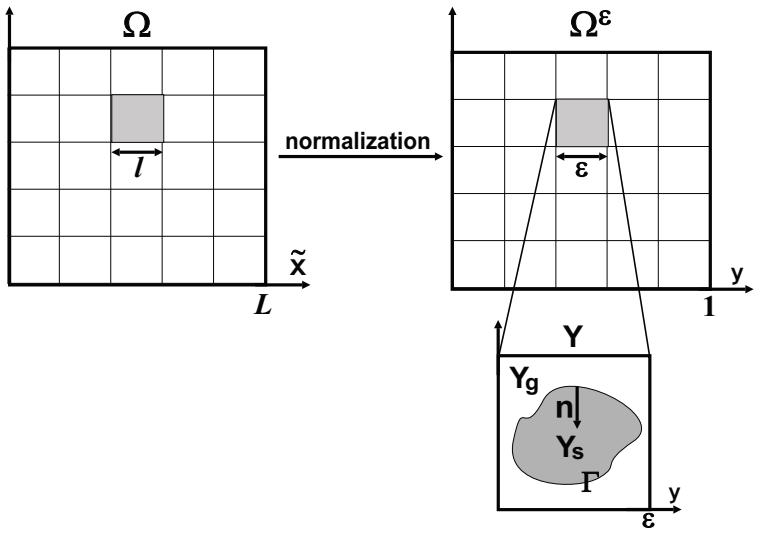

Figure 2.1: Scheme of the macroscopic viewpoint; the representative elementary volume of characteristic length l is normalized with the characteristic size of the domain L; Ω^ϵ is the normalized domain with ϵ-periodically distributed microstructures.

2. Description of the physical process at the pore scale. At this level, it is assumed that the conservation laws, the values of the parameters, the geometry, and the physical quantities which describe the phenomena of interest are known.

3. In the next step, the local problem is nondimensionalized, and then the dimensionless quantities are estimated as a function of powers of the scale parameter ϵ. According to Auriault et al. (2009), the estimation should satisfy

$$\epsilon^{p+1} \ll q \ll \epsilon^{p-1}, \tag{2.4}$$

for any dimensionless quantity q which is of the order $\mathcal{O}(\epsilon^p)$. This step as already pointed out by (Auriault (1991)) is an important stage during which the physics of the problem is taken into account. It is this estimation that determines precisely the structure of the limit problem, which is either a purely macroscopic model or a two-scale model at the upscaled level. The estimation is required before the final step.

4. In the final step, an asymptotic expansion of the form

$$\phi^\epsilon(x) = \phi^{(0)}(x, \frac{x}{\epsilon}) + \epsilon\phi^{(1)}(x, \frac{x}{\epsilon}) + \epsilon^2\phi^{(2)}(x, \frac{x}{\epsilon}) + \mathcal{O}(\epsilon^3), \tag{2.5}$$

is substituted into the normalized local equations, where $\phi^{(i)}, i = 1, 2, \cdots$, are y-periodic and $\phi^{(0)}$, which is of order $\mathcal{O}(1)$ with respect to ϵ in (2.5), is associated with the solution of the homogenized limit problem. For a detailed description of the method and further steps taken to arriving at the homogenization limit, we refer to (see Bensoussan et al., 1978; Sanchez-Palencia, 1980; Hornung, 1997; Auriault et al., 2009, e.g.).

2.2 Formulation of the local problem

This section deals with the mathematical description of the problem at the pore scale. As a first step, we start with the description of the porous structure we have in mind-a thin cellulosic porous material. The main assumption at this stage is that the geometry of the material is periodic, and hence the translational invariance property can be applied. Subsequently, the mathematical description of local processes will be stated, bearing in mind the most important physical phenomenon of interest. Finally, we give a brief discussion of the distributed microstructure combustion model, and end this chapter with few comments on further directions towards the extension of our simplified presentation.

2.2.1 Description of the geometry

Having mentioned that the periodic assumption on the geometry of the medium is not restrictive, it then makes sense to start our description of the medium with such a simplified periodic geometry. In Chapter 5, we will show that for any choice of geometry, the micro-macro upscaling gives an equivalent macroscopic description, which is intrinsic to the material and to the phenomenon of interest. Most porous materials are macroscopically homogeneous at the observational scale. This motivates the development of most purely macroscopic models because of the difficulty in detecting the possibility of a separation in length scales and of the possible inhomogeneity in the considered medium. Thus, the starting point is to reveal the inhomogeneity present in the material structure with the aid of a microscopic. Based on microscopic evidence, the structure of the sample of filter paper consists of a complex perforated arrangement of fibre. This is depicted in Figure 2.2. The pore space and the complex thin-like intersection of fibers are clearly pronounced at

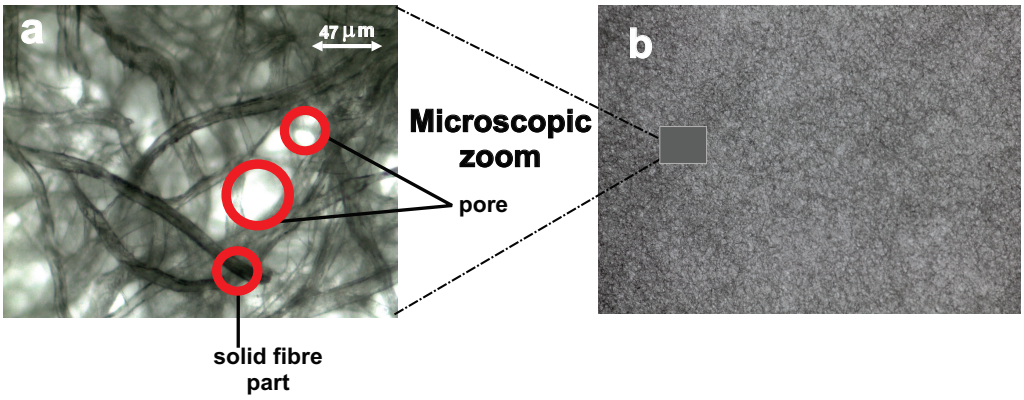

Figure 2.2: A sample of Whatman filter paper showing (a) Microscopic zoom of the sample revealing the perforated fibre structure; the gas-filled parts (pores) and the solid fibre part. (b) the sample at the macroscopic scale. The snapshots are courtesy of N.J Suematsu (Meiji University).

this scale (Figure 2.2a). At the scale of the heterogeneity, air infiltrates the material and

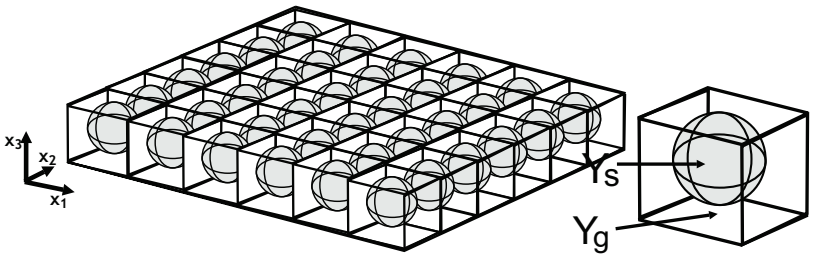

(a) periodic medium (b) The unit cell

Figure 2.3: (a) The periodic medium; (b) Representative elementary volume (REV) showing the gas part Y_g and the solid part Y_s.

interacts with surfaces presented by the solid fibre. Assuming the typical length at the scale of the heterogeneity to be δ, the characteristic length, l, of the REV can be identified, and it is sufficiently large, i.e. $\delta < l$ to represent the features at the pore scale. The constituent of the unit volume consists of a spherical geometry, with a smooth boundary, representative of the solid fibre, which is assumed to be dispersed in a matrix of gas part (see Figure 2.3bb). We assume that the periodic heterogeneous medium (see Figure 2.3a) we have in mind satisfies the following properties:

(i) the typical length L at the macroscopic scale is in the x_1 direction;

(ii) the period l of the structure representing the scale of the heterogeneity is sufficiently small compared to the macroscopic scale;

(iii) the length of the region along x_3-direction is by far small compared to the characteristic lengths in the (x_1, x_2)-directions;

(iv) x_3 has arbitrary periodicity.

Let Ω be a thin sheet of rectangular bounded open set represented by $\Omega = \prod_{j=1}^{3}(0, a_j) \subset \mathbb{R}^3$, with $a_j > 0, j = 1, 2, 3$, and let $\partial\Omega$ be its exterior boundary. The porous medium is endowed with the macroscopic coordinates $\mathbf{x} = (x_1, x_2, x_3)$, and a reference periodicity cell is chosen in $\mathbb{R}^3$:

$$Y := \{(y_1, y_2, y_3) | 0 < y_j < 1, j = 1, 2, 3\}, \tag{2.6}$$

with microscopic coordinates $\mathbf{y} = (y_1, y_2, y_3)$, within which a spherical open set with smooth boundary ∂Y_{s} is represented by:

$$Y_{\mathrm{s}} := \{(y_1, y_2, y_3) | \sum_{j=1}^{3}(y_j - y_j^0)^2 < R^2\} \subset Y. \tag{2.7}$$

In (2.7) R is the radius and $y_j^0, j = 1, 2, 3$, is the centre of the spherical structure and also the centroid of the reference periodicity cell. Henceforth, this structure is referred to as the *solid part*. The solid part is embedded in a pore space $Y_{\mathrm{g}} := Y \setminus \overline{Y}_{\mathrm{s}}$, which is referred to as the *gaseous part*, so that the reference cell can be written as $Y = Y_{\mathrm{g}} \cup \bar{Y}_{\mathrm{s}}$. The boundary ∂Y_{s} represents the interface separating the gas part and the solid part, and ∂Y is the boundaries enclosing the sets in Y and is represented as $S_g := \partial Y$. With the small scale parameter ϵ, the periodicity cell as well as its distinct parts and interior boundary are rescaled and translated to cover the macroscopic domain, i.e.

$$\begin{aligned} Y^\epsilon &:= \{(y_1, y_2, y_3) | 0 < y_j < \epsilon, j = 1, 2, 3\}, \\ Y_s^\epsilon &:= \{(y_1, y_2, y_3) | \sum_{j=1}^{3}(y_j - \epsilon y_j^0)^2 < (\epsilon R)^2\}, \\ Y_g^\epsilon &:= Y^\epsilon \setminus \overline{Y}_s^\epsilon, \end{aligned}$$

so that the translated subsets are represented by

$$Y_{\mathbf{k}}^\epsilon := \{(\overline{y}_1, \overline{y}_2, \overline{y}_3) | \overline{y}_j = y_j + \epsilon k_j, j = 1, 2, 3, (y_1, y_2, y_3) \in Y^\epsilon\}, \ \mathbf{k} = (k_1, k_2, k_3) \in \mathbb{Z}^3.$$

Let the number of cells with respect to the scale parameter ϵ, in each coordinate direction, be defined as $N_j(\epsilon) := |a_j|\epsilon^{-1}$ and the total number of cells in Ω by $N(\epsilon) := \prod_{j=1}^{3} N_j(\epsilon)$. Let $Y_{g,k}^\epsilon = Y_k^\epsilon \setminus \overline{Y}_{s,k}^\epsilon$ be any translated gas part with $Y_{s,k}^\epsilon$, the corresponding solid part. Then the ensemble of the disconnected solid parts is given by

$$\Omega_s^\epsilon := \{(y_1, y_2, y_3) | (y_1, y_2, y_3) \in Y_{s,k}^\epsilon, \mathbf{k} = (k_1, k_2, k_3) \in \mathbb{Z}^3, 0 \leq k_j \leq N_j(\epsilon), j = 1, 2, 3\},$$

such that the matrix of interconnected gas parts can be represented by $\Omega_g^\epsilon := \Omega \setminus \overline{\Omega}_s^\epsilon$. Further, the interior boundaries are represented by

$$\Gamma^\epsilon := \{(y_1, y_2, y_3) | (y_1, y_2, y_3) \in \partial Y_{s,k}^\epsilon, \mathbf{k} = (k_1, k_2, k_3) \in \mathbb{Z}^3, 0 \leq k_j \leq N_j(\epsilon), j = 1, 2, 3\}.$$

2.2.2 Description of the flow field

In this section, the mathematical model of the combustion process occurring on the surface of the solid structure is described. The full fluid dynamics of the problem posed in the porous material follows a creeping flow, but following Fasano et al. (2009) regarding the complications that may arise while investigating the full fluid dynamics, we introduce a simplifying assumption that the flow in the porous medium is a constant *laminar field* $\boldsymbol{u}$ of air in the pore matrix $\Omega_{\mathrm{g}}^{\epsilon}$. The key point justifying this approximation is that, in the smoldering regime we are considering, the mass flow rate is much larger than the mass exchange rate due to combustion; $\boldsymbol{u}$ is not so much influenced by the combustion process (Fasano et al., 2009). Thus, the flow field is given by

$$u^{\epsilon}(\mathbf{x}) = \begin{cases} 0, \mathbf{x} \in \Omega_s^{\epsilon}, \\ \mathbf{v}, \mathbf{x} \in \Omega_g^{\epsilon}, \end{cases} \tag{2.8}$$

where (2.8) implies the restriction of convection to the gas phase region Ω_g^{ϵ}, and hence a spatially periodic flow is assumed, i.e. $u^{\epsilon}(\mathbf{x}) = u(\mathbf{x}, \frac{\mathbf{x}}{\epsilon}) \in \Omega_g^{\epsilon}, \mathbf{y} = \mathbf{x}/\epsilon$, and with the continuous vector field $\mathbf{u}(\mathbf{x}, \mathbf{y})$ defined in $Y_{\mathrm{g}} \times \Omega$ and periodic in $\mathbf{y}$, it satisfies the following incompressibility conditions:

$$\mathrm{div}_{\mathbf{x}}\boldsymbol{u} = 0, \text{ and } \mathrm{div}_{\mathbf{y}}\boldsymbol{u} = 0 \in \mathrm{Y_g}, \text{ and } \boldsymbol{u} \cdot n = 0 \text{ on } \partial Y_{\mathrm{s}},$$

where n is the unit outward normal on ∂Y_{s} with respect to Y_{g}.

2.2.3 Mass transport of the gaseous species

For a combustion process, the flowing gas constitutes a mixture of gaseous chemical species which are governed by mass conservation equations that are similar in form. However, in a simplified presentation, we do not investigate all the gaseous components in the mixture. In particular, we consider the oxygen flow, which is the major component in the gaseous mixture that takes part in the oxidative combustion process. Thus, we assume that its flow is governed by the following convection-diffusion equation

$$\frac{\partial C}{\partial t} + \boldsymbol{u} \cdot \nabla C - \nabla \cdot (D \nabla C) = 0, \quad \boldsymbol{x} \in \Omega_{\mathrm{g}}^{\epsilon}, t > 0, \tag{2.9}$$

where C is the concentration and D is the molecular diffusion coefficient, assumed here to be constant.

2.2.4 Heat transport in the gas and solid phases

The transport of heat in the gas part and the subsequent conduction of heat in the solid part follow from the Fourier law of heat conduction. The gas phase heat equation is governed

by a convection-conduction equation, whereas the predominant mode of heat transport in the solid phase is governed by heat conduction. Thus, we have

$$\mathcal{C}_{\mathrm{g}}\frac{\partial T_{\mathrm{g}}}{\partial t}+\mathcal{C}_{\mathrm{g}}\boldsymbol{u}\cdot\nabla T_{\mathrm{g}}-\nabla\cdot(\lambda_{\mathrm{g}}\nabla T_{\mathrm{g}})=0,\quad \boldsymbol{x}\in\Omega_{\mathrm{g}}^{\epsilon},t>0, \tag{2.10a}$$

$$\mathcal{C}_{\mathrm{s}}\frac{\partial T_{\mathrm{s}}}{\partial t}-\nabla\cdot(\lambda_{\mathrm{s}}\nabla T_{\mathrm{s}})=0,\quad \boldsymbol{x}\in\Omega_{\mathrm{s}}^{\epsilon},t>0, \tag{2.10b}$$

where $C_i=\rho_i c_i$ is the *volumetric heat capacity* of phase i, λ_i is the *heat conductivity* and T_i is the temperature. Since the reaction between the phases is purely heterogeneous and takes place on the surface of the solid, the transport equations are coupled at the pore boundary Γ^{ϵ}.

2.2.5 Description of the chemical process

The chemical process in the considered combustion regime Zik and Moses (1999); Lu and Yortsos (2005a) assumes the following form

$$\text{Solid fuel}+O_2\rightarrow\text{solid product}+\text{gas product}+\text{heat}. \tag{2.11}$$

For an oxygen-limited reaction, the *reaction rate* W is given by a one-step first order reaction with respect to the deficient gaseous reactant. We also assume that adsorption of the reactant on the solid surface is negligible. The temperature-dependent *rate coefficient* k is governed by the *Arrhenius'* law, viz.

$$k(T)=Aexp\left(-\frac{T_a}{T}\right). \tag{2.12}$$

Here, A is the *pre-exponential factor*, T_a is the *activation temperature* of the reaction, and T is the temperature at the gas-solid interface, Γ^{ϵ}, satisfying $T=T_{\mathrm{g}}=T_{\mathrm{s}}$. The micro-heterogeneous reaction, localized on the solid-gas interface, induces coupling terms in form of source/sink terms respectively for the oxygen and heat equations where Q is the *heat release*. The reaction at the surface Γ^{ϵ} is given by the following boundary conditions

Interface conditions

$$(\lambda_{\mathrm{g}}\nabla T_{\mathrm{g}}-\lambda_{\mathrm{s}}\nabla T_{\mathrm{s}})\cdot\boldsymbol{n}=QW(T,C),\qquad \boldsymbol{x}\in\Gamma^{\epsilon},t>0, \tag{2.13a}$$

$$T_{\mathrm{g}}=T_{\mathrm{s}},\qquad \boldsymbol{x}\in\Gamma^{\epsilon},t>0, \tag{2.13b}$$

$$D\nabla C\cdot\boldsymbol{n}=-W(T,C),\qquad \boldsymbol{x}\in\Gamma^{\epsilon},t>0, \tag{2.13c}$$

where $\boldsymbol{n}$ is the outward unit normal vector which points in a direction outside Y_{g}, and $W(T,C)$ is given by

$$W(T,C)=ACexp\left(-\frac{T_a}{T}\right). \tag{2.14}$$

Additionally, the *char product* $\mathcal{R}$, is given by

$$\frac{\partial \mathcal{R}}{\partial t} = W(T, C), \quad \boldsymbol{x} \in \Gamma^{\epsilon}, t > 0. \tag{2.15}$$

So far, the governing equations together with the associated interior coupling conditions have been described. Additionally, the following boundary conditions are prescribed at the exterior boundaries:

Diffusive thermal insulation conditions

$$\boldsymbol{n}\cdot\nabla T_i = 0, \boldsymbol{n}\cdot\nabla C = 0, \quad \partial\Omega \setminus (\{\boldsymbol{x} = 0\} \cup \{\boldsymbol{x} = a_1\}), t > 0. \tag{2.16}$$

Upstream/Downstream boundary conditions

$$T_i = T_{\mathrm{u}}, C = C_{\mathrm{u}}, \qquad \{\boldsymbol{x} = 0\} \cap \partial\Omega, t > 0, \tag{2.17a}$$
$$\boldsymbol{n}\cdot\nabla_{\boldsymbol{x}} T_i = 0, \boldsymbol{n}\cdot\nabla_{\boldsymbol{x}} C = 0, \qquad \{\boldsymbol{x} = a_1\} \cap \partial\Omega, t > 0. \tag{2.17b}$$

Here, u denotes the unburnt or initial values, and $i = g$. The problem is further supplemented with appropriate initial conditions in order to describe the problem fully.

2.2.6 Nondimensionalization

In this section, the system of equations derived in the Section 2.2 are scaled, and hence some dimensionless numbers are introduced, which will allow for the discussion of distinct problems as well as their upscaling. The scaling process fundamentally aids in the estimation of parameters in the system and also to the description of the physics of the phenomena at the microscale. As stated earlier, this is an important step prior to the formal homogenization technique which we will consider in Chapter 3. The spatial-temporal variables are scaled as follows:

$$\boldsymbol{x} = \boldsymbol{x}^* L_c, t = t^* t_c,$$

where L_{c} is the characteristic length scale at the macroscopic level and t_{c}, the characteristic time of the observation. After introducing the following characteristic quantities subscripted with c, First, we introduce some *characteristic values*

$$\begin{aligned}
&\rho_{\mathrm{g}} = \rho_g^* \rho_{\mathrm{gc}}, c_g = c_g^* c_{\mathrm{gc}}, \lambda_{\mathrm{g}} = \lambda_g^* \lambda_{\mathrm{gc}}, T_i = T_i^*(T_b - T_u) + T_u, \\
&\rho_s = \rho_s^* \rho_{\mathrm{sc}}, c_s = c_s^* c_{\mathrm{sc}}, \lambda_{\mathrm{s}} = \lambda_s^* \lambda_{\mathrm{sc}}, A = A_{\mathrm{c}} A^*, Q = Q_{\mathrm{c}} Q^*, \\
&C = C^* C_c, \mathcal{R} = \mathcal{R}^* R_c, D = D^* D_c, \boldsymbol{u} = \mathbf{v} u_c, \Omega = \Omega^* L_{\mathrm{c}},
\end{aligned} \tag{2.18}$$

the dimensionless equations take the following form:

$$\mathcal{C}_{\mathrm{g}}\frac{\partial T_g^*}{\partial t^*} + \mathcal{C}_{\mathrm{g}}\frac{u_{\mathrm{c}}t_{\mathrm{c}}}{L_{\mathrm{c}}}\boldsymbol{v}\cdot\nabla T_g^* - \frac{\mathcal{K}_{\mathrm{gc}}t_{\mathrm{c}}}{L_{\mathrm{c}}^2}\nabla\cdot(\lambda_g^*\nabla T_{\mathrm{g}}^*) = 0, \tag{2.19}$$

$$m\mathcal{C}_{\mathrm{s}}\frac{\partial T_{\mathrm{s}}^*}{\partial t^*} - \frac{\mathcal{K}_{\mathrm{gc}}t_{\mathrm{c}}}{L_{\mathrm{c}}^2}\mathcal{K}\nabla\cdot(\lambda_{\mathrm{s}}^*\nabla T_{\mathrm{s}}^*) = 0, \tag{2.20}$$

where $\mathcal{C}_{\mathrm{g}} = \rho_{\mathrm{g}}^* c_{\mathrm{g}}^*$, and $\mathcal{C}_{\mathrm{s}} = \rho_s^* c_s^*$ are respectively the dimensionless *heat capacities* of the constituents in the gas-phase and solid-phase respectively. Note that the quantities in (2.18) have their usual meanings as given in Section 2.2. The coefficients appearing in (2.19) are defined as:

$$\mathcal{K}_{\mathrm{gc}} := \frac{\lambda_{\mathrm{gc}}}{\rho_{\mathrm{gc}}c_{\mathrm{gc}}}, \mathcal{P}_T := \frac{\mathcal{K}_{\mathrm{gc}}t_{\mathrm{c}}}{L_{\mathrm{c}}^2}, m := \frac{\rho_{\mathrm{sc}}c_{\mathrm{sc}}}{\rho_{\mathrm{gc}}c_{\mathrm{gc}}}, \mathcal{K} := \frac{\lambda_{\mathrm{sc}}}{\lambda_{\mathrm{gc}}},$$

where $\mathcal{K}_{\mathrm{gc}}$ is the gas phase *thermal diffusivity*, $\mathcal{P}_T$, the *ratio of thermal transport* to the time scale of the observation. The *ratio of heat capacities* in the material is denoted as m and the corresponding *ratio of heat conductivities* is $\mathcal{K}$. Further, we define the *temperature of combustion product*, $T_{\mathrm{b}} := T_{\mathrm{u}} + Q_{\mathrm{c}}C_{\mathrm{c}}/\rho_{\mathrm{gc}}c_{\mathrm{gc}}$ and introduce the following global characteristic time scales

$$t_D := \frac{L_c^2}{D_{\mathrm{c}}}, t_A := \frac{L_{\mathrm{c}}}{u_{\mathrm{c}}}, t_{\mathrm{G}} := \frac{L_{\mathrm{c}}}{A_{\mathrm{c}}}, t_R := \frac{R_c}{C_{\mathrm{c}}A_{\mathrm{c}}},$$

where t_D is the *characteristic global diffusion time scale*, t_{A} is the *characteristic global advection time scale*, t_{g} and t_R are respectively the *characteristic time of gas reaction* and the *characteristic time of combustion product*. We introduce also the following characteristic dimensionless numbers

$$\begin{aligned}
\mathcal{P}e_L &:= \frac{L_{\mathrm{c}}u_{\mathrm{c}}}{D_{\mathrm{c}}} = \frac{t_D}{t_{\mathrm{A}}}(\textit{Péclet number}),\\
\mathcal{L}e_{\mathrm{g}} &:= \frac{\mathcal{K}_{\mathrm{gc}}}{D_{\mathrm{c}}}(\textit{gas-phase Lewis number}),\\
\mathcal{D}a &:= \frac{L_cA_{\mathrm{c}}}{D_{\mathrm{c}}} = \frac{t_D}{t_{\mathrm{g}}}(\textit{Damköhler number}).
\end{aligned}$$

We take the characteristic time of diffusion in the subdomain, $\Omega_{\mathrm{g}}^{\epsilon}$, as the characteristic time of the observation at the macroscopic scale, i.e. $t_{\mathrm{c}} = t_D$. Rewriting (2.19) in terms of the introduced dimensionless numbers leads to following:

$$\mathcal{C}_{\mathrm{g}}\frac{\partial T_{\mathrm{g}}^*}{\partial t^*} + \mathcal{C}_{\mathrm{g}}\mathcal{P}e_L\boldsymbol{v}\cdot\nabla T_{\mathrm{g}}^* - \mathcal{L}e_{\mathrm{g}}\nabla\cdot(\lambda_{\mathrm{g}}^*\nabla T_{\mathrm{g}}^*) = 0 \tag{2.21a}$$

$$m\mathcal{C}_{\mathrm{s}}\frac{\partial T_{\mathrm{s}}^*}{\partial t^*} - \mathcal{K}\mathcal{L}e_{\mathrm{g}}\nabla\cdot(\lambda_{\mathrm{s}}^*\nabla T_{\mathrm{s}}^*) = 0. \tag{2.21b}$$

After introducing some simplifications, the corresponding boundary conditions to (2.21a)-(2.21b) are

$$\boldsymbol{n}\cdot(\mathcal{L}e_{\mathrm{g}}\lambda_{\mathrm{g}}^{*}\nabla T_{\mathrm{g}}^{*}-\mathcal{K}\mathcal{L}e_{\mathrm{g}}\lambda_{\mathrm{s}}^{*}\nabla T_{\mathrm{s}}^{*})=\mathcal{D}aQ^{*}W^{*}(T^{*},C^{*}), \tag{2.22a}$$

$$T_{\mathrm{g}}^{*}=T_{\mathrm{s}}^{*}, \tag{2.22b}$$

with

$$W^{*}(T^{*},C^{*})=A^{*}C^{*}\exp\left(-\frac{T_{a}}{T^{*}(T_{b}-T_{u})+T_{u}}\right). \tag{2.23}$$

Similarly, the mass concentration of oxygen in dimensionless form is:

$$\frac{L_{c}^{2}}{D_{\mathrm{c}}t_{\mathrm{c}}}\frac{\partial C^{*}}{\partial t^{*}}+\frac{u_{\mathrm{c}}L_{\mathrm{c}}}{D_{\mathrm{c}}}\boldsymbol{v}\cdot\nabla C^{*}-\nabla\cdot(D^{*}\nabla C^{*})=0, \tag{2.24}$$

where

$$\mathcal{P}_{C}=\frac{L_{c}^{2}}{D_{\mathrm{c}}t_{\mathrm{c}}}\ \textit{the ratio of global characteristic transport times.}$$

With the choice of characteristic time of diffusion t_D, we introduce the Péclet number in (2.24) to get

$$\mathcal{P}_{C}\frac{\partial C^{*}}{\partial t^{*}}+\mathcal{P}e_{L}\boldsymbol{v}\cdot\nabla C^{*}-\nabla\cdot(D^{*}\nabla C^{*})=0. \tag{2.25}$$

The boundary condition corresponding to (2.25) is

$$D^{*}\nabla C^{*}\cdot\boldsymbol{n}=-\mathcal{D}aW^{*}(T^{*},C^{*}). \tag{2.26}$$

The solid char product is given in dimensionless form as

$$\begin{aligned}\frac{\partial\mathcal{R}^{*}}{\partial t^{*}}&=\frac{t_{\mathrm{c}}A_{\mathrm{c}}C_{\mathrm{c}}}{R_{\mathrm{c}}}W^{*}(T^{*},C^{*}),\\&=\frac{t_{D}}{t_{R}}W^{*}(T^{*},C^{*}).\end{aligned} \tag{2.27}$$

Finally, the system is completed with the following scaled initial and boundary conditions:

$$T_{i}^{*}=0,C^{*}=1,\mathcal{R}^{*}=0,\quad \boldsymbol{x}\in\Omega,t=0. \tag{2.28}$$

$$T_{i}^{*}=0,C^{*}=1,\quad \{\boldsymbol{x}=0\}\cap\partial\Omega,t>0, \tag{2.29}$$

$$\boldsymbol{n}\cdot\nabla T_{i}^{*}=0,\boldsymbol{n}\cdot\nabla C^{*}=0,\quad \{\boldsymbol{x}=a_{1}\}\cap\partial\Omega,t>0. \tag{2.30}$$

2.3 Summary

In this chapter, we have described, based on simplified assumptions related to the choice of microstructure, the heat mechanism, the flow and filtration properties, and the filtration combustion of reactive thin porous materials At the pore scale, we used two distinct transport processes, corresponding to the flow of heat and reactants, to model a basic combustion scenario. This is typical to most macroscopic models, in which the equations are introduced directly at the macroscopic level. However, by incorporating the description of material microstructure into the modeling, we intend to develop a system that allows to understand the influence of microstructural properties on the physical problem of interest. This is the main objective of this chapter. We also focussed on the reduction of the pore scale description to its dimensionless form. The latter is crucial (see Auriault, 1991, e.g.,) for the discussions presented in Chapter 3. Here, we basically identified the relevant dimensionless parameters based on the physics of interest.

We also mention some important aspect of the modeling that has been neglected presently. It concerns the role of heat transfer mechanism to the structure formation, the evolution of fingering patterns in terms of the conversion efficiency, and a modeling description resulting in a two-temperature functional equation at the macroscopic level. Although these factors are in the focus of this thesis, we expect that incorporating them into the system will bring us closer to most other models and analysis reported in the literature (see Kagan and Sivashinsky, 1996; Lu and Yortsos, 2005a; Fasano et al., 2009, e.g.).

Presently, we have adopted the classical homogenization approach for the study of flame propagation. Our modeling can be extended to cover problems with "evolving microstructure". This describes a situation where drastic changes in the microstructure due to combustion of the material are taken into consideration. One of the challenges of proceeding in this direction is on the efficient method of integrating the evolving structures in the actual filtration combustion process. Thus, a method for solving the problem of "variable (i.e. evolving) microstructure" may be to consider a situation, resembling to (1.2)–(1.4), in which the conversion efficiency η enters the formulation of the problem, i.e. if the porosity can be related to the amount of material consumed.

The approach in this thesis has the advantage that the periodic averaging procedure shows precisely how the porosity enters the transport and other coefficients. In this way, instead of focusing on the evolving geometry, one may simply focus on the consequence of the changing medium; which is the depletion of the material by combustion. Proceeding in this direction can provide more insights on the influence of variability in geometry, and hence in porosity on the propagation of reaction fronts and then compare this result to the situation in fixed geometries.

Chapter 3

Derivation of macroscopic equations of filtration combustion by periodic homogenization

In this chapter, we consider the homogenization of a counterflow filtration combustion problem, in which a gas containing a gaseous oxidizer is forced opposite to the direction of the reaction front. We have already mentioned in Chapter 1, Section 1.1 that combustion waves resulting from counterflow filtration of a gas are basically driven by conduction. Thus, we will consider homogenization problems that take into account the influence of conductivity contrast that exists between the interacting gaseous and solid phases near the reaction sites. In addition, the form of the homogenization problems derived in this chapter will depend on the proper estimation of the thermodynamic properties of the porous material. For instance, distinct macroscopic combustion models which are based on thermal conductivity of the material will be discussed, which according to the microstructural description introduced in Section 2.2.1, allows to focus on the geometry and thermal properties of the inclusions.

3.1 Porous material with moderately conductive inclusions

3.1.1 Estimation of dimensionless parameters

In this section, we discuss the macroscopic behavior of combustible thin porous materials in which the thermal conductivity of the inclusions is assumed to be comparable[1] to the thermal conductivity of the gas matrix. With respect to the inclusions, the model derived in this section will be referred to as *Moderately Conductive Inclusions* (MCI). This is because the order of magnitude of the conductivity of the inclusions is neither higher nor

[1] In the context of this discussion, "comparable" means that the order of magnitude of the ratio between any two related physical parameters, say of the gas λ_g and the solid phase λ_s, is $\lambda_s = \mathcal{O}(\lambda_g)$.

lower than that of the gas matrix. It will be shown later on, such an estimation generally leads to situations, in which the connectivity of the phases does not affect the form of the homogenized limit problem since no large contrast of conductivity exists. We start off with the system:

$$\mathcal{C}_{\mathrm{g}}\frac{\partial T_{\mathrm{g}}}{\partial t}+\mathcal{C}_{\mathrm{g}}\boldsymbol{v}\cdot\nabla T_{\mathrm{g}}-\nabla\cdot(\lambda_{\mathrm{g}}\nabla T_{\mathrm{g}})=0, \qquad \boldsymbol{x}\in\Omega_{\mathrm{g}}^{\epsilon},t>0, \tag{3.1a}$$

$$\mathcal{C}_{\mathrm{s}}\frac{\partial T_{\mathrm{s}}}{\partial t}-\nabla\cdot(\lambda_{\mathrm{s}}\nabla T_{\mathrm{s}})=0, \qquad \boldsymbol{x}\in\Omega_{\mathrm{s}}^{\epsilon},t>0, \tag{3.1b}$$

$$T_{\mathrm{g}}=T_{\mathrm{s}}, \qquad \boldsymbol{x}\in\Gamma^{\epsilon},t>0, \tag{3.1c}$$

$$\boldsymbol{n}\cdot(\lambda_{\mathrm{g}}\nabla T_{\mathrm{g}}-\lambda_{\mathrm{s}}\nabla T_{\mathrm{s}})=\epsilon QW(T,C), \qquad \boldsymbol{x}\in\Gamma^{\epsilon},t>0. \tag{3.1d}$$

The first step is to assume that solutions to the unknown fields in (3.1a)-(3.1d) follow a two-scale formal asymptotic expansion, namely:

$$T_i(\boldsymbol{x},t)=T_i^{(0)}(\boldsymbol{x},\boldsymbol{y},t)+\epsilon T_i^{(1)}(\boldsymbol{x},\boldsymbol{y},t)+\epsilon^2T_i^{(2)}(\boldsymbol{x},\boldsymbol{y},t)+\mathcal{O}(\epsilon^3), \tag{3.2a}$$

$$C(\boldsymbol{x},t)=C^{(0)}(\boldsymbol{x},\boldsymbol{y},t)+\epsilon C^{(1)}(\boldsymbol{x},\boldsymbol{y},t)+\epsilon^2C^{(2)}(\boldsymbol{x},\boldsymbol{y},t)+\mathcal{O}(\epsilon^3), \tag{3.2b}$$

where $T_i^{(n)}$ and $C^{(n)}, n=1,2,\ldots, i=\{\mathrm{g},\mathrm{s}\}$ are Y periodic in $\boldsymbol{y}$ with $\boldsymbol{y}=\dfrac{\boldsymbol{x}}{\epsilon}$. Due to the scale separation $(x,\dfrac{x}{\epsilon})$, the unknowns in (3.2a) and (3.2b) are functions of three variables: $\boldsymbol{x},\boldsymbol{y}$ and t. Consequently, we transform the derivatives through the chain rule:

$$\nabla_{\boldsymbol{x}}=\nabla_{\boldsymbol{x}}+\frac{1}{\epsilon}\nabla_{\boldsymbol{y}}. \tag{3.3}$$

Applying the expansions (3.2a)-(3.2b), using (3.3) and collecting terms with the same powers of ϵ, we obtain the following sequence of boundary value problems:

Boundary value problem for $T_{\mathrm{g}}^{(0)}$ and $T_{\mathrm{s}}^{(0)}$:

$$\begin{cases} -\nabla_{\boldsymbol{y}}\cdot\lambda_{\mathrm{g}}(\nabla_{\boldsymbol{y}}T_{\mathrm{g}}^{(0)})=0, & \boldsymbol{y}\in Y_{\mathrm{g}},\\ -\nabla_{\boldsymbol{y}}\cdot\lambda_{\mathrm{s}}(\nabla_{\boldsymbol{y}}T_{\mathrm{s}}^{(0)})=0, & \boldsymbol{y}\in Y_{\mathrm{s}},\\ T_{\mathrm{g}}^{(0)}=T_{\mathrm{s}}^{(0)}, & \boldsymbol{y}\in\partial Y_{\mathrm{s}},\\ (\lambda_{\mathrm{g}}\nabla_{\boldsymbol{y}}T_{\mathrm{g}}^{(0)}-\lambda_{\mathrm{s}}\nabla_{\boldsymbol{y}}T_{\mathrm{s}}^{(0)})\cdot\boldsymbol{n}=0, & \boldsymbol{y}\in\partial Y_{\mathrm{s}},\\ T_{\mathrm{g}}^{(0)} \text{ and } T_{\mathrm{g}}^{(0)} \text{ are } Y \text{ periodic.} \end{cases} \tag{3.4}$$

By introducing in (3.4) the following forms

$$\begin{aligned} T^{(n)}(\boldsymbol{x},\boldsymbol{y},t)&=T_{\mathrm{g}}^{(n)}\chi_{Y_{\mathrm{g}}}(\boldsymbol{y})+T_{\mathrm{g}}^{(n)}\chi_{Y_{\mathrm{s}}}(\boldsymbol{y}),\\ \lambda(y)&=\lambda_{\mathrm{g}}\chi_{Y_{\mathrm{g}}}(\boldsymbol{y})+\lambda_{\mathrm{s}}\chi_{Y_{\mathrm{s}}}(\boldsymbol{y}), \end{aligned} \tag{3.5}$$

we can rewrite (3.4) as

$$\begin{cases} \nabla_{\boldsymbol{y}} \cdot (\lambda \nabla_{\boldsymbol{y}} T^{(0)}) = 0, & \boldsymbol{y} \in Y, \\ \left[T^{(0)}\right]_{\partial Y_{\mathrm{s}}} = 0, & \boldsymbol{y} \in \partial Y_{\mathrm{s}}, \\ \left[\lambda \nabla_{\boldsymbol{y}} T^{(0)}\right]_{\partial Y_{\mathrm{s}}} \cdot \boldsymbol{n} = 0, & \boldsymbol{y} \in \partial Y_{\mathrm{s}}, \\ T^{(0)} \text{ is } Y \text{ periodic}, \end{cases} \tag{3.6}$$

where $[\,\cdot\,]_{\partial Y_{\mathrm{s}}}$ represents the jump $T_{\mathrm{g}} - T_{\mathrm{s}}$ across the interface ∂Y_{s}. Problem (3.6) involves only derivatives in $\boldsymbol{y}$, while $\boldsymbol{x}$ and t are present as parameters. The only periodic solution satisfying (3.6) for the local heat problem is that $T^{(0)}(\boldsymbol{x}, \boldsymbol{y}, t)$ must be a constant, i.e.

$$T^{(0)}(\boldsymbol{x}, \boldsymbol{y}, t) = T^{0}(\boldsymbol{x}, t). \tag{3.7}$$

By using (3.5), we write the following boundary value problem for $T^{(1)}$:

Boundary value problem for $T_{\mathrm{g}}^{(1)}$ and $T_{\mathrm{s}}^{(1)}$:

$$\begin{cases} \nabla_{\boldsymbol{y}} \cdot (\lambda(\nabla_{\boldsymbol{y}} T^{(1)} + \nabla_{\boldsymbol{x}} T^{(0)})) = 0, & \boldsymbol{y} \in Y, \\ \left[T^{(1)}\right]_{\partial Y_{\mathrm{s}}} = 0, & \boldsymbol{y} \in \partial Y_{\mathrm{s}}, \\ \left[\lambda(\nabla_{\boldsymbol{y}} T^{(1)} + \nabla_{\boldsymbol{x}} T^{(0)})\right]_{\partial Y_{\mathrm{s}}} \cdot \boldsymbol{n} = 0, & \boldsymbol{y} \in \partial Y_{\mathrm{s}}, \\ T^{(1)} \text{ is } Y \text{ periodic}, \end{cases} \tag{3.8}$$

The linearity of (3.8) makes it possible to consider the following *cell problems* for the components of the vector, $\boldsymbol{\mathcal{N}} = (\mathcal{N}_1, \mathcal{N}_2, \mathcal{N}_3)$, with each problem corresponding to a unit macroscopic gradient $\nabla_{\boldsymbol{x}} T^{(0)} = e_j, j = 1, 2, 3$, where e_j is the canonical orthonormal basis in $\mathbb{R}^3$

$$\begin{cases} \nabla_{\boldsymbol{y}} \cdot (\lambda(\nabla_{\boldsymbol{y}} \boldsymbol{\mathcal{N}} + \mathbf{I})) = 0, & \boldsymbol{y} \in Y, \\ [\boldsymbol{\mathcal{N}}]_{\partial Y_{\mathrm{s}}} = 0, & \boldsymbol{y} \in \partial Y_{\mathrm{s}}, \\ [\lambda(\nabla_{\boldsymbol{y}} \boldsymbol{\mathcal{N}} + \mathbf{I})]_{\partial Y_{\mathrm{s}}} \cdot \boldsymbol{n} = 0, & \boldsymbol{y} \in \partial Y_{\mathrm{s}}, \\ \boldsymbol{\mathcal{N}} = 0, \boldsymbol{\mathcal{N}} \text{ is } Y \text{ periodic}, \end{cases} \tag{3.9}$$

Therefore, the solution to the problem (3.8) can be written as

$$T^{(1)}(\boldsymbol{x}, \boldsymbol{y}, t) = \boldsymbol{\mathcal{N}}(\boldsymbol{y}) \cdot \nabla_{\boldsymbol{x}} T^{(0)}(\boldsymbol{x}, t) + \overline{T}^{(1)}(\boldsymbol{x}, t). \tag{3.10}$$

In (3.10), $\boldsymbol{\mathcal{N}}$ is the vector satisfying (3.9) and $\overline{T}^{(1)}(\boldsymbol{x}, t)$ is basically the average w.r.t. y over $T^{(1)}(\boldsymbol{x}, \boldsymbol{y}, t)$. Again, using the more compact form (3.5), the boundary value problem for $T_{\mathrm{g}}^{(2)}$ and $T_{\mathrm{s}}^{(2)}$ is given viz.

Boundary value problem for $T_{\mathrm{g}}^{(2)}$ and $T_{\mathrm{s}}^{(2)}$:

$$\begin{cases} (\mathcal{C}_{\mathrm{g}}+\mathcal{C}_{\mathrm{s}})\dfrac{\partial T^{(0)}}{\partial t}-\nabla_{\boldsymbol{y}}\cdot(\lambda(\nabla_{\boldsymbol{y}}T^{(2)}+\nabla_{\boldsymbol{x}}T^{(1)}))- & \\ \nabla_{\boldsymbol{x}}\cdot(\lambda(\nabla_{\boldsymbol{y}}T^{(1)}+\nabla_{\boldsymbol{x}}T^{(0)}))+\mathcal{C}_{\mathrm{g}}\boldsymbol{v}\cdot\nabla_{\boldsymbol{x}}T^{(0)}=0, & \boldsymbol{y}\in Y \\ \left[T^{(2)}\right]_{\partial Y_{\mathrm{s}}}=0, & \boldsymbol{y}\in\partial Y_{\mathrm{s}}, \\ \left[\lambda(\nabla_{\boldsymbol{y}}T^{(2)}+\nabla_{\boldsymbol{x}}T^{(1)})\right]_{\partial Y_{\mathrm{s}}}\cdot\boldsymbol{n}=QW(T^{(0)},C^{(0)}), & \boldsymbol{y}\in\partial Y_{\mathrm{s}}, \\ T^{(2)} \text{ is } Y \text{ periodic.} & \end{cases} \tag{3.11}$$

The existence of $T^{(2)}$ enforces a compatibility condition that involves taking the mean of (3.11), applying the divergence theorem and using the prescribed conditions on ∂Y_{s}, i.e.

$$\begin{aligned} &-\frac{1}{|Y|}\int_{Y}\nabla_{\boldsymbol{y}}\cdot(\lambda(\nabla_{\boldsymbol{y}}T^{(2)}+\nabla_{\boldsymbol{x}}T^{(1)})dY=-\cdots \\ &\frac{1}{|Y|}\int_{S_g}\lambda(\nabla_{\boldsymbol{y}}T^{(2)}+\nabla_{\boldsymbol{x}}T^{(1)})\cdot\boldsymbol{n}dS-\frac{1}{|Y|}\int_{\partial Y_{\mathrm{s}}}\lambda(\nabla_{\boldsymbol{y}}T^{(2)}+\nabla_{\boldsymbol{x}}T^{(1)})\cdot\boldsymbol{n}dS \end{aligned} \tag{3.12}$$

The first integral at the right-hand side of (3.12) vanishes due to periodicity in Y and the second integral leads to

$$\frac{1}{|Y|}\int_{\partial Y_{\mathrm{s}}}-QW(T^{(0)},C^{(0)})dS=-\frac{|\partial Y_{\mathrm{s}}|}{|Y|}QW(T^{(0)},C^{(0)}) \tag{3.13}$$

Also, we obtain the following averages:

$$\frac{\partial T^{(0)}}{\partial t}\left[\frac{1}{|Y|}\int_{Y}(\mathcal{C}_{\mathrm{g}}+\mathcal{C}_{\mathrm{s}})dY\right]=\mathcal{C}^{\mathrm{eff}}\frac{\partial T^{(0)}}{\partial t}, \tag{3.14}$$

$$\boldsymbol{v}\cdot\nabla_{\boldsymbol{x}}T^{(0)}\frac{1}{|Y|}\int_{Y_{\mathrm{g}}}\mathcal{C}_{\mathrm{g}}dY=\phi\mathcal{C}_{\mathrm{g}}\boldsymbol{v}\cdot\nabla_{\boldsymbol{x}}T^{(0)}. \tag{3.15}$$

Further, we see, by using (3.10), that

$$\nabla_{\boldsymbol{y}}T^{(1)}+\nabla_{\boldsymbol{x}}T^{(0)}=(\nabla_{\boldsymbol{y}}\boldsymbol{\mathcal{N}}+\mathbf{I})\nabla_{\boldsymbol{x}}T^{(0)}. \tag{3.16}$$

Using (3.16), It follows from (3.11) and using the fact that the integration with respect to $\boldsymbol{y}$ commutes with the derivative with respect to $\boldsymbol{x}$, we have

$$\int_{Y}\nabla_{\boldsymbol{x}}\cdot(\lambda(\nabla_{\boldsymbol{y}}T^{(1)}+\nabla_{\boldsymbol{x}}T^{(0)}))dY=\nabla_{\boldsymbol{x}}\cdot\left(\left(\frac{1}{|Y|}\int_{Y}\lambda(\nabla_{\boldsymbol{y}}\boldsymbol{\mathcal{N}}+\mathbf{I})dY\right)\nabla_{\boldsymbol{x}}T^{(0)}\right) \tag{3.17}$$

Finally, the macroscopic description is viz.

$$\mathcal{C}^{\text{eff}}\frac{\partial T^{(0)}}{\partial t} - \nabla_{\boldsymbol{x}}\cdot(\lambda^{\text{eff}}\nabla_{\boldsymbol{x}}T^{(0)}) + \phi\mathcal{C}_{\text{g}}\boldsymbol{v}\cdot\nabla_{\boldsymbol{x}}T^{(0)} = \phi^{s}QW(T^{(0)}, C^{(0)}), \tag{3.18}$$

with

$$\lambda_{ij}^{\text{eff}} = \frac{1}{|Y|}\left(\int\limits_{Y_{\text{g}}}\lambda_{\text{g}}(I_{ij} + \frac{\partial\mathcal{N}_{\text{g}}^{j}}{\partial y_i})dY + \int\limits_{Y_{\text{s}}}\lambda_{\text{s}}(I_{ij} + \frac{\partial\mathcal{N}_{\text{s}}^{j}}{\partial y_i})dY\right), \quad i,j = 1,2,3 \tag{3.19}$$

$$\mathcal{C}^{\text{eff}} = \frac{1}{|Y|}\left(\int\limits_{Y_{\text{g}}}\mathcal{C}_{\text{g}}dY + \int\limits_{Y_{\text{s}}}\mathcal{C}_{\text{s}}dY\right) \tag{3.20}$$

$$= \phi\mathcal{C}_{\text{g}} + (1-\phi)\mathcal{C}_{\text{s}}, \tag{3.21}$$

where ϕ denotes here the porosity of the material.

3.2 Porous material with highly conductive inclusions

In this section, we discuss the homogenization problem of the local heat model derived in Section 2.2.4 in a framework of high contrast in thermal conductivity. As pointed out earlier (see Olson et al., 1998; Wahle et al., 2003; Zik and Moses, 1999, e.g.)), an important mode of heat transfer for counterflow smolder propagation is solid phase heat conduction. Therefore, we analyze the macroscopic behavior of a porous solid fuel, in which the thermal conductivity of the inclusion is high compared to the matrix (gaseous) thermal conductivity. Thus, we refer to the derived model as the *Highly Conductive Inclusions* (HCI).

3.2.1 Estimation of dimensionless parameters

Prior to the introduction of the asymptotic expansions in the conservation laws, we start with the estimation of the dimensionless parameters introduced in Section 2.2.6. Since the more thermal conductive inclusion Y_{s} is not interconnected, and hence the mechanism of the flow is dominated by the gaseous phase Y_{g}, we choose the time of diffusion in the matrix at the macroscopic scale as the characteristic time of observation t_{c}:

$$t_{\text{c}} = \frac{L_{\text{c}}^{2}}{D_{\text{c}}} \tag{3.22}$$

The contrast of thermal conductivity is such that we assume the following conductivity ratio:

$$\mathcal{K} = \frac{\lambda_{\text{sc}}}{\lambda_{\text{gc}}} = \mathcal{O}(\epsilon^{-1}). \tag{3.23}$$

Alternatively, (3.23) can also be estimated following the line of argument in Lewandowska et al. (2004, 2005); Szymkiewicz (2004): Assuming the time of heat diffusion in the matrix to be the characteristic time of observation at the macroscopic level. We have

$$t_{\mathrm{c}} = \frac{L_{\mathrm{c}}^2}{\mathcal{K}_{\mathrm{gc}}}, \quad \mathcal{K}_{\mathrm{gc}} = \frac{\lambda_{\mathrm{gc}}}{\rho_{\mathrm{gc}} c_{\mathrm{gc}}} \text{ (cf. Section 2.2.6).} \tag{3.24}$$

Then, the ratio (3.23) can be estimated from the ratio of thermal diffusivity:

$$\frac{\mathcal{K}_{\mathrm{sc}}}{\mathcal{K}_{\mathrm{gc}}} = \frac{\lambda_{\mathrm{sc}}}{\lambda_{\mathrm{gc}}} \frac{\rho_{\mathrm{gc}} c_{\mathrm{gc}}}{\rho_{\mathrm{sc}} c_{\mathrm{sc}}}, \tag{3.25}$$

such that we assume the following estimates:

$$\frac{\lambda_{\mathrm{sc}}}{\lambda_{\mathrm{gc}}} = \mathcal{O}(\epsilon^{-1}), \quad \frac{\rho_{\mathrm{gc}} c_{\mathrm{gc}}}{\rho_{\mathrm{sc}} c_{\mathrm{sc}}} = \mathcal{O}(1), \text{ (cf. Section 2.2.6).} \tag{3.26}$$

Other estimates of dimensionless parameters include: $Pe_L = \mathcal{O}(1)$, advection is comparable to mass diffusion at the macroscopic scale; $\mathcal{D}a$, assumes a diffusion-controlled regime at the macroscopic scale. The estimates gives rise to the following normalized equations with respect to ϵ :

$$\mathcal{C}_{\mathrm{g}} \frac{\partial T_{\mathrm{g}}}{\partial t} + \mathcal{C}_{\mathrm{g}} \boldsymbol{v} \cdot \nabla T_{\mathrm{g}} - \nabla \cdot (\lambda_{\mathrm{g}} \nabla T_{\mathrm{g}}) = 0, \qquad \boldsymbol{x} \in \Omega_{\mathrm{g}}^{\epsilon}, t > 0, \tag{3.27a}$$

$$\epsilon \mathcal{C}_{\mathrm{s}} \frac{\partial T_{\mathrm{s}}}{\partial t} - \nabla \cdot (\lambda_{\mathrm{s}} \nabla T_{\mathrm{s}}) = 0, \qquad \boldsymbol{x} \in \Omega_{\mathrm{s}}^{\epsilon}, t > 0, \tag{3.27b}$$

$$T_{\mathrm{g}} = T_{\mathrm{s}}, \qquad \boldsymbol{x} \in \Gamma^{\epsilon}, t > 0, \tag{3.27c}$$

$$\boldsymbol{n} \cdot (\epsilon \lambda_{\mathrm{g}} \nabla T_{\mathrm{g}} - \lambda_{\mathrm{s}} \nabla T_{\mathrm{s}}) = \epsilon^2 Q W(T, C), \qquad \boldsymbol{x} \in \Gamma^{\epsilon}, t > 0. \tag{3.27d}$$

We now solve the following boundary value problems corresponding to the ϵ^{-2} term.

Boundary value problem for $T_{\mathrm{s}}^{(0)}$ and $T_{\mathrm{g}}^{(0)}$

$$\begin{cases} \nabla_{\boldsymbol{y}} \cdot (\lambda_{\mathrm{s}} \nabla_{\boldsymbol{y}} T_{\mathrm{s}}^{(0)}) = 0, & \boldsymbol{y} \in Y_{\mathrm{s}} \\ \lambda_{\mathrm{s}} \nabla_{\boldsymbol{y}} T_{\mathrm{s}}^{(0)} \cdot \boldsymbol{n} = 0, & \boldsymbol{y} \in \partial Y_{\mathrm{s}}, \end{cases} \tag{3.28}$$

whose solution has the form

$$T_{\mathrm{s}}^{(0)}(\boldsymbol{x}, \boldsymbol{y}) = T_{\mathrm{s}}^{(0)}(\boldsymbol{x}), \tag{3.29}$$

while for the problem posed in Y_{g}

$$\begin{cases} \nabla_{\boldsymbol{y}} \cdot (\lambda_{\mathrm{g}} \nabla_{\boldsymbol{y}} T_{\mathrm{g}}^{(0)}) = 0, & \boldsymbol{y} \in Y_{\mathrm{g}} \\ T_{\mathrm{g}}^{(0)} = T_{\mathrm{s}}^{(0)}(\boldsymbol{x}), & \boldsymbol{y} \in \partial Y_{\mathrm{s}}, \end{cases} \tag{3.30}$$

we obtain the following solution:

$$T_{\mathrm{s}}^{(0)}(\boldsymbol{x},\boldsymbol{y}) = T_{\mathrm{s}}^{(0)}(\boldsymbol{x}) = T^{(0)}(\boldsymbol{x}). \tag{3.31}$$

Since $T_{\mathrm{s}}^{(0)}$ and $T_{\mathrm{g}}^{(0)}$ are $\boldsymbol{y}$-independent, all subsequent spatial derivatives in $\boldsymbol{y}$ vanishes. The next problem uses the ϵ^{-1} term of $T_{\mathrm{s}}^{(0)}$ and the ϵ^0 term of the interface condition:

Boundary value problem for $T_{\mathrm{s}}^{(1)}$

$$\begin{cases} \nabla_{\boldsymbol{y}}\cdot(\lambda_{\mathrm{s}}(\nabla_{\boldsymbol{y}}T_{\mathrm{s}}^{(1)} + \nabla_{\boldsymbol{x}}T^{(0)})) = 0, & \boldsymbol{y}\in Y_{\mathrm{s}} \\ \lambda_{\mathrm{s}}(\nabla_{\boldsymbol{y}}T_{\mathrm{s}}^{(1)} + \nabla_{\boldsymbol{x}}T^{(0)})\cdot\boldsymbol{n} = 0, & \boldsymbol{y}\in \partial Y_{\mathrm{s}}. \end{cases} \tag{3.32}$$

The problem (3.32) is different from the problems considered earlier. We multiply the terms in (3.32) by $\boldsymbol{y}\cdot\nabla_{\boldsymbol{x}}T^{(0)}+\overline{T}_{\mathrm{s}}^{(1)}$, integrating by parts over Y_{s}, and using the prescribed condition on ∂Y_{s} :

$$\begin{aligned} &\int\limits_{Y_{\mathrm{s}}} \nabla_{\boldsymbol{y}}\cdot(\lambda_{\mathrm{s}}(\nabla_{\boldsymbol{y}}T_{\mathrm{s}}^{(1)} + \nabla_{\boldsymbol{x}}T^{(0)}))(\boldsymbol{y}\cdot\nabla_{\boldsymbol{x}}T^{(0)} + \overline{T}_{\mathrm{s}}^{(1)})dY \\ &= \int\limits_{Y_{\mathrm{s}}} \lambda_{\mathrm{s}}(\nabla_{\boldsymbol{y}}T_{\mathrm{s}}^{(1)} + \nabla_{\boldsymbol{x}}T^{(0)})^2 dY - \int\limits_{\partial Y_{\mathrm{s}}} \boldsymbol{n}\cdot\lambda_{\mathrm{s}}(\nabla_{\boldsymbol{y}}T_{\mathrm{s}}^{(1)} + \nabla_{\boldsymbol{x}}T^{(0)})(\boldsymbol{y}\cdot\nabla_{\boldsymbol{x}}T^{(0)} + \overline{T}_{\mathrm{s}}^{(1)})dS \\ &= \int\limits_{Y_{\mathrm{s}}} \lambda_{\mathrm{s}}(\nabla_{\boldsymbol{y}}T_{\mathrm{s}}^{(1)} + \nabla_{\boldsymbol{x}}T^{(0)})^2 dY = 0. \end{aligned} \tag{3.33}$$

The positivity of λ_{s} implies that $\nabla_{\boldsymbol{y}}T^{(1)} + \nabla_{\boldsymbol{x}}T^{(0)} = 0$ a.e. in Y_{s}. Thus, we obtain

$$T_{\mathrm{s}}^{(1)}(\boldsymbol{x},\boldsymbol{y}) = -\boldsymbol{y}\cdot\nabla_{\boldsymbol{x}}T^{(0)} + \overline{T}^{(1)}(\boldsymbol{x}) \text{ for } x\in\Omega, y\in Y_{\mathrm{s}} \tag{3.34}$$

Boundary value problem for $T_{\mathrm{g}}^{(1)}$

$$\begin{cases} \nabla_{\boldsymbol{y}}\cdot(\lambda_{\mathrm{g}}(\nabla_{\boldsymbol{y}}T_{\mathrm{g}}^{(1)} + \nabla_{\boldsymbol{x}}T^{(0)})) = 0, & \boldsymbol{y}\in Y_{\mathrm{g}} \\ T_{\mathrm{g}}^{(1)} = T_{\mathrm{s}}^{(1)} = -\boldsymbol{y}\cdot\nabla_{\boldsymbol{x}}T^{(0)} + \overline{T}^{(1)}(\boldsymbol{x}), & \boldsymbol{y}\in \partial Y_{\mathrm{s}}, \end{cases} \tag{3.35}$$

where $\nabla_{\boldsymbol{x}}T^{(0)}$ and $\overline{T}^{(1)}(\boldsymbol{x})$ are taken as forcing terms. The solution of (3.35) can be written in the form:

$$T_{\mathrm{g}}^{(1)}(\boldsymbol{x},\boldsymbol{y}) = \boldsymbol{\mathcal{N}}(\boldsymbol{y})\cdot\nabla_{\boldsymbol{x}}T^{(0)} + \overline{T}^{(1)}(\boldsymbol{x}), \tag{3.36}$$

where the vector $\boldsymbol{\mathcal{N}}(\boldsymbol{y})$ is the solution of the following boundary value problem

$$\begin{cases} \nabla_{\boldsymbol{y}}\cdot(\lambda_{\mathrm{g}}(\nabla_{\boldsymbol{y}}\boldsymbol{\mathcal{N}} + \mathbf{I})) = 0, & \boldsymbol{y}\in Y_{\mathrm{g}} \\ \boldsymbol{\mathcal{N}} + \boldsymbol{y} = 0, & \boldsymbol{y}\in \partial Y_{\mathrm{s}}. \end{cases} \tag{3.37}$$

For the macroscopic equations, we look at the ϵ^0 term from $T_{\mathrm{g}}^{(2)}$ and the ϵ^1 term from $T_{\mathrm{s}}^{(3)}$, i.e.

$$\begin{aligned}
&\mathcal{C}_{\mathrm{g}}\frac{\partial T^{(0)}}{\partial t} = \nabla_{\boldsymbol{y}}\cdot(\lambda_{\mathrm{g}}(\nabla_{\boldsymbol{y}}T_{\mathrm{g}}^{(2)} + \nabla_{\boldsymbol{x}}T_{\mathrm{g}}^{(1)}))+\\
&\nabla_{\boldsymbol{x}}\cdot(\lambda_{\mathrm{g}}(\nabla_{\boldsymbol{y}}T_{\mathrm{g}}^{(1)} + \nabla_{\boldsymbol{x}}T^{(0)})) - \mathcal{C}_{\mathrm{g}}\boldsymbol{v}\cdot\nabla_{\boldsymbol{x}}T_{\mathrm{g}}^{(0)}, \quad \boldsymbol{y}\in Y_{\mathrm{g}},\\
&\mathcal{C}_{\mathrm{s}}\frac{\partial T^{(0)}}{\partial t} = \nabla_{\boldsymbol{y}}\cdot(\lambda_{\mathrm{s}}(\nabla_{\boldsymbol{y}}T_{\mathrm{s}}^{(3)} + \nabla_{\boldsymbol{x}}T_{\mathrm{s}}^{(2)})) + \nabla_{\boldsymbol{x}}\cdot(\lambda_{\mathrm{s}}(\nabla_{\boldsymbol{y}}T_{\mathrm{s}}^{(2)} + \nabla_{\boldsymbol{x}}T_{\mathrm{s}}^{(1)})), \quad \boldsymbol{y}\in Y_{\mathrm{s}},\\
&\lambda_{\mathrm{g}}(\nabla_{\boldsymbol{y}}T_{\mathrm{g}}^{(2)} + \nabla_{\boldsymbol{x}}T_{\mathrm{g}}^{(1)})\cdot\boldsymbol{n} = \lambda_{\mathrm{s}}(\nabla_{\boldsymbol{y}}T_{\mathrm{s}}^{(3)} + \nabla_{\boldsymbol{x}}T_{\mathrm{s}}^{(2)})\cdot\boldsymbol{n} + QW(T^{(0)}, C^{(0)}), \quad \boldsymbol{y}\in\partial Y_{\mathrm{s}}.
\end{aligned} \tag{3.38}$$

Averaging (3.38) over Y_{g} and Y_{s}, and using the prescribed boundary condition, we are led to

$$\begin{aligned}
&((1-\phi)\mathcal{C}_{\mathrm{s}} + \phi\mathcal{C}_{\mathrm{g}})\frac{\partial T^{(0)}}{\partial t} + \phi\mathcal{C}_{\mathrm{g}}\boldsymbol{v}\cdot\nabla_{\boldsymbol{x}}T^{(0)} = \frac{1}{|Y|}\nabla_{\boldsymbol{x}}\cdot\left(\int\limits_{Y_{\mathrm{g}}}\lambda_{\mathrm{g}}(\nabla_{\boldsymbol{y}}T_{\mathrm{g}}^{(1)} + \nabla_{\boldsymbol{x}}T^{(0)})dY\right) +\\
&\frac{1}{|Y|}\nabla_{\boldsymbol{x}}\cdot\left(\int\limits_{Y_{\mathrm{s}}}\lambda_{\mathrm{s}}(\nabla_{\boldsymbol{y}}T_{\mathrm{s}}^{(2)} + \nabla_{\boldsymbol{x}}T_{\mathrm{s}}^{(1)})dY\right) + \phi^s QW(T^{(0)}, C^{(0)}).
\end{aligned} \tag{3.39}$$

Since $T_{\mathrm{s}}^{(2)}$ is unknown, we transform the integrals by identifying the heat fluxes in each constituent (cf. Lewandowska et al., 2005):

$$q_{\mathrm{g}} = \lambda_{\mathrm{g}}(\nabla_{\boldsymbol{y}}T_{\mathrm{g}}^{(1)} + \nabla_{\boldsymbol{x}}T^{(0)}), \tag{3.40a}$$

$$q_{\mathrm{s}} = \lambda_{\mathrm{g}}(\nabla_{\boldsymbol{y}}T_{\mathrm{g}}^{(2)} + \nabla_{\boldsymbol{x}}T_{\mathrm{s}}^{(1)}). \tag{3.40b}$$

The flux in (3.40a) satisfy the following dyadic product identity

$$q_{ik} = \frac{\partial}{\partial y_j}(y_k q_{ij}), \quad \text{where } q_i = \nabla_{\boldsymbol{y}}\cdot(\boldsymbol{y}\otimes q_i), i = \{\mathrm{g},\mathrm{s}\},\ k,j = 1,2,3.$$

Since the solid inclusions are completely embedded in the matrix, it makes sense to apply the divergence theorem to the integrals in (3.39), i.e.

$$\int\limits_{Y_{\mathrm{g}}} q_{\mathrm{g}}dY = \int\limits_{\partial Y_{\mathrm{s}}}(\boldsymbol{y}\otimes q_{\mathrm{g}})\cdot\boldsymbol{n}dS + \int\limits_{S_{\mathrm{g}}}(\boldsymbol{y}\otimes q_{\mathrm{g}})\cdot\boldsymbol{n}dS \tag{3.41a}$$

$$\int\limits_{Y_{\mathrm{s}}} q_{\mathrm{s}}dY = -\int\limits_{\partial Y_{\mathrm{s}}}(\boldsymbol{y}\otimes q_{\mathrm{s}})\cdot\boldsymbol{n}dS, \tag{3.41b}$$

$$(q_{\mathrm{g}} - q_{\mathrm{s}})\cdot\boldsymbol{n} = 0, \quad \boldsymbol{y}\in\partial Y_{\mathrm{s}}. \tag{3.41c}$$

Substituting (3.41a) and (3.41b) for the integrals in (3.39) and making use of the condition of flux continuity (i.e. the boundary condition corresponding to the ϵ^1 term) over $\partial Y_{\rm s}$, we obtain:

$$\mathcal{C}^{\rm eff}\frac{\partial T^{(0)}}{\partial t} + \phi\mathcal{C}_{\rm g}\boldsymbol{v}\cdot\nabla_{\boldsymbol{x}} = \nabla_{\boldsymbol{x}}\cdot(\hat{\lambda}^{\rm eff}\nabla_{\boldsymbol{x}}T^{(0)}) + \phi^s QW(T^{(0)}, C^{(0)}), \tag{3.42}$$

where the effective conductivity tensor, $\hat{\lambda}^{\rm eff}$, is given by the following surface integral:

$$\hat{\lambda}^{\rm eff}_{kj} = \frac{1}{|S^k_{\rm g}|}\int\limits_{S^k_{\rm g}} \lambda^{ki}_{\rm g}\left(\frac{\partial \mathcal{N}_j}{\partial y_i} + I_{ij}\right) y_k n_i dS, \quad i,j,k = 1,2,3. \tag{3.43}$$

From (3.43), we see that the effective conductivity is evaluated over the cross-sectional surface of Y, orthogonal to the kth-direction.

3.3 Porous material with weakly conductive inclusions

In this section, we discuss a different scenario in the homogenization problem of the local heat model derived in Section 2.2.4. In this case, the contrast of thermal conductivity is such that heat conduction in the inclusion is slow, i.e. the thermal conductivity of the inclusion is quite low compared to that of the gaseous phase. Thus, we refer to the derived model as the *Weakly Conductive Inclusions* (WCI). We will see later on that the derived model has the form of the *microstructure models* (see Hornung and Showalter, 1990; Hornung, 1997). In the context of the present study, we may simply refer it as a *distributed-temperature* combustion model since the derived temperature is distributed between the macroscopic medium and the local medium of the inclusion.

3.3.1 Estimation of dimensionless parameters

The estimation of the parameters follows similarly as discussed in the previous section. In this case, the contrast of thermal conductivity is such that we assume the following conductivity ratio:

$$\mathcal{K} = \frac{\lambda_{\rm sc}}{\lambda_{\rm gc}} = \mathcal{O}(\epsilon^2). \tag{3.44}$$

Other estimates of the dimensionless parameters corresponding to $Pe_L, \mathcal{D}a$ and $\mathcal{L}e_{\rm g}$ are given as in the previous section. Now, we consider the following problem:

$$\mathcal{C}_{\rm g}\frac{\partial T_{\rm g}}{\partial t} + \mathcal{C}_{\rm g}\boldsymbol{v}\cdot\nabla T_{\rm g} - \vec{\nabla}(\lambda_{\rm g}\nabla T_{\rm g}) = 0, \tag{3.45}$$

$$\mathcal{C}_{\rm s}\frac{\partial T_{\rm s}}{\partial t} - \epsilon^2\vec{\nabla}(\lambda_{\rm s}\nabla T_{\rm s}) = 0, \tag{3.46}$$

$$\mathbf{n}\cdot(\lambda_{\rm g}\nabla T_{\rm g} - \epsilon^2\lambda_{\rm s}\nabla T_{\rm s}) = \epsilon QW(T,C), \tag{3.47}$$

$$T_{\rm g} = T_{\rm s}, \tag{3.48}$$

The expansion for the gas phase is still valid for the case considered here; in the solid-phase, we have

$$\epsilon^0 \mathcal{C}_{\mathrm{s}} \frac{\partial T_{\mathrm{s}}^{(0)}}{\partial t} + \epsilon^1 \cdots = \epsilon^0 \vec{\nabla}_y (\lambda_{\mathrm{s}} \nabla_y T_{\mathrm{s}}^{(0)}) + \epsilon^1 \mathcal{O}(\epsilon^1) \tag{3.49}$$

The corresponding boundary conditions at the gas-solid interface have the following form

$$\begin{aligned} &\epsilon^{-1}(\lambda_{\mathrm{g}} \mathbf{n} \cdot \nabla_y T_{\mathrm{g}}^{(0)}) + \epsilon^0 (\lambda_{\mathrm{g}} \mathbf{n} \cdot (\nabla_y T_{\mathrm{g}}^{(1)} + \nabla_x T_{\mathrm{g}}^{(0)})) \\ &+ \epsilon^1 (\lambda_{\mathrm{g}} \mathbf{n} \cdot (\nabla_y T_{\mathrm{g}}^{(2)} + \nabla_x T_{\mathrm{g}}^{(1)}) - (\lambda_{\mathrm{s}} \mathbf{n} \cdot \nabla_y T_{\mathrm{s}}^{(0)}) + \cdots \\ &= -\epsilon^1 (QW(T^{(0)}, C^{(0)}) + \mathcal{O}(\epsilon)), \end{aligned} \tag{3.50}$$

and

$$\epsilon^0 T_{\mathrm{g}}^{(0)} + \epsilon^1 T_{\mathrm{g}}^{(1)} + \cdots = \epsilon^0 T_{\mathrm{s}}^{(0)} + \epsilon^1 T_{\mathrm{s}}^{(1)} + \cdots . \tag{3.51}$$

Following the same argument as before, we obtain the following results for the first two terms of the gas-phase temperature:

$$T_{\mathrm{g}}^{(0)}(x, y, t) = T_{\mathrm{g}}^{(0)}(x, t), \tag{3.52}$$

$$T_{\mathrm{g}}^{(1)}(x, y, t) = \mathcal{N}(y) \cdot \nabla_x T_{\mathrm{g}}^{(0)}(x, t) + \overline{T}_{\mathrm{g}}^{(1)}(x, t), \tag{3.53}$$

with the periodic vector $\mathcal{N} = (\mathcal{N}_1, \mathcal{N}_2, \mathcal{N}_3)$ satisfying the following cell problem:

$$\begin{cases} \nabla_y \cdot (\lambda_{\mathrm{g}} (\nabla_y \mathcal{N} + \mathbf{I})) = 0 \quad \text{in } Y_g, \\ \lambda_{\mathrm{g}} (\nabla_y \mathcal{N} + \mathbf{I}) \cdot \mathbf{n} = \mathbf{0} \quad \text{on } \partial Y_{\mathrm{s}}, \\ \mathcal{N} = 0, \mathcal{N} \text{ is } Y \text{ periodic.} \end{cases} \tag{3.54}$$

Further, we look for a corresponding solution to the ϵ^0 term:

$$\mathcal{C}_{\mathrm{g}} \frac{\partial T_{\mathrm{g}}^{(0)}}{\partial t} = \nabla_y \cdot (\lambda_{\mathrm{g}} (\nabla_y T_{\mathrm{g}}^{(2)} + \nabla_x T_{\mathrm{g}}^{(1)})) + \nabla_x \cdot (\lambda_{\mathrm{g}} (\nabla_y T_{\mathrm{g}}^{(1)} + \nabla_x T_{\mathrm{g}}^{(0)})) - \mathcal{C}_{\mathrm{g}} \mathbf{v} \cdot \nabla_x T_{\mathrm{g}}^{(0)}. \tag{3.55}$$

As a result of the compatibility condition for the existence of $T^{(2)}$, we integrate (3.55) over Y_{g} and obtain

$$\begin{aligned} \phi \mathcal{C}_g \frac{\partial T_{\mathrm{g}}^{(0)}}{\partial t} &= \int_{Y_g} \nabla_y \cdot (\lambda_{\mathrm{g}} (\nabla_y T_{\mathrm{g}}^{(2)} + \nabla_x T_{\mathrm{g}}^{(1)})) dY \\ &+ \int_{Y_g} \vec{\nabla}_x (\lambda_{\mathrm{g}} (\nabla_y T_{\mathrm{g}}^{(1)} + \nabla_x T_{\mathrm{g}}^{(0)})) dY - \phi \mathcal{C}_{\mathrm{g}} \mathbf{v} \cdot \nabla_x T_{\mathrm{g}}^{(0)}. \end{aligned} \tag{3.56}$$

By applying the divergence theorem to the integrals on the right hand side of (3.56) in turn, we obtain

$$\begin{aligned}&\int_{Y_g} \nabla_y\cdot(\lambda_{\mathrm{g}}(\nabla_y T_{\mathrm{g}}^{(2)} + \nabla_x T_{\mathrm{g}}^{(1)}))dY \\ &= \int_{S_{\mathrm{g}}} \lambda_{\mathrm{g}}\mathbf{n}\cdot(\nabla_y T_{\mathrm{g}}^{(2)} + \nabla_x T^{(1)})dS + \int_{\partial Y_s} \lambda_{\mathrm{g}}\mathbf{n}\cdot(\nabla_y T_{\mathrm{g}}^{(2)} + \nabla_x T^{(1)})dS.\end{aligned} \tag{3.57}$$

In (3.57), the boundary integral over S_g vanishes due to Y-periodicity of $T_{\mathrm{g}}^{(2)}$ and $T_{\mathrm{g}}^{(1)}$. The integral over ∂Y_s satisfies the following equality, based on the prescribed boundary data:

$$\int_{\partial Y_s} \lambda_{\mathrm{g}}\mathbf{n}\cdot(\nabla_y T_{\mathrm{g}}^{(2)} + \nabla_x T^{(1)})dS = \int_{\partial Y_s} \lambda_{\mathrm{s}}\nabla_y T_{\mathrm{s}}^{(0)}\cdot\mathbf{n}dS - \int_{\partial Y_s} QW(T^{(0)}, C^{(0)})dS, \tag{3.58}$$

where

$$-\int_{\partial Y_s} QW(T^{(0)}, C^{(0)})dS = -\phi^s QW(T^{(0)}, C^{(0)}), \tag{3.59}$$

and by divergence theorem, the second boundary integral is

$$\begin{aligned}\int_{\partial Y_s} \lambda_{\mathrm{s}}\nabla_y T_{\mathrm{s}}^{(0)}\cdot\mathbf{n}dS &= -\int_{Y_s} \nabla_y\cdot(\lambda_{\mathrm{s}}\nabla_y T_{\mathrm{s}}^{(0)})dY \\ &= -\int_{Y_s} \mathcal{C}_{\mathrm{s}}\frac{\partial T_{\mathrm{s}}^{(0)}}{\partial t}dY.\end{aligned} \tag{3.60}$$

The integral in (3.60) changes sign because $\mathbf{n} = \mathbf{n}_g = -\mathbf{n}_{\mathrm{s}}$, where $\mathbf{n}_g$ and $\mathbf{n}_s$ are respectively the gas-phase and solid-phase unit normal vectors. It is clear, by using the solutions in (3.52), that

$$\nabla_y T_{\mathrm{g}}^{(1)} + \nabla_x T_{\mathrm{g}}^{(0)} = (\nabla_y\mathcal{N} + \mathbf{I})\nabla_x T_{\mathrm{g}}^{(0)}, \tag{3.61}$$

so that the last integral in (3.56) reduces to

$$\int_{Y_g} \nabla_x\cdot(\lambda_{\mathrm{g}}(\nabla_y T_{\mathrm{g}}^{(1)} + \nabla_x T_{\mathrm{g}}^{(0)}))dY = \nabla_x\cdot\left(\int_{Y_g} \lambda_{\mathrm{g}}(\nabla_y\mathcal{N} + \mathbf{I})dY\right)\nabla_x T_{\mathrm{g}}^{(0)}. \tag{3.62}$$

From the discussions so far, one can write the following macro-model as the homogenization limit:

$$\begin{aligned}
&\phi\mathcal{C}_{\mathrm{g}}\frac{\partial T_{\mathrm{g}}^{(0)}}{\partial t}(x,t)+\phi\mathcal{C}_{\mathrm{g}}\mathbf{v}\cdot\nabla_x T_{\mathrm{g}}^{(0)}(x,t)+S(x,t)\\
&=\lambda^{\mathrm{eff}}\nabla_x^2 T_{\mathrm{g}}^{(0)}(x,t)+\phi^s Q(T_{\mathrm{g}}^{(0)}(x,t),C^{(0)}(x,t)),\quad x\in\Omega,\\
&\qquad S(x,t)=\int\limits_{\partial Y_s}\lambda_{\mathrm{s}}\nabla_y T_{\mathrm{s}}^{(0)}(x,y,t)\cdot\mathbf{n}dS,\quad x\in\Omega,\\
&\mathcal{C}_{\mathrm{s}}\frac{\partial T_s^{(0)}}{\partial t}(x,y,t)=\nabla_y\cdot(\lambda_{\mathrm{s}}\nabla_y T_{\mathrm{s}}^{(0)}(x,y,t)),\quad x\in\Omega,y\in Y_s,\\
&\qquad T_{\mathrm{s}}^{(0)}(x,y,t)=T_{\mathrm{g}}^{(0)}(x,t),\quad x\in\Omega,y\in\partial Y_s,
\end{aligned}\tag{3.63}$$

where the effective thermal conductivity is given by

$$La_{ij}^{\mathrm{eff}}=\frac{\lambda_{\mathrm{g}}}{|Y|}\int\limits_{Y_{\mathrm{g}}}(I_{ij}+\frac{\partial\mathcal{N}^j}{\partial y_i})dY.\tag{3.64}$$

3.3.2 Convolution formulation of (3.63)

The homogenized limit problem (3.63) can be reformulated as a *one temperature model* without having to deal with a macro-micro coupling as seen in (3.63). In order to work in this direction, we provide an explicit formula for the problem posed in Y_s. First, we consider the form of the source term $S(x,t)$ which provides a coupling between the two phase temperatures. Problems of this nature occur have been dealt with in Hornung (1997), but following a different approach. Here, we simply consider the standard method of eigenfunction expansion. We consider the problem (3.49) as well as the first term of the boundary condition (3.51) corresponding to ϵ^0, i.e.

$$\begin{aligned}
\mathcal{C}_{\mathrm{s}}\frac{\partial T_s^{(0)}}{\partial t}&=\nabla_y\cdot(\lambda_{\mathrm{s}}\nabla_y T_{\mathrm{s}}^{(0)}),\quad x\in\Omega,y\in Y_s,t>0,\\
T_{\mathrm{s}}^{(0)}(x,y,t)&=T_{\mathrm{g}}^{(0)}(x,t),\quad x\in\Omega,y\in\partial Y_s,t>0,\\
T_{\mathrm{s}}^{(0)}(x,y,t)&=T_{\mathrm{s}}(0),\quad x\in\Omega,y\in Y_s,t=0.
\end{aligned}\tag{3.65}$$

Since $T_{\mathrm{g}}^{(0)}(x,t)$ is known, we transform the problem (3.65) by setting

$$T_{\mathrm{s}}^{(0)}(x,y,t)=T_{\mathrm{g}}^{(0)}(x,t)+\mathcal{W}(y,t),\tag{3.66}$$

so that the initial boundary value problem becomes

$$\frac{\partial\mathcal{W}}{\partial t}-\nabla_y\cdot(\alpha\nabla_y\mathcal{W})=-\frac{\partial T_{\mathrm{g}}^{(0)}}{\partial t},\quad x\in\Omega,y\in Y_s,t>0,\tag{3.67}$$

$$\mathcal{W}=0,\quad y\in\partial Y_s,t>0,\tag{3.68}$$

$$\mathcal{W}=T_{\mathrm{s}}(0)-T_{\mathrm{g}}(0),\quad x\in\Omega,y\in Y_s,t=0,\tag{3.69}$$

with $\alpha = \lambda_s/\mathcal{C}_s$ taken to be a positive constant. Here we have transient effects and a source term resulting from the temperature imposed at the boundary. From (3.67), it is clear that the transient effect associated with $\mathcal{W}$ depends linearly on the forcing term associated with $T_{\mathrm{g}}^{(0)}$, where $T_{\mathrm{g}}^{(0)}$ is a constant temperature in Y_g. The problem (3.67) can be solved by Fourier series. The domain of interest Y_s is a ball of radius, R, assumed for the moment to be centered at the origin. Assuming spherical symmetry, the temperature in $\mathcal{W}$ only depends on t and the radial distance r, we transform the initial boundary value problem (3.67) to the radial variable $r = \sqrt{y_1^2 + y_2^2 + y_3^2}$, i.e.

$$\begin{aligned} \frac{\partial \mathcal{U}}{\partial t} - \alpha \frac{\partial^2 \mathcal{U}}{\partial r^2} &= rQ(x,t), \quad 0 < r < R, t > 0, \\ \mathcal{U}(r,0) &= r\mathcal{W}(r,0), \quad 0 < r < R, \\ \mathcal{U}(0,t) &= 0, \quad t > 0, \\ \mathcal{U}(R,t) &= 0, \quad t > 0, \end{aligned} \tag{3.70}$$

where $\mathcal{U}(r,t) = r\mathcal{W}(r,t)$ and $Q(x,t) = -\partial T_g^{(0)}/\partial t$. With the eigenfunctions $\sin(n\pi r/R)$, $n = 1, 2, \ldots$, of the corresponding homogeneous eigenvalue problem, we look for solution in the series form

$$\mathcal{U}(r,t) = \sum_{n=1}^{\infty} \mathcal{U}_n(t) \sin \frac{n\pi r}{R}, \qquad \text{for each fixed } t > 0. \tag{3.71}$$

The coefficients, $\mathcal{U}_n(t)$, are then given by the *Fourier sine coefficients formula*

$$\mathcal{U}_n(t) = \frac{2}{R} \int_0^R \mathcal{U}(r,t) \sin \frac{n\pi r}{R} dr. \tag{3.72}$$

Similarly, the forcing term is expanded viz.

$$rQ(x,t) = \sum_{n=1}^{\infty} Q_n(t) \sin \frac{n\pi r}{R}, \text{ where } Q_n(t) = \frac{2}{R} \int_0^R Q(x,t) \sin \frac{n\pi r}{R} r dr. \tag{3.73}$$

We apply (3.71) in (3.70), i.e.

$$\mathcal{U}_{rr} = -\sum_{n=1}^{\infty} \mathcal{U}_n(t) \left(\frac{n\pi}{R}\right)^2 \sin \frac{n\pi r}{R} \text{ and } \mathcal{U}_t = \sum_{n=1}^{\infty} \mathcal{U}_n'(t) \sin \frac{n\pi r}{R}. \tag{3.74}$$

The Fourier coefficients of $\mathcal{U}_t(r,t)$ are

$$\mathcal{U}_n'(t) = \frac{2}{R} \int_0^R \mathcal{U}_t(r,t) \sin \frac{n\pi r}{R} r dr = \frac{\partial}{\partial t} \left[\frac{2}{R} \int_0^R \mathcal{U}(r,t) \sin \frac{n\pi r}{R} r dr \right]. \tag{3.75}$$

Substituting (3.74) in (3.70), and using the eigen property,

$$\sum_{n=1}^{\infty}\left[\mathcal{U}_n'(t)+\alpha\left(\frac{n\pi}{R}\right)^2\mathcal{U}_n(t)\right]\sin\frac{n\pi r}{R}=\sum_{n=1}^{\infty}Q_n(t)\sin\frac{n\pi r}{R}, \tag{3.76}$$

requires that we consider the following linear ordinary differential equations for the coefficients $\mathcal{U}_n(t)$

$$\mathcal{U}_n'+\alpha\left(\frac{n\pi}{R}\right)^2\mathcal{U}_n=Q_n(t),\ n=1,2,\ldots \tag{3.77}$$

(3.77) is a linear first order differential equation, in which possible methods of solution will be the *integrating factor* or *variation of parameters.* With the integrating factor $e^{\alpha(n\pi/R)^2t}$, (3.77) can be written as

$$\left(e^{\alpha(n\pi/R)^2t}\mathcal{U}_n\right)'=e^{\alpha(n\pi/R)^2t}Q_n(t), \tag{3.78}$$

so that on integration and using the initial condition, we obtain

$$\mathcal{U}_n(t)=\mathcal{U}(r,0)e^{-\alpha(n\pi/R)^2t}+e^{-\alpha(n\pi/R)^2t}\int_0^t e^{\alpha(n\pi/R)^2\tau}Q_n(\tau)d\tau. \tag{3.79}$$

The initial condition $\mathcal{U}(r,0)$ admits the following series expansion

$$\mathcal{U}(r,0)=r\mathcal{W}(r,0)=\sum_{n=1}^{\infty}\mathcal{U}_n(0)\sin\frac{n\pi r}{R},\ \text{and hence}\ \mathcal{U}_n(0)=\frac{2}{R}\int_0^R\mathcal{W}(r,0)\sin\frac{n\pi r}{R}rdr. \tag{3.80}$$

Thus, the solution is given in series form as

$$\mathcal{U}(r,t)=\sum_{n=1}^{\infty}\left[\mathcal{U}_n(0)e^{-\alpha(n\pi/R)^2t}+\int_0^t e^{-\alpha(n\pi/R)^2(\tau-t)}Q_n(\tau)d\tau\right]\sin\frac{n\pi r}{R}, \tag{3.81}$$

where

$$\begin{aligned}U_n(0)&=\frac{2}{R}\int_0^R(T_{\mathrm{s}}(0)-T_{\mathrm{g}}(0))\sin\frac{n\pi r}{R}rdr\\&=\frac{2R}{\pi}\frac{(-1)^{n+1}}{n}(T_{\mathrm{s}}(0)-T_{\mathrm{g}}(0))\end{aligned}$$

and

$$Q_n(t) = -\frac{2}{R}\int_0^R \frac{\partial T_{\rm g}^{(0)}}{\partial t}\sin\frac{n\pi r}{R} r dr,$$
$$= -\frac{2R}{\pi}\frac{(-1)^{n+1}}{n}\frac{\partial T_{\rm g}^{(0)}}{\partial t}.$$

Since the initial condition vanishes for $T_{\rm s}(0) - T_{\rm g}(0) \equiv 0$, we obtain the following series solution

$$\mathcal{W}(r,t) = \frac{2R}{\pi}\sum_{n=1}^{\infty}\frac{(-1)^{n+1}}{n}\left[-\int_0^t e^{-\alpha(n\pi/R)^2(\tau-t)}\frac{\partial T_{\rm g}^{(0)}}{\partial\tau}d\tau\right]\frac{1}{r}\sin\frac{n\pi r}{R}.$$

By divergence theorem, the forcing term, $S(x,t)$, can be then expressed as

$$\begin{aligned} S(x,t) &= \int_{\partial Y_s}\lambda_{\rm s}\nabla_y T_{\rm s}^{(0)}\mathbf{n}dS = -\int_{Y_s}\nabla_y\cdot(\lambda_{\rm s}\nabla_y T_{\rm s}^{(0)})dY \\ &= -\mathcal{C}_{\rm s}\frac{\partial}{\partial t}\int_{Y_s} T_{\rm s}^{(0)}dY. \end{aligned} \tag{3.82}$$

(3.82) implies by using the time convolution notation,

$$(\varphi * \psi)(t) = \int_0^t \varphi(t-\tau)\psi(\tau)d\tau,$$

$$\begin{aligned} &-(1-\phi)\mathcal{C}_s\frac{\partial T_{\rm g}^{(0)}}{\partial t} + 8R\sum_{n=1}^{\infty}\frac{(-1)^{n+1}}{n}\left[-\int_0^t e^{-\alpha(n\pi/R)^2(\tau-t)}\frac{\partial T_{\rm g}^{(0)}}{\partial\tau}d\tau\right]\int_0^R\sin\frac{n\pi r}{R}rdr, \\ &-(1-\phi)\mathcal{C}_s\frac{\partial T_{\rm g}^{(0)}}{\partial t} - \frac{\partial}{\partial t}\left(\zeta(t) * \frac{\partial T_{\rm g}^{(0)}}{\partial t}\right), \end{aligned} \tag{3.83}$$

where the kernel, $\zeta(t)$, in the convolution term of (3.83) is given as

$$\zeta(t) = \frac{8R^3}{\pi}\sum_{n=1}^{\infty}\frac{1}{n^2}e^{-\alpha(n\pi/R)^2 t}. \tag{3.84}$$

Thus, the macroscopic model can be written viz.

$$\begin{aligned} (\phi\mathcal{C}_{\rm g} + (1-\phi)\mathcal{C}_s)\frac{\partial T^{(0)}}{\partial t} + \phi\mathcal{C}_{\rm g}\mathbf{v}\cdot\nabla_x T^{(0)} + \partial_t(\zeta(t) * \partial_t T^{(0)}) \\ = \lambda^{\rm eff}\nabla^2 T^{(0)} + \phi^s Q(T^{(0)}, C^{(0)}), \quad x\in\Omega, t>0. \end{aligned} \tag{3.85}$$

3.4 Homogenization of the filtration gas oxidizer model

As in the case of the temperature models, we derive a macroscopic model for the concentration of the oxidizer. Obviously, in practice, the derivation of the upscaled concentration equation needs to be done simultaneously with the temperature model.

3.4.1 Estimation of dimensionless parameters

We consider the following on the following parameter regime:

$\mathcal{P}e_L = \mathcal{O}(1), \mathcal{P}_C = \mathcal{O}(1), \mathcal{D}a = \mathcal{O}(\epsilon)$

$$\frac{\partial C}{\partial t} + \boldsymbol{v}\cdot\nabla C - \nabla\cdot(D\nabla C) = 0, \qquad \boldsymbol{x} \in \Omega_{\mathrm{g}}^{\epsilon}, t > 0, \tag{3.86a}$$

$$- D\nabla C\cdot\boldsymbol{n} = \epsilon W(T, C), \qquad \boldsymbol{x} \in \Gamma^{\epsilon}, t > 0. \tag{3.86b}$$

We introduce in (3.86a) and (3.86b) the expansions (3.2a) and (3.2b), and identify powers of ϵ. From these expansions, we are led to a few local boundary value problems:

Boundary value problem for $C^{(0)}$:

$$\begin{cases} -\nabla_{\boldsymbol{y}}\cdot(D\nabla_{\boldsymbol{y}}C^{(0)}) = 0, & \boldsymbol{y} \in Y_{\mathrm{g}}, \\ -D\nabla_{\boldsymbol{y}}C^{(0)}\cdot\boldsymbol{n} = 0, & \boldsymbol{y} \in \partial Y_{\mathrm{s}}, \\ C^{(0)} \text{ is } Y \text{ periodic.} \end{cases} \tag{3.87}$$

Similar to (3.6), any solution of (3.87) is unique up to an additive function of $\boldsymbol{x}$ and t, where $\boldsymbol{x}$ and t are parameters. Thus, the solution to (3.87) is

$$C^{(0)}(\boldsymbol{x}, \boldsymbol{y}, t) = C^{(0)}(\boldsymbol{x}, t). \tag{3.88}$$

(3.88) implies that the concentration $C^{(0)}$ is a constant over the period.

Boundary value problem for $C^{(1)}$:

$$\begin{cases} -\nabla_{\boldsymbol{y}}\cdot(D(\nabla_{\boldsymbol{y}}C^{(1)} + \nabla_{\boldsymbol{x}}C^{(0)})) = 0, & \boldsymbol{y} \in Y_{\mathrm{g}}, \\ -D(\nabla_{\boldsymbol{y}}C^{(1)} + \nabla_{\boldsymbol{x}}C^{(0)})\cdot\boldsymbol{n} = 0, & \boldsymbol{y} \in \partial Y_{\mathrm{s}}, \\ C^{(1)} \text{ is } Y \text{ periodic.} \end{cases} \tag{3.89}$$

The gradient,$\nabla_{\boldsymbol{x}} C^{(0)}$, is only present as a source term in (3.89). Due to linearity and the fact that spatial derivatives are only in $\boldsymbol{y}$, it makes sense to consider the following local problem for the periodic vector $\boldsymbol{\mathcal{N}} = (\mathcal{N}_1, \mathcal{N}_2, \mathcal{N}_3)$, with a mean of zero over Y_{g}, i.e.

$$\begin{cases} \nabla_{\boldsymbol{y}} \cdot (D(\nabla_{\boldsymbol{y}} \boldsymbol{\mathcal{N}} + \mathbf{I})) = 0, & \boldsymbol{y} \in Y_{\mathrm{g}}, \\ D(\nabla_{\boldsymbol{y}} \boldsymbol{\mathcal{N}} + \mathbf{I}) \cdot \boldsymbol{n} = 0, & \boldsymbol{y} \in \partial Y_{\mathrm{s}}, \\ \boldsymbol{\mathcal{N}} = 0, \boldsymbol{\mathcal{N}} \text{ is } Y \text{ periodic}, \end{cases} \tag{3.90}$$

where the solution to (3.89) can be written in the form

$$C^{(1)}(\boldsymbol{x}, \boldsymbol{y}, t) = \boldsymbol{\mathcal{N}}(\boldsymbol{y}) \cdot \nabla_{\boldsymbol{x}} C^{(0)} + \overline{C}^{(1)}(\boldsymbol{x}, t), \tag{3.91}$$

and $\overline{C}^{(1)}(\boldsymbol{x}, t)$ is only an arbitrary function of $\boldsymbol{x}$ and t. With the results obtained from (3.88) and (3.91), we write the boundary value problem for $C^{(2)}$ as

Boundary value problem for $C^{(2)}$

$$\begin{cases} \partial_t C^{(0)} - \nabla_{\boldsymbol{y}} \cdot (D(\nabla_{\boldsymbol{y}} C^{(2)} + \nabla_{\boldsymbol{x}} C^{(1)})) - \nabla_{\boldsymbol{x}} \cdot (D(\nabla_{\boldsymbol{y}} C^{(1)} + \nabla_{\boldsymbol{x}} C^{(0)})) + \\ \boldsymbol{v} \cdot \nabla_{\boldsymbol{x}} C^{(0)} = 0, & \boldsymbol{y} \in Y_{\mathrm{g}}, \\ -D(\nabla_{\boldsymbol{y}} C^{(2)} + \nabla_{\boldsymbol{x}} C^{(1)}) \cdot \boldsymbol{n} = W(T^{(0)}, C^{(0)}), & \boldsymbol{y} \in \partial Y_{\mathrm{s}} \\ C^{(2)} \text{ is } Y \text{ periodic}. \end{cases} \tag{3.92}$$

Applying the compatibility condition for the existence of $C^{(2)}$, and using the expressions for $C^{(0)}$ and $C^{(1)}$, respectively in (3.92), we obtain

$$\begin{aligned} &-\frac{1}{|Y|} \int\limits_{Y_{\mathrm{g}}} \nabla_{\boldsymbol{y}} \cdot (D(\nabla_{\boldsymbol{y}} C^{(2)} + \nabla_{\boldsymbol{x}} C^{(1)})) dY = \cdots \\ &-\frac{1}{|Y|} \int\limits_{S_g} (D(\nabla_{\boldsymbol{y}} C^{(2)} + \nabla_{\boldsymbol{x}} C^{(1)})) \cdot \boldsymbol{n} dS - \frac{1}{|Y|} \int\limits_{\partial Y_{\mathrm{s}}} (D(\nabla_{\boldsymbol{y}} C^{(2)} + \nabla_{\boldsymbol{x}} C^{(1)})) \cdot \boldsymbol{n} dS. \end{aligned} \tag{3.93}$$

The first integral at the right-hand side of (3.93) vanishes due to periodicity condition in Y and the second integral yields

$$\frac{1}{|Y|} \int\limits_{\partial Y_{\mathrm{s}}} W(T^{(0)}, C^{(0)}) dS = \phi^s W(T^{(0)}, C^{(0)}) \tag{3.94}$$

The average of the remaining terms in (3.93) is viz.

$$\phi \frac{\partial C^{(0)}}{\partial t} + \phi \boldsymbol{v} \cdot \nabla_{\boldsymbol{x}} C^{(0)} - \nabla_{\boldsymbol{x}} \left(\frac{D}{|Y|} \int\limits_{Y_{\mathrm{g}}} (\nabla_{\boldsymbol{y}} \boldsymbol{\mathcal{N}}(\boldsymbol{y}) + \mathbf{I}) dY \right) \nabla_{\boldsymbol{x}} C^{(0)} \tag{3.95}$$

Collecting the terms together, the macro-model can be written as

$$\phi\frac{\partial C^{(0)}}{\partial t} + \phi \boldsymbol{v}\cdot\nabla_{\boldsymbol{x}} C^{(0)} - \nabla_{\boldsymbol{x}}\cdot(D^{\text{eff}}\nabla_{\boldsymbol{x}} C^{(0)}) = -\phi^s W(T^{(0)}, C^{(0)}), \tag{3.96}$$

where the effective diffusion tensor D^{eff} is defined as:

$$D_{ij}^{\text{eff}} = \frac{D}{|Y|}\int\limits_{Y_{\text{g}}} (I_{ij} + \frac{\partial \mathcal{N}^j}{\partial y_i})dY. \tag{3.97}$$

3.5 Summary

In this chapter, we have derived via the homogenization of periodic structures three macroscopic models from a pore scale description of a combustion process (see details in Chapter 2). These models are representative of distinct macroscopic behaviors, which are based on thermal conductivity contrast. The derivation of the models was based on scaling the ratio of thermal conductivity, $\mathcal{K} = \lambda_{\text{s}}/\lambda_{\text{g}}$, in the order of magnitude, ϵ, i.e. $\mathcal{O}(\epsilon^{\alpha})$.

We point out that based on the choice of α, different classes of equilibrium or non-equilibrium models can be obtained. For instance, when $\alpha = 1$, the thermal conductivity ratio is $\mathcal{O}(\epsilon)$ and the solution of rescaled equation results to a model with local equilibrium as in the case of MCI model, but having an effective thermal conductivity defined in the highly thermal conductivity subdomain (cf. Allaire and Habibi (2013)). This means that the influence of the thermal conductivity λ_{s} of the inclusion becomes negligible, and hence heat conduction is slow in the inclusion. The model also falls in the class of Weakly Conductive Inclusions model. Similarly, for $\alpha \geq 3$ the heat conduction in the inclusion is very slow that we may consider such porous materials as near insulation. The resulting equation is similar in form to the WCI model, but with the exclusion of the exchange term. The problem behaves as a one-temperature system, with the effective thermal conductivity corresponding to the highly thermal conducting subdomain. The case of $\alpha = 2$ falls in the class of distributed microstructure models as we have shown. It represents a class of two-scale models, in which the temperatures of the constituent phases are not in thermal equilibrium. The model arises because the material has a low thermal conductivity in the inclusion compared to the matrix part, and hence is referred to it as Weakly Conductive Inclusions (WCI) (cf. Section 3.3).

Two of the derived models have the functional forms of a one-temperature (equilibrium) filtration combustion model studied in the literature (see Kagan and Sivashinsky, 2008; Oliveira and Kaviany, 2001; Fatehi and Kaviany, 1994, e.g.). In the context of this study, we refer to the two equilibrium models as Moderately Conductive Inclusions (MCI) (with $\alpha = 0$; see Section 3.1) and Highly Conductive Inclusions (HCI) (with $\alpha = -1$; see Section 3.2). The names reflect on the thermal conductivity of the inclusions in relation to the gaseous phase conductivity. The scheme of the resulting equilibrium models is given

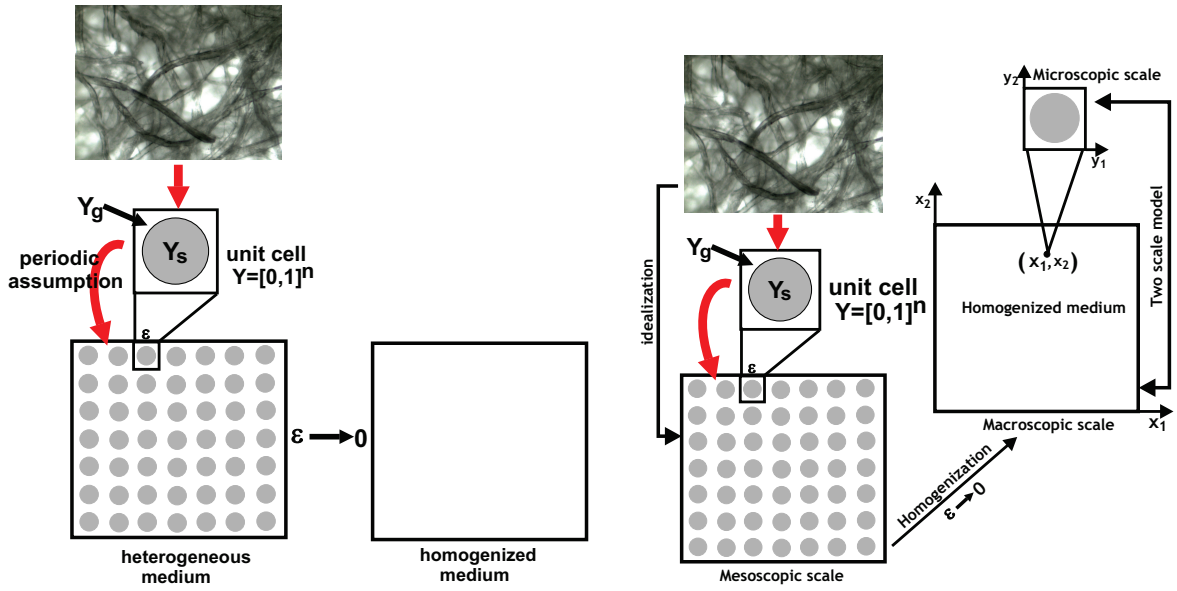

Figure 3.1: Schemes of homogenized limit problems; (a) the one-temperature model as an (homogenized) equilibrium limit; (b) the distributed-temperature model as a two-scale (non-equilibrium) limit.

in Figure 3.1a. The derivation of the macroscopic models does not require the use of the assumption of thermal-diffusive equilibrium. This requirement follows naturally from the rigorous mathematical treatment by the homogenization method. The developed models are in general for the qualitative treatment of the development of patterns in reverse combustion in porous media. Nevertheless, the results of the homogenization technique present an effective way of integrating material microstructural properties into a macroscopic system describing real life processes. Thus, it can serve as a paradigm for further investigation of combustion processes in a rigorous mathematical treatment.

The form of the models are representative of adiabatic models since they were derived under the assumption that the gaseous and solid parts are in perfect contact, and external heat losses to the environment are neglected. This assumption raises further question on the physical implication of external heat losses to the phenomenon of interest. Although the inclusion of such heat mechanisms can provide more insight on the physical process, its exclusion is adequate for the interest of the present study. There is a vast literature modeling combustion in a non-adiabatic setting. These include (Ikeda and Mimura, 2008; Fasano et al., 2009; Oliveira and Kaviany, 2001; Lu and Yortsos, 2005a; Yuan and Lu, 2013; Lu et al., 2006, e.g.). Also, the distributed-temperature model (see Figure 3.1b) is not popular among combustion communities and can be a subject of future investigation.

A prospective research direction in this case involves the usually used notion of “instant-

aneous diffusion" in physical processes, especially in combustion and chemical reaction processes. The problem pertains to a filtration combustion problem whereby thermal diffusion processes in a system is far from equilibrium. For instance, in order to give a precise account for the transport of heat across different phases e.g., in a gaseous and solid phase, consideration has to be given to the different time scales involved. Specifically, one may consider a situation in which heat diffusion across a solid material requires more time to equilibrate compared to the diffusion of heat in the gaseous phase. Hence, the problem exhibits two distinct time scales of diffusion. As we have shown, the two-scale model (see Figure 3.1b) arises as a limit problem from the application of the homogenization method. In this limit problem, we deal with two coupled problems-a macroscopic problem in a homogeneous medium and a micro-scale problem posed in the inclusion.

Chapter 4

Derivation of macroscopic equations of filtration combustion by two-scale convergence

The method employed in Chapter 3 is based on a heuristic approach that the solutions to the unknown fields in the filtration combustion model are in the form of a formal asymptotic expansion in ϵ. Under the assumptions of this ansatz, the unknown fields are approximated by the zeroth order term of the asymptotic series as ϵ tends to zero. In this chapter[1], we proceed by providing a rigorous mathematical justification to the homogenization results presented previously. We will apply the *two-scale convergence* method developed by Nguestseng (1989) and Allaire (1992). This method is attractive since one can simultaneously deduce the homogenized limit problems presented in Chapter 3 and prove the convergence of the homogenization process. Also, the method rigorously justifies the first two terms in the asymptotic expansion of the sequence of unknown fields. It is also suitable for deriving *corrector estimates* which allow to obtain strong convergences by improving on the weak convergence to the homogenized solutions. The corrector problems will be discussed in Chapter 6.

4.1 Description of the geometry

For the considered problem, the geometry is as described in Chapter 2, Figure 2.3a. Here, we reproduce its cross-section along to the direction of flow in Figure 4.1. It consists of circular solid inclusions which are periodically distributed in a gaseous matrix. Let the domain Ω (a bounded open set in $\mathbb{R}^d$), with period ϵY (ϵ is a small positive number, and $Y = (0,1)^d$ is the unit cell. Typically, $d = 2$ or 3). The unit cell Y is divided into two constituent parts–Y_s an open subset of Y with $\overline{Y}_s \subset Y$ (solid part or inclusion) and $Y_s := Y \setminus \overline{Y}_s$, (gaseous part or matrix). We also denote by $\Gamma = \partial Y_s$, the smooth boundary of Y_s. Let $\chi_g(y)$ (respectively $\chi_s(y)$) be the characteristic functions of Y_g (respectively Y_s),

[1]This chapter is partly a joint work with Tasnim Fatima and Adrian Muntean (Eindhoven).

extended by Y-periodicity to the whole of $\mathbb{R}^d$, and satisfying the condition

$$\chi_{\mathrm{g}}(y) + \chi_{\mathrm{s}}(y) = 1 \quad \text{in Y.}$$

Thus, the domain Ω can be split into two subdomains

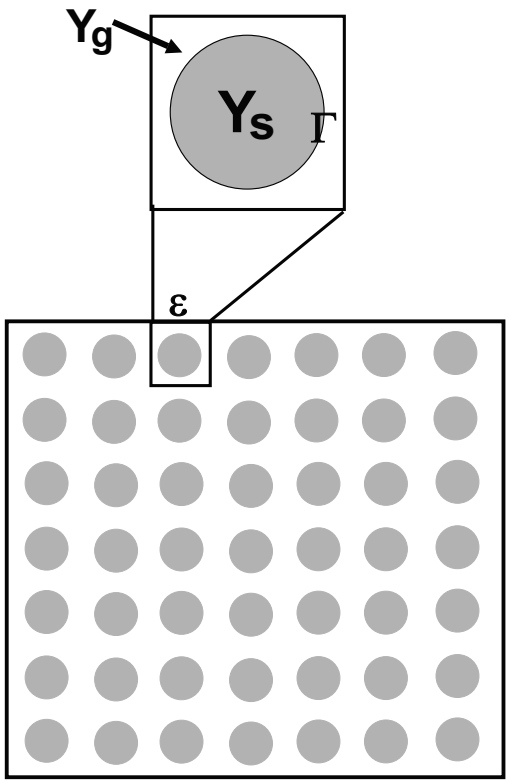

Figure 4.1: Uniformly distributed periodic domain

$$\Omega_{\mathrm{g}}^{\epsilon} = \left\{ x \in \Omega \mid \chi_{\mathrm{g}}\left(\frac{x}{\epsilon}\right) = 1 \right\} \text{ and } \Omega_{\mathrm{s}}^{\epsilon} = \left\{ x \in \Omega \mid \chi_{\mathrm{s}}\left(\frac{x}{\epsilon}\right) = 1 \right\},$$

defined respectively for the constituents in the gaseous (matrix) part and in the solid (inclusion) part.

4.2 Mathematical model

4.2.1 Microscopic model

Let us consider a non-stationary heat diffusion problem with convection in a medium consisting of the two subdomains $\Omega_{\mathrm{g}}^{\epsilon}$ (interconnected matrix) and $\Omega_{\mathrm{s}}^{\epsilon}$ (ensemble of the inclusions). The properties of the medium are such that the coefficients are varying in space, in the sense that they take only two different values of the same order of magnitude. Also,

we introduce in the medium, a gaseous oxidizer, which occupies the gaseous subdomain, $\Omega_{\mathrm{g}}^{\epsilon}$, and reacts with the material at the surface $\Gamma^{\epsilon} = \partial\Omega_{\mathrm{g}}^{\epsilon} \cap \partial\Omega_{\mathrm{s}}^{\epsilon}$ separating the constituents. Note that the surface Γ^{ϵ} is constructed as the union of all translated smooth boundary of Y_{s} with $\partial\Omega \cap \Gamma^{\epsilon} = \emptyset$. This implies that the inclusions do not intersect with the exterior boundary $\partial\Omega$ of the domain Ω. Assume also that the inclusions do not touch each other. Let the thermal conductivity of the constituent parts be defined by the constants λ_{g} and λ_{s}. Hence, we denote the varying conductivity coefficient λ^{ϵ} of the periodic medium Ω by

$$\lambda^{\epsilon}(x) = \lambda_{\mathrm{g}}\chi_{\mathrm{g}}\left(\frac{x}{\epsilon}\right) + \lambda_{\mathrm{s}}\chi_{\mathrm{s}}\left(\frac{x}{\epsilon}\right), \ x \in \Omega. \tag{4.1}$$

Similarly, the volumetric heat capacity, $\mathcal{C}^{\epsilon}$, is defined by

$$\mathcal{C}^{\epsilon}(x) = \mathcal{C}_{\mathrm{g}}\chi_{\mathrm{g}}\left(\frac{x}{\epsilon}\right) + \mathcal{C}_{\mathrm{s}}\chi_{\mathrm{s}}\left(\frac{x}{\epsilon}\right) \ x \in \Omega. \tag{4.2}$$

Convection of gaseous oxidizer only takes place in the gaseous subdomain $\Omega_{\mathrm{g}}^{\epsilon}$. Thus, we define it as follows

$$\boldsymbol{u}^{\epsilon}(x) = \begin{cases} 0, & x \in \Omega_{\mathrm{s}}^{\epsilon}, \\ \mathbf{v}, & x \in \Omega_{\mathrm{g}}^{\epsilon}, \end{cases} \tag{4.3}$$

where (4.3) implies the restriction of convection to the gaseous subdomain Ω_g^{ϵ}, and thus we assume a spatially periodic flow i.e. $\boldsymbol{u}^{\epsilon}(x) = \boldsymbol{u}(x, \dfrac{x}{\epsilon})$ in $\Omega_g^{\epsilon}, y = \mathbf{x}/\epsilon$. The continuous vector field $\boldsymbol{u}(x, y)$, defined in $Y_{\mathrm{g}} \times \Omega$, is periodic in $\mathbf{y}$ and divergence free, i.e.

$$\mathrm{div}_{\mathrm{x}}\boldsymbol{u} = 0, \text{ and } \mathrm{div}_{\mathrm{y}}\boldsymbol{u} = 0 \text{ in } Y_{\mathrm{g}}, \text{ and } \boldsymbol{u} \cdot n = 0 \text{ on } \partial Y_{\mathrm{s}},$$

where n is the unit outward normal on ∂Y_{s} with respect to Y_{g}. Molecular diffusion of gaseous substances is also restricted to $\Omega_{\mathrm{g}}^{\epsilon}$. Let the temperature and mass concentration of oxidizer in the domain Ω be denoted respectively by T^{ϵ} and C^{ϵ}. The temperature can be decomposed as

$$T^{\epsilon}(x) = \begin{cases} T_{\mathrm{s}}^{\epsilon}(x), & x \in \Omega_{\mathrm{s}}^{\epsilon}, \\ T_{\mathrm{g}}^{\epsilon}(x), & x \in \Omega_{\mathrm{g}}^{\epsilon}, \end{cases}$$

where T^{ϵ} is continuous on the interface Γ^{ϵ}. Besides the continuity of temperature across the interface, chemical reactions also take place at the interface Γ^{ϵ} between $\Omega_{\mathrm{g}}^{\epsilon}$ and $\Omega_{\mathrm{s}}^{\epsilon}$ leading to a discontinuity in the heat fluxes across the interface, i.e. the following conditions are given across the interface

$$(\lambda_{\mathrm{g}}\nabla T_{\mathrm{g}}^{\epsilon} - \lambda_s \nabla T_{\mathrm{s}}^{\epsilon}) \cdot n = \epsilon Q W(T^{\epsilon}, C^{\epsilon}), \quad x \in \Gamma^{\epsilon}, t > 0, \tag{4.4}$$

$$T_g^{\epsilon} = T_s^{\epsilon}, \quad x \in \Gamma^{\epsilon}, t > 0, \tag{4.5}$$

where $Q > 0$ is a given constant and $W(T^{\epsilon}, C^{\epsilon})$ is the reaction rate defined by

$$W(T^{\epsilon}, C^{\epsilon}) = AC^{\epsilon} f(T^{\epsilon}), \ A > 0. \tag{4.6}$$

We also assume that the following condition holds across the interface for the concentration of gaseous oxidizer:

$$D\nabla C^\epsilon) \cdot n = -\epsilon W(T^\epsilon, C^\epsilon), \quad x \in \Gamma^\epsilon, t > 0. \tag{4.7}$$

Thus, the governing equations are given by

$$\mathfrak{H}^\epsilon \begin{cases} \mathcal{C}_{\mathrm{g}} \dfrac{\partial T_{\mathrm{g}}^\epsilon}{\partial t} + \mathcal{C}_{\mathrm{g}} \boldsymbol{u}^\epsilon \cdot \nabla T_{\mathrm{g}}^\epsilon - \nabla \cdot (\lambda_{\mathrm{g}} \nabla T_{\mathrm{g}}^\epsilon) = 0, & x \in \Omega_{\mathrm{g}}^\epsilon, t > 0, \\ \mathcal{C}_{\mathrm{s}} \dfrac{\partial T_{\mathrm{s}}^\epsilon}{\partial t} - \nabla \cdot (\lambda_{\mathrm{s}} \nabla T_{\mathrm{s}}^\epsilon) = 0, & x \in \Omega_{\mathrm{s}}^\epsilon, t > 0, \\ T_{\mathrm{g}}^\epsilon = T_{\mathrm{s}}^\epsilon, & x \in \Gamma^\epsilon, t > 0, \\ \mathrm{n} \cdot (\lambda_{\mathrm{g}} \nabla \mathrm{T}_{\mathrm{g}}^\epsilon - \lambda_{\mathrm{s}} \nabla \mathrm{T}_{\mathrm{s}}^\epsilon) = \epsilon \mathrm{QW}(\mathrm{T}_{\mathrm{s}}^\epsilon, \mathrm{C}), & x \in \Gamma^\epsilon, t > 0. \end{cases} \tag{4.8}$$

In terms of the introduced coefficients, (4.8) can be written in a compact form:

$$\begin{cases} \mathcal{C}^\epsilon \dfrac{\partial T^\epsilon}{\partial t} + \chi_{\mathrm{g}} \mathcal{C}_{\mathrm{g}} \boldsymbol{u}^\epsilon \cdot \nabla T^\epsilon - \nabla \cdot (\lambda^\epsilon \nabla T^\epsilon) = 0, & x \in \Omega^\epsilon, t > 0, \\ \lambda^\epsilon \dfrac{\partial T^\epsilon}{\partial \mathrm{n}} = \epsilon Q W(T^\epsilon, C^\epsilon), & x \in \Gamma^\epsilon, t > 0, \\ T^\epsilon \text{ is continuous}, & x \in \Gamma^\epsilon, t > 0. \end{cases} \tag{4.9}$$

The equations for the concentration field is given by

$$\mathfrak{M}^\epsilon \begin{cases} \dfrac{\partial C^\epsilon}{\partial t} + \boldsymbol{u}^\epsilon \cdot \nabla C^\epsilon - \nabla \cdot D \nabla C^\epsilon = 0, & x \in \Omega_{\mathrm{g}}^\epsilon, t > 0, \\ -D \nabla C^\epsilon \cdot \mathrm{n} = \epsilon \mathrm{W}(\mathrm{T}^\epsilon, \mathrm{C}^\epsilon), & x \in \Gamma^\epsilon, t > 0. \end{cases} \tag{4.10}$$

The equation for the solid product is given by

$$\mathfrak{R}^\epsilon \left\{ \frac{\partial R^\epsilon}{\partial t} = W(T^\epsilon, C^\epsilon), \quad x \in \Gamma^\epsilon, t > 0. \right. \tag{4.11}$$

The initial and external boundary conditions are given by

$$T^\epsilon = T_0, C^\epsilon = C_0, R^\epsilon = R_0 \quad x \in \Omega, t = 0, \tag{4.12}$$

$$T^\epsilon = T_D, C^\epsilon = C_D \quad x \in \Gamma_D, t > 0, \tag{4.13}$$

$$\nabla T^\epsilon \cdot \mathrm{n} = 0, \nabla \mathrm{C}^\epsilon \cdot \mathrm{n} = 0, \quad x \in \Gamma_N, t > 0 \tag{4.14}$$

Here, $\Gamma_D \cup \Gamma_N$, with $\Gamma_D \cap \Gamma_N = \emptyset$, represents the external boundaries, where Γ_D, is the Dirichlet boundary and Γ_N, points out the Neumann part of the boundary.

4.2.2 Macroscopic model

We give the macroscopic model derived through formal asymptotics in Chapter 3 in the strong forms, $\mathfrak{H}^0$ and $\mathfrak{M}^0$, respectively for the macroscopic temperature T and macroscopic concentration C. We have

$$\mathfrak{H}^0\begin{cases}\mathcal{C}^{\text{eff}}\dfrac{\partial T}{\partial t}+\dfrac{|Y_{\text{g}}|}{|Y|}\mathcal{C}_{\text{g}}\boldsymbol{u}\cdot\nabla T-\nabla\cdot\left(\lambda^{\text{eff}}\nabla T\right)=\dfrac{|\Gamma|}{|Y|}QW(T,C), & x\in\Omega,t>0,\\ T=T_0, & x\in\Omega,t=0,\\ T=T_D, & x\in\Gamma_D,t>0,\\ \nabla T\cdot\mathrm{n}=0, & x\in\Gamma_N,t>0,\end{cases}\tag{4.15}$$

where the effective coefficients are defined by

$$\lambda_{ik}^{\text{eff}}:=\frac{1}{|Y|}\left(\int\limits_{Y_{\text{g}}}\lambda_{\text{g}}\left(I_{ki}+\frac{\partial\mathcal{N}_{\text{k}}^{\text{g}}}{\partial y_{\text{i}}}\right)dy+\int\limits_{Y_{\text{s}}}\lambda_{\text{s}}\left(I_{ki}+\frac{\partial\mathcal{N}_{\text{k}}^{\text{s}}}{\partial y_i}\right)dy\right),\tag{4.16}$$

and

$$\mathcal{C}^{\text{eff}}:=\frac{1}{|Y|}\Big(\mathcal{C}_{\text{g}}|Y_{\text{g}}|+|Y_{\text{s}}|\mathcal{C}_{\text{s}}\Big).\tag{4.17}$$

The functions $\mathcal{N}_j, j=1,2,3$ solve the following *cell problem*

$$\frac{\partial}{\partial y_i}\left[\lambda_{\text{g}}\left(I_{ik}+\frac{\partial\mathcal{N}_{\text{k}}^{\text{g}}}{\partial y_i}\right)\right]=0, \qquad y\in Y_{\text{g}},\tag{4.18a}$$

$$\frac{\partial}{\partial y_i}\left[\lambda_{\text{s}}\left(I_{ik}+\frac{\partial\mathcal{N}_{\text{k}}^{\text{s}}}{\partial y_i}\right)\right]=0, \qquad y\in Y_{\text{s}},\tag{4.18b}$$

$$\mathcal{N}_k^{\text{g}}=\mathcal{N}_k^{\text{s}}, \qquad y\in\Gamma,\tag{4.18c}$$

$$\lambda_{\text{g}}\left(I_{ik}+\frac{\partial\mathcal{N}_{\text{k}}^{\text{g}}}{\partial y_i}\right)n_i=\lambda_{\text{s}}\left(I_{ik}+\frac{\partial\mathcal{N}_{\text{k}}^{\text{s}}}{\partial y_i}\right)n_i, \qquad y\in\Gamma,\tag{4.18d}$$

where $\mathcal{N}_{\text{k}}^{\text{g}}$ and $\mathcal{N}_{\text{k}}^{\text{s}}, \text{k}=1,2,3$ are y-periodic and satisfy

$$\langle\mathcal{N}\rangle=\frac{1}{|Y|}\left(\int\limits_{Y_{\text{g}}}\mathcal{N}_{\text{k}}^{\text{g}}dy+\int\limits_{Y_{\text{s}}}\mathcal{N}_{\text{k}}^{\text{s}}dy\right)=0.\tag{4.19}$$

Similarly, the macroscopic concentration model is expected to satisfy

$$\mathfrak{M}^0\begin{cases}\dfrac{|Y_{\text{g}}|}{|Y|}\dfrac{\partial C}{\partial t}+\dfrac{|Y_{\text{g}}|}{|Y|}\boldsymbol{u}\cdot\nabla C-\nabla\cdot\left(D^{\text{eff}}\nabla C\right)=-\dfrac{|\Gamma|}{|Y|}W(T,C), & x\in\Omega,t>0.\\ C=C_0, & x\in\Omega,t=0,\\ C=C_D, & x\in\Gamma_D,t>0,\\ \nabla C\cdot\mathrm{n}=0, & x\in\Gamma_N,t>0,\end{cases}\tag{4.20}$$

with the following formula for the computation of the effective mass diffusion coefficient, D^{eff}, defined by

$$D_{ik}^{\text{eff}} = \frac{D}{|Y|} \int\limits_{Y_{\text{g}}} \left(I_{ki} + \frac{\partial \mathcal{N}_{\text{k}}}{\partial y_{\text{i}}} \right) dy, \quad i,k = 1,2,3 \tag{4.21}$$

The functions $\mathcal{N}_{\text{k}}, k = 1,2,3$ solve the following cell problems:

$$\frac{\partial}{\partial y_i} \left[D \left(I_{ik} + \frac{\partial \mathcal{N}_{\text{k}}}{\partial y_i} \right) \right] = 0, \qquad y \in Y_{\text{g}}, \tag{4.22a}$$

$$D \left(I_{ik} + \frac{\partial \mathcal{N}_{\text{k}}}{\partial y_i} \right) n_{\text{i}} = 0, \qquad y \in \Gamma, \tag{4.22b}$$

where $i,k = 1,2,3$, and the vector-valued function $\boldsymbol{\mathcal{N}}$ is y-periodic and satisfy $\langle \boldsymbol{\mathcal{N}} \rangle = 0$. Finally, the macroscopic equation for the solid product

$$\mathfrak{R}^0 \left\{ \frac{\partial R}{\partial t} = W(T,C), \quad x \in \Omega, t > 0. \right. \tag{4.23}$$

4.2.3 Function spaces and norms

In the sequel, we will often use the following function spaces:

$H = L^2(\Omega), (u,v)_\Omega = \int_\Omega u(x)v(x)dx, \|u\|_\Omega = (u,u)_\Omega^{1/2}$

$L^2(0,\tau;H), (u,v)_{\Omega,\tau} = \int_0^\tau (u(t),v(t))_\Omega dt, \|u\|_{\Omega,\tau} = (u,u)_{\Omega,\tau}^{1/2}$

$V = W^{1,2}(\Omega), (u,v)_V = (u,v)_\Omega + (\nabla u, \nabla v)_\Omega$

$\boldsymbol{\mathcal{V}} = L^2(0,\tau;V), (u,v)_{\boldsymbol{\mathcal{V}}} = \int_0^\tau (u(t),v(t))_V dt$

$\boldsymbol{\mathcal{V}}_D = \{v \in \boldsymbol{\mathcal{V}} \mid v = 0 \text{ on } \Gamma_D \text{ a.e. on } (0,\tau)\}$

$\boldsymbol{\mathcal{W}} = \{v \in \boldsymbol{\mathcal{V}} \mid \partial_t v \in \boldsymbol{\mathcal{V}}'\}$, where $\boldsymbol{\mathcal{V}}' = L^2(0,\tau;V')$ is the dual space of $\boldsymbol{\mathcal{V}}$

$\boldsymbol{\mathcal{W}}_D = \boldsymbol{\mathcal{V}}_D \cap \boldsymbol{\mathcal{W}}$

We also use the following

$$(u,v)_{\Gamma,\tau} = \int\limits_0^\tau \int\limits_\Gamma uv d\gamma dt.$$

Likewise, the above descriptions are also applicable for functions defined on perforated domains $\Omega_{\text{g}}^\epsilon, \Omega_{\text{g}}^\epsilon$ and $\Omega^\epsilon \equiv \Omega$ and their boundaries Γ^ϵ. For details of the definitions and properties of the function spaces indicated here, (see Adams and Fournier, 2003).

4.3 Restrictions on parameters and data

In order to establish the uniform boundedness of the sequence of functions $(C^\epsilon, T^\epsilon, R^\epsilon)$, and hence the rigorous passage to the limit of the homogenization process discussed in Chapter 3, we need to introduce a set of restrictions on the data and parameters, which we collect as Assumptions (A).

4.3.1 Assumptions

We assume the following

(A1) $D \in L^\infty(Y_{\mathrm{g}})^{3\times 3}, \lambda^{\mathrm{g}}, \lambda^{\mathrm{s}} \in L^\infty(Y)^{3\times 3}$, and satisfy

$$\sum_{i,j=1}^{3} D_{i,j}\xi_i\xi_j \geq D_0|\xi|^2,\ \forall \xi \in \mathbb{R}^3, \forall y \in Y_{\mathrm{g}}, \qquad |D^\epsilon(x)\xi| \leq D_1|\xi|,\ \forall \xi \in \mathbb{R}^3. \tag{4.24}$$

$$\sum_{i,j=1}^{3} \lambda^{\mathrm{g,s}}_{i,j}\xi_i\xi_j \geq \lambda_0|\xi|^2,\ \forall \xi \in \mathbb{R}^3, \forall y \in Y, \qquad |\lambda^\epsilon(x)\xi| \leq \lambda_1|\xi|,\ \forall \xi \in \mathbb{R}^3, \tag{4.25}$$

for some constants $D_0, D_1, \lambda_0, \lambda_1 > 0$.

(A2) f is bounded and a globally Lipschitz function. Furthermore

$$f(\alpha) = \begin{cases} \text{positive, if } \alpha > 0, \\ 0, \quad \text{otherwise.} \end{cases}$$

(A3) $\mathcal{C}_{\mathrm{g}}, \mathcal{C}_{\mathrm{s}}$ are bounded, i.e. $\mu_0 \leq max\{\mathcal{C}_{\mathrm{g}}, \mathcal{C}_{\mathrm{s}}\} \leq \mu_1; \mu_0, \mu_1 > 0$.

(A4) $C_0, T_0 \in H^1(\Omega) \cap L^\infty_+(\Omega)$ and $R_0 \in L^\infty_+(\Gamma)$.

(A5) $\|\mathbf{u}^\epsilon\|_{L^\infty(\Omega)} \leq M_u < \infty$ and $\mathbf{u}^\epsilon \to \mathbf{u}$ strongly.

(A6) $C_D, T_D \in L^2(0,T; H^1(\Omega^\epsilon_{\mathrm{g}})) \cap L^\infty_+((0,T)\times\Omega)$.

For brevity, the nonlinear reaction term $W(T^\epsilon, C^\epsilon) = AC^\epsilon f(T^\epsilon)$ is represented by W^ϵ.

4.3.2 Trace inequalities for perforated domain

Lemma 4.3.1. *(a) For a function $u \in H^1(Y_g)$ one has the estimate*

$$\|u\|_\Gamma^2 \le C(\|u\|_{Y_g}^2 + \|\nabla u\|_{Y_g}^2). \tag{4.26}$$

(b) For a function $u^\epsilon \in H^1(\Omega_g^\epsilon)$ one has the estimate

$$\epsilon \|u^\epsilon\|_{\Gamma^\epsilon}^2 \le C(\|u^\epsilon\|_{\Omega_g^\epsilon}^2 + \epsilon^2 \|\nabla u^\epsilon\|_{\Omega_g^\epsilon}^2). \tag{4.27}$$

The proof of (4.3.1) is given in Lemma 3 of Hornung and Jäger (1991). We also recall a classical lemma from Allaire and El Ganaoui (2009):

Lemma 4.3.2. *There exists a constant $C > 0$, not depending on ϵ, such that*

$$\sqrt{\epsilon}\,\|u^\epsilon\|_{\Gamma^\epsilon} \le C\,\|u^\epsilon\|_{H^1(\Omega_g^\epsilon)}, \quad \forall u^\epsilon \in H^1(\Omega_g^\epsilon). \tag{4.28}$$

Definition 4.3.3. *We call the triplet $(C^\epsilon, T^\epsilon, R^\epsilon)$ a weak solution to* (4.9)-(4.11)*, if*

$$\begin{aligned} &C^\epsilon \in C_D + \mathscr{W}_D(\Omega_g^\epsilon) \\ &T^\epsilon \in T_D + \mathscr{W}_D(\Omega) \\ &R^\epsilon \in L^2((0,T)\times\Gamma^\epsilon), \end{aligned} \tag{4.29}$$

and the following variational formulation

$$(\partial_t C^\epsilon, \phi)_{\Omega_g^\epsilon,\tau} + (D^\epsilon \nabla C^\epsilon, \nabla\phi)_{\Omega_g^\epsilon} + (\boldsymbol{u}^\epsilon \nabla C^\epsilon, \phi)_{\Omega_g^\epsilon} = -\epsilon(W^\epsilon, \phi)_{\Gamma^\epsilon}, \tag{4.30}$$

$$(\mathcal{C}^\epsilon \partial_t T^\epsilon, \varphi)_{\Omega_s^\epsilon} + (\lambda^\epsilon \nabla T^\epsilon, \nabla\varphi)_{\Omega_s^\epsilon} + (\chi_g^\epsilon \mathcal{C}_g \boldsymbol{u}^\epsilon \nabla T^\epsilon, \varphi)_{\Omega_s^\epsilon} = \epsilon Q(W^\epsilon, \varphi)_{\Gamma^\epsilon}, \tag{4.31}$$

$$(\partial_t R, \psi)_{\Gamma^\epsilon} = (W^\epsilon, \psi)_{\Gamma^\epsilon} \tag{4.32}$$

is satisfied for all $t \in (0,\tau)$ and for all $\phi \in \mathscr{W}_D(\Omega_g^\epsilon)$, $\varphi \in \mathscr{W}_D(\Omega)$, $\psi \in L^2((0,\tau)\times\Gamma^\epsilon)$ and $C^\epsilon(t) \to C_0$ in $L^2(\Omega_g^\epsilon)$, $T^\epsilon(t) \to T_0$ in $L^2(\Omega)$, $R^\epsilon(t) \to 0$ in $L^2(\Gamma^\epsilon)$ as $t \to 0$.

Theorem 4.3.4. *Assume (A1)-(A6). Then there exists at least a global-in-time weak solution in the sense of Definition 4.3.3.*

Proof. The proof is based on the Galerkin argument. Since $W(T^\epsilon, C^\epsilon)$ is a globally Lipschitz function in both variables, this makes the proof rather standard (Evans, 1998). □

Theorem 4.3.5. *Assume (A1)–(A4), then there exist a unique solution of the weak microscopic problems* (4.30)-(4.32)*.*

Proof. We want to show that if $C^\epsilon \in C_D + \mathscr{W}_D(\Omega_g^\epsilon)$, $T^\epsilon \in T_D + \mathscr{W}_D(\Omega)$ and $R^\epsilon \in L^2((0,T)\times\Gamma^\epsilon)$, with $(C^\epsilon(0), T^\epsilon(0), R^\epsilon(0)) \equiv 0$, such that the weak formulations

$$(\partial_t C^\epsilon, \phi)_{\Omega_g^\epsilon} + (D^\epsilon \nabla C^\epsilon, \nabla\phi)_{\Omega_g^\epsilon} = -\epsilon(W^\epsilon, \phi)_{\Gamma^\epsilon} - (\boldsymbol{u}^\epsilon \nabla C^\epsilon, \phi)_{\Omega_g^\epsilon}, \tag{4.33}$$

$$(\mathcal{C}^\epsilon \partial_t T^\epsilon, \varphi)_\Omega + (\lambda^\epsilon \nabla T^\epsilon, \nabla\varphi)_\Omega = \epsilon Q(W^\epsilon, \varphi)_{\Gamma^\epsilon} - (\chi_g^\epsilon \mathcal{C}_g \boldsymbol{u}^\epsilon \nabla T^\epsilon, \varphi)_\Omega, \tag{4.34}$$

$$(\partial_t R, \psi)_{\Gamma^\epsilon} = (W^\epsilon, \psi)_{\Gamma^\epsilon} \tag{4.35}$$

are satisfied a.e. on $(0,\tau)$ for all $\phi,\varphi \in \boldsymbol{\mathcal{V}}_D$ and $\psi \in L^2((0,\tau)\times\Gamma^\epsilon)$, then $(C^\epsilon, T^\epsilon, R^\epsilon) \equiv 0$.

We test the weak formulations (4.30)–(4.32) by $(\phi,\varphi,\psi) \equiv (C^\epsilon, T^\epsilon, R^\epsilon)$, and treat the weak problems separately. In (4.30), the convective term vanishes since $\boldsymbol{u}^\epsilon$ is divergence free. Using the coercivity condition on D^ϵ, the boundedness[2] of f, and the trace inequality (Lemma 4.3.1), we obtain

$$\begin{aligned} &\frac{1}{2}\frac{d}{dt}\left\|C^\epsilon(t)\right\|^2_{\Omega_{\mathrm{g}}^\epsilon} + D_0\left\|\nabla C^\epsilon(t)\right\|^2_{\Omega_{\mathrm{g}}^\epsilon} \le C(\left\|C^\epsilon(t)\right\|^2_{\Omega_{\mathrm{g}}^\epsilon} + \epsilon^2\left\|\nabla C^\epsilon(t)\right\|^2_{\Omega_{\mathrm{g}}^\epsilon}) \\ &\frac{d}{dt}\left\|C^\epsilon(t)\right\|^2_{\Omega_{\mathrm{g}}^\epsilon} + (D_0-\epsilon^2 C)\left\|\nabla C^\epsilon(t)\right\|^2_{\Omega_{\mathrm{g}}^\epsilon} \le \left\|C^\epsilon(t)\right\|^2_{\Omega_{\mathrm{g}}^\epsilon}. \end{aligned} \tag{4.36}$$

Integrating (4.71) from 0 to t

$$\left\|C^\epsilon(t)\right\|^2_{\Omega_{\mathrm{g}}^\epsilon} + (D_0-\epsilon^2 C)\left\|\nabla C^\epsilon\right\|^2_{\Omega_{\mathrm{g}}^\epsilon,\tau} \le C\int_0^t \left\|C^\epsilon(s)\right\|^2_{\Omega_{\mathrm{g}}^\epsilon} ds. \tag{4.37}$$

Applying Gronwall's inequality and taking the supremum along $t\in[0,\tau]$ yields the desired result.

In (4.69), the convective term vanishes for a similar reason. Using the coercivity condition on λ^ϵ and applying a combination of the Schwartz and Young's inequality on the nonlinear term, we obtain

$$\begin{aligned} &\frac{\mu_0}{2}\frac{d}{dt}\left\|T^\epsilon(t)\right\|^2_{\Omega} + \lambda_0\left\|\nabla T^\epsilon(t)\right\|^2_{\Omega} \\ &\le \epsilon C\Big[\frac{1}{2}\int_{\Gamma^\epsilon}(f(T^\epsilon)T^\epsilon)^2 d\gamma + \frac{1}{2}\int_{\Gamma^\epsilon}\left|C^\epsilon\right|^2 d\gamma\Big] \end{aligned} \tag{4.38}$$

The positivity[3]of f is such that

$$\int_{\Gamma^\epsilon}(f(T^\epsilon)T^\epsilon)^2 d\gamma \ge 0, \tag{4.39}$$

and using the trace inequality and (4.37) on the second boundary integral on the right hand side of the inequality, we obtain after integration from 0 to t, the desired result.

$$T^\epsilon = 0. \tag{4.40}$$

The uniqueness of R^ϵ follows naturally from the uniqueness of T^ϵ and C^ϵ. □

[2]One can show that our problem satisfies a weak maximum principle. Thus, we expect C^ϵ, T^ϵ and R^ϵ to be uniformly bounded. Hence, f is bounded.

[3]For our system, we can also show that $C^\epsilon \ge 0$ a.e. in $\Omega_{\mathrm{g}}^\epsilon, T^\epsilon \ge 0$ a.e. in Ω and $R^\epsilon \ge 0$ a.e. on Γ^ϵ. Particularly, $f \ge 0$ a.e. on Γ^ϵ.

Definition 4.3.6. *We call (C,T,R) a weak solution to* (4.15)-(4.23)*, if*

$$\begin{aligned} &C \in C_D + \mathscr{W}_D(\Omega),\\ &T \in T_D + \mathscr{W}_D(\Omega),\\ &R \in L^2((0,T)\times\Omega), \end{aligned} \tag{4.41}$$

and the following variational formulation

$$|Y_{\mathrm{g}}|(\partial_t C,\phi)_\Omega + (D^{\mathrm{eff}}\nabla C,\nabla\phi)_\Omega + |Y_{\mathrm{g}}|(\boldsymbol{u}\nabla C,\phi)_\Omega = -|\Gamma|(W,\phi)_\Omega, \tag{4.42}$$

$$\mathcal{C}^{\mathrm{eff}}(\partial_t T,\varphi)_\Omega + (\lambda^{\mathrm{eff}}\nabla T,\nabla\varphi)_\Omega + \mathcal{C}_{\mathrm{g}}(\boldsymbol{u}\nabla T,\varphi)_\Omega = Q|\Gamma|(W,\varphi)_\Omega, \tag{4.43}$$

$$(\partial_t R,\psi)_\Omega = (W,\psi)_\Omega \tag{4.44}$$

is satisfied for all $t\in(0,\tau)$ and for all $\phi\in\mathscr{V}_D(\Omega)$, $\varphi\in\mathscr{V}_D(\Omega)$, $\psi\in L^2((0,\tau)\times\Omega)$ and $C(t)\to C_0$ in $L^2(\Omega), T(t)\to T_0$ in $L^2(\Omega)$, $R(t)\to 0$ in $L^2(\Omega)$ as $t\to 0$.

Remark 4.3.1. *The existence of weak solutions to* (4.42)-(4.44) *follows by proving the two-scale convergence. In the sequel, we focus on the uniqueness issue.*

Theorem 4.3.7. *Assume (A1)–(A4), then there exist a unique weak solution of the variational formulation* (4.42)-(4.44)*.*

Proof. We show that if $T,C\in\mathscr{W}_D, R\in L^2((0,T)\times\Omega), (\mathrm{C}(0),\mathrm{T}(0),\mathrm{R}(0))\equiv 0$ such that the weak formulations

$$|Y_{\mathrm{g}}|(\partial_t C,\phi)_\Omega + (D^{\mathrm{eff}}\nabla C,\nabla\phi)_\Omega = -|\Gamma|(W,\phi)_\Omega - |Y_{\mathrm{g}}|(\boldsymbol{u}\nabla C,\phi)_\Omega, \tag{4.45}$$

$$\mathcal{C}^{\mathrm{eff}}(\partial_t T,\varphi)_\Omega + (\lambda^{\mathrm{eff}}\nabla T,\nabla\varphi)_\Omega = Q|\Gamma|(W,\varphi)_\Omega - \mathcal{C}_{\mathrm{g}}(\boldsymbol{u}\nabla T,\varphi)_\Omega, \tag{4.46}$$

$$(\partial_t R,\psi)_\Omega = (W,\psi)_\Omega, \tag{4.47}$$

are satisfied a.e. on $(0,\tau)$ for all $\phi,\varphi\in\mathscr{V}_D$ and $\psi\in L^2((0,\tau)\times\Omega)$, then $(C,T,R)\equiv 0$. We test the weak formulations by $(\phi,\varphi,\psi)\equiv(C,T,R)$ to obtain

$$\frac{C_1}{2}\frac{d}{dt}\|C(t)\|_\Omega^2 + (D^{\mathrm{eff}}\nabla C,\nabla C)_\Omega = |\Gamma|(W,C)_\Omega - |Y_{\mathrm{g}}|(\boldsymbol{u}\nabla C,C)_\Omega, \tag{4.48}$$

$$\frac{C_2}{2}\frac{d}{dt}\|T(t)\|_\Omega^2 + (\lambda^{\mathrm{eff}}\nabla T,\nabla\varphi)_\Omega = Q|\Gamma|(W,T)_\Omega - |Y_{\mathrm{g}}|(\boldsymbol{u}\nabla T,T)_\Omega, \tag{4.49}$$

$$\frac{C_3}{2}\frac{d}{dt}\|R(t)\|_\Omega^2 = (W,R)_\Omega. \tag{4.50}$$

The convective term vanishes since $\boldsymbol{u}$ is divergence free. We use the coercivity of D^{eff} and λ^{eff} in the second term on the left hand side of (4.48) and (4.49), the boundedness of f, and Cauchy-Schwartz inequality on the nonlinear reaction terms. We eventually arrive at the following

$$\frac{C_1}{2}\frac{d}{dt}\|C(t)\|_\Omega^2 + D_0\|\nabla C(t)\|_\Omega^2 \le C_5\|C(t)\|_\Omega^2, \tag{4.51}$$

$$\frac{C_2}{2}\frac{d}{dt}\|T(t)\|_\Omega^2 \le C_6(\|T(t)\|_\Omega^2 + \|C(t)\|_\Omega^2 - \lambda_0\|\nabla T(t)\|_\Omega^2), \tag{4.52}$$

$$\frac{C_3}{2}\frac{d}{dt}\|R(t)\|_\Omega^2 \le C_7(\|R(t)\|_\Omega^2 + \|C(t)\|_\Omega^2). \tag{4.53}$$

The conclusion follows by direct application of Gronwall's inequality (see Evans, 1998, e.g.). □

4.4 ϵ-independent estimates

In order to use the two-scale convergence method, we need to establish some a priori (uniform in ϵ) estimates on the unknowns $(C^\epsilon, T^\epsilon, R^\epsilon)$.

Lemma 4.4.1. *Assume (A1)–(A4). Then there exists a constant, C, independent of ϵ such that the weak solution to the microscopic problem* (4.30)–(4.32) *satisfies the following a priori estimates*

$$\|C^\epsilon\|_{L^2(0,\tau;L^2(\Omega_{\rm g}^\epsilon))} + \|\nabla C^\epsilon\|_{L^2(0,\tau;L^2(\Omega_{\rm g}^\epsilon))} + \sqrt{\epsilon}\|C^\epsilon\|_{L^2(0,\tau;L^2(\Gamma^\epsilon))} \leq C, \tag{4.54}$$

$$\|T^\epsilon\|_{L^2(0,\tau;L^2(\Omega))} + \|\nabla T^\epsilon\|_{L^2(0,\tau;L^2(\Omega))} + \sqrt{\epsilon}\,\|T^\epsilon\|_{L^2(0,\tau;L^2(\Gamma^\epsilon))} \leq C, \tag{4.55}$$

$$\sqrt{\epsilon}\|R^\epsilon\|_{L^\infty((0,\tau)\times\Gamma^\epsilon)} + \sqrt{\epsilon}\|\partial_t R^\epsilon\|_{L^2((0,\tau)\times\Gamma^\epsilon)} \leq C. \tag{4.56}$$

Lemma 4.4.2 (Additional *a priori* estimates)**.** *Assume (A1)-(A5). The following ϵ-independent bounds hold:*

$$\|\partial_t C^\epsilon\|_{L^2(0,\tau;L^2(\Omega_{\rm g}^\epsilon))} + \|\partial_t T^\epsilon\|_{L^2(0,\tau;L^2(\Omega))} \leq C, \tag{4.57}$$

where C is a generic constant independent of ϵ.

For the proof of Lemma 4.4.1 and Lemma 4.4.2, see Appendices B and C respectively.

4.4.1 Extensions to Ω

Lemma 4.4.3. *There exists an extension operator $\mathcal{P} \in \mathfrak{L}(H^1(Y_{\rm g}); H^1_\#(Y))$ linear and continuous, such that there exists a constant C satisfying*

$$\|\mathcal{P}u\|_{H^1(Y)} \leq C\|u\|_{H^1(Y_{\rm g})}$$

for every $u \in H^1(Y_{\rm g})$.

Proof. See Lemma 2.4 in Monsurro (2003) for proof details. □

Remark 4.4.1. *Using Lemma 4.4.3, we extend the functions defined in $\Omega_{\rm g}^\epsilon$ in the domain $\Omega_{\rm s}^\epsilon$* (see Allaire, 1992; Allaire and Murat, 1993) covering finally Ω. See also extension results by (Cioranescu and Paulin, 1979).

4.5 Two scale convergence

In this section. we prove a rigorous homogenization result using the two-scale convergence method to verify the results derived in Chapter 3 by using formal asymptotic expansion. This method relies essentially on the *a priori* estimates indicated in the previous section. In what follows, we will recall the notion of two scale convergence for functions defined on periodic domains. Also, in the sequel, we will denote the extension $\mathcal{P}C^\epsilon$ of C^ϵ simply by C^ϵ. Note that the temperature field does not need to be extended.

Definition 4.5.1. *A bounded sequence u^ϵ in $L^2((0,\tau)\times\Omega)$ is said to two-scale converge to a function $u^0(t,x,y)\in L^2((0,\tau)\times\Omega;Y)$ if there exists a subsequence still denoted by u^ϵ such that*

$$\lim_{\epsilon\to 0}\int_0^\tau\!\!\int_\Omega u^\epsilon(t,x)\psi(t,x,\frac{x}{\epsilon})\mathrm{d}x\mathrm{d}t=\frac{1}{|Y|}\int_0^\tau\!\!\int_\Omega\!\!\int_Y u^0(t,x,y)\psi(t,x,y)\mathrm{d}x\mathrm{d}y\mathrm{d}t, \tag{4.58}$$

for any Y-periodic test function $\psi(t,x,y)\in L^2((0,\tau)\times\Omega;C_\#(Y))$.

The notion of two-scale convergence makes sense because of the next compactness theorem (Nguestseng, 1989) and (Allaire, 1992).

Theorem 4.5.2. *From each bounded sequence $u^\epsilon\in L^2((0,\tau)\times\Omega)$, we can extract a subsequence and there exists a limit $u^0(t,x,y)\in L^2(0,\tau,\Omega\times Y)$ such that the subsequence two-scale converges to u^0.*

The generalization of Theorem 4.5.2 to bounded sequences in $L^2(0,\tau;H^1(\Omega))$ is the following:

Proposition 4.5.3. *From each bounded sequence $u^\epsilon(t,x)\in L^2(0,\tau;H^1(\Omega))$, we can extract a subsequence such that there exists two limits $u^0(t,x)\in L^2(0,\tau;H^1(\Omega))$ and $u^1(t,x,y)\in L^2((0,\tau)\times\Omega;H^1_\#(Y))$ such that for the subsequence, $u^\epsilon(t,x)$ converges weakly to $u^0(t,x)$ in $L^2(0,\tau,H^1(\Omega))$ and $\nabla u^\epsilon(x,t)$ two-scale converges to $\nabla_x u^0(t,x)+\nabla_y u^1(x,y)$.*

The concept of two-scale convergence can naturally be extended to sequences defined on periodic surfaces (see Allaire et al., 1995) and (see Neuss-Radu, 1996).

Proposition 4.5.4. *For any sequence u^ϵ in $L^2(\Gamma^\epsilon)$ such that*

$$\epsilon\int_0^\tau\!\!\int_{\Gamma^\epsilon}|u^\epsilon|^2\mathrm{d}x\le C, \tag{4.59}$$

there exist a subsequence, still denoted by u^ϵ, and a limit function $u^0(t,x,y)\in L^2(0,\tau\times\Omega;L^2_\#(\Gamma))$ such that u^ϵ two-scale converges to u^0 in the following sense

$$\lim_{\epsilon\to 0}\epsilon\int_0^\tau\!\!\int_{\Gamma^\epsilon}u^\epsilon(t,x)\psi(t,x,\frac{x}{\epsilon})\mathrm{d}x\mathrm{d}t=\frac{1}{|Y|}\int_0^\tau\!\!\int_\Omega\!\!\int_\Gamma u^0(t,x,y)\psi(t,x,y)\mathrm{d}x\mathrm{d}y\mathrm{d}t, \tag{4.60}$$

for any Y-periodic test function $\psi(t,x,y)\in L^2(0,\tau\times\Omega;C_\#(\Gamma))$.

The estimates in Lemma 4.4.1 and Lemma 4.4.2 lead to the following convergence results:

Lemma 4.5.5. *Assume (A1)–(A6). Then it holds as $\epsilon \to 0$ that:*

(a) $C^\epsilon \rightharpoonup C^0, T^\epsilon \rightharpoonup T^0$ *weakly in* $L^2(0,\tau;H^1(\Omega))$,

(b) $C^\epsilon \overset{*}{\rightharpoonup} C^0, T^\epsilon \overset{*}{\rightharpoonup} T^0$ *weakly in* $L^\infty((0,\tau)\times\Omega)$,

(c) $\partial_t C^\epsilon \rightharpoonup \partial_t C^0, \partial_t T^\epsilon \rightharpoonup \partial_t T^0$ *weakly in* $L^2((0,\tau)\times\Omega)$,

(d) $C^\epsilon \to C^0, T^\epsilon \to T^0$ *strongly in* $L^2(0,\tau;H^\beta(\Omega))$ for $\dfrac{1}{2} < \beta < 1$,
also $\sqrt{\epsilon}\|C^\epsilon - C^0\|_{L^2((0,\tau)\times\Gamma^\epsilon)} \to 0$ and $\sqrt{\epsilon}\|T^\epsilon - T^0\|_{L^2((0,\tau)\times\Gamma^\epsilon)} \to 0$ as $\epsilon \to 0$.

(e) $C^\epsilon \overset{2}{\rightharpoonup} C^0, T^\epsilon \overset{2}{\rightharpoonup} T^0, \nabla C^\epsilon \overset{2}{\rightharpoonup} \nabla_x C^0 + \nabla_y C^1$, $C^1 \in L^2((0,\tau)\times\Omega; H^1_\#(Y_{\mathrm{g}})/\mathbb{R})$, $\nabla T^\epsilon \overset{2}{\rightharpoonup} \nabla_x T^0 + \nabla_y T^1$, $T^1 \in L^2((0,\tau)\times\Omega; H^1_\#(Y)/\mathbb{R})$,

(f) $R^\epsilon \overset{2}{\rightharpoonup} R^0$, and $R^0 \in L^\infty((0,\tau)\times\Omega\times\Gamma)$,

(g) $\partial_t C^\epsilon \overset{2}{\rightharpoonup} \partial_t C^0, \partial_t T^\epsilon \overset{2}{\rightharpoonup} \partial_t T^0$, and $\partial_t R^\epsilon \overset{2}{\rightharpoonup} \partial_t R^0 \in L^2((0,\tau)\times\Omega\times\Gamma)$.

Proof. (a) and (b) are obtained as a direct consequence of the fact that C^ϵ, T^ϵ are bounded in $L^2(0,\tau;H^1(\Omega)) \cap L^\infty((0,\tau)\times\Omega)$; up to a subsequence (still denoted by C^ϵ, T^ϵ) C^ϵ, T^ϵ converges weakly to C^0, T^0 in $L^2(0,\tau;H^1(\Omega)) \cap L^\infty((0,\tau)\times\Omega)$. A similar argument gives (c). To obtain (d), we use the compact embedding $H^{\beta'}(\Omega) \hookrightarrow H^\beta(\Omega)$, for $\beta \in \left(\dfrac{1}{2}, 1\right)$ and $0 < \beta < \beta' \leq 1$ (since Ω has a Lipschitz boundary). We have

$$W := \{C^\epsilon, T^\epsilon \in L^2(0,T^0;H^1(\Omega)) \text{ and } \partial_t C^\epsilon, \partial_t T^\epsilon \in L^2((0,\tau)\times\Omega)\}.$$

For a fixed ϵ, W is compactly embedded in $L^2(0,\tau;H^\beta(\Omega))$ by the Lions-Aubin Lemma; cf. e.g. Lions (1969). Using the trace inequality for oscillating surfaces

$$\begin{aligned}\sqrt{\epsilon}\|C^\epsilon - C^0\|_{L^2((0,\tau)\times\Gamma_\epsilon)} &\leq C\|C^\epsilon - C^0\|_{L^2(0,\tau;H^\beta(\Omega^\epsilon_{\mathrm{g}}))} \\ &\leq C\|C^\epsilon - C^0\|_{L^2(0,\tau;H^\beta(\Omega))}\end{aligned}$$

where $\|C^\epsilon - C^0\|_{L^2(0,\tau;H^\beta(\Omega))} \to 0$ as $\epsilon \to 0$. Similar argument holds for the rest of (d).
To investigate (e), (f) and (g), we use the notion of two-scale convergence as indicated in Definition 4.5.1 and 4.5.4. Since C^ϵ are bounded in $L^2(0,\tau;H^1(\Omega))$, up to a subsequence $C^\epsilon \overset{2}{\rightharpoonup} C^0$ in $L^2((0,\tau)\times\Omega)$, and $\nabla C^\epsilon \overset{2}{\rightharpoonup} \nabla_x C^0 + \nabla_y C^1$, $C^1 \in L^2((0,\tau)\times\Omega; H^1_\#(Y_{\mathrm{g}})/\mathbb{R})$. By Theorem 4.5.4, R^ϵ in $L^\infty((0,\tau)\times\Gamma_\epsilon)$ converges two-scale to $R \in L^\infty((0,\tau)\times\Omega\times\Gamma)$ and $\partial_t R^\epsilon$ converges two-scale to $\partial_t R$ in $L^2((0,\tau)\times\Omega\times\Gamma)$. □

Theorem 4.5.6. *Let* $(C^\epsilon, T^\epsilon, R^\epsilon)$ be the sequence of solutions of (4.9)-(4.11). Let (C^0, T^0, R^0) be the solution of the homogenized problems (4.15)-(4.23). Then the sequences T^ϵ and ∇T^ϵ two-scale converge to T^0 and $(\nabla_x T^0(x,t) + \nabla_y T^1(x,y,t))$ respectively. Denote by $\tilde{\cdot}$ the extension by zero in the domain $\Omega_{\rm s}^\epsilon$. The sequences $\tilde{C^\epsilon}$ and $\nabla\tilde{C^\epsilon}$ two-scale converge to $C^0(t,x)\chi_{\rm g}(y)$ and $\chi_{\rm g}(y)(\nabla_x C^0(x,t) + \nabla_y C^1(x,y,t))$, respectively. (T^0, T^1), (respectively (C^0, C^1)) is the unique solution in $T_D + \mathscr{W}_D(\Omega) \times L^2(0,\tau; L^2(\Omega; H^1_\#(Y)/\mathbb{R}))$ (respectively $C_D + \mathscr{W}_D(\Omega) \times L^2(0,\tau; L^2(\Omega; H^1_\#(Y_{\rm g})/\mathbb{R}))$). Additionally, $R^\epsilon \in L^\infty((0,\tau)\times\Gamma^\epsilon)$ converges two-scale to $R^0 \in L^\infty((0,\tau)\times\Omega\times\Gamma)$

Proof. The a priori estimates in Lemma 4.4.1 and Lemma 4.4.2 imply that, up to a subsequence, T^ϵ two-scale converges to a function $T^0 \in T_D + \mathscr{W}_D(\Omega)$ and ∇T^ϵ two-scale converges to $\nabla_x T^0(x,t) + \nabla_y T^1(x,y,t)$, where $T^1 \in L^2(0,\tau; L^2(\Omega; H^1_\#(Y)/\mathbb{R}))$. Similarly, C^ϵ two-scale converges to a function $C^0\chi_{\rm g}(y) \in C_D + \mathscr{W}_D(\Omega)$ and ∇C^ϵ two-scale converges to $\chi_{\rm g}(y)(\nabla_x C^0(x,t) + \nabla_y C^1(x,y,t))$, where $C^1 \in L^2(0,\tau; L^2(\Omega; H^1_\#(Y_{\rm g})/\mathbb{R}))$. Furthermore, T^ϵ and C^ϵ two-scale converge to T^0 and C^0 on the periodic surface Γ^ϵ, by Proposition 4.5.4.

In a first step, we compute the correctors $T^1(t,x,y)$ and $C^1(t,x,y)$ in terms of the gradients $\nabla_x T^0(x,t)$ and $\nabla_x C^0(x,t)$ respectively. This is done by choosing test functions $\varphi^\epsilon(t,x) = \epsilon\varphi^1(x, \frac{x}{\epsilon})$ and $\phi^\epsilon(t,x) = \epsilon\phi^1(x, \frac{x}{\epsilon})$ respectively in the variational formulations (4.31) and (4.30) for T^ϵ and C^ϵ, where $\varphi^1(t,x,y)$ and $\phi^1(t,x,y)$ are smooth functions in x and Y-periodic in y, i.e.

$$\begin{aligned}
&\epsilon \int_0^\tau\!\!\int_\Omega \mathcal{C}^\epsilon \frac{\partial T^\epsilon}{\partial t}\varphi^1 dxdt + \int_0^\tau\!\!\int_\Omega \lambda^\epsilon \nabla T^\epsilon \nabla_y \varphi^1 dxdt + \epsilon \int_0^\tau\!\!\int_\Omega \chi_{\rm g}^\epsilon \boldsymbol{u}^\epsilon \nabla T^\epsilon \varphi^1 dxdt \qquad (4.61)\\
&= \epsilon^2 \int_0^\tau\!\!\int_{\Gamma^\epsilon} Q W^\epsilon \varphi^1 d\gamma dt
\end{aligned}$$

Passing to the two-scale limit in (4.61), we have

$$\begin{aligned}
&\lim_{\epsilon\to 0} \int_0^\tau\!\!\int_\Omega \lambda^\epsilon \nabla T^\epsilon \nabla_y \varphi^1 dxdt \qquad (4.62)\\
&= \int_0^\tau\!\!\int_\Omega\!\!\int_Y \lambda(y)(\nabla_y T^1(x,y,t) + \nabla_x T^0(x,t)) \cdot \nabla_y \varphi^1(t,x,y) dydxdt\\
&= \int_0^\tau\!\!\int_\Omega\!\!\int_{Y_{\rm g}} \lambda_{\rm g}(y)(\nabla_y T^1(x,y,t) + \nabla_x T^0(x,t)) \cdot \nabla_y \varphi^1(t,x,y) dydxdt\\
&+ \int_0^\tau\!\!\int_\Omega\!\!\int_{Y_{\rm s}} \lambda_{\rm s}(y)(\nabla_y T^1(x,y,t) + \nabla_x T^0(x,t)) \cdot \nabla_y \varphi^1(t,x,y) dydxdt = 0,
\end{aligned}$$

which gives precisely the variational formulation of (3.8) for T^1. Thus, we have shown that

$$T^1(t,x,y) = \sum_{j=1}^{3} \frac{\partial T^0}{\partial x_j}(t,x)\mathcal{N}_j(y), \quad \text{in } \Omega \times Y \text{and a.e. in t} \tag{4.63}$$

In a similar way, we show in (4.30) that

$$\begin{aligned} &\epsilon \int_0^\tau\!\!\int_{\Omega_{\mathrm{g}}^\epsilon} \frac{\partial C^\epsilon}{\partial t}\phi^1 dxdt + \int_0^\tau\!\!\int_{\Omega_{\mathrm{g}}^\epsilon} D^\epsilon \nabla C^\epsilon \nabla_y \phi^1 dxdt + \epsilon \int_0^\tau\!\!\int_{\Omega_{\mathrm{g}}^\epsilon} \boldsymbol{u}^\epsilon \nabla C^\epsilon \phi^1 dxdt \\ &= \epsilon^2 \int_0^\tau\!\!\int_{\Gamma^\epsilon} W^\epsilon \phi^1 d\gamma dt, \end{aligned} \tag{4.64}$$

and passing to the two-scale limit in (4.64)

$$\begin{aligned} &\lim_{\epsilon\to 0} \int_0^\tau\!\!\int_{\Omega_{\mathrm{g}}^\epsilon} D^\epsilon \nabla C^\epsilon \nabla_y \phi^1 dxdt \\ &= \int_0^\tau\!\!\int\!\!\int_{\Omega Y_{\mathrm{g}}} D(y)(\nabla_y C^1(x,y,t) + \nabla_x C^0(x,t)) \cdot \nabla_y \phi^1(t,x,y) dydxdt = 0, \end{aligned} \tag{4.65}$$

which gives the variational formulation of (3.89) for C^1, and hence proving that

$$C^1(t,x,y) = \sum_{j=1}^{3} \frac{\partial C^0}{\partial x_j}(t,x)\mathcal{N}_j(y), \quad \text{in } \Omega \times Y_{\mathrm{g}} \text{ and a.e. in t} \tag{4.66}$$

In a second step, we recover the homogenized problems for T^0 and C^0 by choosing another set of test functions φ^ϵ and ϕ^ϵ in the variational formulations (4.31) and (4.30) for T^ϵ, and C^ϵ respectively. Note that the form of the test functions in both cases are identical, except that the definition of the cell solutions $\mathcal{N}_j$ manifesting in the second terms are different, i.e.

$$\varphi^\epsilon(t,x) = \varphi^0(t,x) + \epsilon\varphi^1(x,\frac{x}{\epsilon}), \text{ with } \varphi^1(t,x,y) = \sum_{j=1}^{3} \frac{\partial \varphi^0}{\partial x_j}(t,x)\mathcal{N}_j(y), \text{ in } \Omega \times Y \tag{4.67}$$

$$\phi^\epsilon(t,x) = \phi^0(t,x) + \epsilon\phi^1(x,\frac{x}{\epsilon}), \text{ with } \phi^1(t,x,y) = \sum_{j=1}^{3} \frac{\partial \phi^0}{\partial x_j}(t,x)\mathcal{N}_j(y), \text{ in } \Omega \times Y_{\mathrm{g}}, \tag{4.68}$$

Using (4.67) in (4.31), we obtain the following

$$\begin{aligned}
&\int_0^\tau\!\!\int_\Omega \mathcal{C}^\epsilon \frac{\partial T^\epsilon}{\partial t}(\varphi^0+\epsilon\varphi^1)dxdt + \int_0^\tau\!\!\int_\Omega \lambda^\epsilon \nabla T^\epsilon(\nabla_x\varphi^0+\nabla_y\varphi^1)dxdt \qquad (4.69)\\
&+\int_0^\tau\!\!\int_\Omega \chi_{\mathrm{g}}^\epsilon \boldsymbol{u}^\epsilon \nabla T^\epsilon(\varphi^0+\epsilon\varphi^1)dxdt\\
&=\int_0^\tau\!\!\int_{\Gamma^\epsilon} QW^\epsilon(\varphi^0+\epsilon\varphi^1)d\gamma dt\\
&=\sum_{j=1}^4 \boldsymbol{\mathcal{I}}_j,
\end{aligned}$$

where $\boldsymbol{\mathcal{I}}_j, j=1,2,\cdots,4$ identifies each integral in (4.69). In order to pass to the two-scale limit in $\boldsymbol{\mathcal{I}}_1$, we first see that

$$\int_0^\tau\!\!\int_\Omega \mathcal{C}^\epsilon \frac{\partial T^\epsilon}{\partial t}\varphi^0 dxdt = -\int_0^\tau\!\!\int_\Omega \mathcal{C}^\epsilon \frac{\partial \varphi^0}{\partial t}T^\epsilon dxdt + \Big[\int_\Omega \mathcal{C}^\epsilon T^\epsilon \varphi^0 dx\Big]\Big|_0^\tau. \qquad (4.70)$$

Now, we pass to the two-scale limit on the right hand side of (4.70),

$$\begin{aligned}
&\lim_{\epsilon\to 0}\int_0^\tau\!\!\int_\Omega \mathcal{C}^\epsilon \frac{\partial T^\epsilon}{\partial t}\varphi^0 dxdt = -\int_0^\tau\!\!\int_\Omega\!\!\int_Y \mathcal{C}(y)\frac{\partial \varphi^0}{\partial t}T^0 dxdydt + \Big[\int_\Omega\!\!\int_Y \mathcal{C}(y)T^0\varphi^0 dx\Big]\Big|_0^\tau \qquad (4.71)\\
&=\int_0^\tau\!\!\int_\Omega\!\!\int_Y \mathcal{C}(y)\frac{\partial T^0}{\partial t}\varphi^0 dxdydt,
\end{aligned}$$

where

$$\int_Y \mathcal{C}(y)dy := \int_Y \chi_{\mathrm{g}}\mathcal{C}_{\mathrm{g}}dy + \int_Y \chi_{\mathrm{s}}\mathcal{C}_{\mathrm{s}}dy = \int_{Y_{\mathrm{g}}} \mathcal{C}_{\mathrm{g}}dy + \int_{Y_{\mathrm{s}}} \mathcal{C}_{\mathrm{s}}dy. \qquad (4.72)$$

Passing to the two-scale limit in $\mathscr{I}_2$, we obtain

$$\begin{aligned}
&\lim_{\epsilon\to 0}\int_0^\tau\int_\Omega \lambda^\epsilon \nabla T^\epsilon(\nabla_x\varphi^0+\nabla_y\varphi^1)dxdt \qquad (4.73)\\
&=\int_0^\tau\int_\Omega\int_Y \lambda(y)(\nabla_x T^0+\nabla_y T^1)\cdot(\nabla_x\varphi^0+\nabla_y\varphi^1)dydxdt\\
&=\int_0^\tau\int_\Omega\int_{Y_{\mathrm{g}}} \lambda_{\mathrm{g}}(\nabla_x T^0+\nabla_y T^1)\cdot(\nabla_x\varphi^0+\nabla_y\varphi^1)dydxdt\\
&+\int_0^\tau\int_\Omega\int_{Y_{\mathrm{s}}} \lambda_{\mathrm{s}}(\nabla_x T^0+\nabla_y T^1)\cdot(\nabla_x\varphi^0+\nabla_y\varphi^1)dydxdt.
\end{aligned}$$

Similarly for $\mathscr{I}_3$, we get

$$\begin{aligned}
\lim_{\epsilon\to 0}\int_0^\tau\int_\Omega \chi_{\mathrm{g}}^\epsilon \boldsymbol{u}^\epsilon\nabla T^\epsilon(\varphi^0+\epsilon\varphi^1)dxdt \quad &= -\lim_{\epsilon\to 0}\int_0^\tau\int_\Omega \chi_{\mathrm{g}}^\epsilon \boldsymbol{u}^\epsilon(\nabla_x\varphi^0+\nabla_y\varphi^1)T^\epsilon dxdt \qquad (4.74)\\
&= -\int_0^\tau\int_\Omega\int_{Y_{\mathrm{g}}} \mathcal{C}_{\mathrm{g}}\boldsymbol{u}(x,y)(\nabla_x\varphi^0+\nabla_y\varphi^1)T^0 dydxdt\\
&= \int_0^\tau\int_\Omega\int_{Y_{\mathrm{g}}} \mathcal{C}_{\mathrm{g}}\boldsymbol{u}(x,y)\cdot\nabla_x T^0\varphi^0 dydxdt,
\end{aligned}$$

where the last integral follows by a simple integration by parts and using the assumptions on the velocity $\boldsymbol{u}$. Passing to the two-scale limit in $\mathscr{I}_4$, we have

$$\begin{aligned}
\lim_{\epsilon\to 0}\epsilon\int_0^\tau\int_{\Gamma^\epsilon} QAC^\epsilon f(T^\epsilon)\varphi^0 d\gamma dt \quad &= \int_0^\tau\int_\Omega\int_\Gamma QAC^0 f(T^0)\varphi^0 d\gamma dxdt \qquad (4.75)\\
&= \int_0^\tau\int_\Omega\int_\Gamma QAW(T^0,C^0)\varphi^0 d\gamma dxdt.
\end{aligned}$$

Summing up the limits of the terms $\mathscr{I}_j, j=1,2,3,4$, we conclude that the limit of the variational formulation of the problem (4.9) is simply the variational formulation of the boundary value problem (4.15) and (3.8) corresponding to the homogenized solution T^0 and the corrector T^1.

To get the two-scale limit of the variational formulation (4.30), we apply the test function

in (4.68), and proceed as follows:

$$\int_0^\tau\!\!\int_{\Omega_g^\epsilon} \frac{\partial C^\epsilon}{\partial t}(\phi^0+\epsilon\phi^1)dxdt + \int_0^\tau\!\!\int_{\Omega_g^\epsilon} D^\epsilon \nabla C^\epsilon(\nabla_x\phi^0+\nabla_y\phi^1)dxdt \tag{4.76}$$
$$+ \int_0^\tau\!\!\int_{\Omega_g^\epsilon} \boldsymbol{u}^\epsilon \nabla C^\epsilon(\phi^0+\epsilon\phi^1)dxdt$$
$$= \sum_{j=1}^4 \mathscr{I}_j.$$

Passing to the two-scale limit in each integral $\mathscr{I}_j$ of (4.76), we arrive at the following formulation

$$\lim_{\epsilon\to 0}\sum_{j=1}^4 \mathscr{I}_j \tag{4.77}$$
$$= \int_0^\tau\!\!\int_\Omega\!\!\int_{Y_g} \frac{\partial C^0}{\partial t}\phi^0 dydxdt + \int_0^\tau\!\!\int_\Omega\!\!\int_{Y_g} D(y)(\nabla_x C^0+\nabla_y C^1)\cdot(\nabla_x\phi^0+\nabla_y\phi^1)dydxdt$$
$$+ \int_0^\tau\!\!\int_\Omega\!\!\int_{Y_g} \boldsymbol{u}\cdot\nabla_x C^0 dydxdt = -\int_0^\tau\!\!\int_\Omega\!\!\int_\Gamma W(T^0,C^0)\phi d\gamma dxdt.$$

Again, we conclude that the limit of the variational formulation of the problem (4.10) is up to some integration by parts manipulations, the variational formulation of the boundary value problem (4.20) and (3.89) corresponding to the homogenized solution C^0 and the corrector C^1. Now, we take $\psi(t,x,\frac{x}{\epsilon}) \in C^\infty((0,\tau)\times\Omega, C^\infty_\#(\Gamma))$ and pass to the following two scale limit

$$\int_0^\tau\!\!\int_{\Omega\times\Gamma} \frac{\partial R^0}{\partial t}\psi(t,x,y)dxd\gamma dt = \int_0^\tau\!\!\int_{\Omega\times\Gamma} W(T^0,C^0)\psi(t,x,y)dxd\gamma dt \tag{4.78}$$

□

Remark 4.5.1. *We point out that by proving the two-scale convergence of the microscopic problem, we have also established the existence of weak solutions to the macroscopic model (i.e. it finds by means of a subsequence the convergence to the macroscopic limit). Thus, the existence of solutions to the macro problem is now shown. Also, since the assertion of Theorem 4.5.6 is based on the convergence of extracted subsequences of solutions, the convergence of the entire sequence follows from Theorem 4.3.7.*

4.5.1 Strong formulation of the two-scale limit equations

In this section, we wish to recover the strong formulation of the homogenization limit equations. In order to achieve this, we use the two-scale variational formulation derived in Theorem 4.5.6. Basically, it is a simple matter of setting $(\phi^1, \varphi^1) \equiv 0$ in the second integral limit $\mathscr{I}_2$ in Theorem 4.5.6 and integrating by parts with respect x, i.e.

$$\begin{aligned}
&\int_0^\tau\!\!\int_\Omega\!\!\int_{Y_\mathrm{g}} D(y)(\nabla_x C^0 + \nabla_y C^1)\cdot\nabla_x\phi^0 dydxdt \qquad (4.79)\\
&= -\int_0^\tau\!\!\int_\Omega \phi^0 \mathrm{div_x}\left[\int_{Y_\mathrm{g}} D(y)(\nabla_x C^0 + \nabla_y C^1)dy\right] dxdt\\
&+ \int_0^\tau\!\!\int_{\partial\Omega} \phi^0 \mathrm{div_x}\left[\int_{Y_\mathrm{g}} D(y)(\nabla_x C^0 + \nabla_y C^1)dy\right]\cdot n ds dt.
\end{aligned}$$

The second integral on the right vanishes due to compact support of ϕ^0. Hence, the remaining integral implies

$$-\mathrm{div_x}\left[\int_{Y_\mathrm{g}} D(y)(\nabla_x C^0 + \nabla_y C^1)dy\right], \quad \text{a.e. in } \Omega \text{ and } t\in[0,\tau]. \qquad (4.80)$$

Now, using (4.66) for C^1 in (4.84), we obtain

$$\begin{aligned}
&-\mathrm{div_x}\left[\int_{Y_\mathrm{g}} D(y)(\nabla_x C^0 + \nabla_y C^1)dy\right] \qquad (4.81)\\
&= -\mathrm{div_x}(D^{\mathrm{eff}}(\nabla_x C^0)), \quad \text{a.e. in } \Omega \text{ and } t\in[0,\tau],
\end{aligned}$$

where

$$D^{\mathrm{eff}}_{jk} = \int_{Y_\mathrm{g}} D(y)\left(I_{jk} + \frac{\partial \mathcal{N}_j}{\partial y_k}\right)dy, \quad j,k = 1,2,3. \qquad (4.82)$$

Repeating the same procedure for the heat equation, we get

$$\begin{aligned}
&\int_0^\tau\!\!\int_\Omega\!\!\int_Y \lambda(y)(\nabla_x T^0 + \nabla_y T^1)\cdot\nabla_x\varphi^0 dydxdt, \qquad (4.83)\\
&= \int_0^\tau\!\!\int_\Omega\!\!\int_{Y_\mathrm{g}} \lambda_\mathrm{g}(\nabla_x T^0 + \nabla_y T^1)\cdot\nabla_x\varphi^0 dydxdt + \int_0^\tau\!\!\int_\Omega\!\!\int_{Y_\mathrm{s}} \lambda_\mathrm{s}(\nabla_x T^0 + \nabla_y T^1)\cdot\nabla_x\varphi^0 dydxdt,
\end{aligned}$$

By a similar argument as before, we are lead to the following

$$-\operatorname{div}_{\mathrm{x}}\left[\int_{Y_{\mathrm{g}}}\lambda_{\mathrm{g}}(y)(\nabla_x T^0+\nabla_y T^1)dy+\int_{Y_{\mathrm{s}}}\lambda_{\mathrm{s}}(y)(\nabla_x T^0+\nabla_y T^1)dy\right], \tag{4.84}$$

a.e. in Ω and $t\in[0,\tau]$.

Similarly, by using formula (4.63), we have

$$\begin{aligned}&-\operatorname{div}_{\mathrm{x}}\left[\int_{Y_{\mathrm{g}}}\lambda_{\mathrm{g}}(y)(\nabla_x T^0+\nabla_y T^1)dy+\int_{Y_{\mathrm{s}}}\lambda_{\mathrm{s}}(y)(\nabla_x T^0+\nabla_y T^1)dy\right] \\ &=-\operatorname{div}_{\mathrm{x}}(\lambda^{\mathrm{eff}}(\nabla_x T^0)),\quad \text{a.e. in } \Omega \text{ and } t\in[0,\tau],\end{aligned} \tag{4.85}$$

where

$$\lambda^{\mathrm{eff}}_{jk}=\int_{Y_{\mathrm{g}}}\lambda_{\mathrm{g}}(y)\left(I_{jk}+\frac{\partial\mathcal{N}_j}{\partial y_k}\right)dy+\int_{Y_{\mathrm{s}}}\lambda_{\mathrm{s}}(y)\left(I_{jk}+\frac{\partial\mathcal{N}_j}{\partial y_k}\right)dy,\quad j,k=1,2,3. \tag{4.86}$$

Repeating the same procedure for the convective term gives the desired results.

Remark 4.5.2. *The tensors defined by formulas* (4.82) *and* (4.86) *are symmetric and positive definite (see Cioranescu and Donato, 1999). In order to recover the strong formulation of the correctors T^1 and C^1, we simply need to set $(\phi^0,\varphi^0)\equiv 0$ and integrate by parts with respect to Y. Summing up all terms in the integral limits $\mathscr{I}_j$ and using the averaging formulas for $\mathcal{C}(y),\boldsymbol{u}$, etc. we arrive at the strong formulation of the homogenization problems $\mathfrak{H}^0$ and $\mathfrak{M}^0$ given respectively in* (4.15) *and* (4.20).

4.6 Strong convergence

The results of the previous section give only a weak convergence of the triple $(C^\epsilon,T^\epsilon,R^\epsilon)$ and the gradients $(\nabla C^\epsilon,\nabla T^\epsilon)$. In this section, we wish to improve this weak convergence in order to achieve strong convergence in $L^2(0,\tau;L^2(\Omega))$. This generally requires some regularity assumptions, specifically that the corrector terms $T^1(t,x,\dfrac{x}{\epsilon})$ and $C^1(t,x,\dfrac{x}{\epsilon})$ belong to the space $H^1(\Omega)$ (see Allaire, 1992, cf. Theorem 2.6). By formulas (4.63) and (4.66), this requirement seems to be satisfied if either the homogenized solutions $(T^0(t,x),C^0(t,x))$ or the solutions to the cell problems $\mathcal{N}_j(y)$ are smooth. The approach we will use in order to determine the strong convergence results is described in (Allaire, 1992) in the context of two-scale convergence.

Theorem 4.6.1. *Assume that $(\nabla_y T^1(x,y,t),\nabla_y C^1(x,y,t))$ is smooth enough and denoting by $\chi^\epsilon_{\mathrm{g}}$ the characteristic function of the gas part $\Omega^\epsilon_{\mathrm{g}}$, then the sequence $(\nabla T^\epsilon(t,x)-$*

$\nabla T^0(t,x) - \nabla_y T^1(t,x,\frac{x}{\epsilon}))$ converges strongly to zero in $L^2(0,\tau;L^2(\Omega)^d)$ and the sequence $(\nabla C^\epsilon(t,x) - \nabla C^0(t,x) - \nabla_y C^1(t,x,\frac{x}{\epsilon}))\chi_{\mathrm{g}}^\epsilon$ converges strongly to zero in $L^2(0,\tau;L^2(\Omega)^d)$.

Proof. We test the variational formulation (4.31) of T^ϵ with the difference $T^\epsilon(t,x) - T^0(t,x) - \epsilon T^1(t,x,\frac{x}{\epsilon})$. Using the coercivity condition on λ^ϵ and the boundedness of $\mathcal{C}^\epsilon$, we obtain

$$
\begin{aligned}
&\frac{\mu_0}{2}\int_0^\tau\!\!\int_\Omega \frac{\partial}{\partial t}\Big|T^\epsilon - T^0 - \epsilon T^1\Big|^2 dxdt \qquad (4.87)\\
&+\lambda_0\int_0^\tau\!\!\int_\Omega \Big|\nabla T^\epsilon(t,x) - \nabla T^0(t,x) - \nabla_y T^1(t,x,\frac{x}{\epsilon})\Big|^2 dxdt\\
&\le \frac{1}{2}\int_0^\tau\!\!\int_\Omega \mathcal{C}^\epsilon\frac{\partial}{\partial t}\Big|T^\epsilon(t,x) - T^0(t,x) - \epsilon T^1(t,x,\frac{x}{\epsilon})\Big|^2 dxdt\\
&+\int_0^\tau\!\!\int_\Omega \lambda^\epsilon\Big|\nabla T^\epsilon(t,x) - \nabla T^0(t,x) - \nabla_y T^1(t,x,\frac{x}{\epsilon})\Big|^2 dxdt\\
&+\int_0^\tau\!\!\int_\Omega \chi_{\mathrm{g}}^\epsilon \boldsymbol{u}^\epsilon\nabla\Big|T^\epsilon(t,x) - T^0(t,x) - \epsilon T^1(t,x,\frac{x}{\epsilon})\Big|^2 dxdt\\
&=\epsilon\int_0^\tau\!\!\int_{\Gamma^\epsilon} QW^\epsilon T^\epsilon d\gamma dt + \frac{1}{2}\int_0^\tau\!\!\int_\Omega \mathcal{C}^\epsilon\frac{\partial}{\partial t}\Big|T^0(t,x) + \epsilon T^1(t,x,\frac{x}{\epsilon})\Big|^2 dxdt\\
&-\int_0^\tau\!\!\int_\Omega \mathcal{C}^\epsilon\frac{\partial}{\partial t}\Big(T^\epsilon(t,x)\Big(T^0(t,x) + \epsilon T^1(t,x,\frac{x}{\epsilon})\Big)\Big)dxdt\\
&+\int_0^\tau\!\!\int_\Omega \lambda^\epsilon\Big|\nabla T^0(t,x) + \nabla_y T^1(t,x,\frac{x}{\epsilon})\Big|^2 dxdt\\
&-2\int_0^\tau\!\!\int_\Omega \lambda^\epsilon\nabla T^\epsilon(t,x)\cdot\Big(\nabla T^0(t,x) + \nabla_y T^1(t,x,\frac{x}{\epsilon})\Big)dxdt\\
&=\sum_{j=1}^5 \boldsymbol{\mathscr{I}}_j
\end{aligned}
$$

We treat each term $\boldsymbol{\mathscr{I}}_j$ in the sum independently, and noting that the convective term vanishes due to the assumptions on $\boldsymbol{u}^\epsilon$. Basically, we require to show that the two-scale

limit of the sum vanishes. First, we pass to the two-scale limit in $\mathscr{I}_1$, and obtain

$$\lim_{\epsilon\to 0}\epsilon\int_0^\tau\!\!\int_{\Gamma^\epsilon} QW(T^\epsilon,C^\epsilon)T^\epsilon d\gamma dt=\int_0^\tau\!\!\int_\Omega\!\!\int_\Gamma QW(T^0,C^0)T^0 dydxdt \tag{4.88}$$
$$=|\Gamma|\int_0^\tau\!\!\int_\Omega QW(T^0,C^0)T^0 dxdt$$

Now, passing to the two-scale limit in the second and third terms, results to the following

$$\lim_{\epsilon\to 0}\Big(\mathscr{I}_2+\mathscr{I}_3\Big)=-\frac{1}{2}\int_0^\tau\!\!\int_\Omega\!\!\int_Y \mathcal{C}(y)\frac{\partial}{\partial t}|T^0(t,x)|^2 dydxdt \tag{4.89}$$
$$-\mathcal{C}^{\text{eff}}\int_0^\tau\!\!\int_\Omega\frac{\partial T^0}{\partial t}T^0 dxdt$$

Passing to the two-scale limit in $\mathscr{I}_4$ and $\mathscr{I}_5$, we have

$$\lim_{\epsilon\to 0}-2\int_0^\tau\!\!\int_\Omega \lambda^\epsilon\nabla T^\epsilon\cdot\Big(\nabla T^0+\nabla_y T^1\Big)dxdt+\int_0^\tau\!\!\int_\Omega\lambda^\epsilon|\nabla T^0+\nabla_y T^1|^2 dxdt \tag{4.90}$$
$$=-\int_0^\tau\!\!\int_\Omega\!\!\int_Y\lambda(y)\Big|\nabla_x T^0(t,x)+\nabla_y T^1(t,x,y)\Big|^2 dydxdt$$
$$=-\int_0^\tau\!\!\int_\Omega\!\!\int_{Y_{\text{g}}}\lambda_{\text{g}}\Big|\nabla_x T^0(t,x)+\nabla_y T^1(t,x,y)\Big|^2 dydxdt$$
$$-\int_0^\tau\!\!\int_\Omega\!\!\int_{Y_{\text{s}}}\lambda_{\text{s}}\Big|\nabla_x T^0(t,x)+\nabla_y T^1(t,x,y)\Big|^2 dydxdt$$

Now, using the formula (4.63) for $T^1(t,x,y)$ in (4.90), we obtain after some simplifications

$$=-\int_0^\tau\!\!\int_\Omega\lambda^{\text{eff}}\nabla_x T^0(t,x)\cdot\nabla_x T^0(t,x)dxdt, \tag{4.91}$$

where λ^{eff} is given by the formula

$$\lambda_{ij}^{\text{eff}}=\int_{Y_{\text{g}}}\lambda_{\text{g}}(\nabla_y\mathcal{N}_i(y)+e_i)\cdot(\nabla_y\mathcal{N}_j(y)+e_j)dy \tag{4.92}$$
$$+\int_{Y_{\text{s}}}\lambda_{\text{s}}(\nabla_y\mathcal{N}_i(y)+e_i)\cdot(\nabla_y\mathcal{N}_j(y)+e_j)dy.$$

Summing up the integral limits yields

$$|\Gamma| \int_0^\tau \int_\Omega QW(T^0, C^0)T^0 dxdt - \mathcal{C}^{\text{eff}} \int_0^\tau \int_\Omega \frac{\partial T^0}{\partial t} T^0 dxdt \tag{4.93}$$
$$- \int_0^\tau \int_\Omega \lambda^{\text{eff}} \nabla_x T^0(t,x) \cdot \nabla_x T^0(t,x) dxdt,$$

which is equal to zero due to the variational formulation of the homogenized problem (4.15). The left hand side of the inequality (4.87) implies that

$$\lambda_0 \lim_{\epsilon \to 0} \left\| \nabla T^\epsilon(t,x) - \nabla T^0(t,x) - \nabla_y T^1(t,x,\frac{x}{\epsilon}) \right\|^2_{L^2(0,\tau;(L^2(\Omega))^d)} \to 0. \tag{4.94}$$

Hence,

$$\nabla T^\epsilon(t,x) - \nabla T^0(t,x) - \nabla_y T^1(t,x,\frac{x}{\epsilon}) \to 0. \tag{4.95}$$

Similarly,

$$\mu_0 \lim_{\epsilon \to 0} \left\| T^\epsilon(t,x) - T^0(t,x) - \epsilon T^1(t,x,\frac{x}{\epsilon}) \right\|^2_{L^2(0,\tau;L^2(\Omega))} \to 0, \tag{4.96}$$

and hence

$$T^\epsilon(t,x) - T^0(t,x) - \epsilon T^1(t,x,\frac{x}{\epsilon}) \to 0. \tag{4.97}$$

Finally, we see, by following a similar argument as in the case of the temperature field, that the strong convergence of the concentration field can be deduced as the following:

$$D_0 \lim_{\epsilon \to 0} \left\| \chi_{\text{g}}^\epsilon \Big(\nabla C^\epsilon(t,x) - \nabla C^0(t,x) - \nabla_y C^1(t,x,\frac{x}{\epsilon}) \Big) \right\|^2_{L^2(0,\tau;(L^2(\Omega))^d)} \to 0. \tag{4.98}$$

$$\nabla C^\epsilon(t,x) - \nabla C^0(t,x) - \nabla_y C^1(t,x,\frac{x}{\epsilon}) \to 0. \tag{4.99}$$

Similarly,

$$\lim_{\epsilon \to 0} \left\| C^\epsilon(t,x) - C^0(t,x) - \epsilon C^1(t,x,\frac{x}{\epsilon}) \right\|^2_{L^2(0,\tau;L^2(\Omega))} \to 0, \tag{4.100}$$

and hence

$$C^\epsilon(t,x) - C^0(t,x) - \epsilon C^1(t,x,\frac{x}{\epsilon}) \to 0. \tag{4.101}$$

□

4.6.1 Basic ideas behind corrector estimates

In the previous section, we have seen how corrector results (see Allaire, 1992; Cioranescu and Donato, 1999, for more details) can be obtained with the two-scale convergence method. The latter method emphasizes on the strong convergence of microscopic solutions to the macroscopic solutions, in which the first two terms

$$T^\epsilon \approx T^0(t,x) + \epsilon T^1(t,x,y) + \mathcal{O}(\epsilon^2),$$
$$C^\epsilon \approx C^0(t,x) + \epsilon C^1(t,x,y) + \mathcal{O}(\epsilon^2).$$

of the asymptotic series is rigorously justified. However, we cannot immediately assess the convergence rates of the homogenization process by simply relying on the strong convergence results. The corrector estimates allow us to access the quality of the averaging (homogenization) method by determining the convergence rates which estimate the error contribution generated when approximating microscopic solutions with macroscopic ones. These estimates also play an important role in the design of multiscale numerical methods. The method we use in this section to establish the corrector estimates is based on the unfolding method. The notion of unfolding provides a systematic way of connecting unfolded sequences defined on fixed domains with sequences defined in ϵ-dependent domain. For details of this method for both fixed and perforated domains, we refer to (Cioranescu et al., 2002, 2006). In Section 4.6.3, we will indicate the expected structure of the corrector estimates relying on a procedure involving the concept of periodic unfolding (see Fatima et al., 2012). For energy-based methods for deriving corrector estimates, we refer to (Muntean and Noorden, 2013, e.g.). In the sequel, we introduce some operators needed for this method.

4.6.2 Basic unfolding operators

Definition 4.6.2 (Domain and boundary unfolding operators $\mathcal{T}^\epsilon$)**.** *Let Ω be an open bounded set in $\mathbb{R}^n$. For each $x \in \mathbb{R}^n$, there exists a unique element in $\mathbb{R}^n$, denoted by $\left[\frac{x}{\epsilon}\right]_Y$, such that*

$$x - \epsilon\left[\frac{x}{\epsilon}\right]_Y = \epsilon\left\{\frac{x}{\epsilon}\right\}_Y \in Y. \tag{4.102}$$

Define

$$\widetilde{\Omega_{\mathrm{g}}^\epsilon} = \mathrm{Int}\Big(\bigcup_{\xi\in\Lambda^\epsilon} \epsilon(\xi + \mathrm{Y})\Big), \text{ where } \Lambda^\epsilon = \{\xi \in \mathbb{Z}^n \mid \epsilon(\xi + \overline{Y}) \cap \Omega\} \neq \emptyset, \tag{4.103}$$

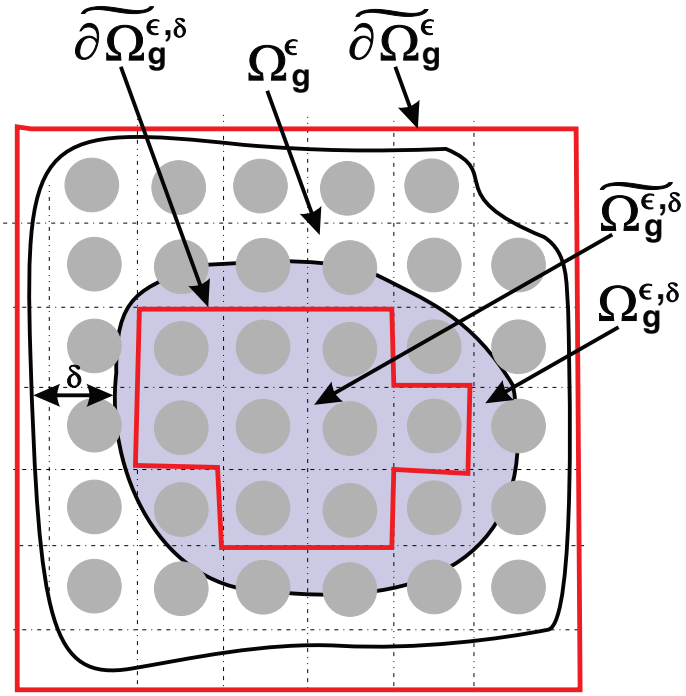

Figure 4.2: The domains $\Omega_g^{\epsilon}, \widetilde{\Omega_g^{\epsilon}}, \Omega_g^{\epsilon,\delta}$ and $\widetilde{\Omega_g^{\epsilon,\delta}}$

where the set $\widetilde{\Omega^{\epsilon}}$ *is the smallest finite union of* ϵY *cells containing* Ω. *We also define a subdomain of* Ω_g^{ϵ}, *i.e. for every* $\delta > 0$,*we set*

$$\begin{aligned} &\Omega_g^{\epsilon,\delta} = \{x \in \Omega \mid d(x, \partial\Omega) > \delta\} \quad \text{and} \\ &\widetilde{\Omega_g^{\epsilon,\delta}} = \mathrm{Int}\Big(\bigcup_{\xi \in \prod^{\epsilon,\delta}} \epsilon(\xi + \mathrm{Y}) \Big) \quad \text{where,} \\ &\prod^{\epsilon,\delta} = \{\xi \in \mathbb{Z}^n \mid \epsilon(\xi + \overline{Y}) \cap \Omega\} \subset \Omega_g^{\epsilon,\delta}\}. \end{aligned} \tag{4.104}$$

1. *For any function* $\phi \in L^p(\Omega_g^{\epsilon}), p \in [1, \infty]$, *the unfolding operators* $\mathcal{T}_{Y_g}^{\epsilon} : \Omega_g^{\epsilon} \to \Omega \times Y_g$ *are defined by*

$$\mathcal{T}_{Y_g}^{\epsilon}(\phi)(x,y) = \begin{cases} \phi(\epsilon \left[\frac{x}{\epsilon}\right]_Y + \epsilon y), & \text{for a.e. } y \in Y_g, x \in \widetilde{\Omega_g^{\epsilon}}, \\ 0, & \text{for a.e. } y \in Y_g, x \in \Omega \setminus \widetilde{\Omega_g^{\epsilon}}, \end{cases} \tag{4.105}$$

2. *For any function* $\phi \in L^p(\Gamma^{\epsilon})$, *the boundary unfolding operator* $\mathcal{T}_{\Gamma^{\epsilon}} : \Gamma^{\epsilon} \to \Omega \times \Gamma$, *is defined by*

$$\mathcal{T}_{\Gamma}^{\epsilon}(\phi)(x,y) = \begin{cases} \phi(\epsilon \left[\frac{x}{\epsilon}\right]_Y + \epsilon y), & \text{for a.e. } y \in \Gamma, x \in \widetilde{\Omega_g^{\epsilon}}, \\ 0, & \text{for a.e. } y \in \Gamma, x \in \Omega \setminus \widetilde{\Omega_g^{\epsilon}}, \end{cases} \tag{4.106}$$

Definition 4.6.3 (Domain and boundary averaging operators)**.** *The following averaging formula hold:*

1. *For any $\phi \in L^p(\Omega_g^\epsilon), p \in [0,\infty]$, we define the local average operator (i.e. the mean in cell Y_g), $\mathcal{M}^\epsilon_{Y_g} : L^p(\Omega_g^\epsilon) \to L^p(\Omega)$, by setting*

$$\mathcal{M}^\epsilon_{Y_g}(\phi)(x) = \frac{1}{|Y_g|}\int\limits_{Y_g} \mathcal{T}^\epsilon_{Y_g}(\phi)(x,y)dy = \frac{1}{\epsilon^n\,|Y_g|}\int\limits_{\epsilon[\frac{x}{\epsilon}]+\epsilon Y_g} \phi(y)dy, \quad x \in \Omega \tag{4.107}$$

2. *The operator $\mathcal{Q}^\epsilon_{Y_g} : L^p(\widetilde{\Omega_g^{\epsilon,\delta}}) \to W^{1,\infty}(\Omega)$, for $p \in [1,\infty]$ is defined as Q_1-interpolation of $\mathcal{M}^\epsilon_{Y_g}(\phi),$: i.e.*

$$\mathcal{Q}^\epsilon_{Y_g}(\phi)(\epsilon\xi) = \mathcal{M}^\epsilon_{Y_g}(\phi)(\epsilon\xi), \quad \text{for } \xi \in \mathbb{Z}^n \tag{4.108}$$

and

$$\mathcal{Q}^\epsilon_{Y_g}(\phi)(x) = \sum_{k\in\{0,1\}^n} \mathcal{Q}^\epsilon_{Y_g}(\phi)(\epsilon\xi+\epsilon k)\overline{x}_1^{k_1}\cdots\overline{x}_n^{k_n}, \quad \text{for } x \in \epsilon(Y+\xi), \xi \in \mathbb{Z}^n, \tag{4.109}$$

where for $k = (k_1,\cdots,k_n) \in \{0,1\}^n$. The points $\overline{x}_l^{k_l}$ are given by

$$\overline{x}_l^{k_l} = \begin{cases} \dfrac{x_l - \epsilon\xi_l}{\epsilon}, & \text{if } k_l = 1, \\ 1 - \dfrac{x_l - \epsilon\xi_l}{\epsilon}, & \text{if } k_l = 0. \end{cases} \tag{4.110}$$

3. *The operator $\mathcal{Q}^\epsilon_{Y_g} : W^{1,p}(\Omega_g^\epsilon) \to W^{1,\infty}(\Omega), p \in [1,\infty]$ is defined by*

$$\mathcal{Q}^\epsilon_{Y_g}(\phi) = \mathcal{Q}^\epsilon_{Y_g}(\mathcal{P}(\phi))\Big|_{\Omega_g^\epsilon},$$

where $\mathcal{Q}^\epsilon_{Y_g}$ is given above, and

$$\mathcal{P} : W^{1,p}(\Omega_g^\epsilon) \to W^{1,p}(\mathbb{R}^n)$$

is an extension operator such that

$$\|\mathcal{P}(\phi)\|_{W^{1,p}(\mathbb{R}^n)} \le C\,\|\phi\|_{W^{1,p}(\Omega^\epsilon)}.$$

We also recall the form of the operator for fixed domains, i.e.

$$\mathcal{Q}^\epsilon_Y(\phi)(\epsilon\xi) = \mathcal{M}^\epsilon_Y(\phi)(\epsilon\xi), \quad \text{for } \xi \in \mathbb{Z}^n, \tag{4.111}$$

where $\mathcal{M}^\epsilon_Y(\phi)$ is the average of ϕ given by

$$\mathcal{M}^\epsilon_Y(\phi)(x) = \frac{1}{|Y|}\int\limits_Y \mathcal{P}(\phi)(\epsilon\xi+x)dx, \quad x \in \Omega. \tag{4.112}$$

4. *For $p \in [1, \infty]$, the averaging operator $\mathcal{U}^{\epsilon}_{Y_{\mathrm{g}}} : L^p(\Omega \times Y_{\mathrm{g}}) \to L^p(\Omega^{\epsilon}_{\mathrm{g}})$ is defined by*

$$\mathcal{U}^{\epsilon}_{Y_i}(\Phi)(x) = \begin{cases} \dfrac{1}{|Y|} \displaystyle\int_Y \Phi(\epsilon \Big[\frac{x}{\epsilon}\Big]_Y + \epsilon z, \Big\{\frac{x}{\epsilon}\Big\}_Y) dz, & \text{a.e. } x \in \widetilde{\Omega}^{\epsilon}_{\mathrm{g,int}} \\ 0, & \text{a.e. } x \in \Omega^{\epsilon}_{\mathrm{g}} \setminus \widetilde{\Omega}^{\epsilon}_{\mathrm{g,int}} \end{cases} \tag{4.113}$$

5. *$\mathcal{U}^{\epsilon}_{\Gamma} : L^p(\Omega \times \Gamma) \to L^p(\Gamma^{\epsilon})$ is defined as*

$$\mathcal{U}^{\epsilon}_{\Gamma}(\Phi)(x) = \begin{cases} \dfrac{1}{|Y|} \displaystyle\int_{\Gamma} \Phi(\epsilon \Big[\frac{x}{\epsilon}\Big]_Y + \epsilon z, \Big\{\frac{x}{\epsilon}\Big\}_Y) dz, & \text{a.e. } x \in \widetilde{\Gamma}^{\epsilon}_{\mathrm{int}} \\ 0, & \text{a.e. } x \in \Gamma^{\epsilon}_{\mathrm{g}} \setminus \widetilde{\Gamma}^{\epsilon}_{\mathrm{int}} \end{cases} \tag{4.114}$$

For more details on the properties of the unfolding operators, see Cioranescu et al. (2002); Griso (2004).

4.6.3 Structure of the corrector estimates

By using the introduced operators and trusting the error estimates deduced in Fatima et al. (2012) for a related multiple scale reaction-diffusion system, we expect that, as $\epsilon \to 0$, the following corrector estimates hold true:

$$\|C^{\epsilon} - C^0\|_{L^2((0,\tau)\times\Omega^{\epsilon}_{\mathrm{g}})} + \|\nabla C^{\epsilon} - \nabla C^0 - \sum_{j=1}^{n} \mathcal{Q}^{\epsilon}_{Y_{\mathrm{g}}}\left(\frac{\partial C^0}{\partial x_j}\right) \nabla_y \mathcal{N}_j\|^2_{L^2((0,\tau)\times\Omega^{\epsilon}_{\mathrm{g}})} \leq C\epsilon^{\frac{1}{2}}, \tag{4.115}$$

$$\|T^{\epsilon} - T^0\|_{L^2((0,\tau)\times\Omega)} + \|\nabla T^{\epsilon} - \nabla T^0 - \sum_{j=1}^{n} \mathcal{Q}^{\epsilon}_{Y}\left(\frac{\partial T^0}{\partial x_j}\right) \nabla_y \mathcal{N}_j\|^2_{L^2((0,\tau)\times\Omega)} \leq C\epsilon^{\frac{1}{2}},$$

$$\epsilon^{\frac{1}{2}} \|R^{\epsilon} - \mathcal{U}^{\epsilon}_{\Gamma}(R^0)\|_{L^2((0,\tau)\times\Gamma^{\epsilon})} \leq C\epsilon^{\frac{1}{2}},$$

where $(C^{\epsilon}, T^{\epsilon}, R^{\epsilon})$ is the solution to the microscopic problem (4.9)–(4.10) and (C^0, T^0, R^0) is the solution to the homogenized problems (4.15)–(4.10). $\mathcal{N}_j$ are the solutions to the cell problems defined by (4.18) and (4.22). The operators $\mathcal{Q}^{\epsilon}_{Y_{\mathrm{g}}}$, $\mathcal{Q}^{\epsilon}_{Y}$ and $\mathcal{U}^{\epsilon}_{\Gamma}$ are defined in (4.108),(4.111), and (4.114) respectively.

Remark 4.6.1. *In view of the corrector estimates* (4.115)*, we expect these estimates to hold for drifts of order of magnitude $\mathcal{O}(\epsilon^{\alpha})$, with $\alpha \in [0, \infty)$; faster drifts would need special handling.*

4.7 Summary

In this chapter, we have shown the rigorous passage to the homogenization limit using the two-scale convergence method; thereby verifying the accuracy of the homogenization

process in Chapter 3, which is based on a formal asymptotic expansion. A similar procedure can also be adapted for the case of high contrast, highly heterogeneous media, but with a few modifications with respect to the a priori estimates and the notion of convergence (see Allaire, 1992). Further, the notion of two-scale convergence allowed us to guess the form of the corrector estimates (6.24) based on the details presentation in Fatima et al. (2012). The latter is the main scope of Chapter 6, where we will use a multiscale reconstruction algorithm to show the agreement of our numerical corrector estimates with the theoretical estimates presented here. In addition, we also indicated corrector results for our two-scale limit problem. Alternatively, one may also proceed differently: we can compare the quality of our corrector results with error estimates deduced from a purely diffusion problem as shown in (Allaire and El Ganaoui, 2009; Allaire and Habibi, 2013; Bensoussan et al., 1978).

Chapter 5

Numerical verification of the effective diffusion tensors

The HPS method applied in Chapter 3 allows the derivation of upscaled equations which describe in an effective way the behavior of the microscopic description at the pore scale. It is important to study the rigorous convergence of the microscopic equations to the macroscopic equation since the method, which is only based on a formal mathematical approach, raises further questions on the validity of the derived macroscopic equations with effective (constant) diffusion tensors. Also, it is important to verify that the effective coefficients are consistent with some known theoretical estimates. In Chapter 4, the convergence proof of the system of equations have already been stated using the two-scale convergence method. In this chapter, we proceed differently. Specifically, we are interested more on the numerical justification of the derived effective diffusion tensors. Thus, the outline of this chapter is the following: The effective diffusion tensors are numerically calculated using the derived formula in Chapter 3 (see Eqs (3.19),(3.43) and (3.64)). These calculations require solving local boundary value problems (cell problems) posed on a single period. We point out that the cell problems may be different based on the interconnectivity of the inclusions and on the phase that dominates the transport process at the macroscopic level. Thus, distinct cell problems are to be solved for each of the considered homogenization problems. The main interest in this section is to investigate the sensitivity of the effective tensors to variations in the thermal conductivity contrast, the volume fraction of the inclusions, and in the anisotropy of the medium. Subsequently, the effective diffusion tensors are compared with some known theoretical bounds (see Hashin and Shtrikman, 1963; Hashin, 1983, e.g.). We also refer to Auriault et al. (2009) for a discussion of the Voigts upper bound and Reuss lower bound.

5.1 Computation and analysis of the effective coefficients

In this section, we consider the computation of the effective thermal conductivity tensors for the three different model problems described in Chapter 3. Subsequently, the effective tensors are analyzed based on a number of factors that influence the effective tensors. The cell problems resulting from the model problems are based on the thermal conductivity contrast of the gas and solid parts of the medium. The conductivity coefficients are assumed to be homogeneous and locally isotropic in both subdomains. For the thin porous structure we have in mind, we neglect the contribution to the effective thermal conductivity in the vertical direction and hence focus more on two dimensional geometries.

5.1.1 Bounds for the effective thermal conductivity

We briefly describe some of the known upper and lower bounds which we intend to use for the analysis of the effective thermal conductivity tensors. These bounds are given in terms of the properties of the medium such as the volume fractions and thermal conductivities. As it is usually the case in the study of effective properties of composite structures or aggregates (see Wendt et al., 1970; Szymkiewicz, 2004; Wall, 1997, for more details), and in problems related to multiphase flows in porous media (Hashin, 1983; Hashin and Shtrikman, 1963), the effective properties of materials can be compared with some known upper and lower bounds. The highlight of the HPS method is the computation of effective properties which characterize the behavior of the observation at the macroscopic level. For a porous medium consisting of a complex arrangement of its constituents with varying pore sizes across the medium, the effective thermal conductivity will depend generally on the local properties of the constituent phases such as the volume fractions, the thermal conductivities of the phases and the spatial arrangement of the constituents.
The relation defining the upper Voigt bound (V) and lower Reuss (R) bound (see Auriault et al., 2009, e.g.) is:

$$\lambda^R \leq \lambda^{\text{eff}} \leq \lambda^V, \tag{5.1}$$

where $\lambda^{\text{eff}}, \lambda^R$ and λ^V are constants (i.e. for an isotropic geometry) representing respectively the effective thermal conductivity, the lower Reuss bound and the upper Voigt bound. The bounds are defined as follows:

$$\lambda^R = \frac{\lambda_{\text{g}}\lambda_{\text{s}}}{V_{\text{s}}\lambda_{\text{g}} + V_{\text{g}}\lambda_{\text{s}}}, \tag{5.2a}$$

$$\lambda^V = V_{\text{g}}\lambda_{\text{g}} + V_{\text{s}}\lambda_{\text{s}}, \tag{5.2b}$$

where V_{g} and V_{s} are respectively the volume fraction of the matrix and inclusions. λ^R defines the harmonic mean of the constituent conductivities and λ^V, their arithmetic mean. Both λ^R and λ^V are known as fundamental bounds because the relation (5.1) is always true. However, there are stronger bounds, based on additional assumption that the material is

isotropic on the macroscopic scale. These are called the Hashin and Shtrikman bounds, named after the founders Hashin and Shtrikman (Hashin and Shtrikman (1963)). The Hashin-Shtrikman lower λ^{HS-} and upper λ^{HS+} bounds are defined for $\lambda_{\mathrm{g}} > \lambda_{\mathrm{s}}$:

$$\lambda^{HS-} = \lambda^{V} - \frac{V_{\mathrm{g}} V_{\mathrm{s}} (\lambda_{\mathrm{g}} - \lambda_{\mathrm{s}})^2}{(D - V_{\mathrm{s}})\lambda_{\mathrm{s}} + V_{\mathrm{s}}\lambda_{\mathrm{g}}} \leq \lambda^{\mathrm{eff}} \leq \lambda^{V} - \frac{V_{\mathrm{g}} V_{\mathrm{s}} (\lambda_{\mathrm{g}} - \lambda_{\mathrm{s}})^2}{(D - V_{\mathrm{g}})\lambda_{\mathrm{g}} + V_{\mathrm{g}}\lambda_{\mathrm{s}}} = \lambda^{HS+}, \tag{5.3}$$

where D is the dimension of the geometry. The lower bound λ^{HS-} corresponds to situations in which a low conductivity inclusion (usually a sphere) is embedded in a highly conductive matrix., whereas the reverse is the case for the upper bound λ^{HS+}.

5.1.2 Effective thermal conductivity for the MCI model

For the Moderately Conductive Inclusions (MCI) model, the cell problems are defined over the entire period cell Y:

$$\frac{\partial}{\partial y_i}\left[\lambda_{\mathrm{g}}\left(I_{ik} + \frac{\partial \mathcal{N}_{\mathrm{k}}^{\mathrm{g}}}{\partial y_i}\right)\right] = 0, \qquad y \in Y_{\mathrm{g}}, \tag{5.4a}$$

$$\frac{\partial}{\partial y_i}\left[\lambda_{\mathrm{s}}\left(I_{ik} + \frac{\partial \mathcal{N}_{\mathrm{k}}^{\mathrm{s}}}{\partial y_i}\right)\right] = 0, \qquad y \in Y_{\mathrm{s}}, \tag{5.4b}$$

$$\mathcal{N}_k^{\mathrm{g}} = \mathcal{N}_k^{\mathrm{s}}, \qquad y \in \Gamma, \tag{5.4c}$$

$$\lambda_{\mathrm{g}}\left(I_{ik} + \frac{\partial \mathcal{N}_{\mathrm{k}}^{\mathrm{g}}}{\partial y_{\mathrm{i}}}\right) n_i = \lambda_{\mathrm{s}}\left(I_{ik} + \frac{\partial \mathcal{N}_{\mathrm{k}}^{\mathrm{s}}}{\partial y_{\mathrm{i}}}\right) n_i, \qquad y \in \Gamma, \tag{5.4d}$$

where $i, k = 1, 2; \mathcal{N}_{\mathrm{k}}^{\mathrm{g}}$ and $\mathcal{N}_{\mathrm{k}}^{\mathrm{s}}, k = 1, 2$ are y-periodic and satisfy

$$\langle \mathcal{N} \rangle = \frac{1}{|Y|}\left(\int_{Y_{\mathrm{g}}} \mathcal{N}_{\mathrm{k}}^{\mathrm{g}} dY + \int_{Y_{\mathrm{s}}} \mathcal{N}_{\mathrm{k}}^{\mathrm{s}} dY\right) = 0. \tag{5.5}$$

$\boldsymbol{n}$ is the outward unit normal on Γ with respect to the gas part. The problem (5.4a)-(5.4d) and (5.5) is solved in each of the k-directions, with $k = 1, 2$ for a two dimensional geometry. After the numerical computations of the cell problems, the effective conductivity is then calculated from the following formula:

$$\lambda_{ik}^{\mathrm{eff}} = \frac{1}{|Y|}\left(\int_{Y_{\mathrm{g}}} \lambda_{\mathrm{g}}\left(I_{ki} + \frac{\partial \mathcal{N}_{\mathrm{k}}^{\mathrm{g}}}{\partial y_i}\right) dY + \int_{Y_{\mathrm{s}}} \lambda_{\mathrm{s}}\left(I_{ki} + \frac{\partial \mathcal{N}_{\mathrm{k}}^{\mathrm{s}}}{\partial y_i}\right) dY\right), \quad i, k = 1, 2. \tag{5.6}$$

Note that in most cases, the geometry used is symmetric, and hence the effective thermal conductivity tensors in such cases is isotropic, i.e. $\lambda_{11}^{\mathrm{eff}} = \lambda_{22}^{\mathrm{eff}}$. In order to calculate the effective thermal conductivity tensor defined by (5.6), we first solve the solution of the cell probems of (5.4). These solutions are illustrated for the two canonical directions in Figure 5.1.

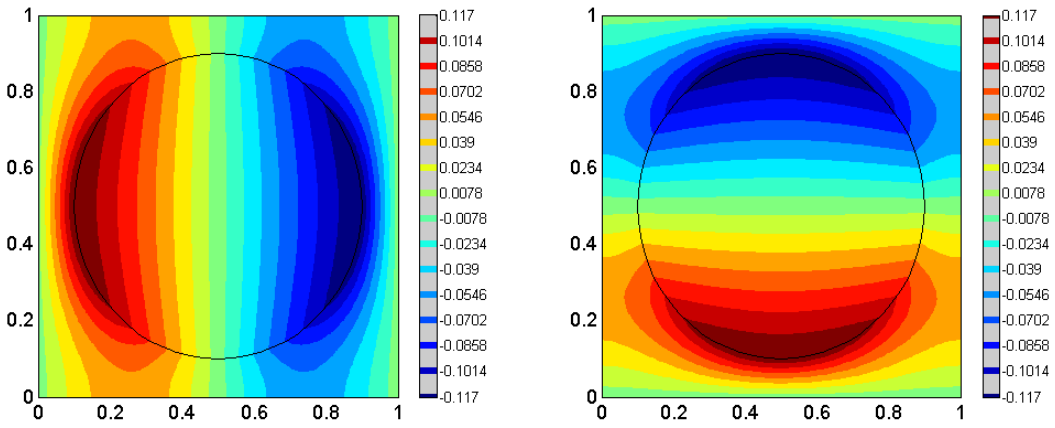

Figure 5.1: Solution of the local boundary value problem for the MCI model with a centered circular inclusion of volume fraction $V_\mathrm{s} = 0.502$. (left): function $\mathcal{N}_1$ and (right): function $\mathcal{N}_2$.

5.1.3 Effective thermal conductivity for the HCI model

For the Highly Conductive Inclusions (HCI) model, the cell problems are restricted to the gas part Y_g of the period cell Y, with an inhomogeneous Dirichlet condition prescribed on the surface Γ. The cell problem in this case has the following form:

$$\frac{\partial}{\partial y_i}\left[\lambda_\mathrm{g}\left(I_{ik} + \frac{\partial \mathcal{N}_\mathrm{k}}{\partial y_i}\right)\right] = 0, \qquad y \in Y_\mathrm{g}, \tag{5.7a}$$

$$\mathcal{N}_\mathrm{k} + y_\mathrm{k} = 0, \qquad y \in \Gamma, \tag{5.7b}$$

where $i, k = 1, 2$; the vector-valued function $\boldsymbol{\mathcal{N}}$ is y-periodic and $\boldsymbol{n}$ is the outward unit normal on Γ with respect to the gas part. The effective thermal conductivity is given by a surface integral:

$$\lambda_{jk}^{\mathrm{eff}} = \frac{\lambda_\mathrm{g}}{|S_\mathrm{g}^j|}\int\limits_{S_\mathrm{g}^j}\left(I_{ik} + \frac{\partial \mathcal{N}_\mathrm{k}}{\partial y_\mathrm{i}}\right) y_\mathrm{j} n_\mathrm{i} dS, \quad i, j, k = 1, 2. \tag{5.8}$$

In (5.8), S_g represents the surface of the period domain Y which is orthogonal to the k-th direction. The solutions to the local boundary value problems are depicted in Figure 5.2. The local thermal conductivity in this case is dominated by the connected gas phase, since the inclusions are not connected. However, the influence of the high thermal conductivity of the inclusion is not negligible.

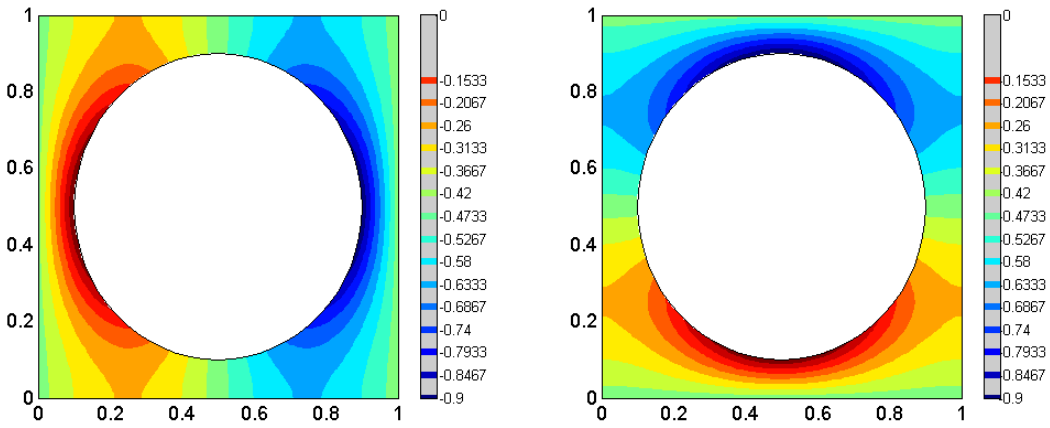

Figure 5.2: Solution of the local boundary value problem for the HCI model with a centered circular inclusion of volume fraction $V_s = 0.502$. (left): function $\mathcal{N}_1$ and (right): function $\mathcal{N}_2$.

5.1.4 Effective thermal conductivity for the WCI model

For the case of Weakly Conductive Inclusions (WCI) model, the cell problem is restricted to the gas part Y_g of the period cell Y, with a Neumann condition at the interface Γ:

$$\frac{\partial}{\partial y_i}\left[\lambda_g\left(I_{ik}+\frac{\partial \mathcal{N}_k}{\partial y_i}\right)\right]=0, \qquad y\in Y_g, \tag{5.9a}$$

$$\lambda_g\left(I_{ik}+\frac{\partial \mathcal{N}_k}{\partial y_i}\right)n_i=0, \qquad y\in \Gamma, \tag{5.9b}$$

where $i,k=1,2$; the vector-valued function $\boldsymbol{\mathcal{N}}$ is $\boldsymbol{y}$-periodic and satisfy $\langle \boldsymbol{\mathcal{N}}\rangle = 0$. The effective thermal conductivity is defined by the following formula:

$$\lambda_{ik}^{\text{eff}}=\frac{\lambda_g}{|Y|}\int_{Y_g}\left(I_{ki}+\frac{\partial \mathcal{N}_k}{\partial y_i}\right)dY, \quad i,k=1,2. \tag{5.10}$$

Similar to the local boundary value problem of the HCI model, the local thermal diffusion is dominated in the gas phase since the thermal conductivity of the solid phase is relatively small. In Figure 5.3, the solutions to the local boundary problems are calculated. Note that these solutions are both qualitatively and quantitatively identical to the problem of mass diffusivity in the gas phase. However, the difference between the two transport processes is given by their diffusion coefficients. The effective thermal conductivity constant calculated from formula (5.10) is given by $\lambda^{\text{eff}} = 7.67\times 10^{-5}$, while the effective mass diffusivity constant is $D^{\text{eff}} = 8.1\times 10^{-2}$. The latter is calculated simply by replacing the thermal conductivity 2.38×10^{-4}W/cm K of the gas with the molecular diffusion constant $D = 0.25$ cm/s^2. We point out that the effective tensors described here are constants since they are obtained for an isotropic geometry.

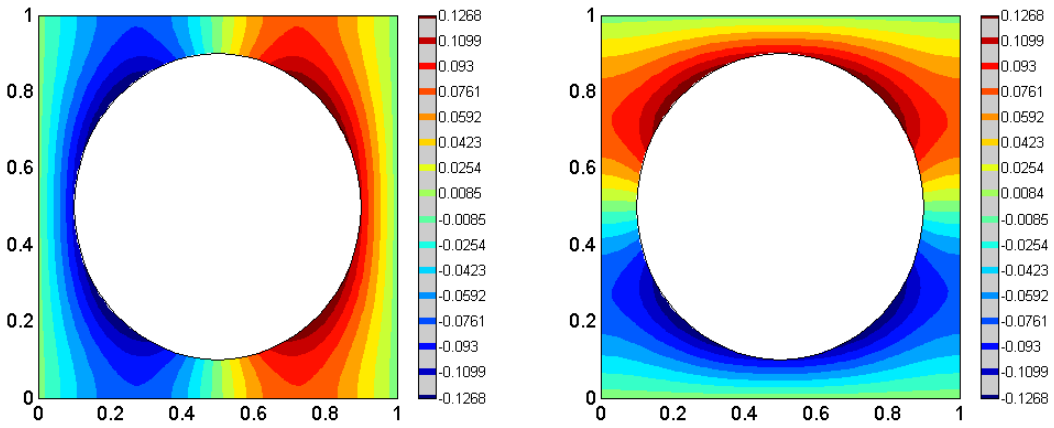

Figure 5.3: Solution of the local boundary value problem for the WCI model with a centered circular inclusion of volume fraction $V_s = 0.502$. (left): function $\mathcal{N}_1$ and (right): function $\mathcal{N}_2$.

5.2 Derivation of limiting cases from cell problem of the MCI model

In this section, we study the local boundary value problem of the MCI model (5.4) in order to determine the limiting passage to the local boundary value problems described in (5.7) and (5.9). The idea is to perform a series of numerical simulations for the problem (5.4) on a simple two dimensional local geometry. The geometry is locally isotropic in the respective constituent phases and consists of centered circular inclusion. The volume fraction of the inclusion for the geometry is $V_s = 0.502$. The numerical simulation was carried out by varying the ratio of the thermal conductivity of the inclusion λ_s to the thermal conductivity of the matrix λ_g within a range from $\lambda_s/\lambda_g = 10^{-6}$ to $\lambda_s/\lambda_g = 10^{-6}$. We point out that in the numerical calculations, the given ratio serves as the conductivity of the inclusion in problem (5.4), and also in the calculation of the effective thermal conductivity through formula (5.6). The ratio of the effective thermal conductivity normalized by the thermal conductivity of the matrix $\lambda^{\text{eff}}/\lambda_g$ is plotted as a function of λ_s/λ_g (Figure 5.4), and its asymptotic behavior is such that the effective thermal conductivity λ^{eff} approaches a constant value $\lambda^{\text{eff}} = 0.32\lambda_g$ at the far left limit for $\lambda_s/\lambda_g \ll 10^{-2}$. This value coincides with the value of the effective thermal conductivity calculated for problem (5.9) using formula (5.6). Similarly, at the far right limit for $\lambda_s/\lambda_g \gg 10^3$, λ^{eff} approaches a constant value $\lambda^{\text{eff}} = 3.1\lambda_g$, which also coincides with the effective thermal conductivity of the HCI model calculated with (5.7) and (5.8). By comparing the numerical results with the bounds, we see that the numerical results are in good agreement with the upper (if $\lambda_s/\lambda_g < 1$) and lower (if $\lambda_s/\lambda_g > 1$) Hashin-Shtrikman bounds. Based on the asymptotic behavior of λ^{eff} , we conclude that the problem (5.9) can be regarded as the limiting case of the problem (5.4) when $\lambda_s/\lambda_g \to 0$, whereas the problem (5.7) is a limiting case of the problem (5.4) when

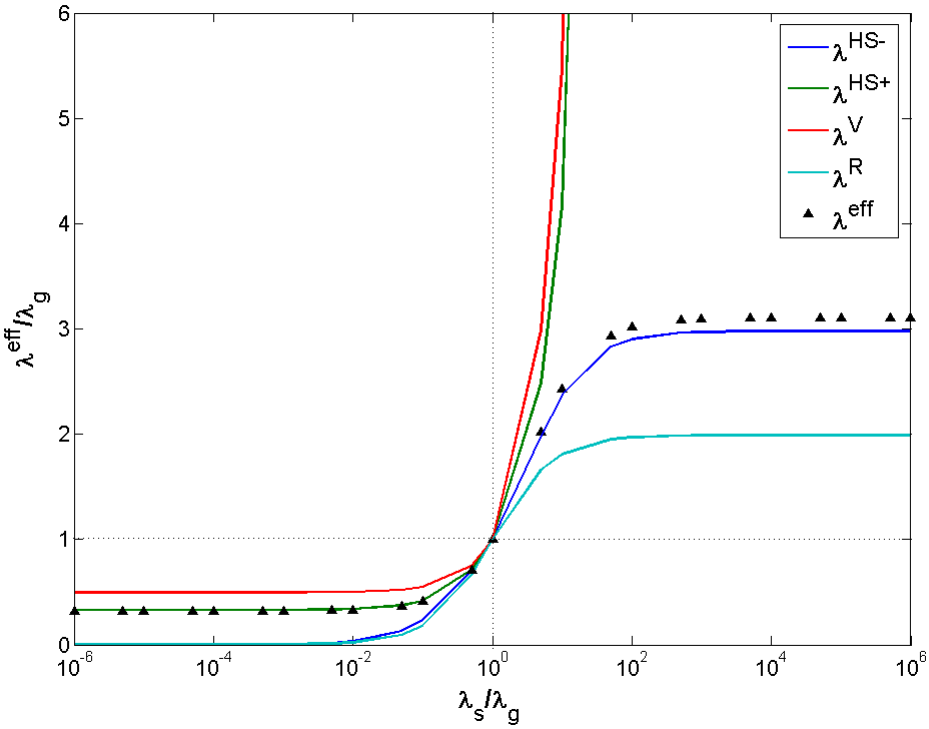

Figure 5.4: Effective thermal conductivity of the isotropic medium consisting of circular inclusions (▲) as a function of the ratio of the inclusions thermal conductivity to the matrix thermal conductivity λ_s/λ_g. The effective thermal conductivity tends to a constant value $\lambda^{\text{eff}} = 0.32\lambda_g$ at the far left limit for $\lambda_s/\lambda_g \ll 10^{-2}$ and to $\lambda^{\text{eff}} = 3.1\lambda_g$ for $\lambda_s/\lambda_g \gg 10^3$ at the far right limit. The numerical results are compared with the bounds of Hashin and Shtrikman ($\lambda^{\text{HS}+}$ and $\lambda^{\text{HS}-}$), and also Voigt (λ^{V}) and Reuss (λ^{R}).

$\lambda_s/\lambda_g \to \infty$. These results are also consistent with other studies related to the effective properties of porous media (e.g. Szymkiewicz, 2004; Auriault et al., 2009).

5.3 Effect of volume fraction of inclusions

The effective thermal conductivity (cf. mass diffusivity) of a porous material can be influenced by the volume fraction of inclusions. In this section, we analyze the behavior of the effective thermal conductivity of a typical porous medium with variations in the volume fraction of inclusion. Different forms of geometries are also possible, and they have been studied in much details in other contexts related to the analysis of the effective properties of porous media (see Auriault et al., 2009; Szymkiewicz, 2004, and references therein). In these studies, it was shown that the difference in the estimates of distinct geometries are not significant. Thus, for brevity of presentation, we consider a simple geometry consisting of a centered circular inclusion. Note that if the ratio of conductivity is of the same order

of magnitude (i.e. if $\lambda_s/\lambda_g = 10^0$) as in Figure 5.4, the bounds coincide with the numerical value of the effective thermal conductivity. This is indicated by the dotted lines in the Figure 5.4. However, since this ratio is rarely satisfied in physical systems, we show in Figure 5.5 the evolution of the numerical values of the effective thermal conductivity λ^{eff} with the volume fraction of inclusions V_s. In the same plot, we also compared the numerical values with the respective bounds. In Figure 5.5, we compared the effective thermal conductivity

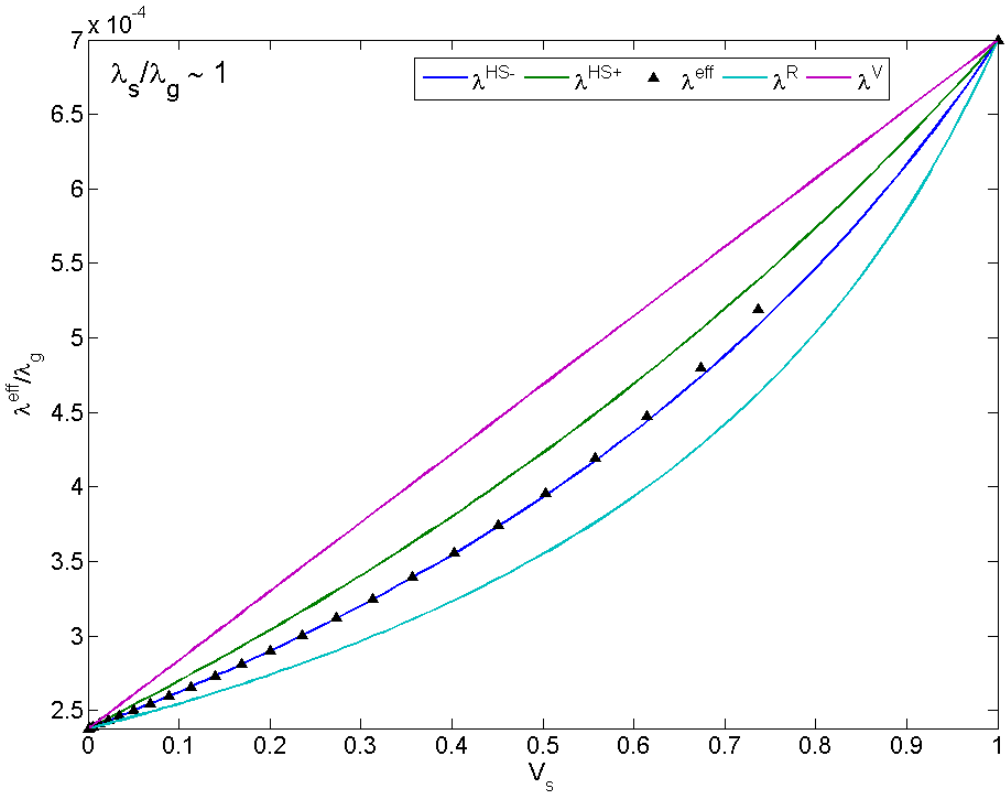

Figure 5.5: Evolution of the effective thermal conductivity of the MCI model having a centered circular inclusion with the volume fraction of the inclusion.

of the MCI model with the bounds of Hashin and Shtrikman ($\lambda^{\text{HS}+}$ and $\lambda^{\text{HS}-}$). Also, we see that the fundamental bounds (λ^{V} and λ^{R}) are satisfied for this problem. The thermal conductivity contrast in the problem is assumed to be moderate in the sense that $\lambda_s/\lambda_g \sim 1$. In the numerical calculation, we used the physical values of the solid and gas phase thermal conductivities $\lambda_s = 7 \times 10^{-4}$W/cm K and $\lambda_g = 2.38 \times 10^{-4}$W/cm K. respectively.

Furthermore, let us consider a more interesting case as depicted in Figures 5.7a and 5.7b, when the conductivity ratio satisfies $\lambda_s/\lambda_g \ll 1$. Figure 5.7a corresponds to a case of an insulation material at $\lambda_s = 0$. This implies that the flow is dominated solely by the matrix conductivity λ_g, in which case λ^{eff} is obtained by solving problem (5.9). As we mentioned

earlier, the latter is functionally identical to the local boundary value problem for the effective mass diffusivity D^{eff} given in (3.90). In Figure 5.7b, the ratio is given by $\lambda_s/\lambda_g = 10^{-2}$. In both cases, the numerical values are compared with the theoretical bounds of Hashin-Shtrikman and Voigt-Reuss. In Figure 5.7, the lower bounds are close to zero. The values of the effective thermal conductivity coincide with the Hashin-Shtrikman upper bound. In Figure 5.7, we see that when the diameter of the circular inclusion is close to the period length, the effective thermal conductivity is close to zero because the circles are touching each other and heat conductivity can no longer be dominated in the gaseous phase.

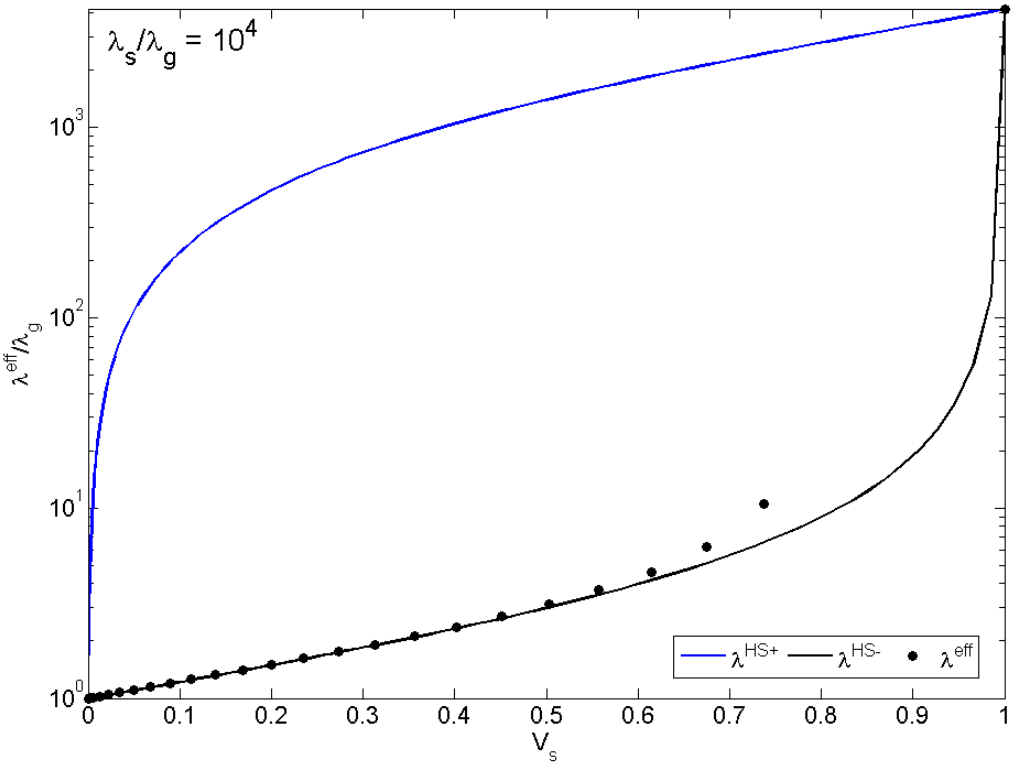

Figure 5.6: Evolution of the effective thermal conductivity of the HCI model having a centered circular inclusion with the volume fraction of the inclusion.

For the medium with highly conductive inclusions, we assumed the ratio of thermal conductivity to be $\lambda_s/\lambda_g = 10^4$. Figure 5.6 shows the evolution of the effective thermal conductivity with the volume fraction of inclusion. Unlike the WCI model, the values of the effective thermal conductivity for the HCI model coincide with the lower Hashin-Shtrikman bound. The effective thermal conductivity, which is obtained from (5.7) tends to infinity when the volume fraction of the inclusion V_s approaches 1.

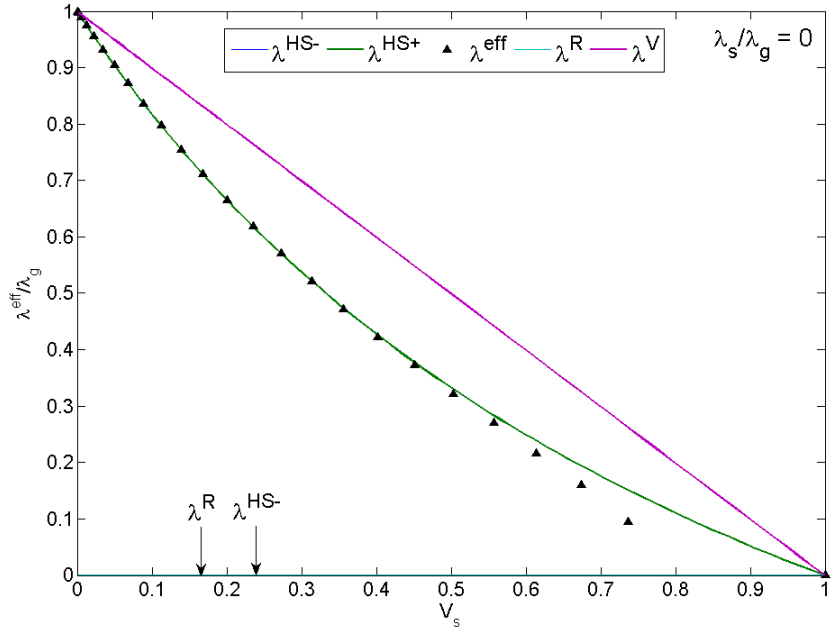

(a) Evolution of the effective thermal conductivity of the WCI model having a centered circular inclusion with the volume fraction of the inclusion. The thermal conductivity ratio is $\lambda_s/\lambda_g = 0$.

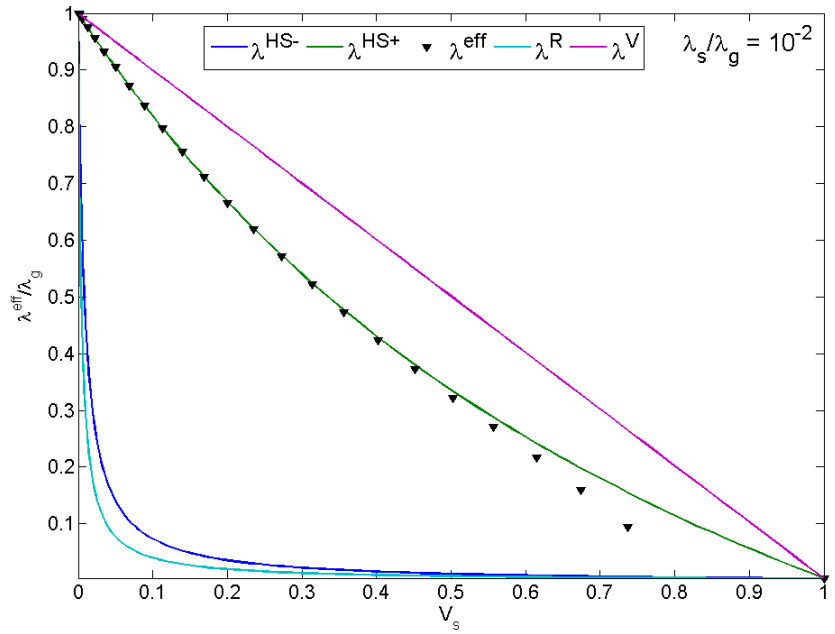

(b) Evolution of the effective thermal conductivity of the WCI model having a centered circular inclusion with the volume fraction of the inclusion. The thermal conductivity ratio is $\lambda_s/\lambda_g = 10^-2$.

Figure 5.7: Effective thermal conductivity of the WCI model, and comparison of the effective thermal conductivity with the Hashin-Shtrikman and Voigt-Reuss bounds.

5.4 Anisotropy of the effective thermal conductivity tensor

Anisotropy effects is a property of nonuniform porous materials. It means that the direction of flow in such a medium is not simply the direction of the gradient of the transport processes. In order to mimic a physical material that exhibits anisotropy, we performed numerical simulations for a geometry with a centered elliptical inclusion. We take, for

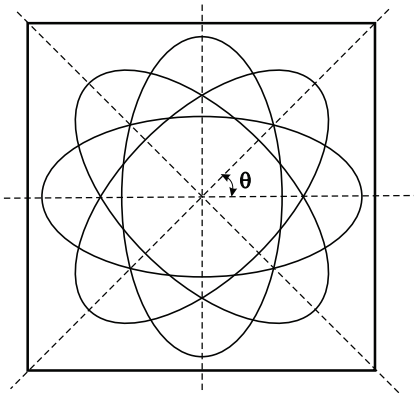

Figure 5.8: Different orientations of the inclusion with the angular orientation θ.

example, a typical ellipse that has a A-semiaxes of $a = 0.3$ and a B-semiaxes of $b = 0.48$. Thus, the volume fraction of the inclusion is fixed to $V_s = 0.451433$. On the other hand, the angular orientation, θ, of the ellipse is varied in increments of 15 about its major axis (see Figure 5.8). We chose a range $\theta = 0, 15, \cdots, 180$. Note that within the given range, the resulting tensors have distinct properties. The form of the tensors can be grouped into two categories namely diagonally anisotropic and symmetrically anisotropic tensors. The derived effective tensors on the other half of the range, i.e. $\theta = 105, 120, \cdots$, have negative off-diagonal entries which, for a generic tensor

$$\lambda = \begin{pmatrix} a & b \\ c & d \end{pmatrix},$$

defined in the first half of the range, one can obtain tensors on the other half by the following representation

$$\lambda^\theta = \begin{pmatrix} a & \mu b \\ \mu c & d \end{pmatrix},$$

where $\mu = \operatorname{sgn} \cos\theta$. Figure 5.9 shows the solutions to the local boundary value problem (5.7) for values of the orientation angle: $\theta = 0, 45, 60, 105$. Following the presentation of the previous section, we analyze the effect of anisotropy for the HCI and WCI local boundary

value problems. In all cases, the effective thermal conductivity tensor depends on the angular orientation of the inclusion, which gives rise to different forms of anisotropic tensors. At $\theta = 0, 90$, and 180, the effective thermal conductivity is diagonally anisotropic (DA), as shown in Figures 5.10a and 5.10b. In between these locations, the tensors are basically symmetrically anisotropic. We also compared the numerical values of the anisotropic tensors with Voigt-Reuss bounds. For the WCI model, the values of $\lambda^{\text{eff}}_{\text{WCI}}$ for the diagonally anisotropic tensors are more closer to the Voigt upper bound λ^{V}. On the other hand, for the HCI model, the diagonally anisotropic tensors are closer to the Reuss lower bound λ^{V}. However, the off-diagonal entries are farther below λ^{R}. This result implies that the Voigt-Reuss bounds are consistent with the principal direction of flow in both cases, even though the off-diagonal directions may not be insignificant.

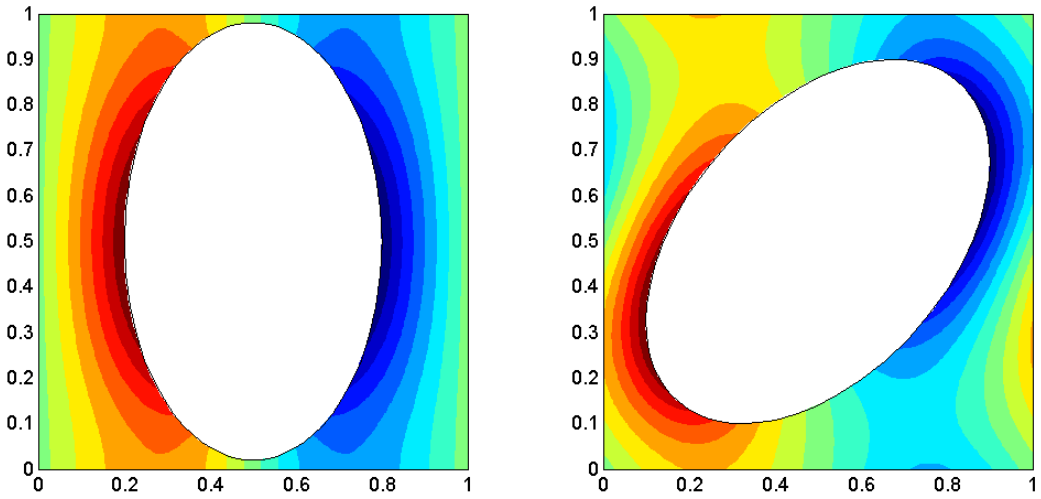

(a) Angular orientations of the inclusion. Left: $\theta = 0°$; right: $\theta = 45°$.

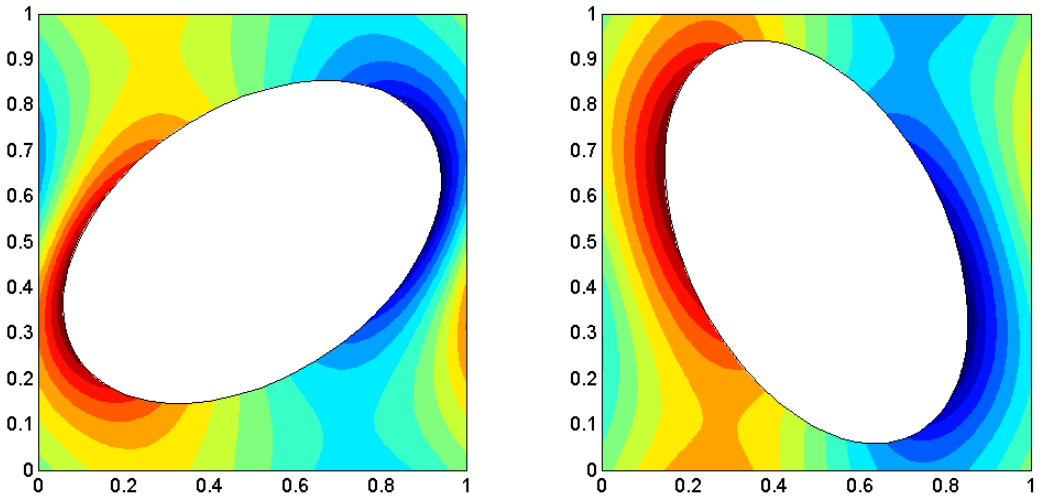

(b) Angular orientations of the inclusion. Left: $\theta = 60°$; right: $\theta = 105°$.

Figure 5.9: Solution of the local boundary value problem (5.7) with centered elliptical inclusion.

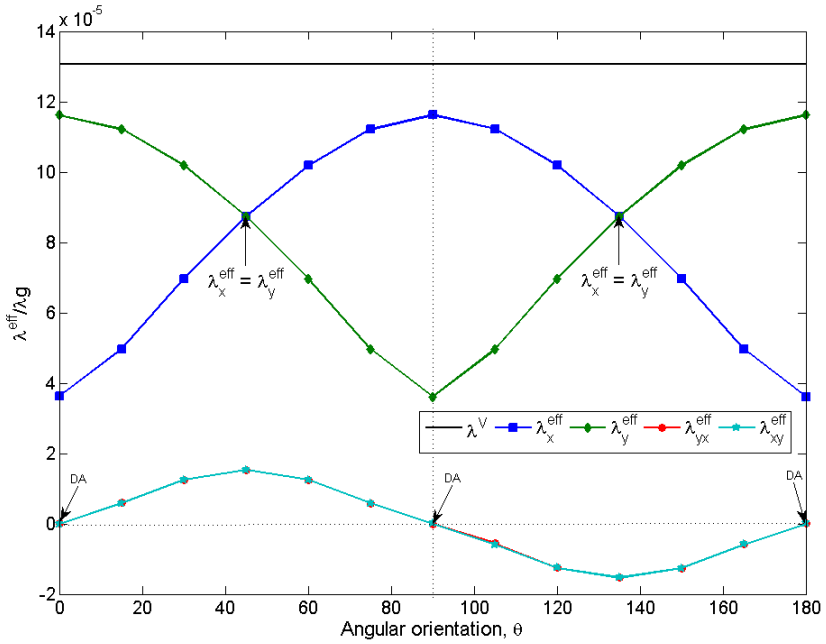

(a) Comparison of the effective thermal conductivity of the HCI model having a centered elliptic inclusion with the angular orientation, θ, of the inclusion. The thermal conductivity ratio is $\lambda_s/\lambda_g = 10^4$.

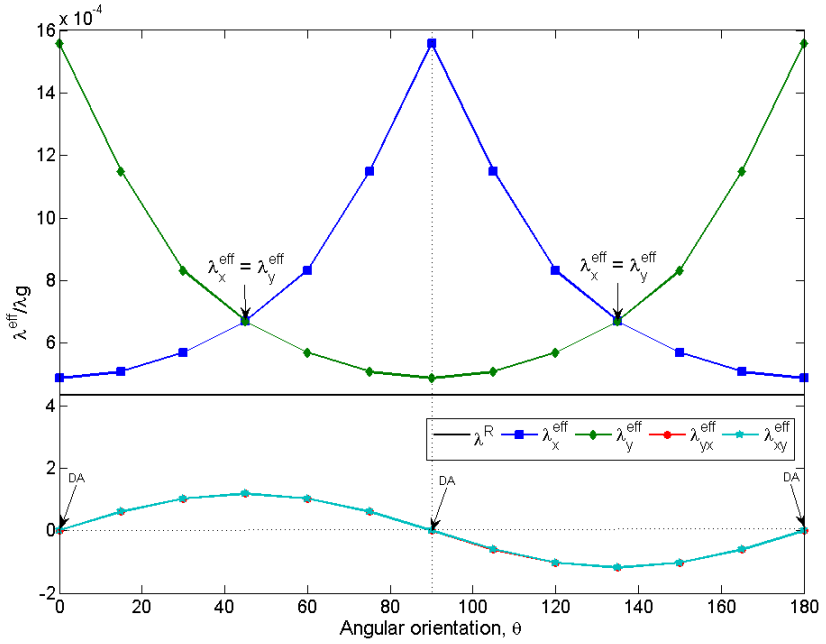

(b) Comparison of the effective thermal conductivity of the WCI model having a centered elliptic inclusion with the angular orientation, θ, of the inclusion. The thermal conductivity ratio is $\lambda_s/\lambda_g = 0$.

Figure 5.10: Evolution of effective thermal conductivity of the WCI and HCI models, and their comparison with the Voigt-Reuss bounds.

5.5 Summary

In this chapter, we have discussed the behavior of the effective diffusion tensor when changing various relevant parameters. Specifically, the analysis has been limited to two dimensional geometries, in which the inclusion (circle and ellipse) is centered within the unit period. The present study has neglected treatment of other geometries and their arrangements within the unit period, simply because their contribution is not so significant for the same volume fraction of inclusion (see Szymkiewicz, 2004, e.g.). The effective thermal conductivity tensor depends strongly on the volume fraction of inclusion. We point out that a similar treatment to the two dimensional problems considered presently is also viable for three-dimensional geometries. Most of these have been treated in other contexts (see Auriault et al., 2009; Szymkiewicz, 2004, and references therein).

We have shown that for a large contrast in the constituent thermal conductivity, the effective thermal conductivity is determined by the thermal conductivity of the interconnected phase, as clearly detailed for the HCI and WCI models. It was also shown that the local boundary value problems (5.7) and (5.9) are limiting cases of the problem (5.4), which was used in determining the effective thermal conductivity for the HCI and WCI models. The implication of the contrast is such that the influence of the thermal conductivity of the inclusions may be neglected if $\lambda_s/\lambda_g \ll 10^2$. For the considered isotropic geometry (circle), the values of λ^{eff} obtained for the weakly conductive inclusion correspond to the upper bound, $\lambda^{\text{HS}+}$, of Hashin-Shtrikman, while for the highly conductive inclusions, λ^{eff} is in agreement with the lower bound, $\lambda^{\text{HS}-}$, of Hashin-Shtrikman.

We also considered the effect of anisotropy in the medium by varying the angular orientation of the inclusion, for a fixed volume fraction of the elliptical inclusion. The result includes distinct forms of anisotropic tensors. The diagonally anisotropic tensors satisfy the Voigt-Reuss bounds. Specifically, the diagonal entries for the HCI model satisfy the Reuss bound, λ^{R}, while the Voigt upper bound is satisfied for the WCI model. However, the off-diagonal entries are farther below λ^{R} for the HCI model. They also fall below λ^{R} for most values of θ. Thus, we conclude that the Voigt-Reuss bounds are consistent with the principal directions of flow (diagonal entries) in both cases, even though the off-diagonal entries may not be insignificant. The characterization of the effect of anisotropy is the subject of Chapter 8. In the context of the phenomenon of interest in the present study, we will consider in Chapters 7 and 8 the contribution of the effective properties derived through homogenization to the macroscopic behavior of fingering instability in both uniform and nonuniform media.

Chapter 6

Numerical verification of the macroscopic equations

As pointed out in Chapter 2, either of two viewpoints can be adopted in the study of homogenization theory. In Chapter 3, we derived the macroscopic system of equations by using the macroscopic viewpoint (see Figure 2.1). In this viewpoint, problems are solved in a fixed domain with cells of size ϵ, which tend to zero. However, following the microscopic viewpoint (see Auriault et al., 2009; Allaire and El Ganaoui, 2009, e.g.), the size of the period cell, normalized with l, is of unit size and independent of ϵ (see Figure 6.1). This implies that as ϵ tends to zero, the periodicity cells do not tend to zero. However, the total number of cells is increased, i.e. the size of the macroscopic domain is of order ϵ^{-1}. In this viewpoint, instead of using the macroscopic space variable $\boldsymbol{x} \in \Omega$, we use the microscopic space variable $\boldsymbol{y} = \boldsymbol{x}/\epsilon$. Thus, in the $\boldsymbol{y}$-coordinate system, the computational domain increases with the scaling, $\epsilon^{-1}\Omega$ as ϵ tends to zero. Following Allaire and El Ganaoui

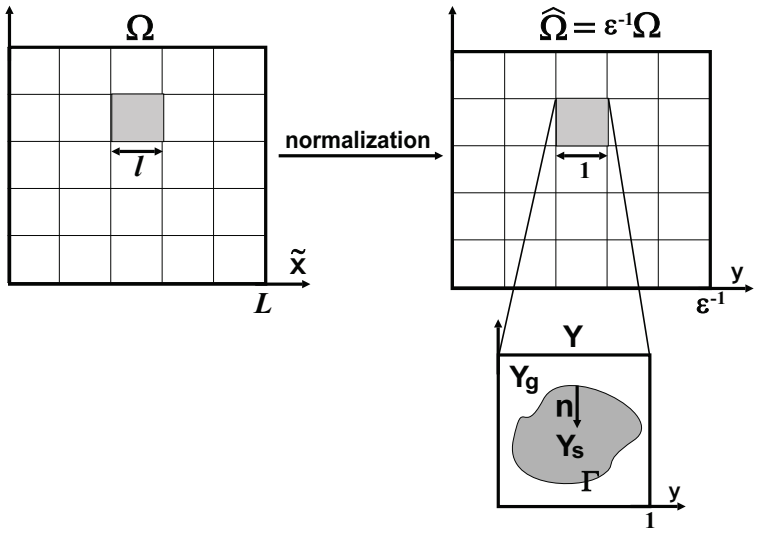

Figure 6.1: The scheme of the microscopic viewpoint used here for computational purposes.

(2009), we describe the physical and computational domains as follows: let the fixed domain be represented viz.:

$$\Omega := \prod_{j=1}^{2}(0, a_j),$$

then, the rescaled computational domain is defined by:

$$\widehat{\Omega} := \epsilon^{-1}\Omega = \prod_{j=1}^{2}(0, a_j/\epsilon).$$

There exist integers N_j such that $a_j/\epsilon = N_j l_j$, for $j = 1, 2$. Note that this definition ensures that only periodicity cells of unit size belong to $\widehat{\Omega}$. For any function $u(x)$ defined on Ω, the rescaled function $\widehat{u}(y)$ defined on $\widehat{\Omega}$ satisfies the following relations:

$$\widehat{u}(y) = u(\epsilon y) = u(x), \tag{6.1a}$$
$$\nabla_y \widehat{u}(y) = \epsilon(\nabla_x u)(\epsilon y) = \epsilon \nabla_x u(x) \tag{6.1b}$$

We point out that all physical quantities defined on $\widehat{\Omega}$ are denoted with a hat $\widehat{\ }$ symbol. The ensemble of the respective solid and gas parts, $\widehat{\Omega}_\mathrm{s}$ and $\widehat{\Omega}_\mathrm{g}$, are also defined according to the same transformation relating Ω and $\widehat{\Omega}$. We restrict the discussion in this section to the MCI model, in which the full governing equations are given as follows:

$$\mathfrak{H}^\epsilon \begin{cases} \mathcal{C}_\mathrm{g}\dfrac{\partial T_\mathrm{g}}{\partial t} + \mathcal{C}_\mathrm{g}\boldsymbol{v}\cdot\nabla T_\mathrm{g} - \nabla\cdot(\lambda_\mathrm{g}\nabla T_\mathrm{g}) = 0, & \boldsymbol{x} \in \Omega_\mathrm{g}^\epsilon, t > 0, \\ \mathcal{C}_\mathrm{s}\dfrac{\partial T_\mathrm{s}}{\partial t} - \nabla\cdot(\lambda_\mathrm{s}\nabla T_\mathrm{s}) = 0, & \boldsymbol{x} \in \Omega_\mathrm{s}^\epsilon, t > 0, \\ T_\mathrm{g} = T_\mathrm{s}, & \boldsymbol{x} \in \Gamma^\epsilon, t > 0, \\ \boldsymbol{n}\cdot(\lambda_\mathrm{g}\nabla T_\mathrm{g} - \lambda_\mathrm{s}\nabla T_\mathrm{s}) = \epsilon Q W(T_\mathrm{s}, C), & \boldsymbol{x} \in \Gamma^\epsilon, t > 0. \end{cases} \tag{6.2}$$

$$\mathfrak{M}^\epsilon \begin{cases} \gamma\dfrac{\partial C}{\partial t} + \boldsymbol{v}\cdot\nabla C - \nabla\cdot D\nabla C = 0, & \boldsymbol{x} \in \Omega_\mathrm{g}^\epsilon, t > 0, \\ -D\nabla C\cdot\boldsymbol{n} = \epsilon\beta W(T_\mathrm{s}, C), & \boldsymbol{x} \in \Gamma^\epsilon, t > 0, \end{cases} \tag{6.3}$$

where the coefficients γ and β have no physical meaning in the problem at hand and satisfy $\gamma = \beta = 1$. In the new coordinate system, (6.2) and (6.3) take the following form

$$\widehat{\mathfrak{H}}^\epsilon \begin{cases} \epsilon^2\widehat{\mathcal{C}}_\mathrm{g}\dfrac{\partial \widehat{T}_\mathrm{g}}{\partial t} + \epsilon\widehat{\boldsymbol{V}_T}\cdot\nabla\widehat{T}_\mathrm{g} - \nabla\cdot(\widehat{\lambda}_\mathrm{g}\nabla\widehat{T}_\mathrm{g}) = 0, & \boldsymbol{y} \in \widehat{\Omega}_\mathrm{g}, t > 0, \\ \epsilon^2\widehat{\mathcal{C}}_\mathrm{s}\dfrac{\partial \widehat{T}_\mathrm{s}}{\partial t} - \nabla\cdot(\widehat{\lambda}_\mathrm{s}\nabla\widehat{T}_\mathrm{s}) = 0, & \boldsymbol{y} \in \widehat{\Omega}_\mathrm{s}, t > 0, \\ \widehat{T}_\mathrm{g} = \widehat{T}_\mathrm{s}, & \boldsymbol{y} \in \widehat{\Gamma}, t > 0, \\ (\widehat{\lambda}_\mathrm{g}\nabla\widehat{T}_\mathrm{g} - \widehat{\lambda}_\mathrm{s}\nabla\widehat{T}_\mathrm{s})\cdot\boldsymbol{n} = \epsilon^2\widehat{Q}W(\widehat{T}_\mathrm{s}, \widehat{C}), & \boldsymbol{y} \in \widehat{\Gamma}, t > 0. \end{cases} \tag{6.4}$$

$$\widehat{\mathfrak{M}}^{\epsilon}\begin{cases}\epsilon^2\widehat{\gamma}\dfrac{\partial\widehat{C}}{\partial t}+\epsilon\widehat{\boldsymbol{V}_C}\cdot\nabla\widehat{C}-\nabla\cdot\widehat{D}\nabla\widehat{C}=0, & \boldsymbol{y}\in\widehat{\Omega}_{\mathrm{g}},t>0,\\ -\widehat{D}\nabla\widehat{C}\cdot\boldsymbol{n}=\epsilon^2\widehat{\beta}W(\widehat{T}_{\mathrm{s}},\widehat{C}), & \boldsymbol{y}\in\widehat{\Gamma},t>0.\end{cases}\tag{6.5}$$

In a similar way, the homogenized problems become

$$\widehat{\mathfrak{H}^0}\left\{\epsilon^2\widehat{\mathcal{C}}^{\mathrm{eff}}\frac{\partial\widehat{T}}{\partial t}+\epsilon\widehat{\boldsymbol{V}_T}\phi\cdot\nabla\widehat{T}-\nabla\cdot(\widehat{\lambda}^{\mathrm{eff}}\nabla\widehat{T})=\epsilon^2\widehat{Q}\phi^{\mathrm{s}}W(\widehat{T},\widehat{C}),\boldsymbol{y}\in\widehat{\Omega},t>0.\right.\tag{6.6}$$

$$\widehat{\mathfrak{M}^0}\left\{\epsilon^2\widehat{\gamma}\phi\frac{\partial\widehat{C}}{\partial t}+\epsilon\widehat{\boldsymbol{V}_C}\phi\cdot\nabla\widehat{C}-\nabla\cdot(\widehat{D}^{\mathrm{eff}}\nabla\widehat{C})=-\epsilon^2\widehat{\beta}\phi^{\mathrm{s}}W(\widehat{T},\widehat{C}),\boldsymbol{y}\in\widehat{\Omega},t>0.\right.\tag{6.7}$$

We are interested in the first order homogenization approximation

$$u^{\epsilon}(\boldsymbol{x})\approx u^0(\boldsymbol{x})+\epsilon u^1(\boldsymbol{x},\frac{\boldsymbol{x}}{\epsilon}),$$

which, under the coordinate transformation, is equivalent to:

$$\widehat{u}^{\epsilon}(\boldsymbol{y})\approx\widehat{u}^0(\boldsymbol{y})+\widehat{u}^1(\boldsymbol{y}).\tag{6.8}$$

Thus, the first order correction to the homogenized problems (6.6) and (6.7) is defined as

$$\widehat{u}^1(\boldsymbol{y})=\epsilon u^1(\epsilon\boldsymbol{y},\boldsymbol{y})=\epsilon u^1(\boldsymbol{x},\frac{\boldsymbol{x}}{\epsilon})=\sum_{j=1}^{2}\frac{\partial\widehat{u}^0}{\partial y_j}(\boldsymbol{y})\mathcal{N}_j(\boldsymbol{y}).\tag{6.9}$$

In (6.9), we see that the solution $\boldsymbol{\mathcal{N}}(\boldsymbol{y})$ to the cell problems are not rescaled since they are already defined on the unit periodicity cell in the $\boldsymbol{y}$-coordinate. Also, for the considered problems, the cell problems are solved only once because they satisfy the translational invariance property and do not depend on the field variables $\widehat{T}$ and $\widehat{C}$.

Error estimates and rate of convergence of the homogenization process

The error estimates between the exact and the reconstructed solutions will be given in the discrete form of the L^2-norms. However, following the line of argument in Allaire and Habibi (2013), we compute relative errors between the reconstructed solutions of the form (6.8) and the exact solutions. It can be shown that the relative errors are invariant under the coordinate transformation and are given as

$$\frac{\|u^{\epsilon}(\boldsymbol{x})-(u^0(\boldsymbol{x})+\epsilon u^1(\boldsymbol{x},\frac{\boldsymbol{x}}{\epsilon}))\|_{L^2(0,\tau;\Omega)}}{\|u^{\epsilon}(\boldsymbol{x})\|_{L^2(0,\tau;\Omega)}}=\frac{\|\widehat{u}^{\epsilon}(\boldsymbol{y})-(\widehat{u}^0(\boldsymbol{y})+\widehat{u}^1(\boldsymbol{y}))\|_{L^2(0,\tau;\widehat{\Omega})}}{\|\widehat{u}^{\epsilon}(\boldsymbol{y})\|_{L^2(0,\tau;\widehat{\Omega})}}\tag{6.10}$$

and

$$\frac{\|\nabla u^{\epsilon}(\boldsymbol{x})-\nabla(u^0(\boldsymbol{x})+\epsilon u^1(\boldsymbol{x},\frac{\boldsymbol{x}}{\epsilon}))\|_{L^2(0,\tau;\Omega)}}{\|\nabla u^{\epsilon}(\boldsymbol{x})\|_{L^2(0,\tau;\Omega)}}=\frac{\|\nabla\widehat{u}^{\epsilon}(\boldsymbol{y})-\nabla(\widehat{u}^0(\boldsymbol{y})+\widehat{u}^1(\boldsymbol{y}))\|_{L^2(0,\tau;\widehat{\Omega})}}{\|\nabla\widehat{u}^{\epsilon}(\boldsymbol{y})\|_{L^2(0,\tau;\widehat{\Omega})}}.\tag{6.11}$$

In order to verify the convergence rate of our homogenization results, the error estimates (6.10) and (6.11) defined respectively for a generic scalar field $\widehat{u}$ and its gradient are compared with the slopes of ϵ and $\sqrt{\epsilon}$. We define these estimates for the temperature and concentration fields as well as their gradients by

$$ERR(T) = \frac{\|\widehat{T}^{\epsilon}(\boldsymbol{y}) - (\widehat{T}^{0}(\boldsymbol{y}) + \widehat{T}^{1}(\boldsymbol{y}))\|_{L^2(0,\tau;\widehat{\Omega})}}{\|\widehat{T}^{\epsilon}(\boldsymbol{y})\|_{L^2(0,\tau;\widehat{\Omega})}} \leq C\epsilon, \tag{6.12}$$

$$ERR(C) = \frac{\|\widehat{C}^{\epsilon}(\boldsymbol{y}) - (\widehat{C}^{0}(\boldsymbol{y}) + \widehat{C}^{1}(\boldsymbol{y}))\|_{L^2(0,\tau;\widehat{\Omega})}}{\|\widehat{C}^{\epsilon}(\boldsymbol{y})\|_{L^2(0,\tau;\widehat{\Omega})}} \leq C\epsilon, \tag{6.13}$$

and

$$ERR(\nabla T) = \frac{\|\nabla\widehat{T}^{\epsilon}(\boldsymbol{y}) - \nabla(\widehat{T}^{0}(\boldsymbol{y}) + \widehat{T}^{1}(\boldsymbol{y}))\|_{L^2(0,\tau;\widehat{\Omega})}}{\|\nabla\widehat{T}^{\epsilon}(\boldsymbol{y})\|_{L^2(0,\tau;\widehat{\Omega})}} \leq C\sqrt{\epsilon}, \tag{6.14}$$

$$ERR(\nabla C) = \frac{\|\nabla\widehat{C}^{\epsilon}(\boldsymbol{y}) - \nabla(\widehat{C}^{0}(\boldsymbol{y}) + \widehat{C}^{1}(\boldsymbol{y}))\|_{L^2(0,\tau;\widehat{\Omega})}}{\|\nabla\widehat{C}^{\epsilon}(\boldsymbol{y})\|_{L^2(0,\tau;\widehat{\Omega})}} \leq C\sqrt{\epsilon}. \tag{6.15}$$

The error estimates are also consistent with the theoretical estimates deduced in Section 4.6.1 Eq. (4.115).

6.1 Algorithm for reconstructing solutions to the homogenization problem

We detail in this section the computational procedure used to reconstructing an approximate homogenized solution, in order to recover the details in the pore scale description, and hence achieve better convergence between the homogenized problems and the exact problems. The method presented here is solely based on post-processing of the computed cell solutions and the homogenized solutions. The first approach (see Algorithm 1) can be understood as a reconstruction by interpolation at grid points of the computational domain. The second approach is based on successive generation of cell solutions $\boldsymbol{\mathcal{N}}(y)$ that cover the discrete computational domain $\widehat{\Omega}_h$. First, we recall the method of computation for the general homogenization procedure for periodic structures:

1. Solve the cell problems in each of the canonical e_j directions for the temperature and concentration fields
2. Calculate the effective thermal conductivity and diffusion tensors using the solutions of the cell problems
3. Solve the coupled system of homogenized problems for the temperature $\widehat{T}^0$ and concentration $\widehat{C}^0$ fields

4. For the purpose of reconstructing an approximate solution to the homogenized problems, the following two steps are required:

   (a) Compute the corrector (6.9),

   (b) Reconstruct an approximate solution (6.8).

6.1.1 Two reconstruction algorithms

Algorithm 1

Data: Given $\widehat{u}^0(y), \nabla_{y_j}\widehat{u}^0(y)$ defined on $\widehat{\Omega}_h$ and $\mathcal{N}_j, j = 1, 2.$ defined on a periodicity unit cell Y.
Result: Generate data for $\widehat{u}^0(y_i), \nabla_{y_j}\widehat{u}^0(y_i)$, at subgrids $\widehat{\Omega}_{h,i}$ of unit size and compute $\widehat{u}^0(y) + \widehat{u}^1(y)$ using $\mathcal{N}_j(y)$.
Partition the grid $\widehat{\Omega}_h$ into a number of subgrids $\widehat{\Omega}_{h,i}$ such that

$$\widehat{\Omega}_h = \bigcup_{i=1}^{N_h} \widehat{\Omega}_{h,i}$$

For each $\widehat{\Omega}_{h,i}$, interpolate

$$\widehat{u}^0(y_i), \frac{\partial \widehat{u}^0}{\partial y_j}(y_i),\ y_i \in \widehat{\Omega}_{h,i}, i = 1, 2, \cdots, N_h.$$

Compute the sum

$$\widehat{u}^1(y_i) = \sum_{j=1}^{2} \frac{\partial \widehat{u}^0}{\partial y_j}(y_i)\mathcal{N}_j(y),\ y_i \in \widehat{\Omega}_{h,i}.$$

Assemble subgrid solutions in $\widehat{\Omega}_{h,i}$ and reconstruct an approximate solution

$$\widehat{u}^0(y) + \widehat{u}^1(y),\ y \in \widehat{\Omega}$$

Algorithm 1: Reconstruction of solution by partitioning of grid points and interpolation.

In Algorithm 1, the reconstruction is based on the fact the gradients $\nabla\widehat{u}^0$ of the homogenized solutions can be recovered through interpolation on subgrids $\widehat{\Omega}_{h,i}$ of unit size. This implies a sequence of interpolations of the gradients at the subgrid, $\widehat{\Omega}_{h,i}$ level. This operation is memory inefficient and increases the computational time.

Data: Given $\widehat{u}^0(y), \nabla_{y_j}\widehat{u}^0(y)$ defined on $\widehat{\Omega}_h$ and $\mathcal{N}_j, j = 1, 2.$ defined on a periodicity unit cell Y.
Result: Generate a lattice of copies of $\mathcal{N}_j$ and compute $\widehat{u}^0(y) + \widehat{u}^1(y)$ using $\mathcal{N}_j(y)$.
Generate copies of $\mathcal{N}_j$ to cover the grid $\widehat{\Omega}_h$
Compute the sum

$$\widehat{u}^1(y) = \sum_{j=1}^{2} \frac{\partial \widehat{u}^0}{\partial y_j}(y)\mathcal{N}_j(y),\ y \in \widehat{\Omega}_h.$$

Reconstruct an approximate solution

$$\widehat{u}^0(y) + \widehat{u}^1(y),\ y \in \widehat{\Omega}.$$

Algorithm 2: Reconstruction of solution by generation of lattice of copies of $\mathcal{N}$.

Algorithm 2

Alternatively, instead of generating a sequence of subgrid gradients $\nabla_{y_i}\widehat{u}^0, y_i \in \widehat{\Omega}_{h,i}$, we generate a lattice of copies of cell solutions $\mathcal{N}_j$, in which each $\mathcal{N}_j$ belongs to $\widehat{\Omega}_{h,i}$ and their union covers a grid of size $\widehat{\Omega}_h$ (see Figure 6.2). Then, the reconstruction proceeds by computing the sum (6.9) directly on the grid $\widehat{\Omega}_h$, and subsequently adding the sum to the homogenized solution $\widehat{u}^0(y)$ that is already available in the computational domain $\widehat{\Omega}_h$. The algorithm is as given in Algorithm 2.

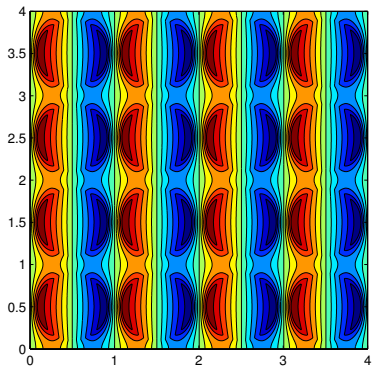

(a) $\mathcal{N}_1$ in the e_1 direction for problem $\widehat{\mathfrak{H}}$.

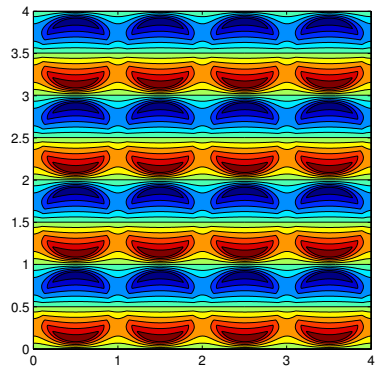

(b) $\mathcal{N}_2$ in the e_2 direction for problem $\widehat{\mathfrak{H}}$.

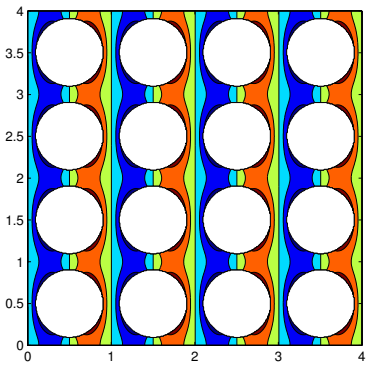

(c) $\mathcal{N}_1$ in the e_1 direction for problem $\widehat{\mathfrak{M}}$.

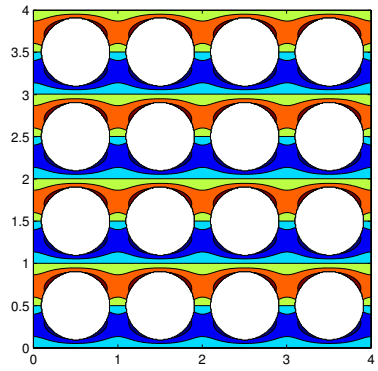

(d) $\mathcal{N}_2$ in the e_2 direction for problem $\widehat{\mathfrak{M}}$.

Figure 6.2: Lattices of cell solutions used in the reconstruction algorithm (2) for a typical reference computation $\epsilon_0 = 1/4$.

6.2 Numerical verification of the homogenization process

In order to check the efficiency of the reconstruction algorithms 1 and 2, we consider a simple case of the model problems (6.4)-(6.5) and (6.6)-(6.7), in which we neglect the reaction terms, hence decoupling of the system of equations. This allows for studying the respective heat and concentration models independently. The convection term, on the other hand, is considered relatively small with respect to the problem at hand. This is consistent with the classical HPS method[1] used in the present study. [2]

[1]The classical HPS method is adopted in the present study to investigate a combustion phenomenon that exhibits diffusional instability. In this sense, the convective flux is relatively low.

[2]We refer to the presentation in Auriault and Adler (1995) and the recent extension to the classical HPS method-two-scale expansion with drift Allaire et al. (2010)-for treating problems with strong convection and chemical reactions.

We start with a computation domain $\widehat{\Omega} = \epsilon^{-1}\Omega = \prod_{j=1}^{2}(0, a_j/\epsilon)$, with $a_j/\epsilon = N_j l_j$, where $l_j = 1$cm corresponds to the length of the unit periodicity cell and $N_j = 4$ in the reference computation[3]. The two-dimensional periodicity cell (see Figure 6.3) has been chosen as a cross-section of the three dimensional periodic medium (see Figure 2.3a) along the direction of flow. Alternatively, since the thin layer of the medium is negligible, the geometry of the periodic medium can be considered in the (y_1, y_2)-plane. The radius of the solid part

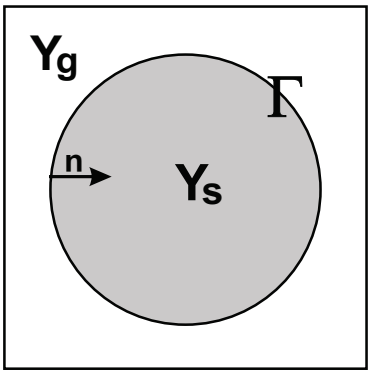

Figure 6.3: Two dimensional periodicity cell.

in Figure 6.3 is $r = 0.4$ cm, such that the volume fraction of the gas part is calculated as $|Y_{\mathrm{g}}| = \phi = 1 - \pi r^2$. In the considered geometry, the physical quantities related to the diffusion and thermal conductivity are isotropic, and their values are given in Table A.1. For a generic physical quantity $\widehat{\varphi}$ defined in (6.4) and (6.5), and respectively in (6.6) and (6.7), its value is associated with the physical value for a generic quantity φ described in the physical domain Ω. That is, in the rescaled problems $\widehat{\mathfrak{H}}$ and $\widehat{\mathfrak{M}}$, the quantity $\widehat{\varphi}$ varies with ϵ. However, in a reference computation, the value of $\widehat{\varphi}$ matches exactly the physical value. That is, for a given reference computation $\epsilon_0 = \epsilon$, the quantity $\widehat{\varphi}$ defined in the $\boldsymbol{y}$-coordinate system, in relation to a generic quantity φ defined in the original (macroscopic viewpoint) $\boldsymbol{x}$-coordinate system, satisfies the following relation:

$$\epsilon^{\mathrm{d}}\widehat{\varphi} := \varphi. \tag{6.16}$$

However, in the test for convergence of the homogenization process, the physical quantities defined in $\widehat{\Omega}$ vary with ϵ according to $\epsilon^d\widehat{\varphi}$, where d represents the exponent of ϵ in the rescaled problems (i.e. problems defined in the $\boldsymbol{y}$-coordinate system). Specifically, by using (6.16) in (6.4) and (6.5), respectively (6.6) and (6.7), the physical quantities with ϵ coefficients are chosen, for the reference computation, as follows:

$$\epsilon^2\widehat{\mathcal{C}}_{\mathrm{g,s}} = \mathcal{C}_{\mathrm{g,s}}, \epsilon^2\widehat{\mathcal{C}}^{\mathrm{eff}} = \mathcal{C}^{\mathrm{eff}}, \epsilon^2\widehat{Q} = Q, \tag{6.17}$$

$$\epsilon^2\widehat{\gamma} = \gamma, \epsilon^2\widehat{\beta} = \beta, \epsilon\widehat{\boldsymbol{V}_\alpha} = \boldsymbol{v}_\alpha, \tag{6.18}$$

[3]A typical computation in which the physical quantities in the computational domain $\widehat{\Omega}$ retain their physical values.

where $\boldsymbol{v}_\alpha$ are defined according to problems $\widehat{\mathfrak{H}}$ and $\widehat{\mathfrak{M}}$, with $\alpha = T, C$.

We prescribe Dirichlet boundary condition for the temperature and concentration fields on the left boundary and a Neumann boundary condition at the right boundary. Specifically, the corresponding boundary conditions are:

$$\widehat{T} = 300K, \widehat{C} = 0.46, \quad \text{at } y_1 = 0, \tag{6.19a}$$

$$\frac{\partial \widehat{T}}{\partial y_1} = \frac{\partial \widehat{C}}{\partial y_1} = 0, \quad \text{at } y_1 = a_1/\epsilon. \tag{6.19b}$$

In order to test for the rate of convergence of the homogenization process as ϵ tends to zero, (alternatively, as the number of periodic cells tends to infinity), we are required to add cells in both directions, in each subsequent computation from a reference computation (see Figure 6.4a) This is equivalent to allowing ϵ become smaller and smaller. Alternatively, we can also enforce periodic boundary conditions in the y_2-direction (see Figure 6.4b) simply for computational efficiency. This means that it is not necessary to add cells in the y_2-direction; hence N_2 is fixed and we simply add cells in the y_1-direction. The value of N_1 is increased by a unit step in each computation, with N_1 ranging from 4 to 12, i.e. the number of cells in the y_1-direction increases according to

$$\epsilon = \frac{1}{N_1}. \tag{6.20}$$

The initial conditions for temperature and concentration are given by:

$$\widehat{T} = 500K, \widehat{C} = 0.23. \tag{6.21}$$

We also note that the domain of the homogenized problems has the same domain size and boundary conditions as described above, except that the domain is homogeneous. All computations are performed with a finite element algorithm for each of the distinct problems, and are implemented in the finite element application, COMSOL Multiphysics®, with quadratic triangular elements. The application allows to handle complex domain shapes and easy implementation of the periodic boundary conditions. However, the reconstruction procedure is implemented in Matlab® as a post-processing step. The solutions to the cell problem (5.4), corresponding to the MCI model, are computed on the unit cell depicted in Figure 6.3, whereas computations of the cell solutions are restricted only to the gas part, Y_g, of the unit cell since the diffusion mechanism is dominated by the gas phase. For the implementation of the cell solutions, the coefficients must satisfy the scaling in powers of ϵ which is implied in each of the model problems. For instance, this condition is trivially satisfied for the MCI model since the coefficients, in each part of the medium, assume their physical values, and hence satisfy the order of magnitude $\mathcal{O}(1)$ with respect to ϵ.

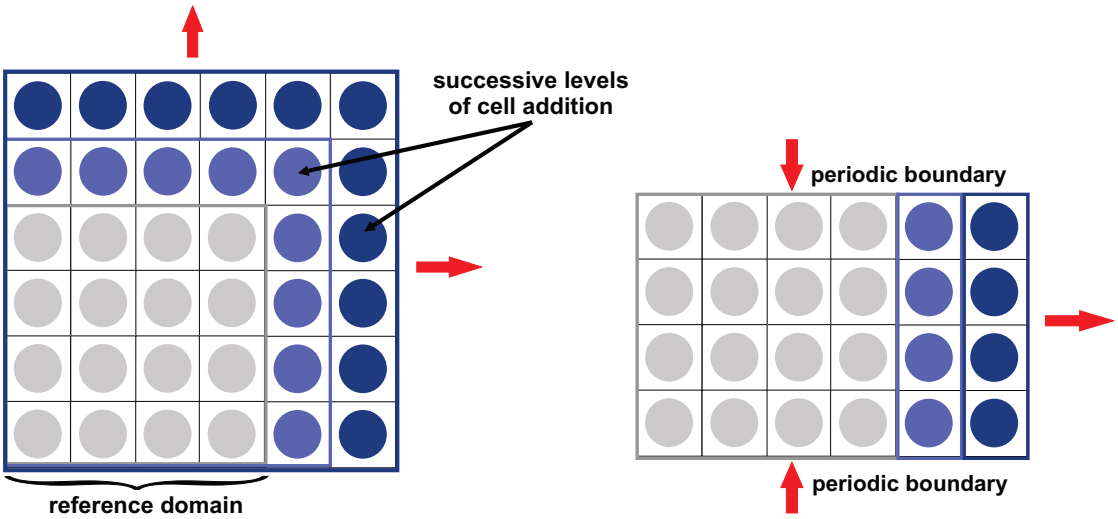

(a) Two directional cell addition. (b) One directional cell addition.

Figure 6.4: The scheme of domain $\widehat{\Omega}$ for the microscopic viewpoint with constant periodicity cells of unit size and successive levels of cell additions for each value of ϵ.

6.3 Simulation results for problems $\widehat{\mathfrak{H}}^{\epsilon}$ and $\widehat{\mathfrak{H}}^{0}$

In this section, we describe the solutions to problems $\widehat{\mathfrak{H}}^{\epsilon}$ and $\widehat{\mathfrak{H}}^{0}$ for a reference computation corresponding to $\epsilon_0 = \epsilon = 1/7$. The decoupled equations are now in the form of a convection-diffusion equation. Hence, the question of how much of the convective transport is adequate for the validity of the HPS method used in this study has to be treated. Thus, in this section, we consider the influence of convective transport on error estimates related to the temperature and its gradient. Specifically, we consider the following problems:

1. Computation of the first order correction to the homogenized solution, $\widehat{T}^0(y)$.

2. Estimation of error for a reference computation $\epsilon_0 = 1/7$, in which we vary the strength of convection in small increments, for each successive computation. This will allow us to access the range of the flow velocity, under which the problems $\widehat{\mathfrak{H}}^{\epsilon}$ and $\widehat{\mathfrak{H}}^{0}$ remain valid.

3. Furthermore, the validity of the model will be judged based on the convergence of the reconstructed solution $\widehat{T}^0(y) + \widehat{T}^1(y)$ to the exact solution, $\widehat{T}^{\epsilon}(y)$. Hence, plots of error estimates of the temperature and its gradients are related to different flow velocities.

4. Since the corrector term $\widehat{T}^1(y)$ does not satisfy a Dirichlet boundary condition, we use Neumann-type boundary conditions in order to avoid complications with boundary layers; but only in the reference computation presented in this section. The following

initial condition is used:

$$\widehat{T}^{\epsilon,0}(y,0) = 500 + \sigma \exp\{-(y - a_1/\epsilon)^2\}, \text{ with } \sigma > 0. \tag{6.22}$$

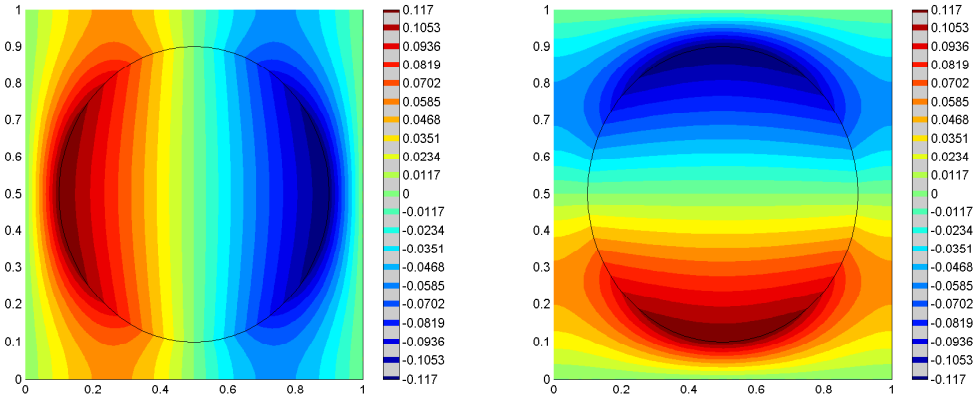

Figure 6.5: Solutions to the cell problems $\mathcal{N}_1$ and $\mathcal{N}_2$ corresponding to problem $\widehat{\mathfrak{H}}$.

As a first step, we compute the solution to the cell problems in the considered geometry (see Figure 6.3). The solutions are depicted in Figure 6.5, and correspond to the problem, $\widehat{\mathfrak{H}}$. The solutions allow to compute the effective thermal conductivity tensor; in this case, for the MCI model. Since the geometry of the problem is symmetric, the effective thermal conductivity tensor is isotropic and the calculated value is given by

$$\widehat{\lambda}^{\text{eff}} = \begin{pmatrix} 3.96 \cdot 10^{-4} & 0.00 \\ 0.00 & 3.96 \cdot 10^{-4} \end{pmatrix}. \tag{6.23}$$

The top panel of Figure 6.7 (from left to right) depicts respectively the solutions to the exact temperature $\widehat{T}^{\epsilon}$ and homogenized temperature $\widehat{T}^{0}$, whereas the bottom panel (from left to right) shows the reconstructed temperature $\widehat{T}^{0} + \widehat{T}^{1}$ and the difference $\widehat{T}^{\epsilon} - (\widehat{T}^{0} + \widehat{T}^{1})$, between the exact and reconstructed solutions. The solution of the first order term, $\widehat{T}^{1}$ (see Figure 6.6), depends on the gradient of the homogenized temperature, and is computed as the sum

$$\widehat{T}^{1}(y) = \sum_{j=1}^{2} \frac{\partial \widehat{T}^{0}}{\partial y_j}(\boldsymbol{y}) \mathcal{N}_j(\boldsymbol{y}), \tag{6.24}$$

where $\mathcal{N}_j$ are the solutions to cell problems illustrated in Figure 6.5. While the homogenized temperature $\widehat{T}^{0}$ represents the non-oscillatory (averaged) term in the asymptotic sum that approximates the exact solution $\widehat{T}^{\epsilon}$, the oscillatory behavior of solution to the exact problem $\widehat{\mathfrak{H}}^{\epsilon}$ are contained in higher order terms of the asymptotic expansion of $\widehat{T}^{\epsilon}$. The oscillatory behavior can be recovered by adding more terms of the asymptotic expansion

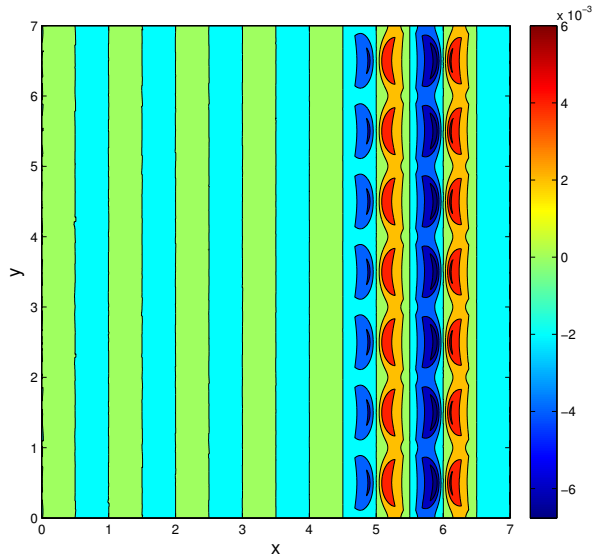

Figure 6.6: Solution to the first order term $\widehat{T}^1$ of the asymptotic expansion of $\widehat{T}^\epsilon$ computed from (6.24).

to the zeroth order (homogenized) term depicted in Figure 6.7b. Specifically, it can be seen in Figure 6.6 (see also Figure 6.8b) that the first order term $\widehat{T}^1$ is oscillating. This is what we require in the present study in order to correct the homogenized solution. Note that if the small scale parameter ϵ is quite small, the contribution of the first order corrector as well as higher order correctors become less important. Figure 6.9 shows the magnitude of the temperatures for the exact solution and the reconstructed solution. Clearly, it can be seen that the magnitude of the error is quite small.

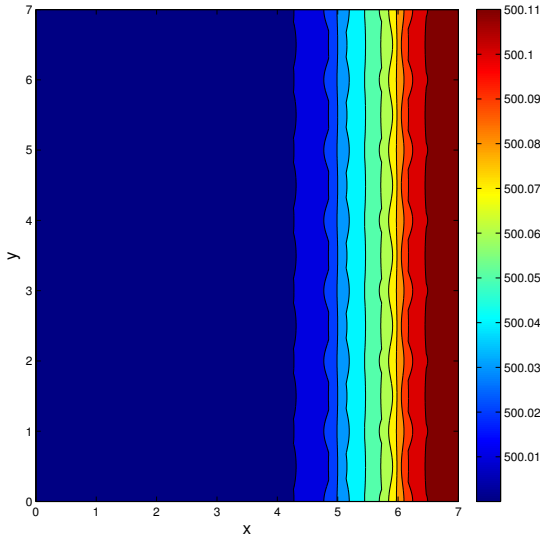

(a) $\widehat{T}^\epsilon$

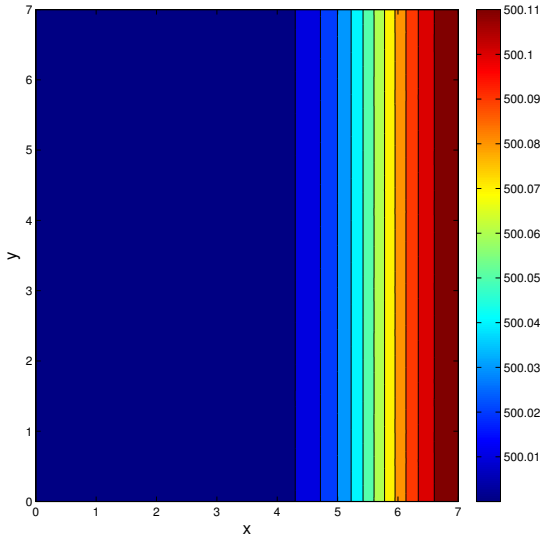

(b) $\widehat{T}^0$.

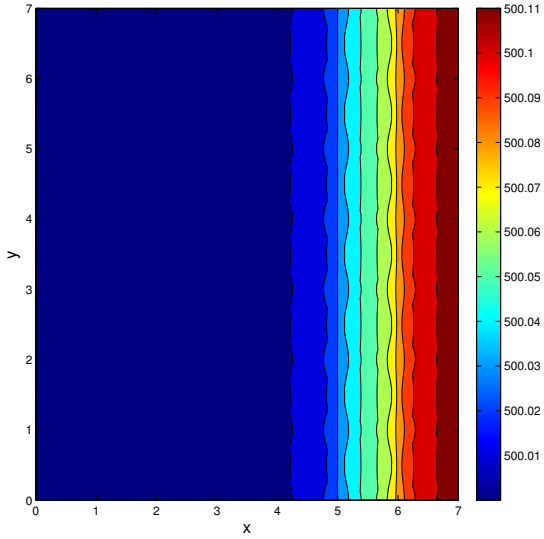

(c) $\widehat{T}^0 + \widehat{T}^1$

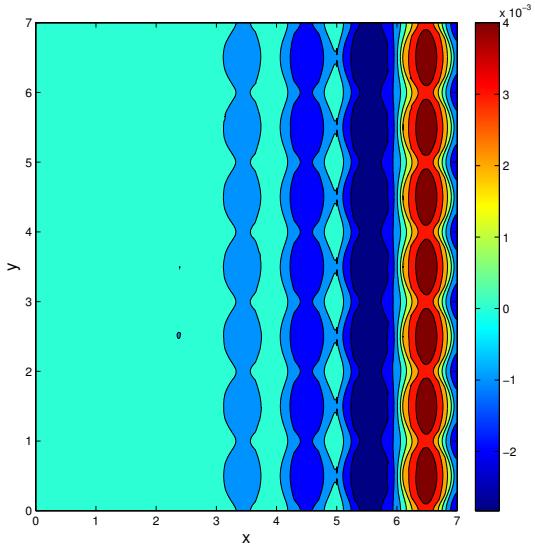

(d) $\widehat{T}^\epsilon - (\widehat{T}^0 + \widehat{T}^1)$

Figure 6.7: Solutions to problems $\widehat{\mathfrak{H}^\epsilon}$ and $\widehat{\mathfrak{H}^0}$ at $t = 400s$, for the reference computation $\epsilon_0 = \epsilon = 1/7$.

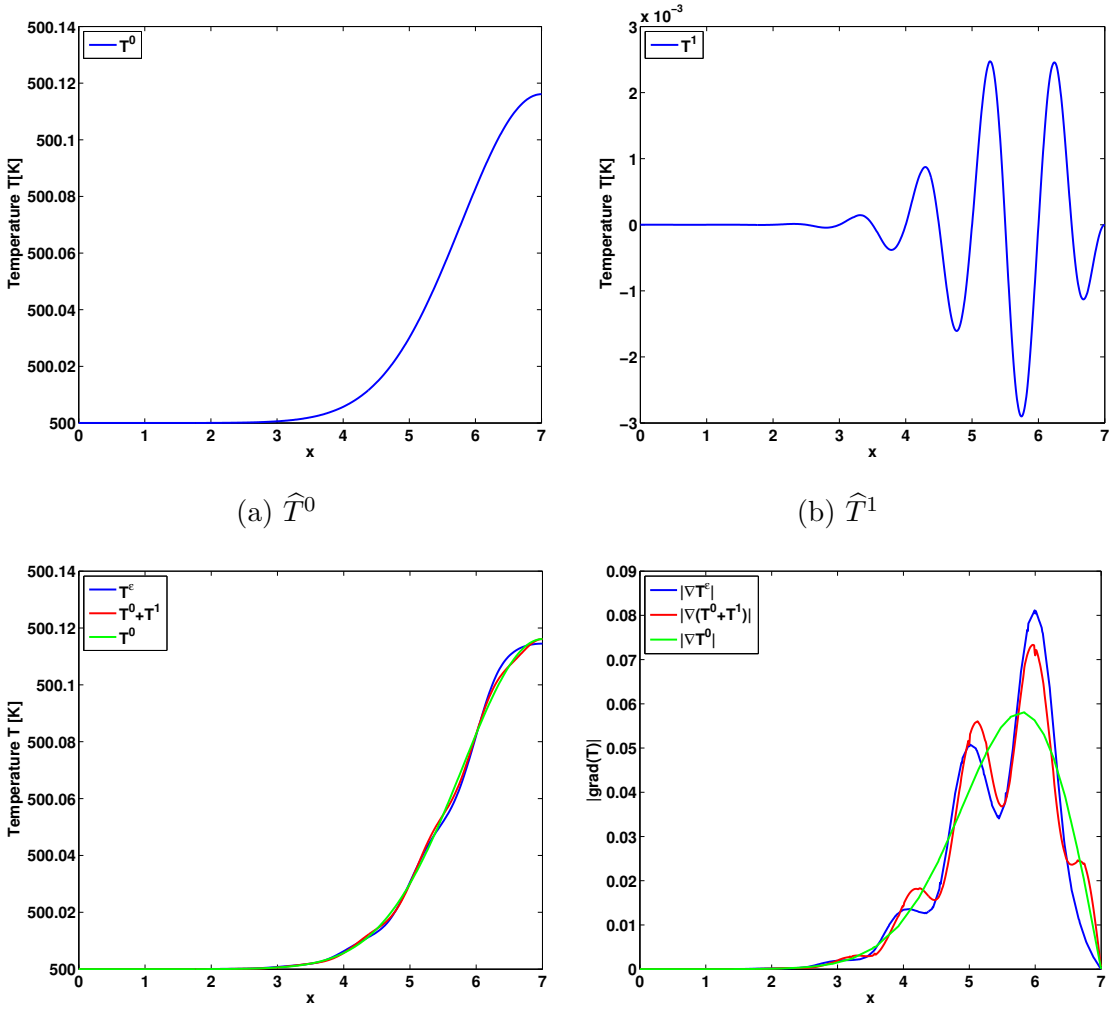

(a) $\widehat{T}^0$ (b) $\widehat{T}^1$

(c) $\widehat{T}^\epsilon, \widehat{T}^0$ and $\widehat{T}^0 + \widehat{T}^1$ (d) $|\nabla\widehat{T}^\epsilon|, |\nabla\widehat{T}^0|$ and $|\nabla(\widehat{T}^0 + \widehat{T}^1)|$

Figure 6.8: Longitudinal cross-section of solutions at $t = 400s$ showing (a) Zeroth order (homogenized) temperature $\widehat{T}^0$; (b) First order temperature, $\widehat{T}^1$; (c) comparison of the various temperatures $\widehat{T}^\epsilon, \widehat{T}^0$ and $\widehat{T}^0 + \widehat{T}^1$; (d) comparison of the gradients of the temperatures $|\nabla\widehat{T}^\epsilon|, |\nabla\widehat{T}^0|$ and $|\nabla(\widehat{T}^0 + \widehat{T}^1)|$. All computations refer to $\epsilon_0 = \epsilon = 1/7$, and V=0.0 cm/s.

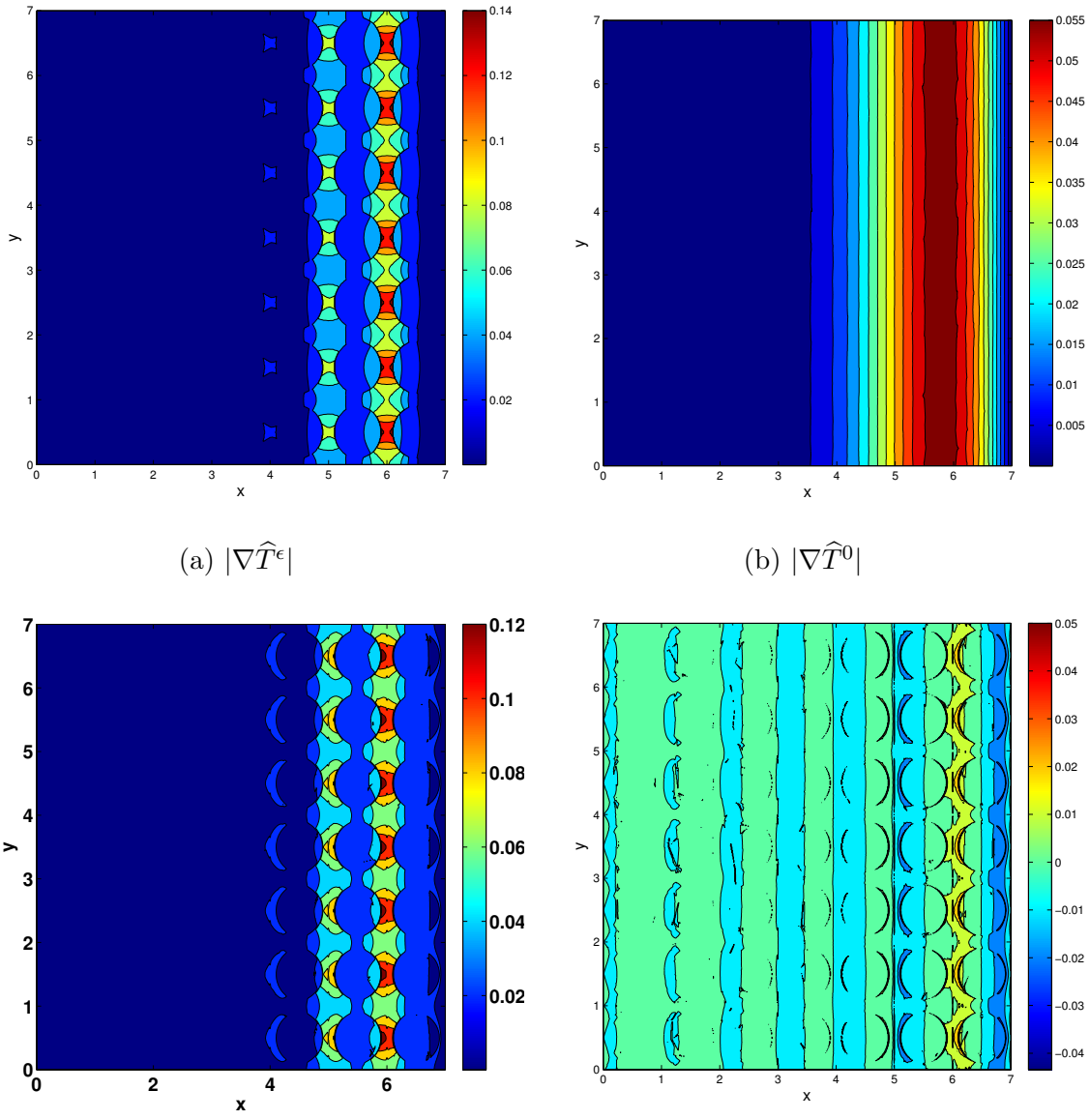

(a) $|\nabla \widehat{T}^\epsilon|$ (b) $|\nabla \widehat{T}^0|$

(c) $|\nabla(\widehat{T}^0 + \widehat{T}^1)|$ (d) $|\nabla \widehat{T}^\epsilon - \nabla(\widehat{T}^0 + \widehat{T}^1)|$

Figure 6.9: Magnitude of solution gradients to problems $\widehat{\mathfrak{H}^\epsilon}$ and $\widehat{\mathfrak{H}^0}$ at $t = 400s$, for the reference computation $\epsilon_0 = \epsilon = 1/7$.

6.4 Simulation results for problems $\widehat{\mathfrak{M}}^\epsilon$ and $\widehat{\mathfrak{M}}^0$

In this section, we simply follow the outline given in Section 6.3. Also, we restrict the discussions to a reference computation corresponding to $\epsilon_0 = \epsilon = 1/7$. Unlike in the previous section, an inhomogeneous Dirichlet boundary condition is prescribed at the left boundary. For the problems $\widehat{\mathfrak{M}}^\epsilon$ and $\widehat{\mathfrak{M}}^0$, the reconstructed solution is given by $\widehat{C}^0 + \widehat{C}^1$, where the first order term of the asymptotic expansion

$$\widehat{C}^\epsilon(y) \approx \widehat{C}^0(y) + \widehat{C}^1(y) + \cdots \tag{6.25}$$

is defined as a sum similar to (6.24). The solutions $\mathcal{N}_1$ and $\mathcal{N}_2$ to the cell problems, in this

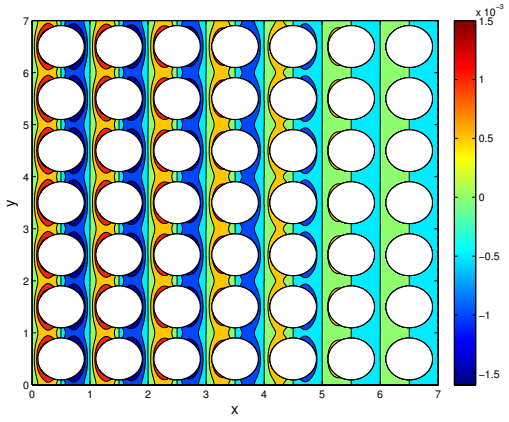

Figure 6.10: Solution to the first order term $\widehat{C}^1$ of the asymptotic expansion of $\widehat{C}^\epsilon$.

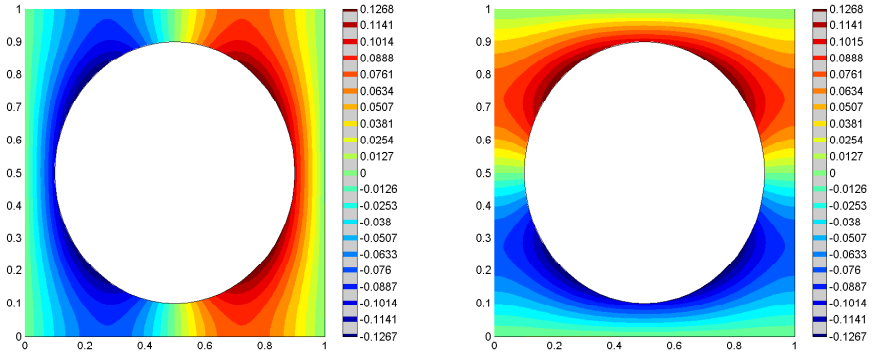

Figure 6.11: Solutions to the cell problems (left) $\mathcal{N}_1$ and (right) $\mathcal{N}_2$, corresponding to problem $\widehat{\mathfrak{M}}$.

case, are restricted to the gas part Y_g of the periodicity cell, and are illustrated in Figure

6.11. The effective diffusion tensor is computed using the solutions $\mathcal{N}_1$ and $\mathcal{N}_2$. It can be seen that the tensor is isotropic, owing to the nature of the considered geometry, i.e.

$$\widehat{D}^{\text{eff}} = \begin{pmatrix} 0.080523 & 0.00 \\ 0.00 & 0.080523 \end{pmatrix}. \tag{6.26}$$

The solutions to the exact problem $\widehat{\mathfrak{M}}^\epsilon$ and homogenized problem $\widehat{\mathfrak{M}}^0$ are given in Figure 6.12 Figure 6.14 shows the magnitude of the temperatures for the exact solution and the

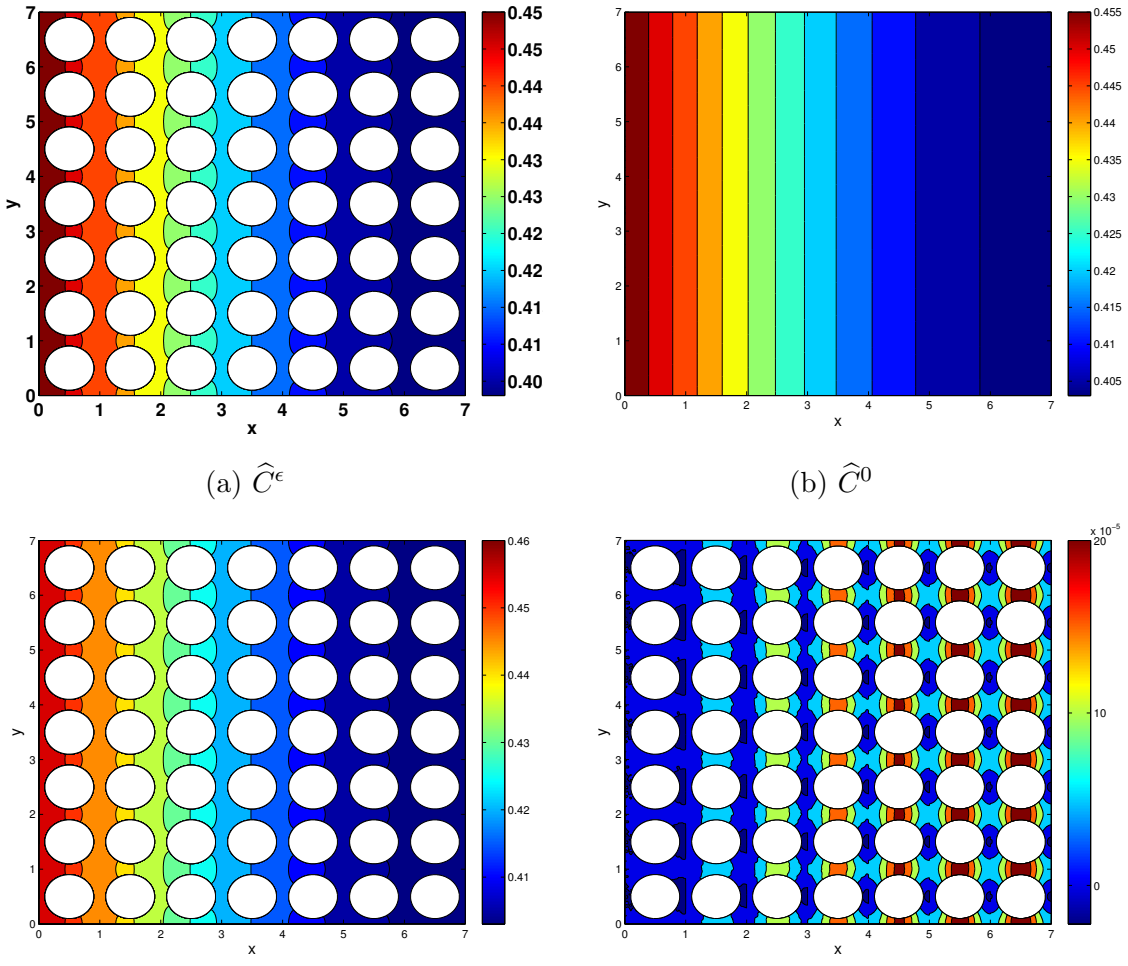

(a) $\widehat{C}^\epsilon$ (b) $\widehat{C}^0$

(c) $\widehat{C}^0 + \widehat{C}^1$ (d) $\widehat{C}^\epsilon - (\widehat{C}^0 + \widehat{C}^1)$

Figure 6.12: Solutions to problems $\widehat{\mathfrak{M}}^\epsilon$ and $\widehat{\mathfrak{M}}^0$ at $t = 200s$, for the reference computation $\epsilon_0 = \epsilon = 1/7$.

reconstructed solution. It can be seen that the magnitude of the error is quite small.

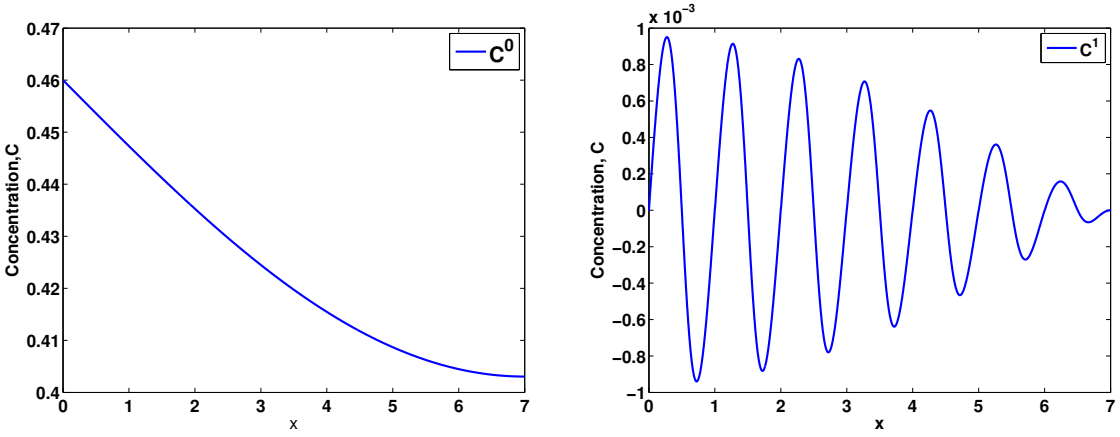

(a) $\widehat{C}^0$ (b) $\widehat{C}^1$

(c) $\widehat{C}^\epsilon, \widehat{C}^0$ and $\widehat{C}^0 + \widehat{C}^1$ (d) $|\nabla\widehat{C}^\epsilon|, |\nabla\widehat{C}^0|$ and $|\nabla(\widehat{C}^0 + \widehat{C}^1)|$

Figure 6.13: Longitudinal cross-section of solutions at $t = 200s$ showing (a) Zeroth order (homogenized) concentration $\widehat{C}^0$; (b) First order concentration, $\widehat{C}^1$; (c) comparison of the various concentrations $\widehat{C}^\epsilon, \widehat{C}^0$ and $\widehat{C}^0 + \widehat{C}^1$; (d) comparison of the gradients of the concentrations $|\nabla\widehat{C}^\epsilon|, |\nabla\widehat{C}^0|$ and $|\nabla(\widehat{C}^0 + \widehat{C}^1)|$. All computations refer to $\epsilon_0 = \epsilon = 1/7$, and V=0.0 cm/s.

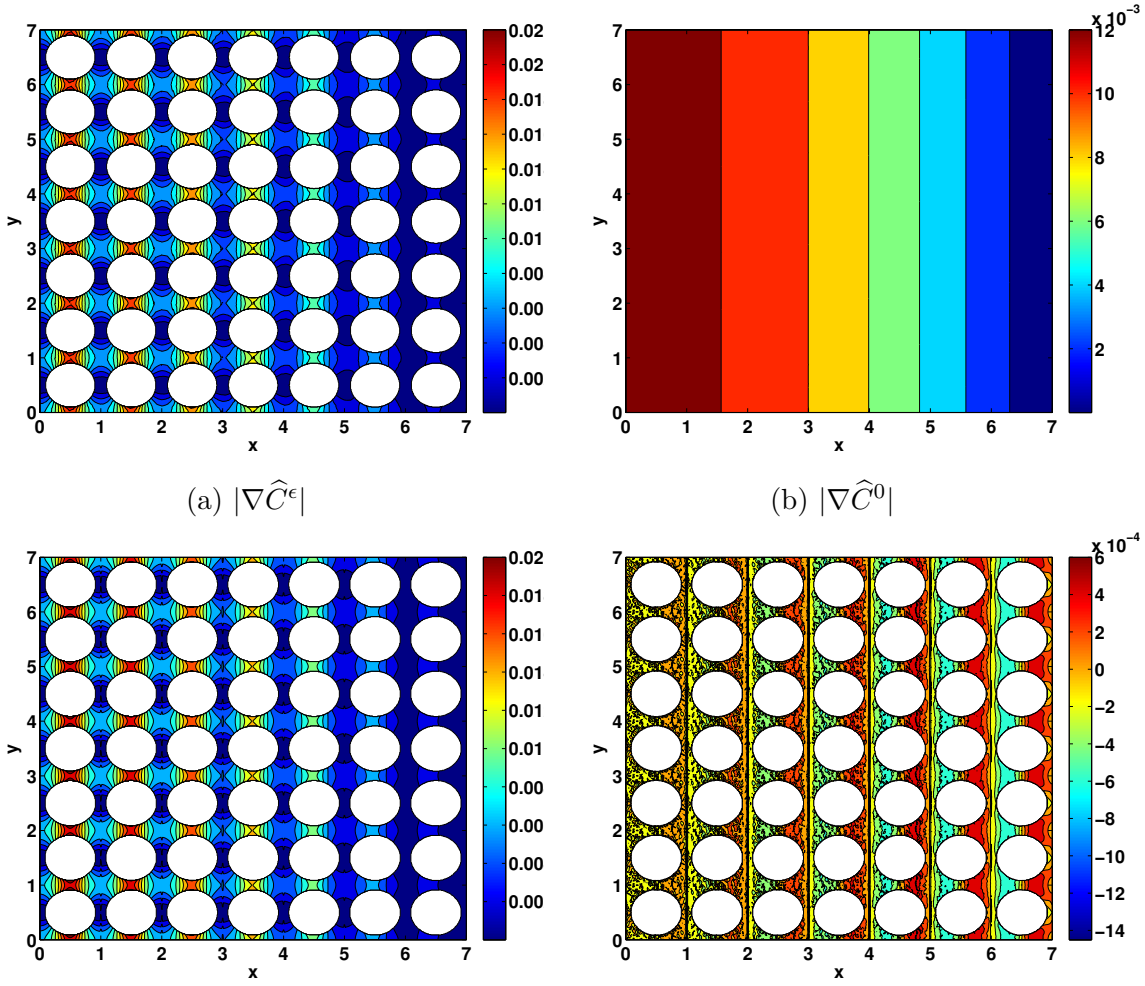

(a) $|\nabla \widehat{C}^\epsilon|$

(b) $|\nabla \widehat{C}^0|$

(c) $|\nabla(\widehat{C}^0 + \widehat{C}^1)|$

(d) $|\nabla \widehat{C}^\epsilon - \nabla(\widehat{C}^0 + \widehat{C}^1)|$

Figure 6.14: Magnitude of solution gradients to problems $\widehat{\mathfrak{M}}^\epsilon$ and $\widehat{\mathfrak{M}}^0$ at $t = 200s$, for the reference computation $\epsilon_0 = \epsilon = 1/7$.

6.5 Simulation results for the coupled problems $\widehat{\mathfrak{H}}$ and $\widehat{\mathfrak{M}}$

The nonlinear system of convection reaction-diffusion equations is considered using the data of Table A.1. We are particularly interested in estimating the convergence of the homogenization process and to access the numerical rate of convergence as ϵ tends to zero. This is done respectively in the relative L^2 norms (6.10) and (6.11) between the exact and reconstructed solutions and between their gradients. We proceed as in the previous section by computing the solutions for the problems $\widehat{\mathfrak{H}}$ and $\widehat{\mathfrak{M}}$. The heat of reaction Q is chosen in a moderate regime, in which there is no resulting flame propagation. For the problems described in this section, we prescribe Dirichlet boundary conditions on the left boundary (i.e. $y_1 = 0$) for the temperature and concentration fields and a homogeneous Neumann conditions at the right boundary, i.e.

$$\widehat{T} = 300K, \widehat{C} = 0.23, \quad \text{at } y_1 = 0, \frac{\partial \widehat{T}}{\partial y_1} = \frac{\partial \widehat{C}}{\partial y_1} = 0, \quad \text{at } y_1 = a_1/\epsilon. \tag{6.27}$$

For checking the numerical convergence of the homogenization process, we chose the following initial condition (6.28) for the temperature, so that the physical behavior of the solutions do not change drastically as ϵ tends to zero.

$$\widehat{T}^{\epsilon,0}(y,0) = 1000 + \sigma \exp\{-(y - a_1/\epsilon)^2\}, \text{ with } \sigma \geq 0. \tag{6.28}$$

6.5.1 Convergence rates for the coupled system with no convection

First, we consider the coupled problem, in which the flow field $\boldsymbol{V} = (0,0,0)$cm/s. In this case, the two directional scheme (Figure 6.4a) of domain for cell addition is adopted, which involves adding cells in both y-directions at each successive computation (or at each decrease in the value of ϵ). We only consider moderate simulations for which the total number of cells $N(\epsilon)$ in the domain is not so large. The total number of cells in each computation is given in Tables 6.1 and 6.2. Also, a Neumann-type boundary condition is prescribed in the y_2-directions. The resulting relative errors on the temperature field and its gradient, given respectively by (6.12) and (6.14), are plotted in Figures 6.15 and 6.16. The relative errors are compared respectively with linear plots of ϵ and $\sqrt{\epsilon}$. In Figures 6.15 and 6.16, it can be seen that the relative error estimates satisfy the theoretical estimates given in Section 4.6.1. Similarly, the relative errors on the concentration field and its gradient, given respectively by (6.13) and (6.15), are plotted in Figures 6.17 and 6.18 as functions of ϵ. We also see that the convergence rates described in Section 4.6.1 are satisfied. These results are also depicted in Tables 6.1 and 6.2.

$N(\epsilon)$	ϵ	$ERR(T)$	$\sqrt{\epsilon}$	$ERR(\nabla T)$
16	$2.500 \cdot 10^{-1}$	$9.344 \cdot 10^{-3}$	$5.000 \cdot 10^{-1}$	$1.145 \cdot 10^{-1}$
25	$2.000 \cdot 10^{-1}$	$5.469 \cdot 10^{-3}$	$4.472 \cdot 10^{-1}$	$9.047 \cdot 10^{-2}$
36	$1.667 \cdot 10^{-1}$	$3.485 \cdot 10^{-3}$	$4.082 \cdot 10^{-1}$	$7.818 \cdot 10^{-2}$
49	$1.429 \cdot 10^{-1}$	$2.621 \cdot 10^{-3}$	$3.780 \cdot 10^{-1}$	$7.129 \cdot 10^{-2}$
64	$1.250 \cdot 10^{-1}$	$1.858 \cdot 10^{-3}$	$3.536 \cdot 10^{-1}$	$6.645 \cdot 10^{-2}$
81	$1.111 \cdot 10^{-1}$	$1.447 \cdot 10^{-3}$	$3.333 \cdot 10^{-1}$	$6.323 \cdot 10^{-2}$
100	$1.000 \cdot 10^{-1}$	$1.175 \cdot 10^{-3}$	$3.162 \cdot 10^{-1}$	$6.105 \cdot 10^{-2}$
121	$0.909 \cdot 10^{-1}$	$9.025 \cdot 10^{-4}$	$3.015 \cdot 10^{-1}$	$5.946 \cdot 10^{-2}$
144	$0.833 \cdot 10^{-1}$	$7.407 \cdot 10^{-4}$	$2.887 \cdot 10^{-1}$	$5.809 \cdot 10^{-2}$

Table 6.1: Relative error estimates at distinct values of ϵ for the nonlinear problem with no convection.

N(ϵ)	ϵ	$ERR(C)$	$\sqrt{\epsilon}$	$ERR(\nabla C)$
16	$2.500 \cdot 10^{-1}$	$4.718 \cdot 10^{-3}$	$5.000 \cdot 10^{-1}$	$1.285 \cdot 10^{-2}$
25	$2.000 \cdot 10^{-1}$	$3.209 \cdot 10^{-3}$	$4.472 \cdot 10^{-1}$	$9.379 \cdot 10^{-3}$
36	$1.667 \cdot 10^{-1}$	$2.853 \cdot 10^{-3}$	$4.082 \cdot 10^{-1}$	$7.184 \cdot 10^{-3}$
49	$1.429 \cdot 10^{-1}$	$1.570 \cdot 10^{-3}$	$3.780 \cdot 10^{-1}$	$5.476 \cdot 10^{-3}$
64	$1.250 \cdot 10^{-1}$	$1.313 \cdot 10^{-3}$	$3.536 \cdot 10^{-1}$	$4.584 \cdot 10^{-3}$
81	$1.111 \cdot 10^{-1}$	$1.071 \cdot 10^{-3}$	$3.333 \cdot 10^{-1}$	$3.927 \cdot 10^{-3}$
100	$1.000 \cdot 10^{-1}$	$8.645 \cdot 10^{-4}$	$3.162 \cdot 10^{-1}$	$3.449 \cdot 10^{-3}$
121	$0.909 \cdot 10^{-1}$	$7.265 \cdot 10^{-4}$	$3.015 \cdot 10^{-1}$	$3.096 \cdot 10^{-3}$
144	$0.833 \cdot 10^{-1}$	$6.866 \cdot 10^{-4}$	$2.887 \cdot 10^{-1}$	$2.831 \cdot 10^{-3}$

Table 6.2: Relative error estimates at distinct values of ϵ for the nonlinear problem with no convection.

6.5.2 Convergence rates for the coupled system with convection

We now illustrate the relative errors on the coupled system of reaction diffusion equations with convection. We chose a flow field along the y_1-direction $\boldsymbol{V} = (0.05, 0, 0)$, which is

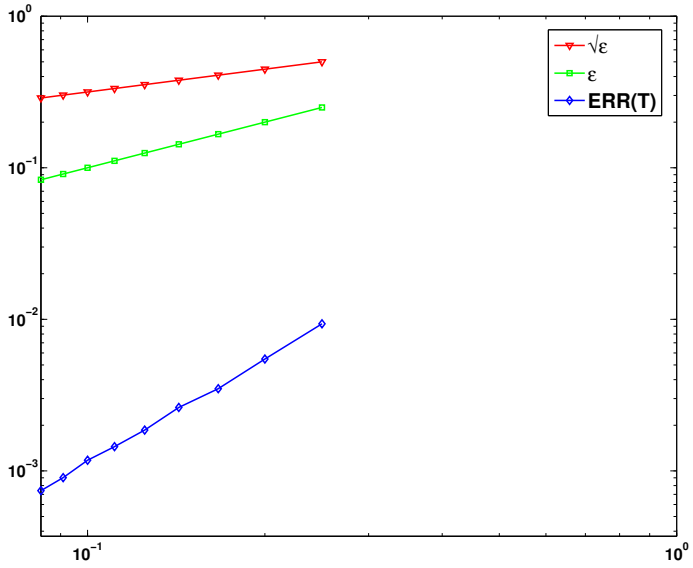

Figure 6.15: Relative error on the temperature as a function of ϵ.

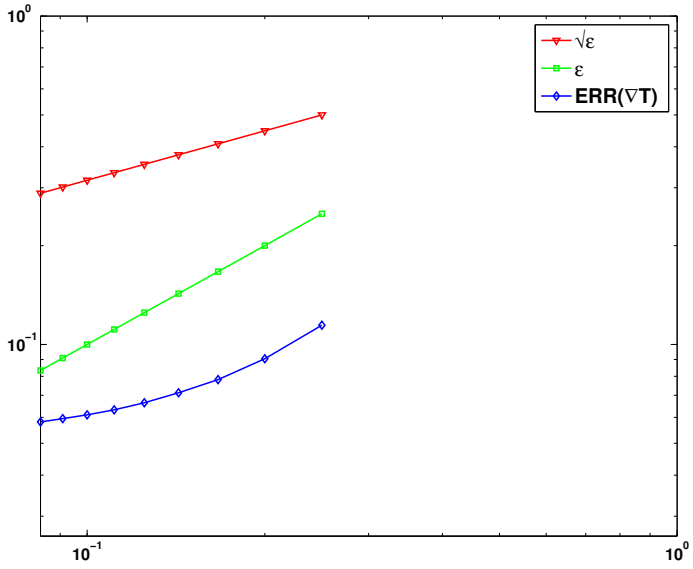

Figure 6.16: Relative error on the temperature gradient as a function of ϵ.

within a moderate regime for flows described for the problem at hand. We adopt the one-directional scheme (Figure 6.4b) of the domain for cell addition. This scheme implies the use of periodic boundary conditions in the y_2-direction, so that we do not require additional cells in the y_2-direction; we simply add cells in the y_1-direction. The total number of

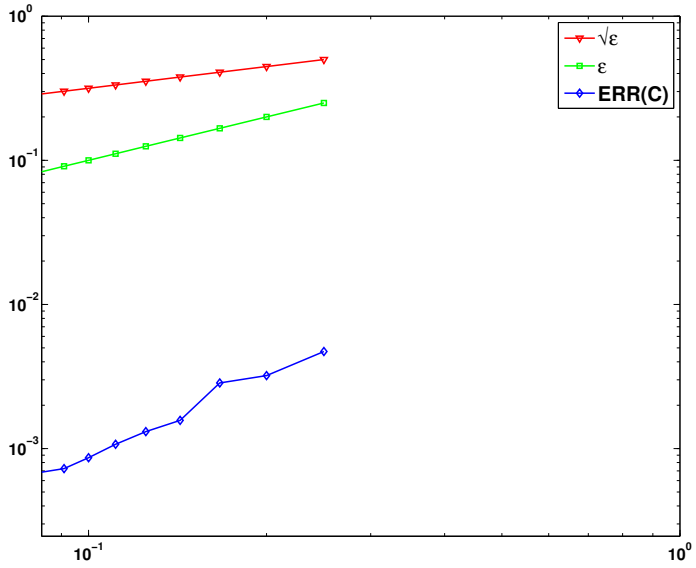

Figure 6.17: Relative error on the concentration as a function of ϵ.

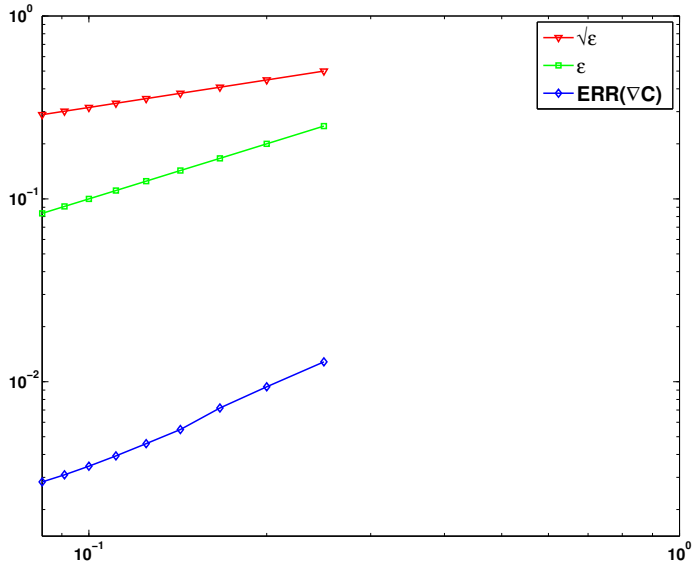

Figure 6.18: Relative error on the concentration gradient as a function of ϵ.

cells in each computation is given in Tables 6.3 and 6.4. As will be illustrated later on, the scheme cuts down on the total number of cells, and hence a gain in CPU resources is achieved. Figures 6.23 and 6.24 illustrate respectively simulation results at $t = 40$s, for the temperature and concentration fields. The resulting relative errors $ERR(T)$ and

$N(\epsilon)$	ϵ	$ERR(T)$	$\sqrt{\epsilon}$	$ERR(\nabla T)$
16	$2.500 \cdot 10^{-1}$	$9.989 \cdot 10^{-2}$	$5.000 \cdot 10^{-1}$	$1.189 \cdot 10^{-1}$
20	$2.000 \cdot 10^{-1}$	$6.005 \cdot 10^{-3}$	$4.472 \cdot 10^{-1}$	$9.340 \cdot 10^{-2}$
24	$1.667 \cdot 10^{-1}$	$4.370 \cdot 10^{-3}$	$4.082 \cdot 10^{-1}$	$8.116 \cdot 10^{-2}$
28	$1.429 \cdot 10^{-1}$	$3.131 \cdot 10^{-3}$	$3.780 \cdot 10^{-1}$	$7.315 \cdot 10^{-2}$
32	$1.250 \cdot 10^{-1}$	$2.286 \cdot 10^{-3}$	$3.536 \cdot 10^{-1}$	$6.779 \cdot 10^{-2}$
36	$1.111 \cdot 10^{-1}$	$1.947 \cdot 10^{-3}$	$3.333 \cdot 10^{-1}$	$6.440 \cdot 10^{-2}$
40	$1.000 \cdot 10^{-1}$	$1.582 \cdot 10^{-3}$	$3.162 \cdot 10^{-1}$	$6.201 \cdot 10^{-2}$
44	$0.909 \cdot 10^{-1}$	$1.460 \cdot 10^{-3}$	$3.015 \cdot 10^{-1}$	$6.028 \cdot 10^{-2}$
48	$0.833 \cdot 10^{-1}$	$1.328 \cdot 10^{-3}$	$2.887 \cdot 10^{-1}$	$5.892 \cdot 10^{-2}$

Table 6.3: Relative error estimates at distinct values of ϵ for the nonlinear problem with $\boldsymbol{V} = (0.05, 0, 0)$cm/s.

N(ϵ)	ϵ	$ERR(C)$	$\sqrt{\epsilon}$	$ERR(\nabla C)$
16	$2.500 \cdot 10^{-1}$	$1.192 \cdot 10^{-2}$	$5.000 \cdot 10^{-1}$	$1.931 \cdot 10^{-2}$
20	$2.000 \cdot 10^{-1}$	$1.092 \cdot 10^{-2}$	$4.472 \cdot 10^{-1}$	$1.549 \cdot 10^{-2}$
24	$1.667 \cdot 10^{-1}$	$1.010 \cdot 10^{-2}$	$4.082 \cdot 10^{-1}$	$1.244 \cdot 10^{-2}$
28	$1.429 \cdot 10^{-1}$	$9.976 \cdot 10^{-2}$	$3.780 \cdot 10^{-1}$	$1.087 \cdot 10^{-2}$
32	$1.250 \cdot 10^{-1}$	$9.354 \cdot 10^{-3}$	$3.536 \cdot 10^{-1}$	$9.338 \cdot 10^{-3}$
36	$1.111 \cdot 10^{-1}$	$8.997 \cdot 10^{-3}$	$3.333 \cdot 10^{-1}$	$8.337 \cdot 10^{-3}$
40	$1.000 \cdot 10^{-1}$	$8.817 \cdot 10^{-3}$	$3.162 \cdot 10^{-1}$	$7.631 \cdot 10^{-3}$
44	$0.909 \cdot 10^{-1}$	$8.680 \cdot 10^{-3}$	$3.015 \cdot 10^{-1}$	$7.084 \cdot 10^{-3}$
48	$0.833 \cdot 10^{-1}$	$8.595 \cdot 10^{-3}$	$2.887 \cdot 10^{-1}$	$6.658 \cdot 10^{-3}$

Table 6.4: Relative error estimates at distinct values of ϵ for the nonlinear problem with $\boldsymbol{V} = (0.05, 0, 0)$cm/s.

$ERR(\nabla T)$ respectively for the temperature and its gradient are depicted in Figure 6.19 and Figure 6.20 and also on Table 6.3. We see that the convergence rates, calculated within the chosen flow field, are consistence with the theoretical estimates (4.115).

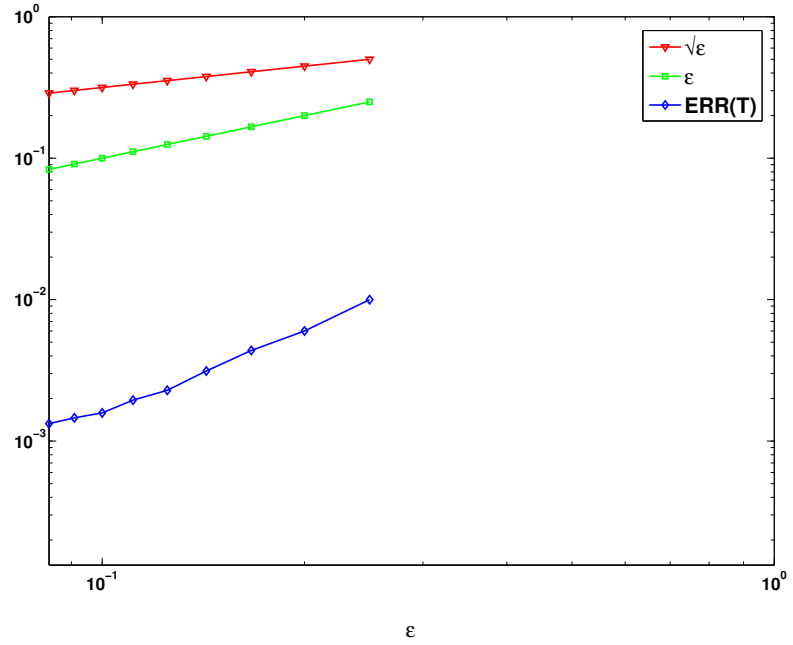

Figure 6.19: Relative error on the temperature as a function of ϵ for $\boldsymbol{V} = (0.05, 0, 0)$cm/s.

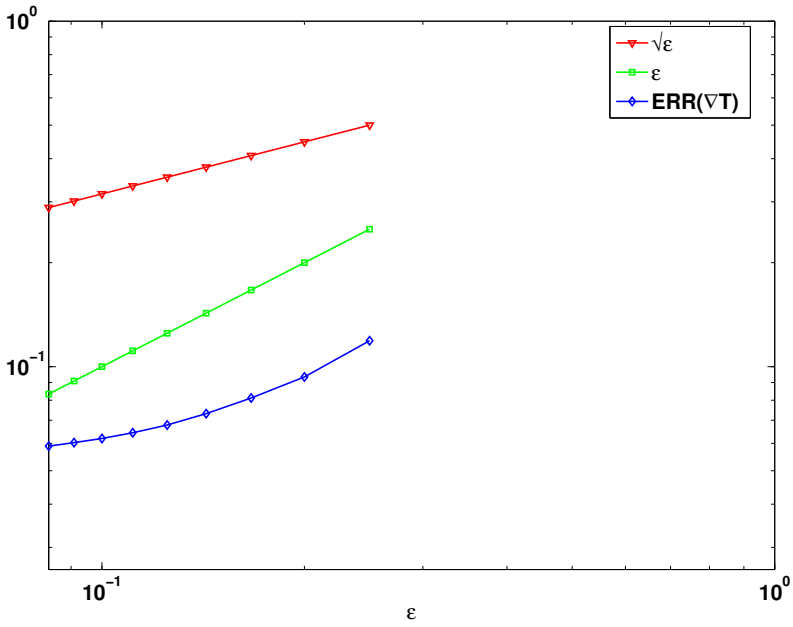

Figure 6.20: Relative error on the temperature gradient as a function of ϵ for $\boldsymbol{V} = (0.05, 0, 0)$cm/s.

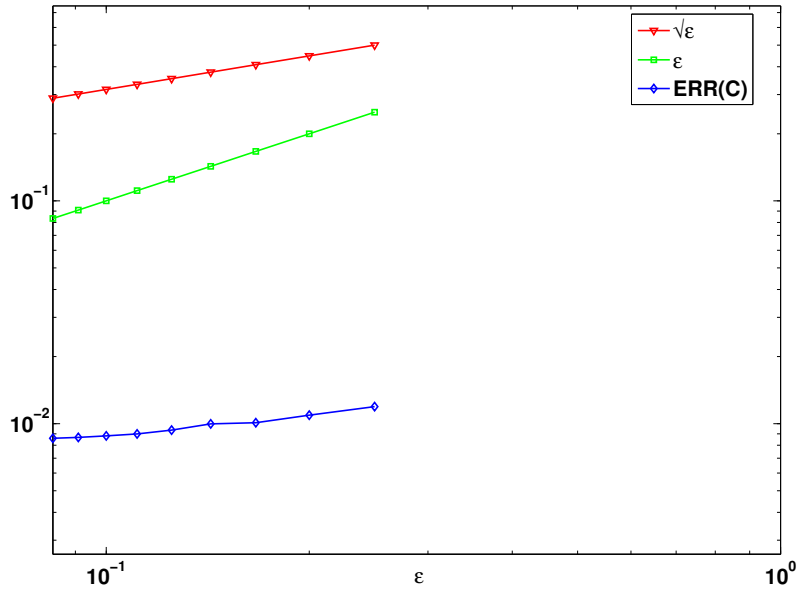

Figure 6.21: Relative error on the concentration as a function of ϵ for $\boldsymbol{V} = (0.05, 0, 0)$cm/s.

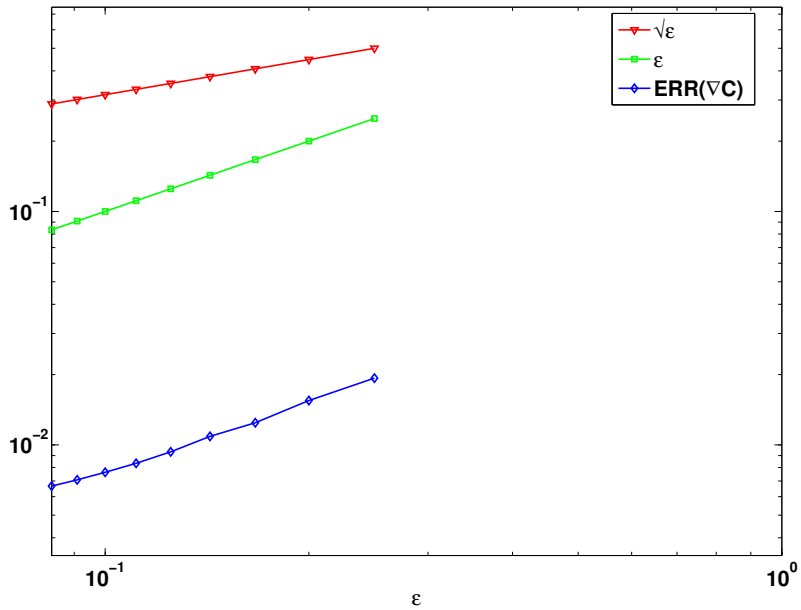

Figure 6.22: Relative error on the concentration gradient as a function of ϵ for $\boldsymbol{V} = (0.05, 0, 0)$cm/s.

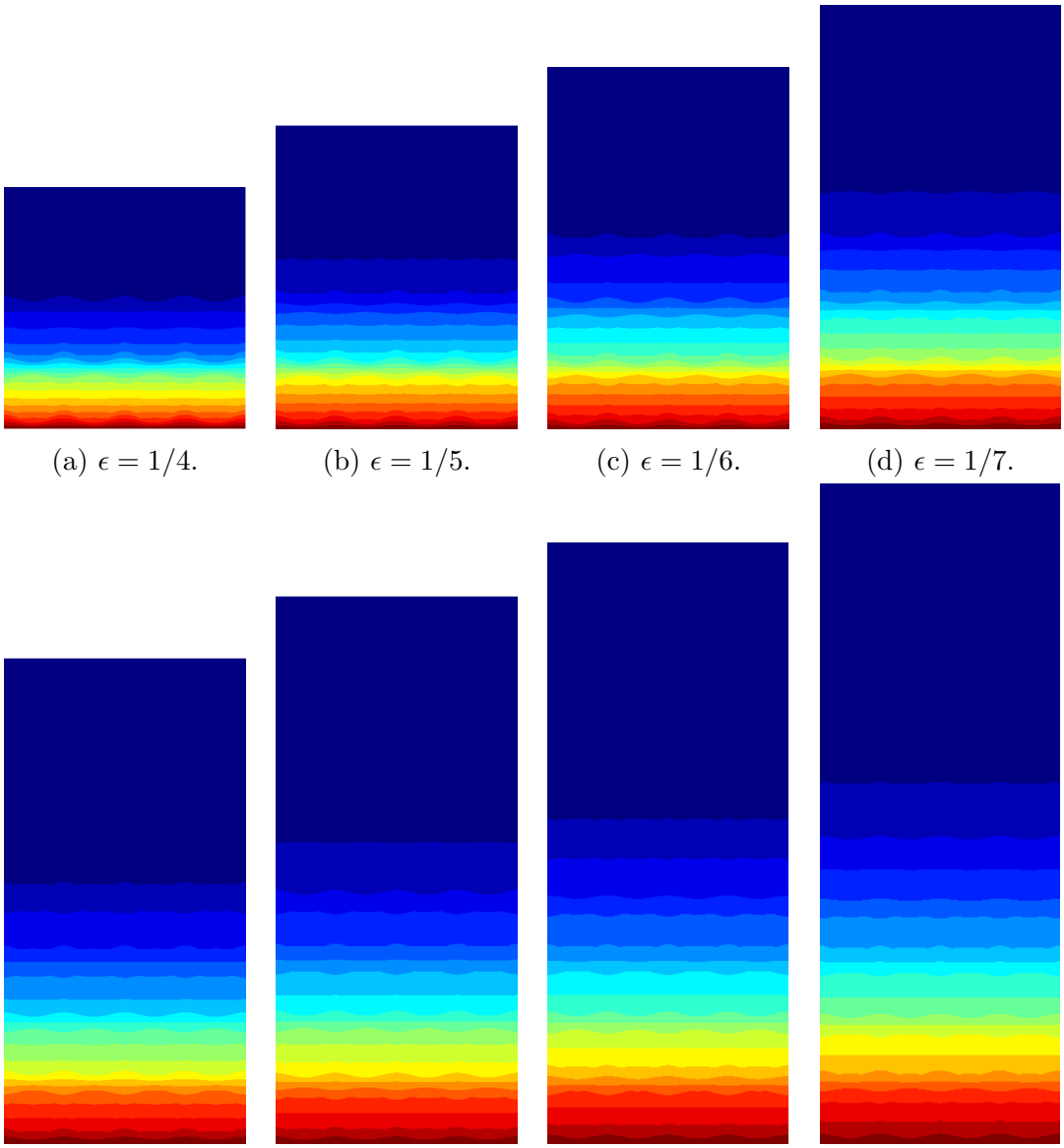

(a) $\epsilon = 1/4$. (b) $\epsilon = 1/5$. (c) $\epsilon = 1/6$. (d) $\epsilon = 1/7$.

(e) $\epsilon = 1/8$. (f) $\epsilon = 1/9$. (g) $\epsilon = 1/10$. (h) $\epsilon = 1/11$.

Figure 6.23: Collage of temperature profiles for distinct values of ϵ, using the one directional scheme of cell addition. Cells are added at each successive simulation corresponding to a value of ϵ. The top and bottom of the domain represent the y_1-direction, from which cells are added while the y_2-direction is fixed.

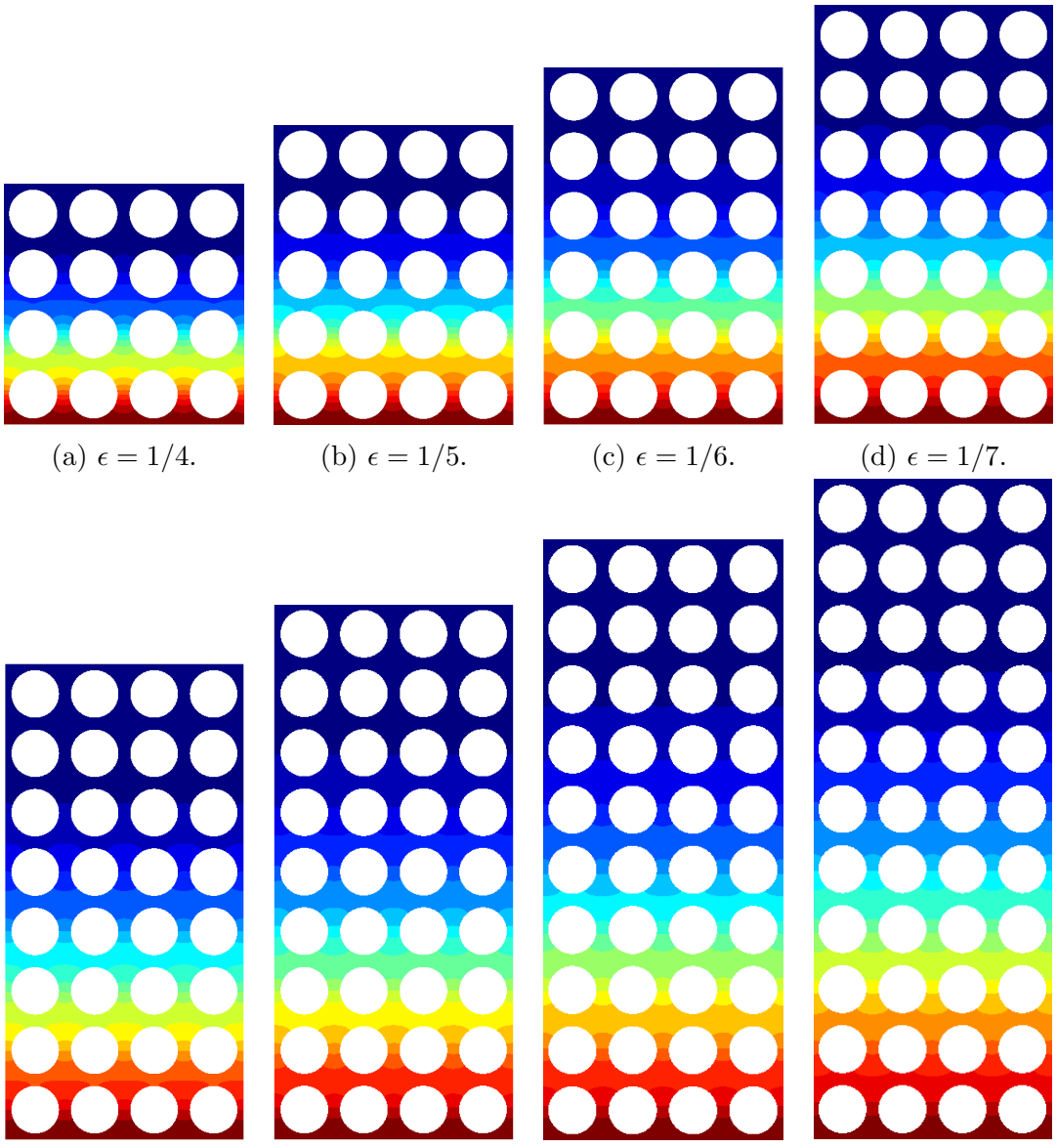

(a) $\epsilon = 1/4$. (b) $\epsilon = 1/5$. (c) $\epsilon = 1/6$. (d) $\epsilon = 1/7$.

(e) $\epsilon = 1/8$. (f) $\epsilon = 1/9$. (g) $\epsilon = 1/10$. (h) $\epsilon = 1/11$.

Figure 6.24: Collage of concentration profiles for distinct values of ϵ, using the one directional scheme of cell addition.

6.6 Summary

In this chapter, we have presented numerical simulation results to follow the theoretical estimates established in Section 4.6.1 of Chapter 4. The method used in this chapter is due to Auriault et al. (2009); Allaire and El Ganaoui (2009); Allaire et al. (2010), where a microscopic viewpoint is used in order to show numerically the convergence rate of a homogenization process. In this thesis, we developed two reconstruction algorithms, which are based on different treatment of the cell solutions. The first algorithm is based on partitioning of a discrete domain $\widehat{\Omega}_h$ into subgrids $\widehat{\Omega}_{h,i}$ of unit size, such that the field variables and their gradients can be reconstructed on the reduced grid, making it possible to reconstruct solutions of the corrector terms T^1 and C^1 at the subgrid level. This process generally is not so efficient, as it places high demands on the memory and CPU time. Based on this problem, a second algorithm was formulated. The latter improves on the problems encountered with the first algorithm. For this, we only require to generate a lattice of copies of the cell solutions to periodically cover the computational domain $\widehat{\Omega}$.

In this chapter, we focused on the reconstruction of an approximate homogenized solution in order to recover the oscillations in the microscopic model, and hence show the convergence rate of our homogenization process. By doing so, we showed that the pore scale description detailed in Chapter 2 converges strongly to the homogenization results in Chapter 3. The error estimates were established in the relative L^2-norms for the variables and their gradients. Distinct scenarios were also considered. In the first case, we considered the model problems-heat and mass transport equations-separately by studying the system without the nonlinear reaction terms. The results of our numerical computations in this case coincide with the theoretical estimates established in Chapter 4, and further recovers the microscopic behavior, at the first level of approximation (e.g. $T^\epsilon(t,x) \approx T^0(t,x) + \epsilon T^1(t,x,\frac{x}{\epsilon})$). We also observed some shortcoming of the homogenization method-the approach seems to fail for high flow velocities. This is also observed from the results of the coupled nonlinear system with and without convection, in which we investigate the effect of simultaneous convection and reaction on the convergence rates (see Section 6.5). It was concluded that within the limit of a suitable flow regime, the predictions of our numerical results are consistent with the theoretical estimates in Section 4.6.1; much in the spirit of Fatima et al. (2012).

As a future consideration, we expect that the convergence rates detailed in this chapter can be extended for the case of anisotropic effective tensors since the difference between isotropic and anisotropic tensors is reflected on the form of the inclusion considered. While the analysis of this chapter has been restricted to the case of MCI model, the limit models (HCI and WCI) to the MCI model can also be treated similarly without much adjustment to the procedure presented here. Our numerical algorithms have only been tested on two-dimensional problems, and may require further improvements in order to handle three-dimensional geometries. We also point out that provided the scale parameter in the

asymptotic expansion is not so small, higher order terms, and hence the reconstruction procedure remains important. In this case, we expect a higher approximation of the problem. Otherwise, the inclusion of higher order terms become insignificant.

Chapter 7

Pattern formation in reverse smoldering combustion of isotropic porous medium

In this chapter[1], the macroscopic equations developed in Chapter 3 are investigated in a framework of reverse (counterflow) smoldering combustion of thin isotropic porous media. The isotropic behavior of the media is reflected on the calculated effective diffusion and thermal conductivity matrices. We recall that we have derived the distinct models based on thermal conductivity contrast. In a first consideration, the behavior of fingering patterns are studied here strictly through the effective thermal (diffusion) conductivity tensor for the distinct models. This implies that the control parameter in the rescaled system, e.g. the Lewis number, which relates the strength of thermal diffusion to that of molecular diffusion, is considered a *fixed* parameter. In this case, the rescaled models result to a characteristic length scale that is defined in terms of the thermal diffusivity. This will allow for treatment of distinct thermal conductivity models in order to ascertain their disparities, namely, of time of ignition, pattern behavior, etc. and the significance of heat transfer in counterflow smoldering. On the other hand, the ignition mechanism will depend on appropriately chosen parameter space for the pre-exponential kinetic factor, valid for numerical study of the distinct models, i.e. we do not require an external heat source for ignition in this case. Specifically, this approach gives a dependence of the kinetic factor on the domain size. We will refer to the pattern behavior emanating from this consideration as *fingering patterns of the first kind* since they arise merely as an attempt to justify the implication of the conductivity contrast to pattern behavior based on *effective Lewis number*. In subsequent sections, we discuss the fingering behavior with respect to the distinct models by controlling respectively the gas flow rate and the heat flow through the Péclet number and the Lewis number. In this case, the Lewis number is considered a *free* parameter, and hence

[1]Part of the results included in this chapter have been published in Combustion Theory and Modelling, 17(2),2013.

the mechanism of thermal-diffusion instability of flames[2] suffices. However, the instability is mainly controlled through the Lewis number, while the Péclet number only "conditions" the patterns for the distinct fingering regimes. We refer to such fingering patterns as *fingering patterns of the second kind* since they arise due to the mechanism of thermal-diffusion instability.

The objective of the present chapter is to use the derived macroscopic (homogenized) models to verify most of the fingering regimes exhibited by the experimental observation of two-dimensional fingering instability of a filter paper sample detailed in Zik and Moses (1999). While the presently studied system is distinct from the system studied in the experiments, we aim to show, by using the mechanism of thermal-diffusion instability, a close resemblance of our pattern-forming dynamics to the diffusional instability exhibited in the fingering patterns reported in the fundamental work of Zik and Moses (1999), see also (Zik and Moses, 1998; Zik et al., 1998). The present discussion also follows the experimental observations of finger-like patterns in microgravity presented by Olson et al. (1998). In this chapter, we focus on isotropic microstructures, which eventually result to isotropic effective diffusion coefficients. We point out that this consideration is consistent with the structure of material (i.e. requirement for a uniform material) used for measurement purposes in the experiment. In addition, the major mechanism of heat transfer is conduction, and we focus more on adiabatic combustion.[3] Besides investigating various regimes of the fingering instability, we are interested in understanding the contribution of the conductivity contrast on heat transfer processes related to the distinct models; and the effect of heat release on the characteristic finger width of the fingering patterns.

7.1 Macroscopic model

We recall the functional form of the macroscopic equations in the simple case of isotropic effective parameters:

$$\begin{aligned} \mathcal{C}^{\text{eff}}\frac{\partial T}{\partial t} - \lambda^{\text{eff}}\nabla^2 T \pm \phi\mathcal{C}_{\text{g}} v\cdot\nabla T &= \phi^s Q W(T,C), \\ \phi\frac{\partial C}{\partial t} - D^{\text{eff}}\nabla^2 C \pm \phi v\cdot\nabla C &= -\phi^s W(T,C), \\ \frac{\partial \mathcal{R}}{\partial t} &= W(T,C). \end{aligned} \tag{7.1}$$

[2]Thermal-diffusion instability refers to a combustion instability that is based on two competing transport processes-the transport of reactants and the transport of heat. The transport of reactants has a destabilizing effect, while the transport of heat has a stabilizing effect on the combustion wave (see Sivashinsky, 1983; Pelce and Clavin, 1982, e.g.).

[3]A combustion process in which there is no consideration to heat exchange to the environment.

System (7.1) is analyzed in its dimensionless form by introducing some characteristic units based on the effective equations and the typical values given in Table A.1.

$$\begin{aligned} \tilde{C} = \frac{C}{C_0}, \tilde{\mathcal{R}} = \frac{\mathcal{R}}{R_0}, \tilde{T} = \frac{T}{T_\mathrm{b}}, \tau = t\frac{U^2}{\alpha}, \tilde{x} = \frac{x}{l_{th}}, \\ N = \frac{T_\mathrm{a}}{T_\mathrm{b}}, \tilde{A} = \frac{\phi^s A\alpha}{U^2 N e^N}, \tilde{W} = \frac{W\alpha}{U^2}, l_\mathrm{th} = \frac{\alpha}{U}, \end{aligned} \tag{7.2}$$

where C_0 and R_0 are respectively the initial/unburnt concentrations of the deficient oxidizer and the fuel sample. α is the effective thermal diffusivity defined as $\alpha := \lambda^{\mathrm{eff}}/\mathcal{C}^{\mathrm{eff}}$ and $T_\mathrm{b} := QC_0/C^{\mathrm{eff}}$ is the temperature of combustion product, U is a virtual velocity of a uniformly propagating plane reaction front. N is a dimensionless activation temperature, $\tilde{W}$ is a dimensionless reaction rate and the parameter $\tilde{A}$ is introduced to normalize the virtual velocity of normal propagation to one (Matkowsky and Sivashinsky (1978)). In terms of the quantities introduced, the dimensionless system is given by

$$\begin{aligned} \frac{\partial \tilde{T}}{\partial \tau} - \nabla^2 \tilde{T} \pm \phi \Lambda Pe \cdot \nabla \tilde{T} = W(\tilde{T}, \tilde{C}), \\ \phi \frac{\partial \tilde{C}}{\partial \tau} - \frac{1}{Le}\nabla^2 \tilde{C} \pm \phi Pe \cdot \nabla \tilde{C} = -W(\tilde{T}, \tilde{C}), \\ \frac{\partial \tilde{\mathcal{R}}}{\partial \tau} = H_R W(\tilde{T}, \tilde{C}), \end{aligned} \tag{7.3}$$

where

$$W = \tilde{A} N \tilde{C} \exp\{N(1 - 1/\tilde{T})\}.$$

In (7.3), $Pe = (vl_\mathrm{th}/\alpha, 0)$ and $Le = \alpha/D^{\mathrm{eff}}$ are respectively the effective Péclet number and Lewis number. $H_R = C_0/\phi^s R_0$ and $\Lambda = C_\mathrm{g}/C^{\mathrm{eff}}$ represent dimensionless coefficients. System (7.3) is solved numerically using the Streamline Upstream Petrov–Garlekin (SUPG) scheme. The time integration was performed using an implicit BDF solver. The set of equations (7.1) and (7.3) are functionally identical to Eqs. (25), (26) of Kagan and Sivashinsky (2008) provided that the derived effective properties in (7.1) can be associated with those in Eqs. (25), (26) of Kagan and Sivashinsky (2008). The system (7.3) was solved using the typical values in Table A.1. A feature of the presented numerical results lies on the chosen characteristic length and range of chosen Péclet numbers.

Remark 7.1.1. *In systems* (7.1) *and* (7.3)*, we have generalized the sign of the convective term simply to emphasize the fact that the gaseous oxidizer can be passed either from the downstream or the upstream end. For the problem of reverse smoldering, the ignition is always located opposite to the direction of the infiltrating gaseous oxidizer.*

7.2 Fingering patterns of the first kind

We recall that the homogenization process allows us to investigate the macroscopic behavior of the effective homogenized equations as the limit of the pore scale description. This

description, however, poses a formidable challenge for combustion applications due to the distributed nature of the reaction rate, the presence of highly oscillating coefficients, and the dependence of the system on $\epsilon \ll 1$ (cf. Section 1.3 of Chapter 1 and also Figure 1.4). In this section, the macroscopic equations with effective diffusion tensors are investigated in a counterflow smoldering combustion scenario, in which the control (free) parameter is the Péclet number. We distinguish different problems by relating the characteristic length scale of the domain with the thermal diffusion. This invariably places a restriction on the choice of kinetic factor, A, for the distinct models. The models[4] are functionally similar, except that their diffusion tensors are different. Unlike the MCI and HCI models, the WCI heat model has a distributed temperature[5]. However, we focus on the limiting case of this problem corresponding the choice of the ratio of thermal conductivity $\mathcal{O}(\epsilon)$. In our numerical simulation, the value of the dimensionless pre-exponential factor A, was chosen within the range $[1 \times 10^2 - 10^4]$, and all other parameters correspond to the typical values given in Table A.1. We point out that in all cases considered, the combustion process is incomplete. Figure 7.1 depicts the two-dimensional structure of the smolder front; the location in space, and at each given time, for the flame can be identified at the reaction region that is delineated within a limited vicinity of tips of the fingers. This region is traced by darker shades in Figure 7.1 (d), where oxygen is fully consumed as the front advances. Behind (or along) the fragmented advancing flame front, there is no reaction, but only a trace of the heterogeneous charred region (see Figure 7.1 (b)). The uncharred area (i.e. the unburnt reactant region between the charred (dark shaded) region) of the pattern represents the quenched parts of the fragmented reaction zone and smoldering is only intensified at the tips of the fingers where the oxidant is fully consumed.

7.2.1 Effect of the Péclet number

In this subsection, we focus on a fingering regime that is conditioned by the effective Lewis number represented by

$$Le = \frac{\lambda^{\text{eff}}}{(C_{\text{g}}\phi + C_{\text{s}}(1-\phi))D^{\text{eff}}}, \tag{7.4}$$

where λ^{eff} and D^{eff} correspond respectively to the values of the effective thermal conductivity and diffusivity tensors derived from the homogenization procedure. In (7.4), we see that the Lewis number depends on the porosity of the medium through the heat capacity. The emerging fingering instability is controlled through the Péclet number, Pe. At a relatively low blowing rate, the char pattern emerged as *sparse fingers* that are strictly distinct from each other (Figure 7.2). The patterns show a low contrast in the spatially heterogeneous *conversion depth*. The conversion depth describes the intensity of the solid fuel conversion to char. Darker shades in Figure 7.2(a)-(b) represent regions of the pattern with high conversion intensity or more clearly, this region is shown in lighter shades in Figure 7.2(c)-(d).

[4]We often refer to the MCI, HCI and WCI models simply as the models.

[5]The temperature is not in equilibrium. It is distributed between the gas phase and solid phase. In other contexts, we say that the system exhibits memory effects.

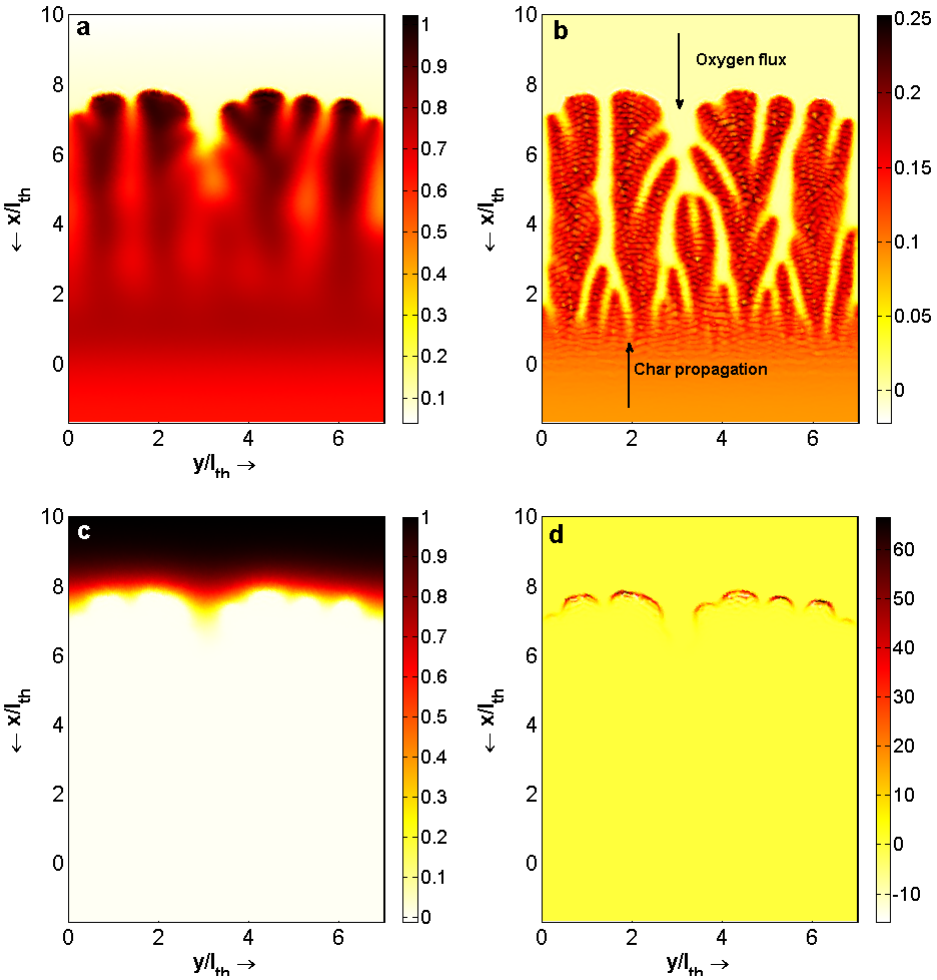

Figure 7.1: Spatial profiles of the flame structure: (a) temperature (b) char (c) concentration (d) heat release rate. Solution of the HCI model for $Pe = 10, Le = 0.09$. Ignition at bottom, char propagation from bottom to top, gas inlet from top. The spatial axis are in units of the thermal length of the flame, l_{th}.

At the vicinity of the tips which are indicated in lighter shades, the *hotspots* emerge prior to extinction. These are points of higher temperature values in the numerical simulations. The maximum temperature at an active finger may also alternate from one finger to another due to the localized reaction at the reaction zone. In this adiabatic consideration, it can be seen that the visibility of the patterns is impaired by the inability of the fingers to lose heat, thus the persistence of fingers with weak hotspot. The latter may also contribute to the eventual widening around the tip of fingers closest to the oxygen source. Consequently, the fingers shield adjacent fingers, i.e. fingers with weak hot spots, from the oxygen supply. A further increase in the Péclet number, i.e. $Pe = 17$ increases the contrast in conversion depth and the fingers *tip-split* (Figure 7.3).

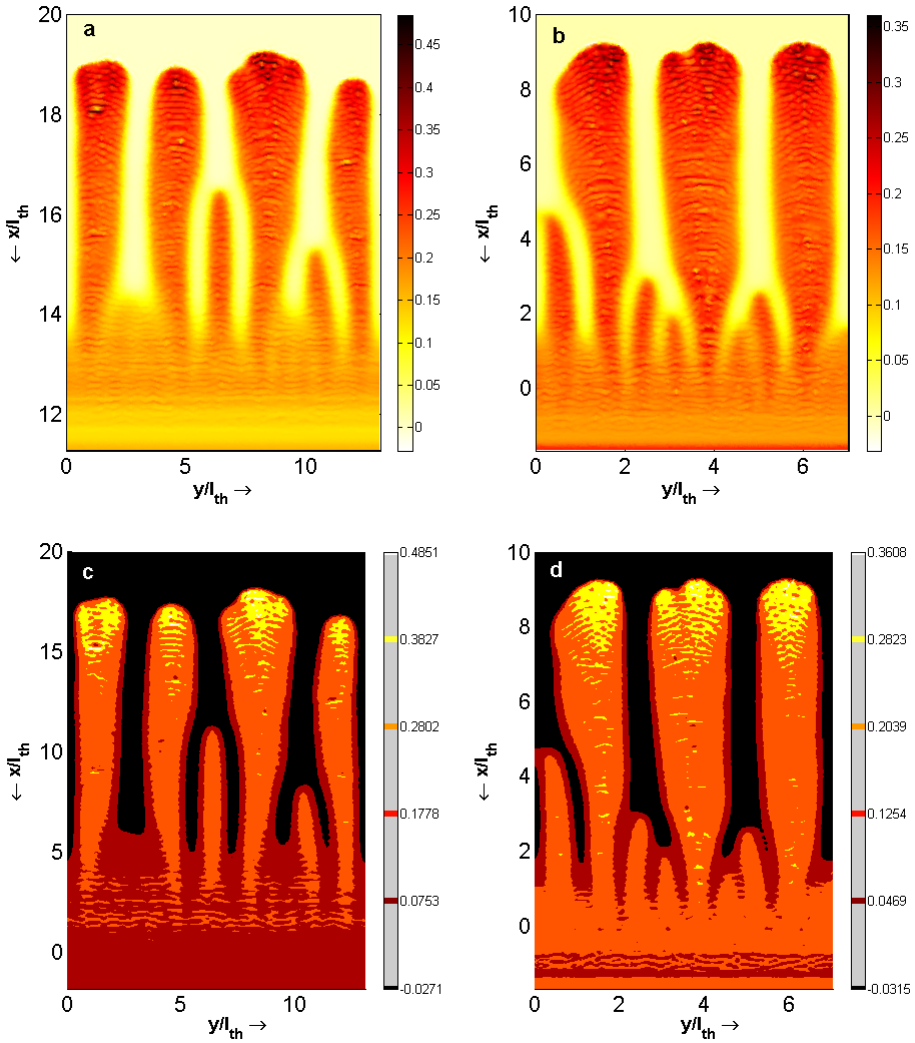

Figure 7.2: Spatial profiles of char pattern for (a) the MCI model at $Pe = 0.01, Le^{\text{eff}} = 0.01422, A = 0.27 \times 10^4$, (b) the HCI model at $Pe = 0.01, Le^{\text{eff}} = 0.026563, A = 1 \times 10^4$. The fingering patterns are sparse with no tip-splitting. (c)-(d) contour plots showing hot spots at the vicinity of the tips and regions of higher conversion depths (lighter shade).

7.2.2 Fingering behavior in weakly conductive materials

We investigate the behavior of the fingering patterns for the WCI model as the limit of weakly conductive materials, i.e. we neglect the memory term arising from the solid phase heat conduction because the conductive mechanism is dominated by the gas phase. We attempt therefore to explain the contribution of the conductive heat transfer to the behavior of fingering patterns arising from the WCI model since besides radiative heat mechanism, conduction is a major heat transfer mechanism for reverse smolder propagation. First, we

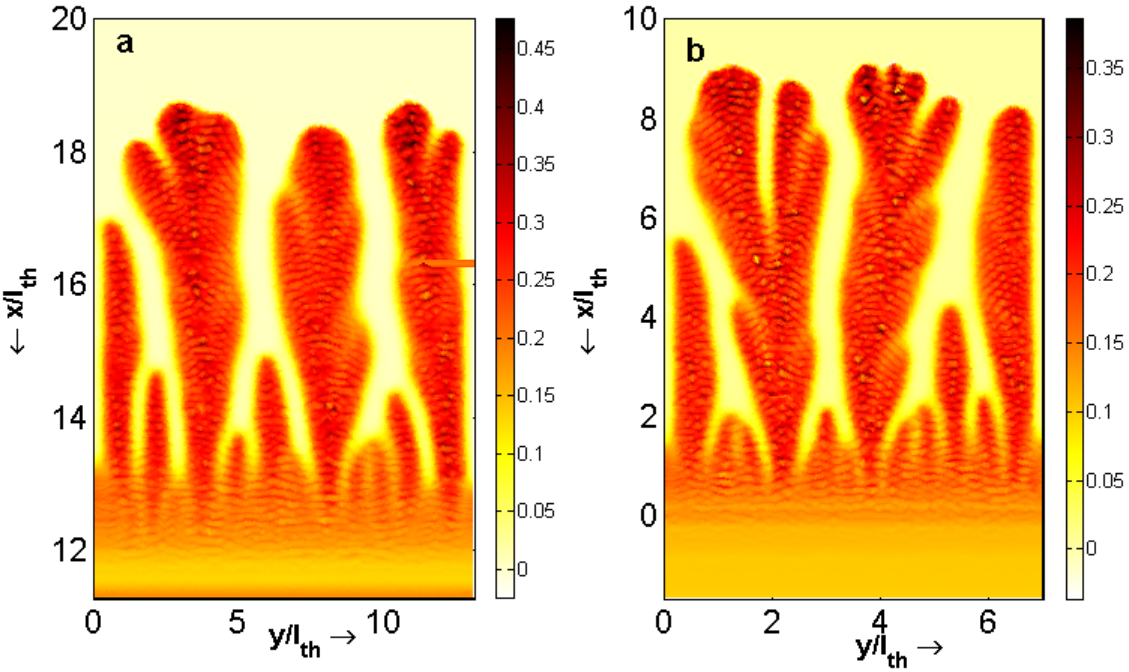

Figure 7.3: Spatial profiles of char pattern for (a) the MCI model at $Pe = 17, Le^{\text{eff}} = 0.01422, A = 0.27 \times 10^4$, (b) the HCI model at $Pe = 17, Le^{\text{eff}} = 0.026563, A = 1 \times 10^4$. Fingering patterns with tip-splitting and low conversion depth.

recall the temperature model for the WCI in its convolution form viz.

$$\mathcal{C}^{\text{eff}} \frac{\partial T}{\partial t} + \phi \mathcal{C}_{\text{g}} \mathbf{v} \cdot \nabla_x T + \partial_t (\zeta(t) * \partial_t T) = \lambda^{\text{eff}} \nabla^2 T + \phi^s Q(T, C), \quad x \in \Omega, t > 0, \tag{7.5}$$

where

$$\zeta(t) = \frac{8R^3}{\pi} \sum_{n=1}^{\infty} \frac{1}{n^2} e^{-\alpha_{\text{s}}(n\pi/R)^2 t}. \tag{7.6}$$

α_{s} is the solid phase thermal diffusion coefficient and R is the radius for the case of spherical inclusions. Assuming now the limiting case, i.e. $\alpha_{\text{s}} \to 0$, then (7.5) takes the form (7.1), as well as (7.3) in dimensionless form. At this point, the WCI model is functionally identical to the MCI and HCI models, except for the contrast in their thermal conductivities. This corresponds to the case in which the contrast of conductivity is of the order of magnitude $\mathcal{K} = \mathcal{O}(\epsilon)$.

7.2.3 Disparity in the models

Up to this point, the behavior of fingering patterns has been described for three distinct macroscopic combustion models, under a framework of fingering patterns of the first kind.

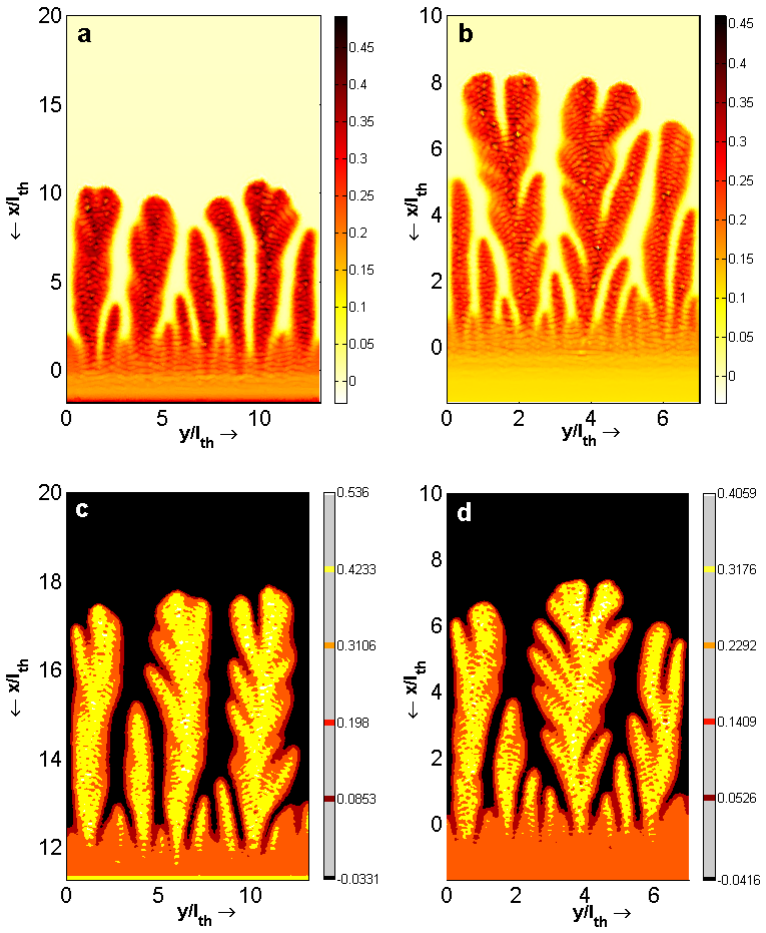

Figure 7.4: Spatial profiles of char pattern for (a) the MCI model at $Pe = 40, Le^{\text{eff}} = 0.01422, A = 0.27 \times 10^4$, decrease in the spatial extent of the front, (b) HCI model at $Pe = 40, Le^{\text{eff}} = 0.026563$. Patterns with characteristic features of tip-splitting and branching. (c) fingering state at $A = 0.23 \times 10^4$ for the MCI model, (d) fingering state at $A = 0.85 \times 10^4$ for the HCI model. In all cases computational time decreases with an increase in A.

A distinctive line of argument has been to relate the thermal conductivity contrast with the fingering instability, in order to ascertain the importance of the conductive mechanism in reverse smolder, and to what extent heat conduction influences structure formation in combustion. The effective conductivity enters the nondimensionalized forms of the macroscopic equations through the Lewis number. Thus, the purpose of this subsection is an attempt to clarify the consequence of the contrast in the models to the behavior of the developed fingering state. Figures 7.4(a)-(b) indicate fingering patterns at $Pe = 40$, respectively for the MCI model and the HCI model. In Figure 7.4(b), the pattern is fully developed with the characteristic features of tip-splitting, increase in conversion depth and *branching* of fingers. Branching of fingers describes the splitting of a sole finger into multiple fingers.

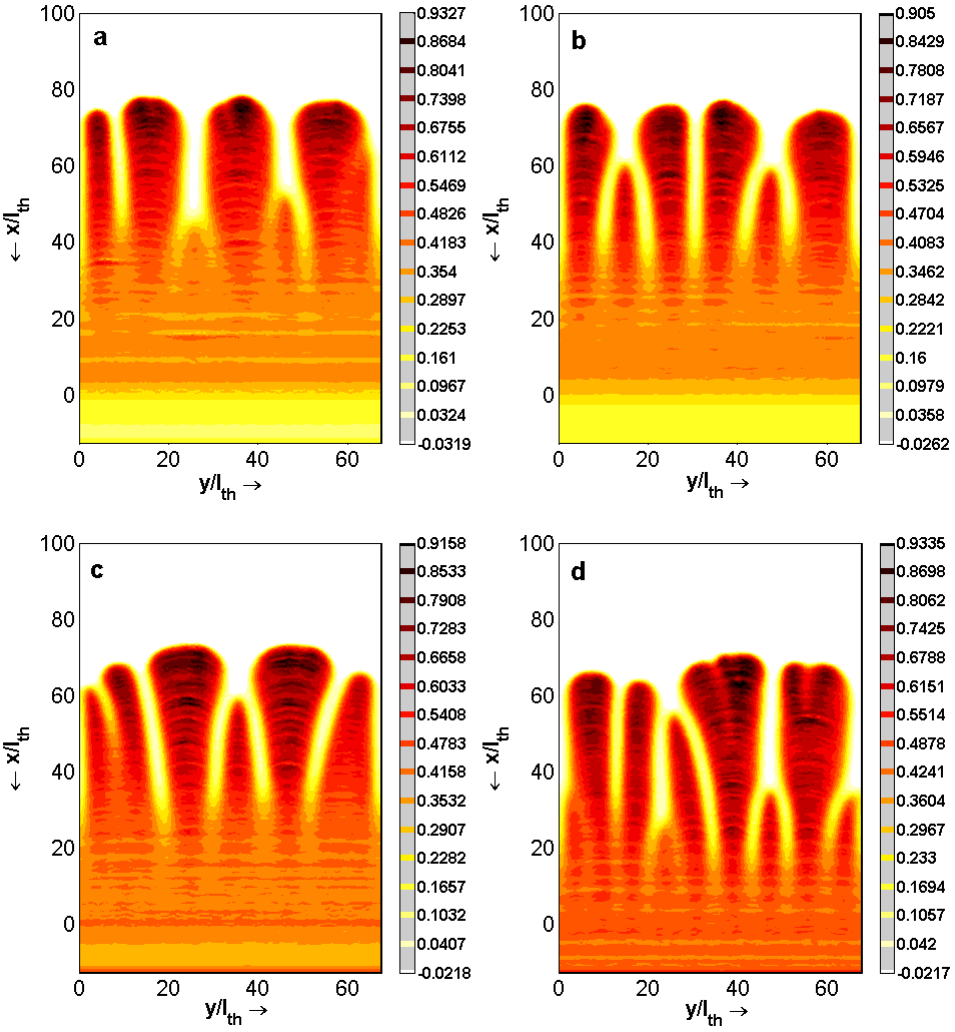

Figure 7.5: Spatial profiles of char pattern for the WCI model at (a) $Pe = 0.01$; (b) $Pe = 1$; (c) $Pe = 5$ (d) $Pe = 10$. From (a)-(d), $Le^{\text{eff}} = 0.002755$ and $A = 10^2$. The thermal diffusivity in this case is low, hence the domain size is larger (in units of l_{th}) compared to the MCI and HCI models. The low thermal diffusivity in WCI model leads to substantially higher temperatures in the reacting regions, resulting into high fuel conversion inside the fingers (darker shades within the fingers). The patterns also show suppressed ability to tip-splitting at all Pe values due to the production of smaller number of hot spots.

However, these features are not substantial for the MCI model (see Figure 7.4(a)). Likewise in Figure 7.5, the patterns show suppressed ability to tip-splitting due to smaller number of hotspots. A reason for the qualitative difference in the three models can be seen from their sensitivity to the choice of the dimensionless frequency factor A which depends invariably on the characteristic length of the computational domains. For instance, ignition does not

occur for some choice of A in the models. In the WCI model, the value of the frequency factor is small compared to the minimum value sufficient for the onset of ignition for the MCI and HCI models. This implies that the time of ignition is higher in the WCI model compared to the ignition times for the MCI and HCI models. It is lowest in the latter. In the numerical simulations, the higher value of the frequency factor in the HCI model, relative to the other models, affects the solution viz.

(i) decreases the time required for onset of ignition, and hence faster front velocities,

(ii) improves the strength of the convective transport, thus enhancing the visibility of the patterns,

(iii) increases the heat release rate, and hence the sensitivity of fingers to tip split due to increased number of hot spots.

From (iii), the higher heat release rate in the HCI model leads to increased number of localized hotspots due to the ability of the front to release heat. The excess heat at the reaction zone promotes the combustion process and the ability of single fingers to tip split and develop into branches. This behavior is not pronounced in the MCI model, which shows a higher tendency to tip split and an increase in the spatial extent of the reaction zone at a frequency factor of $A = 0.23 \times 10^4$ (see Figure 7.4(c)). Figure 7.4(d) indicates the pattern behavior at a frequency factor $A = 0.85 \times 10^4$ for the HCI model. (i) is consistent with other studies in combustion processes (Aly, 1990; Leach et al., 1990). (ii) follows from the fact that a robust reverse combustion and convective transport may enhance the visibility of patterns (see Lu and Yortsos, 2005a). The lower thermal conductivity exhibited by the WCI model leads to much sharper temperature gradients near the tip, hence to the formation of smaller number of propagating hotspots. The result is reduced ability for ignition and suppression of tip-splitting. The low thermal conductivity also result to substantially higher temperatures in the reacting regions, thus causing intense fuel conversion inside the fingers. This observation is consistent in other studies for materials of low thermal conductivity (Lu and Yortsos (2005a)). Also, the patterns are sharper towards the tips of the fingers, but the visibility of the patterns is impaired in the onset region.

7.3 Fingering patterns of the second kind

In this section, the fingering behavior is treated in terms of thermal-diffusion instability. While we have used in the previous section the effective Lewis number arising from the effective diffusion tensors to ascertain the behavior of the different models, by varying only the Péclet number, the Lewis number is used presently as the main controlling parameter in order to investigate the emergence of distinct fingering states. However, the Péclet number is also an important parameter in the model as it conditions the fingering patterns in the distinct fingering regimes. Thus, the three most important fingering regimes-connected, sparse and tip-splitting regimes-are currently investigated.

7.3.1 Effect of the Lewis number

The macroscopic models describe, in an effective sense, a one temperature gas-solid system for the coupled two temperature microscopic model. Unlike the results presented in the previous subsection, the behavior of system (7.3) is analyzed by considering the Lewis number as a free parameter. This allows us to examine the fingering behavior based on the mechanism of thermal-diffusion instability. According to Olson et al. (1998), the Lewis number is not the controlling transport mechanism for the fingering behavior. However, in the models discussed presently, we point out that it introduces some characteristic features to the fingering behavior. It relates heat transport to mass transport. Thus, it can characterize different flow regimes in a system with simultaneous convective mass and heat transport. The focus of this subsection is to show the close resemblance of the mechanism of the diffusive instability (Zik and Moses (1999); Olson et al. (1998)) to the well-studied thermal-diffusive instability occurring in low Lewis number premixed gas flames. At a very low blowing rate, the effective oxygen mass transport is dominant, and hence the Lewis number is close to a value that is much smaller than unity ($Le \ll 1$). Figure 7.6(a) illustrates the result of fingering pattern for the HCI model at $Pe = 0.01$. In this regime, convective heat transport is suppressed by an order of 10^{-6}. Specifically, $\phi\Lambda Pe \sim 10^{-6}$. The fingering pattern shows a steady state of elongated fingers with no tip-splitting, but sparse fingering in the sense of $d/w \gg 1$ (Zik and Moses (1999)) did not emerge. Here, d represents the distance between fingers and w, the finger width. The emergence of such steady state regime of sparse fingers with $d/w \gg 1$ is presented in (Ikeda and Mimura (2008); Lu and Yortsos (2005a)), but in a nonadiabatic situation where the effect of heat losses conditions the state of the emerging fingers. In Figure 7.7(a)-(c) and Figure 7.8(a)-(c), the flow rate is moderate and the development of fingering patterns with characteristic features of tip-splitting is substantial. The spacing between the fingers can be controlled by varying the Lewis number, i.e. an increase in the strength of the convective flux decreases the spacing between fingers. On the other hand, the inlet velocity or dimensionless Péclet number affects the development of the pattern. In Figures 7.7 and 7.8, it is evident that the Pe changes the relative spatial extents of the pattern. In the high Pe limit, however, the topology of the fingers is very dense and the process may extinct. It is also clear that some regions of the pattern also exhibited *screening effect* (Zik and Moses (1999)). Such screening of fingers by adjacent fingers that are close to the oxygen source causes the screened fingers to stop growing and the tips of the screening fingers to split. The behavior of the patterns at large flow rates is shown in Figure 7.6(b) for the HCI model. This regime corresponds to a Lewis number close to unity (i.e. $Le = 1$). The result in Figure 7.6(b) indicates a stable planar front that advances without fragmentation of the reaction zone. The finger patterns combine together into an unbroken reaction front and no visible pattern is observed. This regime of connected front is also valid for Lewis number ranges which are much greater than unity. For example, in the analysis of Britten and Kranz (1985), the results predict stable patterns in an infinite effective Lewis number.

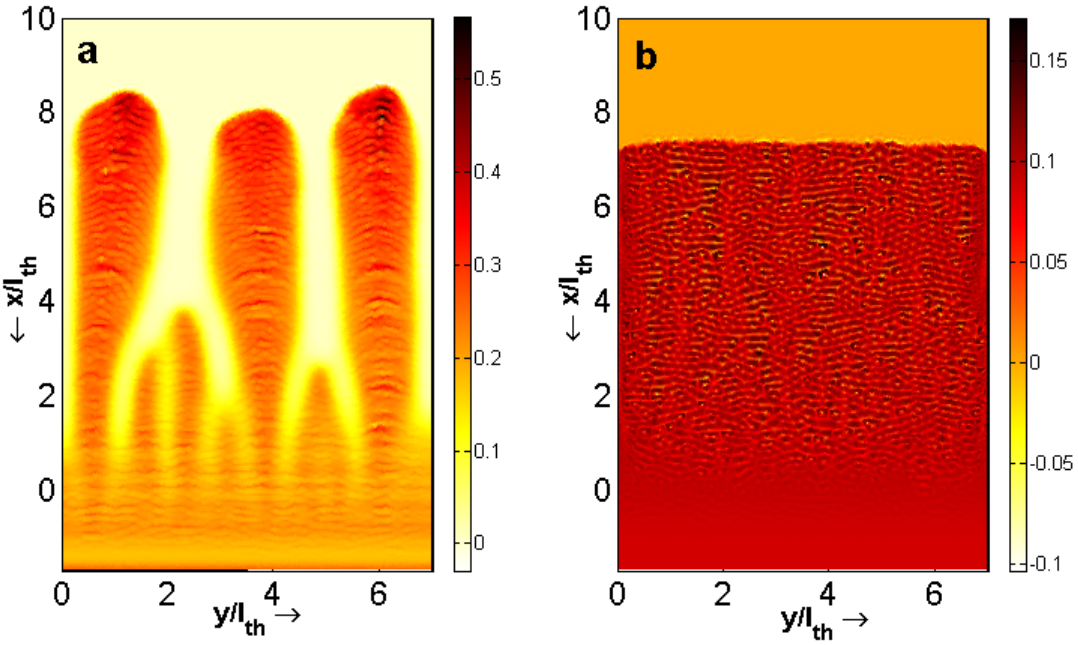

Figure 7.6: Spatial profiles of char patterns for the HCI model, showing (a) regime of constant fingers with no tip-splitting at $Pe = 0.01$ and $Le = 0.01$ (b) limit of large flows at $Pe = 10$ and $Le = 1$.

7.3.2 Fingering behavior in larger domains

We investigate the behavior of fingering patterns in a large domain by using the relationship between the thermal diffusivity and the characteristic length scale. The consideration presented in this section corresponds to the domain of the WCI model, in a thermal-diffusion instability framework, which is similar to the discussions of the previous subsection. We basically aim to verify the reproducibility of the patterns in larger domain sizes, in spite of decreasing strength of the pre-exponential factor, and hence the heat release rate. Under this consideration, we will see that while it is difficult to ignite the material at the vicinity of the outlet and longer time of ignition, the mechanism of thermal-diffusion instability remains adequate for reproducing the distinct fingering regimes of the previous subsection. In this case, the range of Pe values for the fingering behavior to manifest is much shorter than those of the MCI and HCI models. The visibility of the structure formation is, however, impaired in the regime of sparse fingers, otherwise the pattern behavior is considerably akin to those in smaller domains. The size of the domain depicted in Figure 7.9 is about 10 times larger than the size of the domain of the HCI model. The value of the pre-exponential factor is of magnitude 10^2 less than the value for the HCI model and about 10^1 less than that of the MCI model.

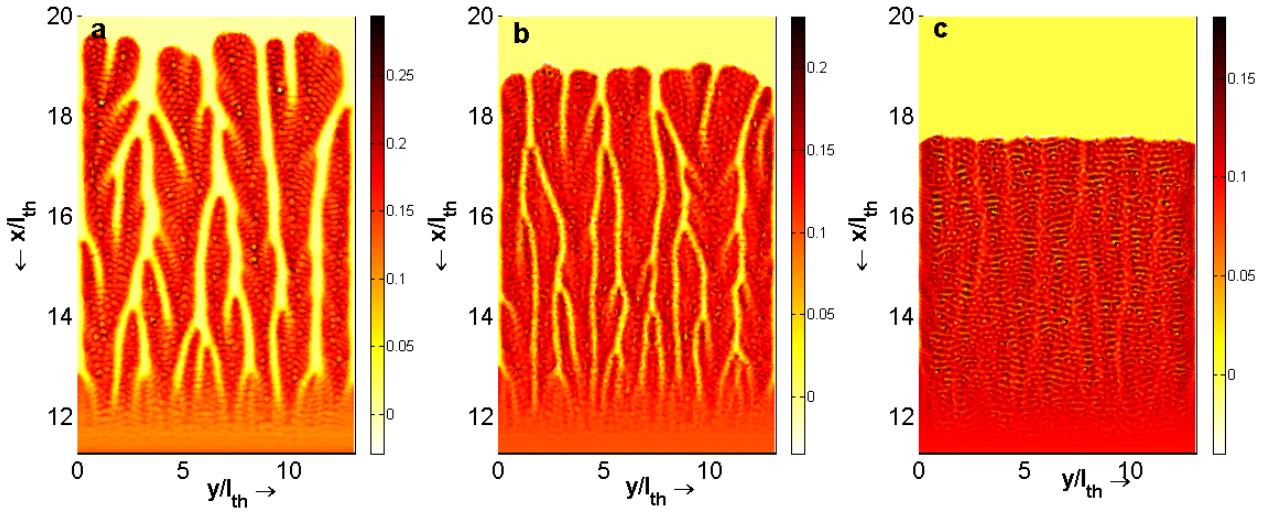

Figure 7.7: Collage of fingering patterns for the MCI model in the tip-splitting regime showing the variation of the distance between fingers at (a) $Le = 0.1$, (b) $Le = 0.25$, (c) $Le = 0.7$. In all cases, $Pe = 10$.

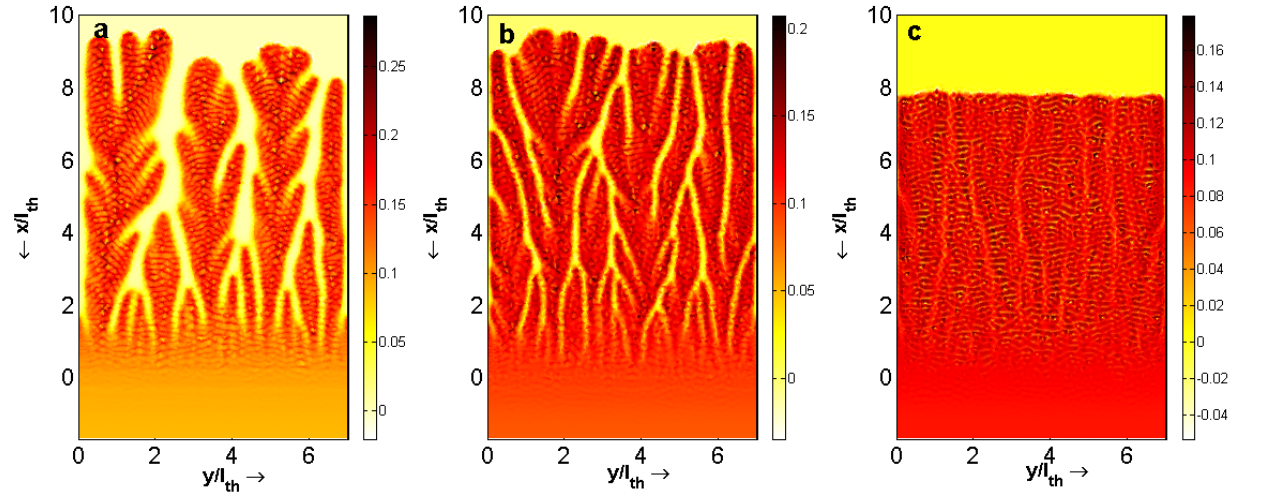

Figure 7.8: Collage of fingering patterns for the HCI model in the tip-splitting regime showing the variation of the distance between fingers at (a) $Le = 0.1$, (b) $Le = 0.25$, (c) $Le = 0.7$. In all cases, $Pe = 10$.

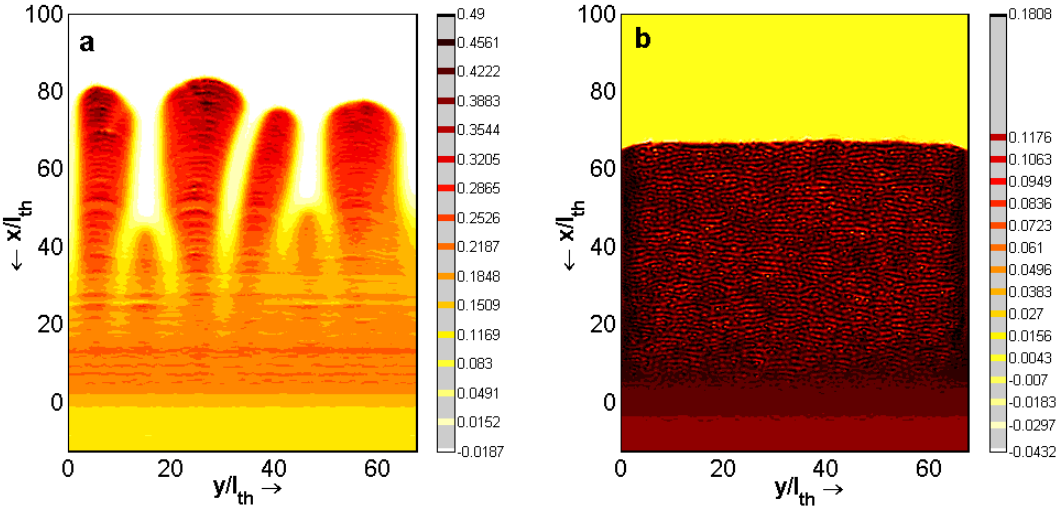

Figure 7.9: Spatial profiles of char patterns for the WCI model, showing (a) regime of constant fingers with no tip-splitting at $Pe = 0.01$, and $Le = 0.01$ (b) limit of large flows at $Pe = 3$ and $Le = 1$.

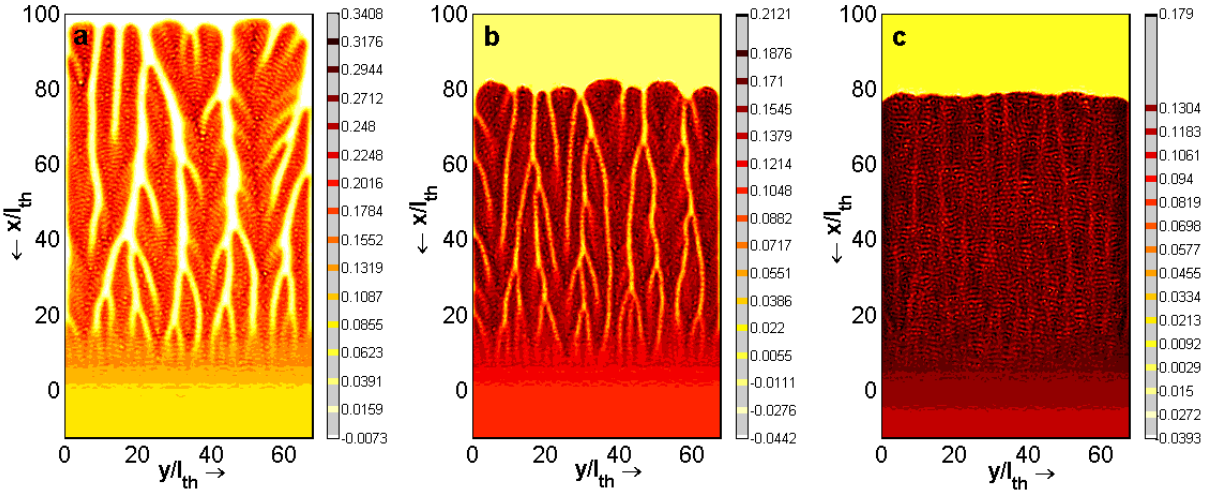

Figure 7.10: Collage of fingering patterns for the WCI model in the tip-splitting regime showing the variation of the distance between fingers at (a) $Le = 0.1$, (b) $Le = 0.25$, (c) $Le = 0.7$. In all cases, $Pe = 3$ and $A = 10^2$.

7.4 Ignition through an external heat source and effect of heat release rate

The ignition mechanism employed in the previous sections does not allow much freedom of choice for the kinetic factor since a constrained parameter range is required in order to initiate ignition. However, the advantage of initiating the combustion process through external heat sources is that we have more freedom of controlling the behavior of the fingering patterns through the kinetic coefficient. Also, ignition can be initiated at any location (or can be nonuniform) within the computational domain. Thus, the target of this section is to

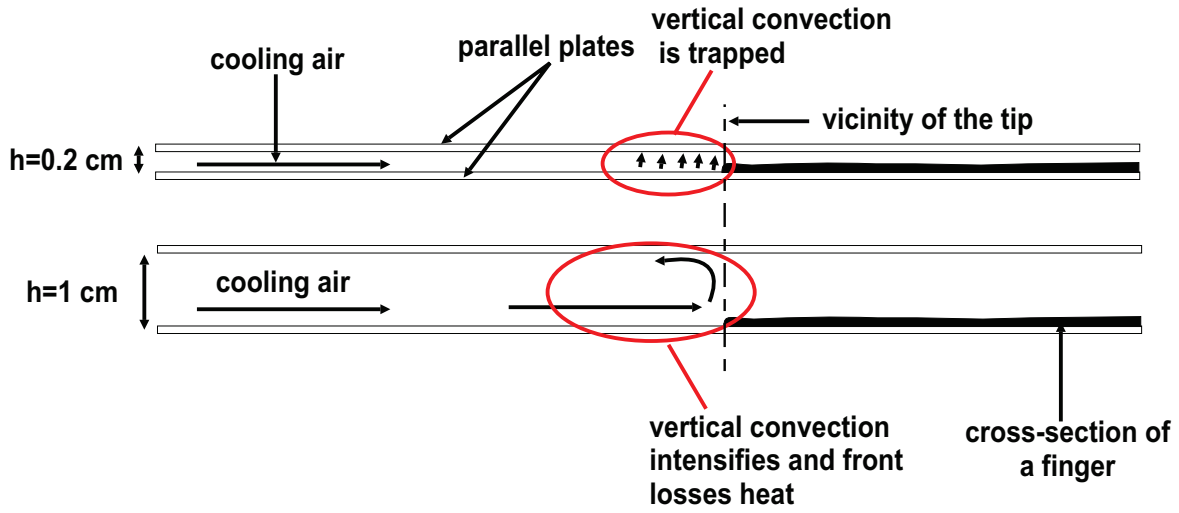

Figure 7.11: Schematic of the heat release mechanism in the experiment.

use external heat source to achieve ignition, and further attempt to investigate the effect of heat release rate on the characteristic finger width. According to Zik and Moses (1999), the finger width depends on the ability of the fingers to release heat. In order to verify the latter, Zik and Moses showed that the finger width can be related to the heat losses in the system by gradually introducing vertical convection through the spacing between plates of the Hele-Shaw geometry (see Figure 7.11); As the spacing increases the intensity of vertical convection increases, and heat in the vicinity of the tips are constantly cooled by the infiltrating gaseous oxidizer. This lowers the heat release rate, and hence the creation of smaller number of hotspots. The result is suppression of tip-splitting of the fingers. Further suppression of tip-splitting gives rise to the thickening of fingers. In the absence of a heat loss mechanism in the considered one-temperature adiabatic model, the strategy employed is to understand how forced suppression of the heat release rate contributes to the suppression of tip-splitting, and eventual thickening of fingers.

The external ignition source has the form of a piecewise function defined by

$$T_{ign}(t) = \begin{cases} T_1, & \text{if } 0 < t < t_i \\ T_0, & \text{otherwise} \end{cases}, \tag{7.7}$$

where T_0 and T_1 are constants. (7.7) is prescribed at the outlet end for the heat equation and a Dirichlet boundary $T = T_0$ is used at the inlet. For the concentration equation, convective boundary conditions are used at both ends, i.e.

$$\frac{\partial C}{\partial x} = 0, \qquad x = 0, L_x; t > 0. \tag{7.8}$$

Similar to the numerical results presented earlier, we use thermal-diffusive insulation conditions at the lateral boundaries. All numerical results are well within the tip-splitting regime conditioned at a Lewis and Péclet numbers of $Le = 0.1$ and $Pe = 10$. Figure 7.12 depicts numerical simulation results describing the effect of varying the pre-exponential factor A on the fingering patterns. As the value of A decreases, the heat release rate decreases, and results to the creation of smaller number of hotspots. The result is a reduction in the ability of the fingers to tip-split. Decreasing the value of A further gives rise to the widening of the fingers. This implies that the amount of heat released by the front influences the width of the fingering pattern.

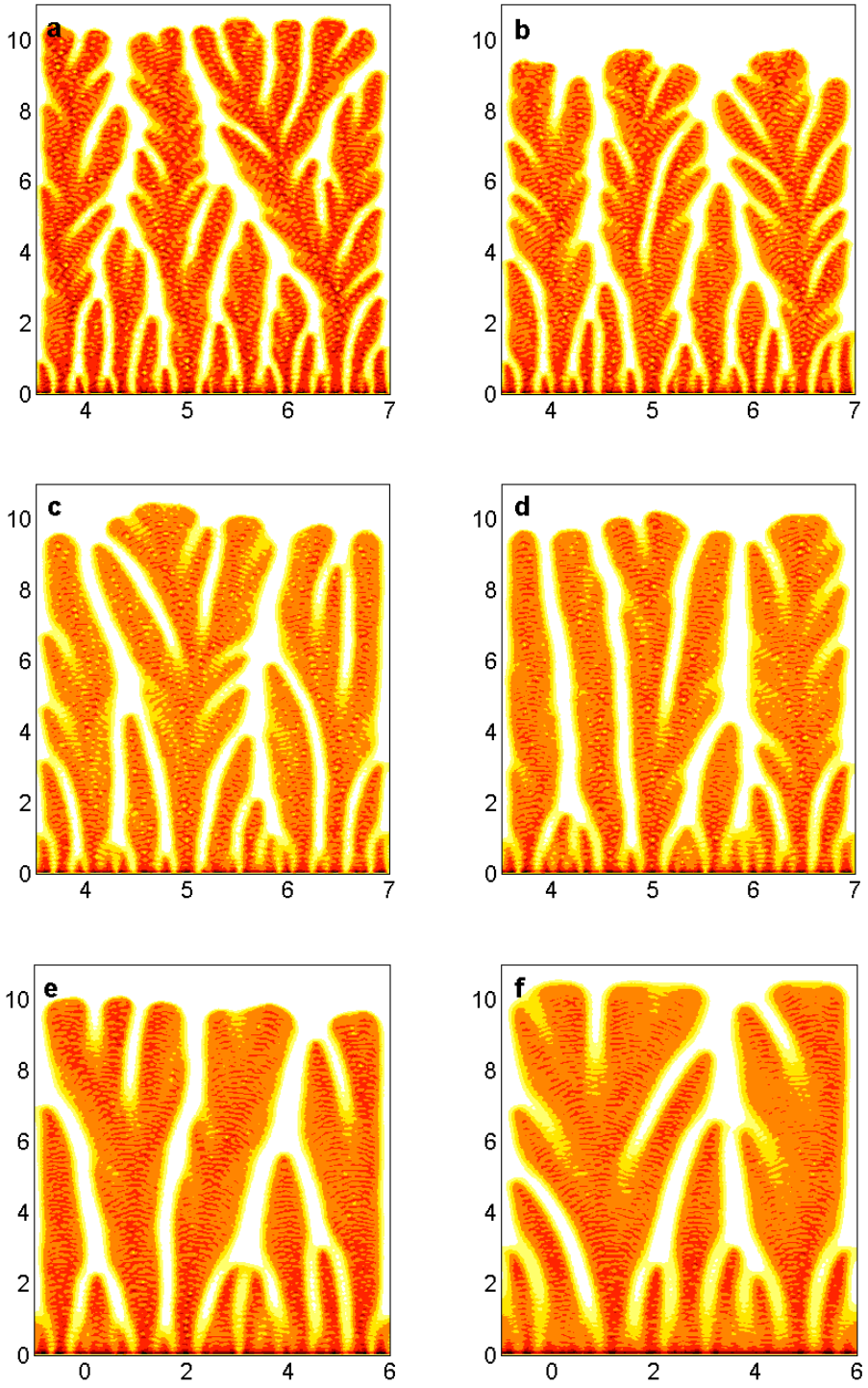

Figure 7.12: Spatial profiles of char patterns showing the evolution of finger width with heat release rate. (a) $A = 1.7 \times 10^4$; (b) 1.5×10^4; (c) 1.0×10^4; (d) 0.85×10^4; (e) 0.65×10^4;(f) 0.45×10^4. The numerical simulations are well within the tip-splitting regime at $Le = 0.1$ and $Pe = 10$.

7.5 Summary

In this chapter, we analyzed the behavior of fingering instability in three distinct isotropic porous materials that differ in terms of thermal conductivity contrast. We examined the pattern behavior using two different approaches. The first approach is based on the effective diffusion constants derived from homogenization, in which the distinct models are analyzed in order to understand the contribution of the thermal conductivity contrast. This can be viewed under three different factors: the time for onset of ignition, the ability of fingers to tip-split and intensity of fuel conversion within the fingers. The time of ignition is shortest for the HCI model, and longest for the WCI model. However, the WCI model showed high fuel conversion within the fingers, with less ability of the fingers to tip-split. The HCI model showed a higher tendency to tip-splitting due to the high heat release rate. The influence of conductivity for the considered factors is always at the moderate regime for the MCI model. The macroscopic behavior of the limit models is restricted only to the regimes of the instability, i.e. the regime of tip-splitting and sparse fingers. The regime of connected front did not emerge in all range of considered Péclet number; the regime of tip-splitting fingers is observed at considerably higher flow rates for the HCI and MCI models. Since the three models exhibit fingering in spite of differences in conductivity, we conclude that conductivity contrast is not the controlling factor for pattern behavior, i.e. fingering pattern is not fuel dependent, and can be observed in a vast number of combustible media. We referred to this approach as the fingering patterns of the first kind since the pattern behavior is an attempt to confirm the contribution of the homogenization method.

In the second approach, the models are examined for pattern behavior by replacing the effective diffusion coefficient with a dimensionless Lewis number. This allows for analyzing the fingering patterns in terms of diffusion-thermal instability mechanism (see Kagan and Sivashinsky, 1996; Sivashinsky, 1983). In this case, the models are selected through the dependence of domain size on the thermal diffusivity of the respective models. Within the limit of theoretical assumptions in the problem formulation, we demonstrated that, in a set of macroscopic numerical simulations, the proposed models of reverse combustion capture the basic physics underlying the experimental observations of (Zik and Moses, 1999, 1998; Zik et al., 1998) and Olson et al. (1998). While the approach explored in this study is quite different from those reported in other literatures (see Lu and Yortsos, 2005a; Ikeda and Mimura, 2008; Fasano et al., 2009, e.g.), the results of the numerical simulations showed a close resemblance of the pattern-forming dynamics presented in this study with the mechanism of diffusion driven instability (Zik and Moses, 1999; Olson et al., 1998). The developed patterns in this case are treated under fingering patterns of the second kind since the pattern behavior emerge via the mechanism of thermal-diffusion instability.

However, the disparity arising from the models indicates the need for a detailed understanding of the effects of kinetic and fuel property interactions to the emerging fingering instability. While the effect of heat losses has not been considered in the present study, the results of the numerical simulations presented in this study suggest that heat trans-

port mechanisms play an important role to the structure of the patterns. We showed that variations in the heat release rate have influence on the morphology of the patterns. Thus, a better understanding of the interplay between various heat transport mechanism is still required. We also examined the influence of heat release on the finger width. The result of numerical simulation showed that the widening of the finger width can be interpreted in terms of inability of the fingers to tip-split.

Finally, we see that developed models can be adapted for qualitative treatment of the development of patterns in reverse combustion in porous media. Nevertheless, the results of the homogenization method present an effective way of integrating material microstructural properties into a macroscopic system describing real life processes. Thus, it can serve as a paradigm for further investigation of combustion processes in a rigorous mathematical treatment.

Chapter 8

Effect of anisotropy on fingering instability in reverse smoldering combustion

Following the discussions in Chapter 7, we focus now on the characteristic behavior of the fingering instability resulting from the influence of the material microstructure. While the emergence of fingering patterns is not dependent on the arrangement of microstructures of porous materials and on the type of material used, the microstructure can potentially induce some forms of nonuniformity on the patterns. This investigation is basically introduced presently as a completion, to further elucidate how nonuniformities can be introduced in the studied homogenized models through the effective thermal conductivity and mass diffusion tensors. The tensors are calculated on idealized anisotropic unit cells. There are a couple of literature sources dealing with anisotropy effects, induced through effective transport properties (Cheng et al., 2012; Shkadinskii and Firsov, 1996). The forms of these tensors serve as a measure of the direction of mass and heat transport. According to Zik and Moses (1999), experimental evidence indicates that for a highly anisotropic thin porous material, the uniformity and reproducibility of the fingering behavior is reduced, otherwise material anisotropy does not have any significant effect on the patterns. We point out that the derivation of the macroscopic models of anisotropic media studied presently are identical to the macroscopic models of Chapter 3, since anisotropy is only induced into the system via the geometry of the medium. However, the effective tensors for anisotropic media are different; they are scalars in the case of isotropic media, whereas they are second order tensors with full entries in most cases, for anisotropic media. Different forms of anisotropic effective tensors can be realized based on the form of the local geometry; diagonally anisotropic, symmetrically anisotropic, and full anisotropic tensors can be realized through the homogenization procedure, and they usually possess distinctive characteristic properties which influence the pattern behavior distinctly. We examine the behavior of the different forms in the sequel.

8.1 Examples of anisotropic geometries and their effective tensors

Since the effect of anisotropy is introduced into the system of homogenized equations through the effective diffusion coefficients, we present examples of anisotropic geometries and their corresponding effective tensors. It should be pointed out that the forms of the cell problems for the computation of the effective tensors are similar to the isotropic case. In real life processes, various kinds of materials exhibit different forms of anisotropic behavior in their microstructures. However, for brevity of presentation, we describe the behavior of tensors arising from some chosen anisotropic geometries, such as depicted in Figure 8.1. The geometries will serve as a framework for discussing different forms of material anisotropy and their influence on pattern behavior. In Figure 8.1a, the geometry of the inclusion

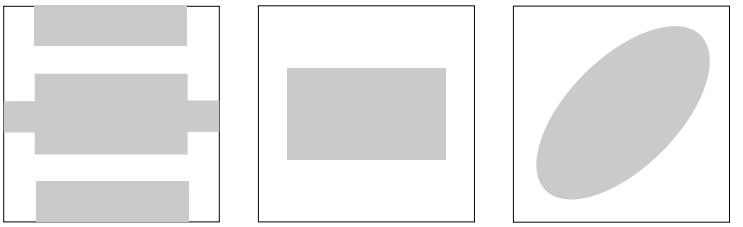

(a) stacked slabs (b) centered slab (c) centered ellipse

Figure 8.1: Examples of anisotropic geometries with intrinsic inclusions.

consists of a cross-section of slabs, which lie adjacent to each other. The central inclusion is connected to smaller sized rectangles, with two others stacked to the lateral walls. This configuration allows connectivity of the microstructure, which are identified in Chapters 3 and 6 as periodic translations of a single period (see Figure 8.2a). We show later in Subsection

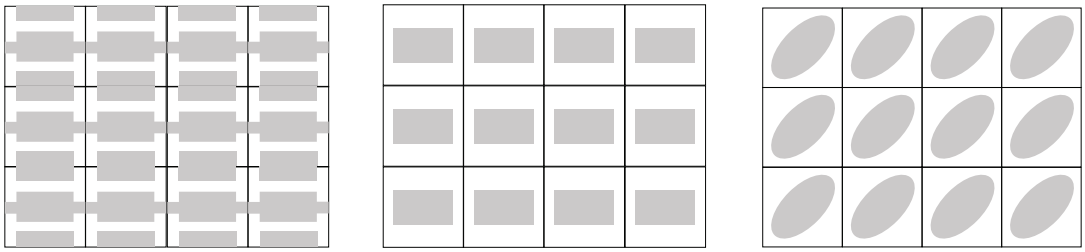

(a) (b) (c)

Figure 8.2: Examples of configurations of periodic anisotropic media for flows in thin porous materials.

8.1.1 that longitudinal diffusion clearly dominates the transverse diffusion in the geometry depicted in Figure 8.1a. In Figure 8.1b, however, the inclusions are disconnected and their periodic translation is illustrated in Figure 8.2b. In this case, the effect of anisotropy also

dominates in the longitudinal direction, with an enhancement of the effective mass diffusivity. This is simply due to the high porosity of the unit cell. In the two geometries (Figures 8.2a and 8.2b), the principal transport direction is dominated in the longitudinal direction; the latter direction promotes longitudinal smolder propagation. Lastly, the geometry depicted in Figure 8.2c contains an elliptical inclusion, which is oriented at an angle of 45°. The orientation ensures that the effective diffusion tensors are symmetrically anisotropic. The principal direction of flow in this case is in the main diagonal entry.

8.1.1 Calculation of effective tensors and parameters

For the homogenization problem, the effective quantities entering the system of equations include the effective thermal conductivity tensor, λ^{eff}, effective mass diffusion tensor, D^{eff}, and respectively the volume and surface porosities ϕ and ϕ^s. These quantities are required in order to solve the homogenized system of equations. The physical parameters necessary for the computation of these effective quantities are given in Table A.1. The effective thermal and diffusion tensors for the stacked slabs are given by:

$$\lambda^{\text{eff}} = \begin{pmatrix} 5.081 \cdot 10^{-4} & 0.00 \\ 0.00 & 4.634 \cdot 10^{-4} \end{pmatrix}, \quad D^{\text{eff}} = \begin{pmatrix} 0.0550 & 0.00 \\ 0.00 & 0.0 \end{pmatrix}. \tag{8.1}$$

From (8.1), λ^{eff} is calculated to 11 digits of precision, while D^{eff} has 12 digits of precision. The tensor λ^{eff}, is diagonally anisotropic, with a principal longitudinal direction. However, the mass diffusion tensor D^{eff} is a scalar pointing in the longitudinal direction. This reduces the mass diffusion equation to one dimension, and hence one may simply consider the problem in one-dimension. Clearly, for one-dimensional problems, no visible fingering patterns can be observed. This implies that reproducing fingering patterns on the geometry consisting of stacked slabs may not be possible. The volume and surface porosities are given respectively by $\phi = 0.32$ and $\phi^s = 4.8$.

The effective thermal and mass diffusion tensors for the centered slab are given by:

$$\lambda^{\text{eff}} = \begin{pmatrix} 3.535 \cdot 10^{-4} & 0.00 \\ 0.00 & 3.117 \cdot 10^{-4} \end{pmatrix}, \quad D^{\text{eff}} = \begin{pmatrix} 0.1532 & 0.00 \\ 0.00 & 0.0745 \end{pmatrix}. \tag{8.2}$$

Likewise, we have diagonal anisotropy for both λ^{eff} and D^{eff}. In this case, the precision of λ^{eff} tensor is 12 while that of D^{eff} is 6. λ^{eff} and D^{eff} are also dominant in the longitudinal direction.The volume and surface porosities are given respectively by $\phi = 0.8817$ and $\phi^s = 2.0$.

Lastly, for the geometry depicted in Figure 8.2c, the effective thermal and mass diffusion tensors are symmetrically anisotropic because of the orientation of the inclusion. The dependence of the inclusion on angular orientation may serve as a generalization for treating fully anisotropic effective tensors, as described in Section 5.4 of Chapter 5. The entries

of the symmetrically anisotropic tensors are given by:

$$\lambda^{\text{eff}} = \begin{pmatrix} 4.03695 \cdot 10^{-4} & 1.8507846 \cdot 10^{-5} \\ 1.8507846 \cdot 10^{-5} & 4.03695 \cdot 10^{-4} \end{pmatrix}, \quad D^{\text{eff}} = \begin{pmatrix} 0.07618 & 0.01948 \\ 0.01948 & 0.07618 \end{pmatrix}. \tag{8.3}$$

For this geometry, the volume and surface fractions are respectively given by $\phi = 0.482912$ and $\phi^s = 2.727364$.

8.2 Macroscopic model for general anisotropic tensors

In this section, we begin by describing the general form of the anisotropic system of equations, which is of interest for the phenomenon of interest. (8.4) can serve as a generalization of the isotropic case treated in Chapter 7. We recall that the objective of this chapter is to analyze nonuniformity on the structure of the fingering patterns, based on anisotropy induced through the effective transport coefficients. For highly anisotropic porous materials, we are required to use the general form of anisotropic equation (8.4).

$$\begin{aligned} \mathcal{C}^{\text{eff}} \frac{\partial T}{\partial t} \pm \phi \mathcal{C}_{\text{g}} \upsilon \frac{\partial T}{\partial x} &= \lambda_{\text{x}}^{\text{eff}} \frac{\partial^2 T}{\partial x^2} + \lambda_{\text{yx}}^{\text{eff}} \frac{\partial^2 T}{\partial y \partial x} + \lambda_{\text{xy}}^{\text{eff}} \frac{\partial^2 T}{\partial x \partial y} + \lambda_{\text{y}}^{\text{eff}} \frac{\partial^2 T}{\partial y^2} + \phi^s Q W(T, C), \\ \phi \frac{\partial C}{\partial t} \pm \phi \upsilon \frac{\partial C}{\partial x} &= D_{\text{x}}^{\text{eff}} \frac{\partial^2 C}{\partial x^2} + D_{\text{yx}}^{\text{eff}} \frac{\partial^2 C}{\partial y \partial x} + D_{\text{xy}}^{\text{eff}} \frac{\partial^2 C}{\partial x \partial y} + D_{\text{y}}^{\text{eff}} \frac{\partial^2 C}{\partial y^2} - \phi^s W(T, C), \\ \frac{\partial \mathcal{R}}{\partial t} &= W(T, C). \end{aligned} \tag{8.4}$$

In (8.4), the anisotropic effect is such that the direction of mass and heat fluxes are not simply the direction of the gradients. Depending on the entries of the diffusion tensors, mass and heat transport are more pronounced towards a direction relative to other directions. Thus, for the problem of thermal-diffusion instability studied presently, the collective contribution of the mass and heat transport mechanisms will be considered. First, we consider a simpler problem, in which the model conforms to effective diffusion tensors resulting from the geometries 8.1 and 8.2 discussed in the previous section.

8.2.1 Macroscopic model for diagonally anisotropic tensors

The macroscopic equations for diagonally anisotropic diffusion tensors can be realized from the general anisotropic equation (8.4) by setting the off-diagonal entries of the anisotropic tensors to zero, i.e.

$$\lambda_{\text{yx}}^{\text{eff}} = \lambda_{\text{xy}}^{\text{eff}} = 0, \quad D_{\text{yx}}^{\text{eff}} = D_{\text{xy}}^{\text{eff}} = 0,$$

such that the system of equation (8.4) reduces to the following:

$$\begin{aligned} \mathcal{C}^{\text{eff}}\frac{\partial T}{\partial t} \pm \phi\mathcal{C}_{\text{g}}v\frac{\partial T}{\partial x} &= \lambda_{\text{x}}^{\text{eff}}\frac{\partial^2 T}{\partial x^2} + \lambda_{\text{y}}^{\text{eff}}\frac{\partial^2 T}{\partial y^2} + \phi^s QW(T,C), \\ \phi\frac{\partial C}{\partial t} \pm \phi v\frac{\partial C}{\partial x} &= D_{\text{x}}^{\text{eff}}\frac{\partial^2 C}{\partial x^2} + D_{\text{y}}^{\text{eff}}\frac{\partial^2 C}{\partial y^2} - \phi^s W(T,C), \\ \frac{\partial \mathcal{R}}{\partial t} &= W(T,C). \end{aligned} \tag{8.5}$$

Similar to the case of macroscopic (isotropic) equations[1], system (8.5) can be reduced to dimensionless form by introducing some characteristic units on the effective equations.

$$\begin{aligned} \frac{\partial T}{\partial t} \pm \phi\Lambda Pe\frac{\partial T}{\partial x} &= \frac{\partial^2 T}{\partial x^2} + \gamma\frac{\partial^2 T}{\partial y^2} + W(T,C), \\ \phi\frac{\partial C}{\partial t} \pm \phi Pe\frac{\partial C}{\partial x} &= \frac{1}{\mathfrak{L}_{\text{L}}}\frac{\partial^2 C}{\partial x^2} + \frac{1}{\mathfrak{L}_{\text{T}}}\frac{\partial^2 C}{\partial y^2} - W(T,C), \\ \frac{\partial \mathcal{R}}{\partial t} &= H_R W(T,C), \end{aligned} \tag{8.6}$$

where the following simplifications have been introduced in (8.6):

$$\gamma = \frac{\lambda_{\text{y}}^{\text{eff}}}{\lambda_{\text{x}}^{\text{eff}}}, \alpha_{\text{x}} = \frac{\lambda_{\text{x}}^{\text{eff}}}{\mathcal{C}^{\text{eff}}}, \mathfrak{L}_{\text{L}}^{-1} = \frac{D_{\text{x}}^{\text{eff}}}{\alpha_{\text{x}}}, \mathfrak{L}_{\text{T}}^{-1} = \frac{D_{\text{y}}^{\text{eff}}}{\alpha_{\text{x}}}. \tag{8.7}$$

In (8.10), α_{x} is the longitudinal thermal diffusivity, and $\mathfrak{L}_{\text{L}}$ and $\mathfrak{L}_{\text{T}}$ are respectively the longitudinal and transverse Lewis numbers.

Remark 8.2.1. *The consequence of the anisotropy in the system is the introduction of an anisotropy factor, γ, in* (8.6)*. This dimensionless scale parameter allows for discussion of different test cases. It generalizes the anisotropy in the system for the diagonally anisotropic media, i.e. we assume γ to be an anisotropy indicator such that we set*

$$\mathfrak{L}_{\text{T}}^{-1} := \gamma\mathfrak{L}_{\text{L}}^{-1}. \tag{8.8}$$

The consideration here makes sense since the primary control parameter for the pattern behavior is the Lewis number, and thermal anisotropy dominates in the system; hence, we do not treat $\mathfrak{L}_{\text{T}}^{-1}$ separately.

8.2.2 Macroscopic model for symmetrically anisotropic tensors

The macroscopic equations for the case of symmetrically anisotropic diffusion tensors can be realized from the general anisotropic equation (8.4) by setting the off-diagonal entries of the anisotropic tensors to:

$$\lambda_{\text{yx}}^{\text{eff}} = \lambda_{\text{xy}}^{\text{eff}}, \quad D_{\text{yx}}^{\text{eff}} = D_{\text{xy}}^{\text{eff}},$$

[1]The macroscopic equations can be regarded simply as anisotropic or isotropic equation in order to differentiate different problems based on their effective diffusion tensors.

such that the system of equation (8.4) can be rewritten in dimensionless form as:

$$\begin{aligned}\frac{\partial T}{\partial t} \pm \phi\Lambda Pe\frac{\partial T}{\partial x} &= \frac{\partial^2 T}{\partial x^2} + 2\mu\frac{\partial^2 T}{\partial y \partial x} + \gamma\frac{\partial^2 T}{\partial y^2} + W(T,C),\\ \phi\frac{\partial C}{\partial t} \pm \phi Pe\frac{\partial C}{\partial x} &= \frac{1}{\mathfrak{L}_{\mathrm{L}}}\frac{\partial^2 C}{\partial x^2} + \frac{2}{\mathfrak{L}_0}\frac{\partial^2 C}{\partial y \partial x} + \frac{1}{\mathfrak{L}_{\mathrm{T}}}\frac{\partial^2 C}{\partial y^2} - W(T,C),\\ \frac{\partial \mathcal{R}}{\partial t} &= H_R W(T,C),\end{aligned} \tag{8.9}$$

where the following simplifications have been introduced in (8.6):

$$\gamma = \frac{\lambda_{\mathrm{y}}^{\mathrm{eff}}}{\lambda_{\mathrm{x}}^{\mathrm{eff}}}, \mu = \frac{\lambda_{\mathrm{yx}}^{\mathrm{eff}}}{\lambda_{\mathrm{x}}^{\mathrm{eff}}}, \alpha_{\mathrm{x}} = \frac{\lambda_{\mathrm{x}}^{\mathrm{eff}}}{\mathcal{C}^{\mathrm{eff}}}, \mathfrak{L}_{\mathrm{L}}^{-1} = \frac{D_{\mathrm{x}}^{\mathrm{eff}}}{\alpha_{\mathrm{x}}}, \mathfrak{L}_{\mathrm{T}}^{-1} = \frac{D_{\mathrm{y}}^{\mathrm{eff}}}{\alpha_{\mathrm{x}}}, \mathfrak{L}_0^{-1} = \frac{D_{\mathrm{yx}}^{\mathrm{eff}}}{\alpha_{\mathrm{x}}}. \tag{8.10}$$

The general form of the anisotropic tensors for the dimensionless system (8.9) is given by

$$\lambda = \begin{pmatrix} 1 & \mu \\ \mu & \gamma \end{pmatrix}, \quad D = \begin{pmatrix} L_{\mathrm{d}}^{-1} & \mu L_0^{-1} \\ \mu L_0^{-1} & \gamma L_{\mathrm{d}}^{-1} \end{pmatrix}, \tag{8.11}$$

where γ and μ are anisotropy indicators in the system and L_{d} is simply the Lewis number. However, assuming in addition that the diagonal entries of the anisotropic tensors are the same, i.e.

$$\lambda_{\mathrm{x}}^{\mathrm{eff}} = \lambda_{\mathrm{y}}^{\mathrm{eff}}, \quad D_{\mathrm{x}}^{\mathrm{eff}} = D_{\mathrm{y}}^{\mathrm{eff}},$$

then, the nondimensional coefficient tensors reduces to

$$\lambda = \begin{pmatrix} 1 & \mu \\ \mu & 1 \end{pmatrix}, \quad D = \begin{pmatrix} L_{\mathrm{d}}^{-1} & \mu L_0^{-1} \\ \mu L_0^{-1} & L_{\mathrm{d}}^{-1} \end{pmatrix}, \tag{8.12}$$

Remark 8.2.2. *The form of the anisotropic tensors introduced by* (8.11) *and* (8.12) *can further be simplified, i.e. we can chose* μL_0^{-1} *simply as* μ. *We also adapt the general form* (8.11) *in our numerical examples.*

8.3 Fingering patterns of the first kind

In this section, we investigate the behavior of the macroscopic system with effective tensors, in a manner similar to the presentation of Section 7.2 of Chapter 7. However, we are interested in understanding the influence of the effective tensors on structure formation. The effective diffusion tensors are anisotropic, and conform to the tensors given in (8.11) and (8.12). The behavior of the system will be also be analyzed by using different forms of ignition mechanisms. In the first case, we investigate the anisotropic system by using a form of *autoignition*[2], analogous to the numerical results presented in most sections of Chapter 7.

[2]autoignition here describes an ignition without a direct imposition of an external heat source.

8.3.1 Fingering behavior based on anisotropic effective tensors

For the problems considered in this section, the Lewis number depends on the effective diffusion tensors. Thus, we simply analyze the anisotropic system of equations by varying the Péclet number. First, let us consider the behavior of the anisotropic system with diagonally anisotropic tensors.

We consider a problem posed in the geometry depicted in Figure 8.1a. For this geometry, the diffusion process is dominated in the longitudinal direction (i.e. for $D_{\mathrm{y}}^{\mathrm{eff}} \to 0$, and thus $\mathfrak{L}_{\mathrm{T}}^{-1} \to 0$). The result is that no visible pattern is observed (see Figure 8.3a). This implies that diffusive transverse perturbation is essential for pattern behavior. Based on this intuitive understanding of the pattern behavior, it makes sense to examine the situation corresponding to the far right limit, i.e. $\mathfrak{L}_{\mathrm{T}}^{-1} \to \infty$. In this case, the fingering pattern manifests as sparse fingers which satisfy $w/d \ll 1$. Here, w is the width of the fingers and d, the distance between fingers. The result is depicted in Figure 8.3b. For the second

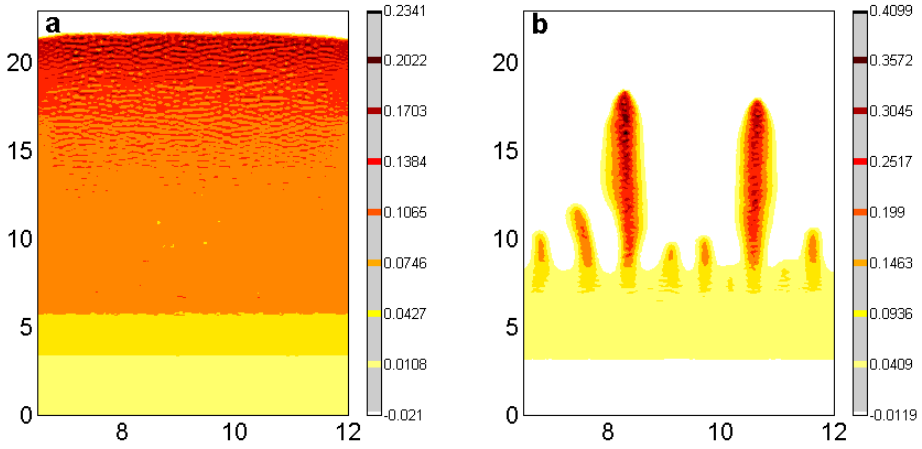

Figure 8.3: Spatial profile of char pattern for a typical anisotropic material depicted in Figure 8.2a. (a) shows the situation when the diffusion process is dominated in the longitudinal direction and $\mathfrak{L}_{T}^{-1} \to 0$. (b) shows the behavior of the fingering pattern at large transverse perturbation, i.e. $\mathfrak{L}_{T}^{-1} \to \infty$. The parameters of this numerical result corresponds to the effective thermal and diffusion tensors and at $Pe = 10$.

problem (see Figure 8.1b) of diagonally anisotropic tensors, the pattern behavior is highly influenced by the dominant mass diffusivity, due to the volume fraction of the gaseous part ($\phi = 0.8817$) of the medium. The fingering pattern is compact with respect to the spacing between adjacent fingers and the extent of propagation of the smolder front is limited, i.e. we have extinction due to the dominant mass flux in the system.

Lastly, we consider the problem posed on the geometry with the elliptical inclusion. Here, the inclusions are oriented at an angle of 45 degrees from the center of the unit cell (see Fig-

ure 8.1c). The physical quantities defined in the unit cell are homogeneous with respect to the phases. However, the effective diffusion tensors are anisotropic because of the orientation of the inclusion. This results to a symmetrically anisotropic system, with tensors conforming to (8.12). Figure 8.4 shows the influence of the anisotropic medium on the fingering behavior by relying specifically on the effective diffusion coefficients, but varying the values of Pe. In Figure 8.4, we show the behavior of the fingering patterns at various values of Pe.

Furthermore, at all chosen values of Pe, the fingering patterns are nonuniform and tend to propagate along one side of the lateral boundary; the effect of material anisotropy is such that propagation of the front is more pronounced along the lateral boundary and reproducibility of the patterns at low Pe is not viable. To observe the tip-splitting of fingers, the range of Pe values has to be increased. For example, the results illustrated in Figure 8.4 correspond to a Pe range of $Pe = 10$ to $Pe = 50$. These results show increased fuel conversion within fingers and emergence of tip-splitting fingers. This observation is consistent with the isotropic results presented in the previous chapter.

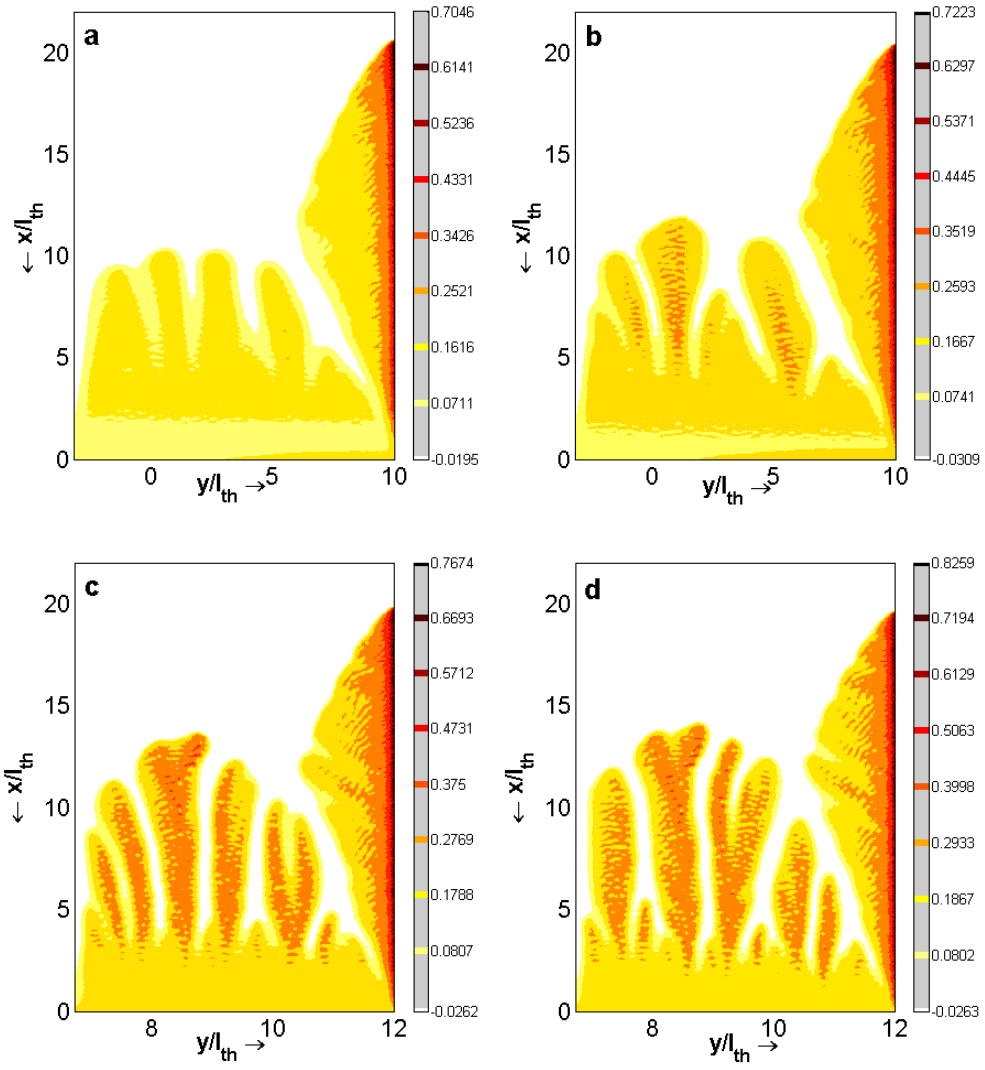

Figure 8.4: Spatial profiles of char patterns for a typical symmetrically anisotropic material with elliptical inclusions depicted in Figure 8.2c. The material anisotropy is more intense along a lateral boundary and reproducibility of the patterns at low values of Pe is not viable; (a) fingering behavior at $Pe = 10$ with very low fuel conversion with the fingers except at the right lateral boundary where the fuel conversion is more intense; (b) fingering behavior at $Pe = 20$ showing increasing fuel conversion and sharper smolder front; (c) at $Pe = 40$, the sharpness of the fingers is enhanced with an onset of tip-splitting; (d) fingering with characteristic features of tip-splitting at at $Pe = 50$.

8.4 Fingering behavior based on anisotropically induced thermal-diffusion instability

In this section, we illustrate the effect of material anisotropy on the fingering patterns by using the mechanism of thermal-diffusion instability. The numerical results are solved using an external ignition source as defined by (7.7). The objective of this section is to show how material anisotropy affects the uniformity as well as reproducibility of the various regimes of the fingering patterns.

8.4.1 Fingering behavior in diagonally anisotropic medium

The mechanism of thermal-diffusion instability can now be used in order to analyze pattern behavior in "weakly" anisotropic material by considering a generic diagonally anisotropic medium satisfying $\mu = 0$ and $0 < \gamma < 2$ in (8.11). The problem in an isotropic medium can immediately be recovered from this system by setting $\gamma = 1$. Figure 8.5 shows spatial profiles of char pattern for varying intensity of the anisotropy factor γ. The fingering patterns are considered in the tip-splitting regime, which corresponds to $Le = 0.1$ and $Pe = 10$.

The numerical results discussed here is typical for a weakly anisotropic medium, in which the uniformity and reproducibility of the fingering behavior is not significantly affected. The anisotropy is such that the population (density) of the fingers is changed. For values of the anisotropy factor γ less than unity, the fingering pattern is dense (see Figure 8.5(a)-(f)). The increase in the number of fingers is basically due to an increase in the convective transport in the system. However, for some values of γ greater than unity, the fingers become more distinct from each other (see Figure 8.5(g)-(i)).

This characteristic behavior accounts for the effect of transverse perturbation that manifests at $\mathfrak{L}_{\mathrm{T}}^{-1} > \mathfrak{L}_{\mathrm{L}}^{-1}$, which increases the spacing between adjacent fingers. Figure 8.5(g) corresponds to the isotropic case at $\gamma = 1$, which has been included simply for comparison. It can be seen that pattern behavior for diagonally anisotropic media have qualitative resemblance to the isotropic media, except for the increase in the population of fingers. In Figure 8.6, the spatial profiles of char patterns at distinct fingering regimes are illustrated. The numerical simulations were calculated for an anisotropy factor of $\gamma = 0.5$. In Figure 8.6, we show the reproducibility of the distinct fingering regimes. The regime of sparse fingers is depicted in Figure 8.6a. The pattern behavior is qualitatively similar to the isotropic case since the nonuniformity of the pattern is not obvious. Figure 8.6b shows the tip-splitting regime, and by increasing the Lewis number from $Le = 0.2$ to $Le = 1$, we arrive at the regime of connected front. (see Figure 8.6(c)(f)). Thus, we conclude that the distinct fingering regimes can be reproduced for problems posed in a diagonally anisotropic material. In all cases, the anisotropy indicators are set to $\gamma = 0.5$, and $\mu = 0$.

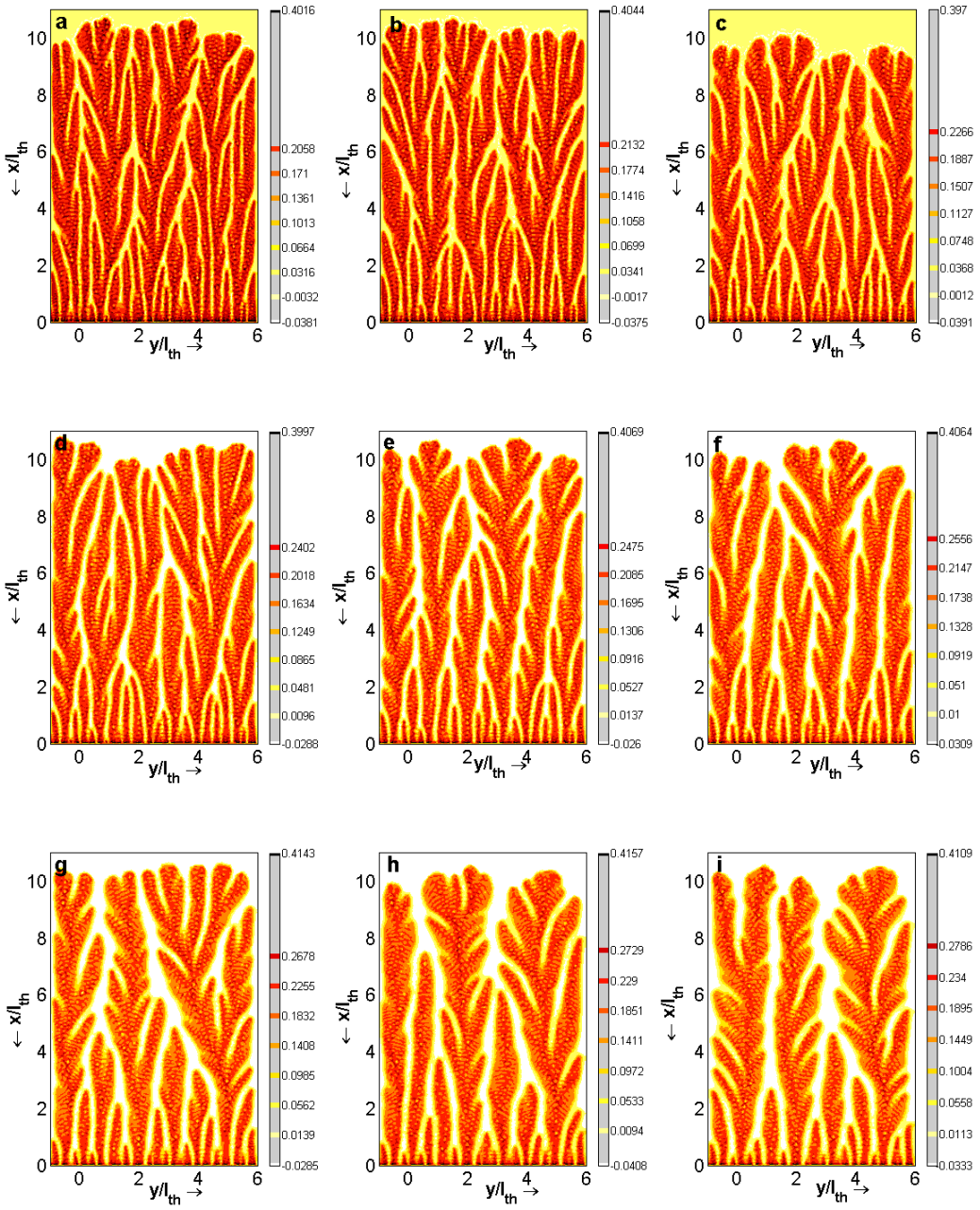

Figure 8.5: Spatial profiles of char patterns for a generic diagonally anisotropic material. The material is weakly anisotropic and all regimes of the pattern behavior can be reproduced; (a) fingering behavior at $\gamma = 0.35$ (b) $\gamma = 0.4$; (c) $\gamma = 0.5$; (d) $\gamma = 0.6$; (e) $\gamma = 0.7$;(f) $\gamma = 0.8$;(g) $\gamma = 1$ (Isotropic case); (h) $\gamma = 1.2$; (i) $\gamma = 1.4$; the numerical simulation corresponds to the tip-splitting regime at $Le = 0.1$.

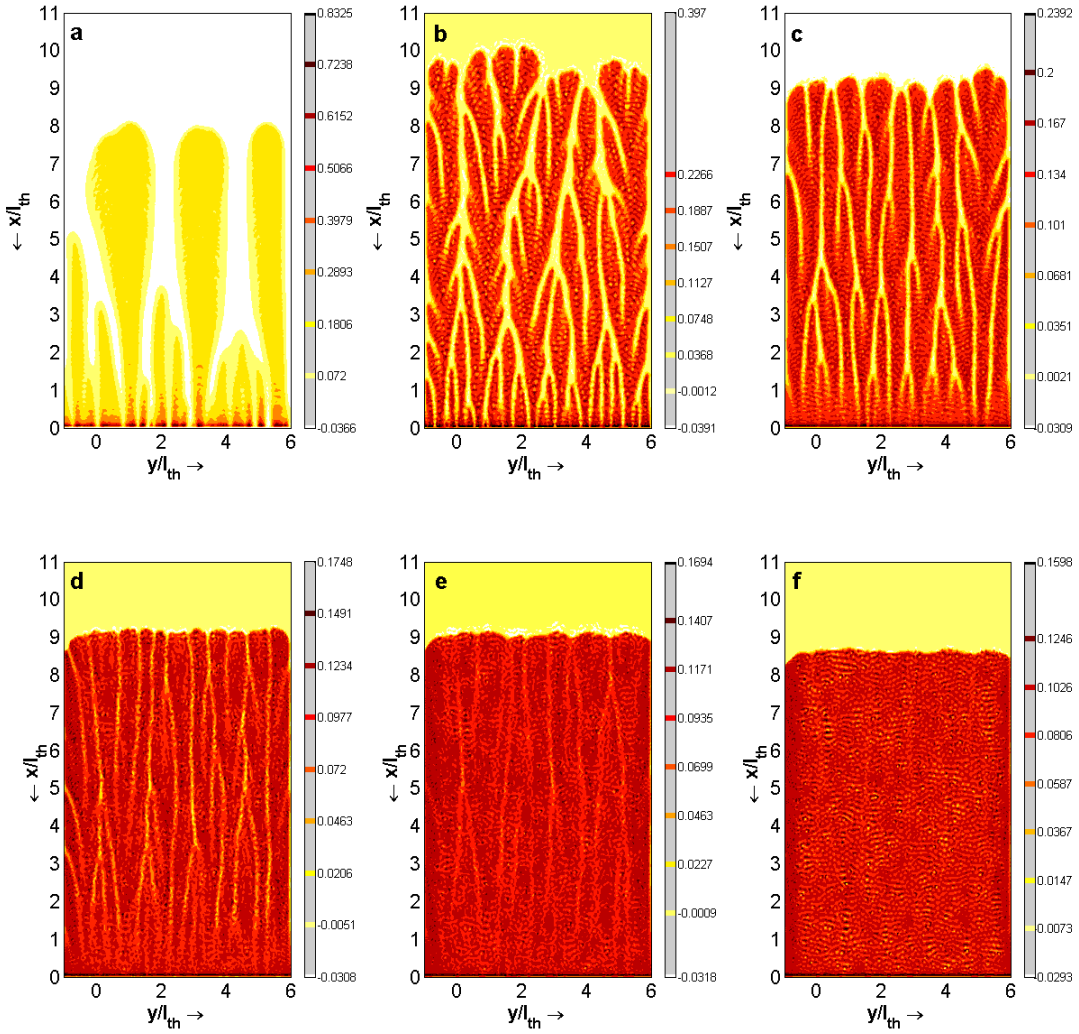

Figure 8.6: Spatial profiles of char patterns for a generic diagonally anisotropic material. The material is weakly anisotropic. In all cases $\gamma = 0.5, \mu = 0$. From (b)-(f), $Pe = 10$; (a) $Le = 0.015, Pe = 0.1$ (sparse fingering regime) (b) $Le = 0.1$ (tip-splitting regime) ; (c) $Le = 0.2$; (d) $Le = 0.5$; (e) $Le = 0.7$;(f) $Le = 1$ (regime of connected front). The distinct fingering regimes can be reproduced and nonuniformity on the patterns is not pronounced.

8.4.2 Fingering behavior in a symmetrically anisotropic medium

In this subsection, we investigate the pattern behavior arising from an anisotropic medium with periodically distributed elliptical inclusions. All parameters in the model are taken from calculations on the unit cell shown in Figure 8.1c. However, the effective Lewis number for the system is replaced by values of the free parameters defined in (8.12). In Figure 8.7, the spatial profiles of char patterns are illustrated for the distinct fingering regime for the

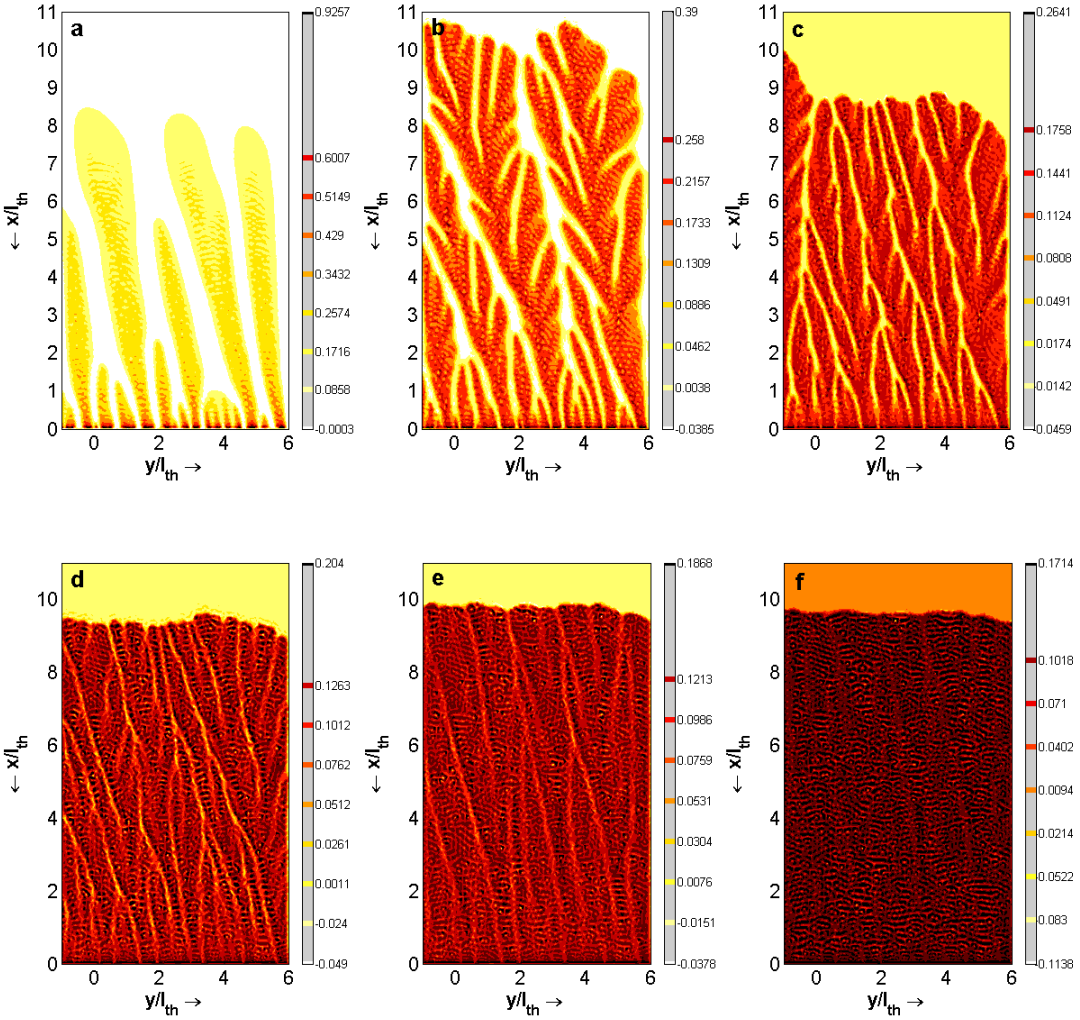

Figure 8.7: Spatial profiles of char patterns for a symmetrically anisotropic material with inclusion oriented clockwise at angle -45. The material is highly anisotropic. In all cases $\gamma = 1, \mu = 0.2$. (a) $Le = 0.02$ (sparse fingering regime) (b) $Le = 0.1$ (tip-splitting regime) ; (c) $Le = 0.25$; (d) $Le = 0.5$; (e) $Le = 0.7$;(f) $Le = 1$ (regime of connected front). The distinct fingering regimes can be reproduced with a reduction in uniformity.

problem posed in a symmetrically anisotropic material, in which the inclusions are oriented clockwise at angle of -45. In this case, the material is highly anisotropic, since nonuniformity on the patterns is pronounced. In all the computations, $\gamma = 1, \mu = 0.2$. Figure 8.7a corresponds to the regime of sparse fingers at $Le = 0.02$. It can be seen clearly that the uniformity of the fingering patterns is reduced since the fingers are directed toward a lateral boundary. The tip-splitting regime is showed in Figure 8.7b. In this case, the nonuniformity on the pattern is also obvious. Similarly, for increasing values of the Lewis number, from

$Le = 0.25$ to $Le = 1$, we approach the regime of connected front (Figure 8.7f). While the fingering behavior manifested nonuniformity at all the fingering regimes, the distinct fingering states are still reproducible. This confirms that material anisotropy is not significant to the emergence of the distinct fingering states. In Figure 8.8, we illustrate the spatial

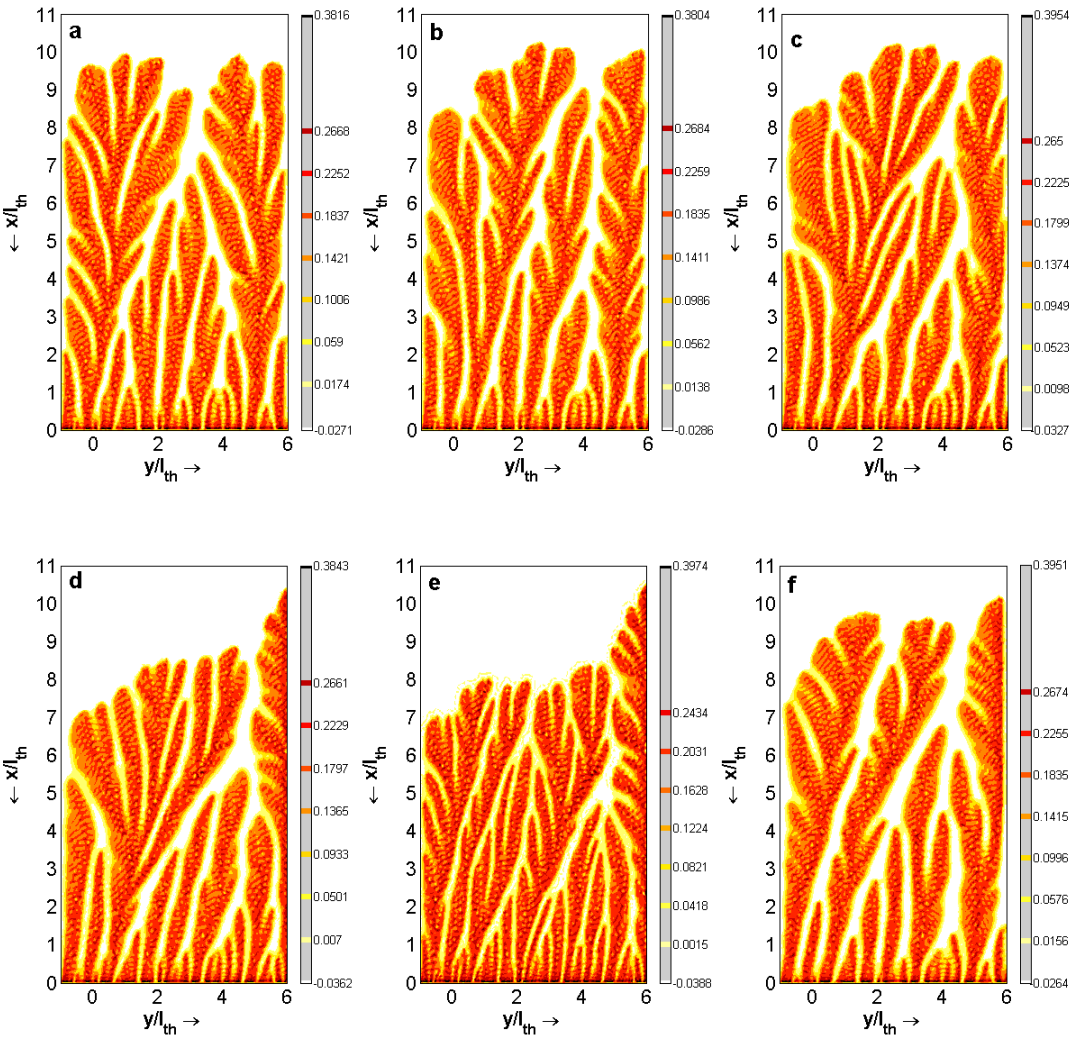

Figure 8.8: Spatial profiles of char patterns for a symmetrically anisotropic material with inclusions oriented counterclockwise at an angle of 45. From (a)- (d) $\gamma = 1, \mu = -0.085, -0.15, -0.2, -0.25$; (d) the nonuniformity extends to the right lateral boundary. (e) $\gamma = 0.5, \mu = -0.2$ (highly anisotropic case); the fingers are dense; (f) For $\gamma = 1.5, \mu = -0.2$, the patterns are more distinct due to increase in transverse perturbation.

profiles of char patterns for a problem posed in a symmetrically anisotropic material with inclusions oriented counterclockwise at an angle of 45. In this case, the anisotropy indicator μ has negative values, which only affects the direction of the fingering patterns. The

patterns are directed toward the right lateral boundary compared to the fingering behavior depicted in Figure 8.7. In Figure 8.8(a)–(d), $\gamma = 1, \mu = -0.085, -0.15, -0.2, -0.25$. The nonuniformity on the patterns increases for increasing magnitude of μ. In Figure 8.8(d), we see an enhancement of the nonuniformity on the patterns, which extends to the right lateral boundary with front propagation along this boundary. Figure 8.8(e) corresponds to the case $\gamma = 0.5, \mu = -0.2$; the system is highly anisotropic, with increased density of fingers and propagation along lateral boundary. In Figure 8.8(f), the fingering patterns are distinct due to increase in transverse perturbation at $\gamma = 1.5$.

8.5 Summary

In this chapter, we analyzed the behavior of the fingering patterns in terms of material anisotropy. The latter has been considered by investigating the behavior of fingering patterns for different geometry types and arrangements. Specifically, anisotropy was accounted for in a system of balance laws through the effective transport tensors-the thermal conductivity and mass diffusion tensors. The properties of these tensors include diagonally anisotropic, symmetrically anisotropic and fully anisotropic tensors. We considered different scenarios. First, for the medium consisting of stacked slabs, it was shown that the fingering behavior did not manifest due to the inability of mass diffusion in the transverse direction. This situation mimics the behavior of patterns at large flows, and corresponds to a system with a limiting zero transverse perturbation. However, for large perturbations in the transverse direction (y-direction), the fingers are more distinct, with a temperature profile that resembles those from a non-adiabatic combustion model. The behavior of fingering patterns at large transverse perturbation is consistent with the behavior observed in the literature (see Ikeda and Mimura, 2008; Fasano et al., 2009; Lu and Yortsos, 2005a, e.g.), and in other context (see Lu and Yortsos, 2005b; Lu and Dong, 2011; Kagan and Sivashinsky, 1996, e.g.) for a non-adiabatic situation. We conclude that transverse perturbations and hence mass diffusion is an important process for the emergence of fingering patterns in diffusion-limited system. On the other hand, a diagonally anisotropic system exhibits less observable effect on the fingering behavior, in terms of nonuniformity on the patterns. The morphology of the patterns for such systems is almost isotropic, except that the population of fingers changes with the anisotropy factor.

The explanation for the observed behavior can be viewed from the following direction: fingering instability in reverse combustion is a form of directional fingering, in the sense that its direction is mostly pre-dominant in the direction of the flow. An anisotropy effect in this direction basically promotes the propagation of the fingers along this direction. We classified materials with such properties as moderately anisotropic materials.

A class of symmetrically anisotropic system was exhibited in a domain consisting of elliptical inclusions with a given angular orientation. It should be noted that a pronounced anisotropic effect in a class of highly anisotropic materials has been described as the effect

that tends to deviate the fingering instability from its principal direction, and which can promote propagation along lateral boundaries. A detailed analysis of the geometry with elliptical inclusions was given in Chapter 5. The next viable step was to investigate the behavior of the fingers in the framework of fingering patterns of the first and second kinds. For the patterns of the second kind we conclude that in a highly anisotropic media, the uniformity and reproducibility of the fingering behavior is reduced, otherwise the distinct experimentally observed fingering regimes manifested, i.e. material anisotropy has no significant effect on the fingering behavior. This observation is consistent with the experimental work of (Zik and Moses, 1999; Zik et al., 1998; Zik and Moses, 1998).

Furthermore, still open in this research area are a detailed linear stability analysis for a highly anisotropic media, the influence of spread rate and other filtration properties of the porous media. One can also consider other scenarios leading to hydrodynamic behavior of the fingering patterns, which have been reported in other contexts (see Aldushin and Matkowsky, 1998; Kang et al., 2003; Kadowaki, 2005; Ozerkovskaya et al., 2010; Aldushin and Braverman, 2009, e.g.). In the present study, the flow field has been considered to be uniform. It could also be of interest in a future consideration to investigate a system, in which the flow is nonuniform. We also observed some form of nonuniform structure formation for the case of nonuniform ignition, which still requires additional work on the form of ignition sources. For more detail on aspects of ignition, we refer to (Shah et al., 2007; Yarin et al., 2004, e.g.).

Chapter 9

Conclusions

In this chapter, we summarize the most significant results discussed in this thesis. The present study concerns the modeling of reverse filtration combustion in thin porous materials, which is intended to support our understanding of the development of fingering patterns in a constrained experimental observation under microgravity conditions.

The main result of the study is the derivation of macroscopic models of filtration combustion of a thin porous material by homogenization of periodic structures. This was the scope of Chapter 3. The underlying physical process is governed by two competing transport processes-the transport of heat and the transport of reactants. Thus, at the pore scale description, we assumed conservation laws for heat and mass transport for the material and the gaseous oxidizer. Since the phenomenon of interest is dominated by heat conduction, we analyzed three different porous samples that differ in thermal conductivity. This allowed us to study the influence of conductivity contrast, between the constituent solid and gaseous phases, to the developed fingering patterns. Thus, three distinct models describe the macroscopic response to the thermal conductivity contrast. These include the moderately conductive inclusions (MCI) model, the highly conductive inclusions (HCI) model and the weakly conductive inclusions (WCI) model.

The first two models have the form of a one-temperature filtration combustion model. The MCI model is obtained when the thermal conductivity ratio of the constituent phases has an order of magnitude of $\lambda_s/\lambda_g = \mathcal{O}(1)$ with respect to the scale parameter, ϵ. This implies a comparable thermal conduction between the two phases, and hence the phases approach thermal equilibrium as a result. The effective thermal conductivity is determined by the conductivities of the constituent phases. For the HCI model, the thermal conductivity ratio satisfies the order of magnitude, $\lambda_s/\lambda_g = \mathcal{O}(1/\varepsilon)$, which implies a high contrast in conductivity; The solid inclusion has high thermal conductivity compared to the interconnected matrix conductivity. In this case, the thermal flow is dominated by the interconnected gaseous phase, although the solid phase conductivity is significant. This interplay between the phases also results to thermal equilibrium of the phases. The effective thermal conductivity is determined by the conductivity of the gaseous matrix and the local

geometry.

The last model is the WCI model, which is a non-equilibrium model, i.e. a distributed-temperature filtration combustion model in which two temperature equations arise at the limit problem; one describing macroscopic flow and the other microscopic flow. This describes a form of distributed microstructure model like those studied in other contexts (see Hornung and Showalter, 1990; Lewandowska et al., 2004; Arbogast et al., 1990, e.g.,). The model is obtained when the thermal conductivity ratio is $\lambda_s/\lambda_g = \mathcal{O}(\varepsilon^2)$, i.e., the thermal conductivity of the inclusion is near insulation, and thus is not significant in the thermal diffusion. The resulting model can be formulated as a single integro-differential equation, in which the integral term describes the exchange of heat between the matrix and the inclusions. The effective thermal conductivity is determined by the conductivity of the matrix.

The next logical step is the rigorous justification of the formal asymptotic method of Chapter 3. We do this by using the two-scale convergence method. We not only recovered the previous forms of the homogenized models, but also we indicated corrector results.

In Chapter 5, we analyzed the influence of the local geometry on the effective thermal conductivity based on a number of factors: the ratio of thermal conductivity of the two components, the volume fraction of inclusions, and the material anisotropy. The results of these analyses were compared with some known theoretical bounds in the literature. Specifically, the results were compared with the Hashin-Shtrikman and Voigt-Reuss bounds. The major result of this chapter is that the effective thermal conductivity obtained from homogenization coincides with the Hashin-Shtrikman bounds and depends solely on the volume fractions of the constituent phases. We showed the influence of local geometry on the anisotropy of the effective conductivity tensor by using elliptical inclusions as a typical anisotropic geometry.

Furthermore, in Chapter 6, we performed numerical simulations for the MCI model to verify the results of the homogenization process in appropriate relative L^2 norms, illustrating the strong convergence between the pore-scale description and the reconstructed homogenized problems. Two distinct reconstruction algorithms were developed specifically for this purpose. At the heart of the reconstruction algorithm were the solutions to the cell problems. We showed that the convergence rates of our homogenization process is consistent with the theoretical corrector estimates indicated in Chapter 4.

In Chapter 7, the derived upscaled models were further investigated for a scenario of reverse smoldering combustion for an isotropic porous material. The disparity between the distinct upscaled models were analyzed in terms of thermal conductivity differences, the intensity of fuel conversion within the fingers, the time for onset of ignition, and the ability of fingers to tip-split. These results are specifically related to the effective thermal properties obtained through homogenization. In this regard, we refer to such analysis of finger patterns as *fingering patterns of the first kind*. In the next step, we examined the

fingering behavior by using the mechanism of thermal-diffusion instability. In this case, the effective thermal properties derived from homogenization are not considered. Instead, we considered the *Lewis number* as a free parameter. This consideration allowed us to investigate distinct fingering states: connected front, sparse fingers and tip-splitting fingers. The result of this analysis showed that the pattern forming dynamics used in this study has a close resemblance to the experimentally observed fingering behavior (Zik and Moses, 1999; Olson et al., 1998) and most other results in the literature (Ikeda and Mimura, 2008; Lu and Yortsos, 2005a). For the latter analysis, the fingering patterns were referred to as *fingering patterns of the second kind*.

The motivation behind Chapter 8 is due to a previous treatment of fingering behavior in isotropic media (see Ijioma et al., 2013), and also in Chapter 7 of this thesis. In this chapter, some basic questions were raised: What is the behavior of the fingering patterns in an *anisotropic* porous medium. Can we reproduce the distinct fingering states in a highly anisotropic media?. The answers to these questions were pointed out in the experimental paper by Zik and Moses (1999). They concluded that "...for a highly anisotropic media, the uniformity and reproducibility of the pattern is reduced, otherwise anisotropy has no significant effect on the fingering behavior". We examined this conclusion via mathematical modeling based on homogenization and diffusive-thermal instability approaches. The conclusions based on our multiscale computational modeling are as follows:

(i) The mathematical modeling, in an anisotropic porous media, is simply a generalization of the isotropic case, which is considered in many filtration combustion scenarios (see Sivashinsky, 1983; Kagan and Sivashinsky, 2008; Oliveira and Kaviany, 2001; Rein, 2005; Chen et al., 1992; Yuan and Lu, 2013, e.g.) and in mathematical modeling of reverse smoldering combustion (see Ikeda and Mimura, 2008; Fasano et al., 2009; Lu and Yortsos, 2005a; Ijioma et al., 2013, e.g.).

(ii) The material anisotropy enters the governing equations through the effective anisotropic diffusion tensors.

(iii) Since the patterns are in the form of directional fingering, an anisotropy in the direction of propagation affects weakly the uniformity, but changes the density of fingers. In this case, the fingering regimes also manifested.

(iv) In a highly anisotropic media, the uniformity of the patterns is strongly influenced. This can be seen as directional fingering towards a given boundary and subsequent propagation of the fingers along that boundary. In addition, the distinct fingering regimes are also observed

Based on these results, we conclude that material anisotropy influences the uniformity of the fingering patterns, but the distinct fingering states are observable. This is consistent with the experimental observations, and further confirms that material anisotropy is not responsible for the observed fingering behavior.

Appendix A

Physical parameter values

Parameter	Unit	Gas	Solid	Other
c_{p}	$\mathrm{Jkg^{-1}\ K^{-1}}$	1142	1270	–
ρ	$\mathrm{kgm^{-3}}$	1376	540	–
D	$\mathrm{m^2s^{-1}}$	$2.5\ \times 10^{-5}$	–	–
λ	$\mathrm{Wm^{-1}\ K^{-1}}$	0.0238	0.07	–
T_a	K	–	–	14432
T_u	K	300	300	–
Q	$\mathrm{Jmol^{-1}}$	–	–	11200
A	$\mathrm{s^{-1}}$	–	–	$2\ \times 10^{6}$

Table A.1: Physico-chemical parameters.

Appendix B

Proof of Lemma 4.4.1

B.1 Energy estimate for C^ϵ

Proof. Consider the functions (C_D, T_D) to be extended in the whole of $\overline{\Omega}$ to be smooth enough. Let $C_j, j = 1, 2, 3, \cdots$ be constants not depending on ϵ, but depending on the data and parameters of the microscopic equations. We take $\phi = C^\epsilon - C_D$ in (4.30), and we obtain

$$\begin{aligned} &\iint_{0\Omega_g^\epsilon}^{t} \frac{\partial C^\epsilon}{\partial s}(C^\epsilon - C_D)dxds + \iint_{0\Omega_g^\epsilon}^{t} D\nabla C^\epsilon \nabla(C^\epsilon - C_D)dxds \qquad \text{(B.1)} \\ &+ \iint_{0\Omega_g^\epsilon}^{t} \boldsymbol{u}^\epsilon \nabla C^\epsilon (C^\epsilon - C_D)dxds = -\epsilon \iint_{0\Gamma^\epsilon}^{t} C^\epsilon f(T^\epsilon)(C^\epsilon - C_D)d\gamma ds. \end{aligned}$$

We use the boundedness of f on the right hand side integral of (B.1)

$$\begin{aligned} &\int_{\Omega_g^\epsilon} |C^\epsilon|^2 dx + D \iint_{0\Omega_g^\epsilon}^{t} |\nabla C^\epsilon|^2 dxds \qquad \text{(B.2)} \\ &= \iint_{0\Omega_g^\epsilon}^{t} \frac{\partial C^\epsilon}{\partial s} C_D dxds + \iint_{0\Omega_g^\epsilon}^{t} D\nabla C^\epsilon \nabla C_D dxds - \iint_{0\Omega_g^\epsilon}^{t} \boldsymbol{u}^\epsilon \cdot \nabla C^\epsilon C^\epsilon dxds + \iint_{0\Omega_g^\epsilon}^{t} \boldsymbol{u}^\epsilon \nabla C^\epsilon C_D dxds \\ &+ \epsilon \left(\iint_{0\Gamma^\epsilon}^{t} (C^\epsilon C_D - |C^\epsilon|^2) d\gamma ds \right) + \frac{1}{2} \int_{\Omega} |C^\epsilon(0)|^2 dx \\ &= \sum_{j=1}^{6} \mathscr{I}_j, \end{aligned}$$

where the summation represents the integral sum on the right hand side of (B.2). We estimate the terms $\mathscr{I}_j, j = 1, 2, \cdots, 6$ separately. Integrating $\mathscr{I}_1$ by parts with respect to

the time variable, we obtain

$$\begin{aligned}
&\int_0^t\int_{\Omega_g^\epsilon} \frac{\partial C^\epsilon}{\partial s} C_D dx ds = -\int_0^t\int_{\Omega_g^\epsilon} \frac{\partial C_D}{\partial s} C^\epsilon dx ds + \Big[\int_{\Omega_g^\epsilon} C^\epsilon(s) C_D(s) dx\Big]\Big|_{s=0}^{s=t} \qquad \text{(B.3)}\\
&\leq \frac{1}{2}\int_0^t\int_{\Omega_g^\epsilon} (|C^\epsilon|^2 + \Big|\frac{\partial C_D}{\partial t}\Big|^2) dx ds + \int_{\Omega_g^\epsilon} (\frac{\delta}{2}|C^\epsilon|^2 + \frac{1}{2\delta}|C_D|^2) dx\\
&+ \int_\Omega (\frac{1}{2}|C^\epsilon(0)|^2 + \frac{1}{2}|C_D(0)|^2) dx.\\
&\leq C_3 \left\|C^\epsilon\right\|^2_{\Omega_g^\epsilon,\tau} + C_4 \left\|\frac{\partial C_D}{\partial t}\right\|^2_{\Omega,\tau} + C_1(\delta)\left\|C^\epsilon(t)\right\|^2_{\Omega_g^\epsilon} + C_2(\delta)\left\|C_D(t)\right\|^2_{\Omega}\\
&+ C_3(\delta)\left\|C^\epsilon(0)\right\|^2_{\Omega_g^\epsilon} + C_4(\delta)\left\|C_D(0)\right\|^2_{\Omega}.
\end{aligned}$$

where the last integrals on the right hand side of (B.3) follow by a combination of Cauchy-Schwartz and Young's inequalities. Similarly, $\mathscr{I}_2$ is given by

$$\begin{aligned}
&\int_0^t\int_{\Omega_g^\epsilon} C_1 \nabla C^\epsilon \nabla C_D dx ds \leq D\int_0^t\int_{\Omega_g^\epsilon} (|\nabla C^\epsilon|^2 + |\nabla C_D|^2) dx ds \qquad \text{(B.4)}\\
&\leq C_1\left\|\nabla C^\epsilon\right\|^2_{\Omega_g^\epsilon,\tau} + C_2\left\|C_D\right\|^2_{\Omega,\tau}.
\end{aligned}$$

$\mathscr{I}_3$ vanishes due $\boldsymbol{u}^\epsilon$ is divergence free in Ω_g^ϵ and $n\cdot\boldsymbol{u}^\epsilon\Big|_{\partial\Omega} = 0, \boldsymbol{u}\Big|_{\Gamma^\epsilon} = 0$, i.e.

$$\begin{aligned}
&\int_0^t\int_{\Omega_g^\epsilon} \boldsymbol{u}^\epsilon\cdot\nabla C^\epsilon C^\epsilon dx ds = \frac{1}{2}\int_0^t\int_{\Omega_g^\epsilon} \boldsymbol{u}^\epsilon\cdot\nabla|C^\epsilon|^2 dx ds \qquad \text{(B.5)}\\
&= -\frac{1}{2}\int_0^t\int_{\Omega_g^\epsilon} \nabla\boldsymbol{u}^\epsilon\nabla|C^\epsilon|^2 dx ds - \int_0^t\int_{\partial\Omega} n\cdot\boldsymbol{u}^\epsilon dx ds = 0.
\end{aligned}$$

The next term $\mathscr{I}_4$ can be estimated as follows: we use the uniform bound on $\boldsymbol{u}^\epsilon$ (cf. A5 of Subsection 4.3.1), and a combination of Cauchy-Schwartz and Young's inequalities

$$\begin{aligned}
&\int_0^t\int_{\Omega_g^\epsilon} \boldsymbol{u}^\epsilon\nabla C^\epsilon C_D dx ds \leq M_u\int_0^t\Big(\int_{\Omega_g^\epsilon} |\nabla C^\epsilon(t)|^2 dx\Big)^{1/2}\Big(\int_\Omega |C_D(s)|^2 dx\Big)^{1/2} ds \qquad \text{(B.6)}\\
&\leq \frac{\delta M_u}{2}\left\|\nabla C^\epsilon\right\|^2_{\Omega_g^\epsilon,\tau} + \frac{1}{2\delta}\left\|C_D\right\|^2_{\Omega,\tau}.
\end{aligned}$$

The term $\mathscr{I}_5$ is estimated by using the trace inequality given in Lemma 4.27. We obtain

$$\epsilon\left(\int_0^t\int_{\Gamma^\epsilon}(C^\epsilon C_D-|C^\epsilon|^2)d\gamma ds\right)=C_6(\|C^\epsilon\|^2_{\Omega_g^\epsilon,\tau}+\epsilon^2\|\nabla C^\epsilon\|^2_{\Omega_g^\epsilon,\tau}) \tag{B.7}$$
$$+C_7(\|C_D\|^2_{\Omega,\tau}+\epsilon^2\|\nabla C_D\|^2_{\Omega,\tau}).$$

Summing up all the terms and choosing δ conveniently with $\epsilon<1$ gives

$$\|C^\epsilon(t)\|^2_{\Omega_g^\epsilon}+(D-C(\delta)-\epsilon^2C_{12})\|\nabla C^\epsilon\|^2_{\Omega_g^\epsilon,\tau} \tag{B.8}$$
$$\leq C_8\|C^\epsilon\|^2_{\Omega_g^\epsilon,\tau}+C_9\left\|\frac{\partial C_D}{\partial t}\right\|^2_{\Omega_g^\epsilon,\tau}+C_{10}(\|C^\epsilon(0)\|^2_\Omega+\|C_D(0)\|^2_\Omega)$$
$$+C_{12}\|C_D\|^2_{\Omega,\tau}+(\epsilon^2C_{13}+D)\|\nabla C_D\|^2_{\Omega,\tau}+C_{14}\|C^\epsilon(0)\|^2_{\Omega_g^\epsilon}.$$

The desired estimate is deduced after application of the Gronwall inequality. Now, using the results established in (B.8) and Lemma 4.3.2, there exist a constant C which is independent of ϵ such that

$$\sqrt{\epsilon}\,\|C^\epsilon\|_{L^2(0,\tau;L^2(\Gamma^\epsilon))}\leq C\,\|C^\epsilon\|_{L^2(0,\tau;H^1(\Omega_g^\epsilon))}. \tag{B.9}$$

□

B.2 Energy estimate for T^ϵ

Proof. We take $\varphi=T^\epsilon-T_D$ in (4.31), to get

$$\int_0^t\int_\Omega\mathcal{C}^\epsilon\frac{\partial T^\epsilon}{\partial s}(T^\epsilon-T_D)dxds+\int_0^t\int_\Omega\lambda^\epsilon\nabla T^\epsilon\nabla(T^\epsilon-T_D)dxds \tag{B.10}$$
$$+\int_0^t\int_\Omega\chi_g^\epsilon\mathcal{C}_g\boldsymbol{u}^\epsilon\nabla T^\epsilon(T^\epsilon-T_D)dxds=\epsilon Q\int_0^t\int_{\Gamma^\epsilon}C^\epsilon f(T^\epsilon)(T^\epsilon-T_D)d\gamma ds.$$

Since f is a positive function on the closed surface Γ^ϵ and C^ϵ is bounded according to (B.9), we have that

$$\int_0^t\int_{\Gamma^\epsilon}f(T^\epsilon)(T^\epsilon-T_D)d\gamma ds\geq 0. \tag{B.11}$$

Using the boundedness of $\mathcal{C}^\epsilon$ in the first integral, the coercivity and boundedness of λ^ϵ in the second integral, and the fact that the convective term vanishes in the energy term

$|\nabla T^\epsilon|^2$ of the third integral, we obtain successively for each of the integral terms:

$$\int_0^t\int_\Omega \mathcal{C}^\epsilon \frac{\partial T^\epsilon}{\partial s}(T^\epsilon - T_D)dxds = \frac{\mu_0}{2}\int_0^t\int_\Omega \frac{\partial}{\partial s}\left|T^\epsilon\right|^2 dxds - \mu_0\int_0^t\int_\Omega \frac{\partial T^\epsilon}{\partial s}T_D dxds \quad \text{(B.12)}$$

$$= \frac{\mu_0}{2}\int_0^t\int_\Omega \frac{\partial}{\partial s}\left|T^\epsilon\right|^2 dxds + \mu_0\int_0^t\int_\Omega \frac{\partial T_D}{\partial s}T^\epsilon dxds - \left[\mu_0\int_\Omega T_D(s)T^\epsilon(s)dx\right]\Big|_{s=0}^{s=t}.$$

Applying the Young's inequality and collecting terms on the proper sides, we have

$$\frac{\mu_0}{2}(1-\frac{\delta}{2})\left\|T^\epsilon\right\|_\Omega^2 \le \frac{\mu_0}{2}(1+\delta)\left\|T^\epsilon(0)\right\|_\Omega^2 + \frac{\mu_0}{2}\left\|\frac{\partial T_D}{\partial s}\right\|_{\Omega,\tau}^2 \quad \text{(B.13)}$$

$$+\frac{\mu_0}{2\delta}\left\|T_D(0)\right\|_\Omega^2 + \frac{\mu_0}{2\delta}\left\|T_D\right\|_\Omega^2 + \frac{\mu_0}{2\delta}\left\|T_D(0)\right\|_\Omega^2.$$

The last two integral terms give

$$(\lambda_0 - \frac{\delta\lambda_1}{2})\left\|\nabla T^\epsilon\right\|_{\Omega,\tau}^2 \le \frac{\lambda_1}{2\delta}\left\|\nabla T_D\right\|_{\Omega,\tau}^2 + \frac{\mu_1 M_u}{2}\left\|\nabla T^\epsilon\right\|_{\Omega,\tau}^2 + \frac{1}{2}\left\|T_D\right\|_{\Omega,\tau}^2. \quad \text{(B.14)}$$

Summing up (B.13)–(B.14), we obtain

$$\mu_0(1-\frac{\delta}{2})\left\|T^\epsilon\right\|_\Omega^2 + (C_3 - \frac{\lambda_1\delta}{2})\left\|\nabla T^\epsilon\right\|_{\Omega,\tau}^2 \quad \text{(B.15)}$$

$$\le C_1(\left\|T_D\right\|_{\Omega,\tau}^2 + \left\|\nabla T_D\right\|_{\Omega,\tau}^2 + \left\|\frac{\partial T_D}{\partial t}\right\|_{\Omega,\tau}^2$$

$$+ \left\|T_D(0)\right\|_\Omega^2 + \left\|T_D\right\|_\Omega^2 + \left\|T^\epsilon(0)\right\|_{\Omega,\tau}^2) + C_2\left\|T^\epsilon\right\|_{\Omega,\tau}^2.$$

Now, choosing δ conveniently and applying Gronwall's inequality, we obtain the desired result

$$\left\|T^\epsilon\right\|_{L^2(0,\tau;L^2(\Omega))} + \left\|\nabla T^\epsilon\right\|_{L^2(0,\tau;L^2(\Omega))} \le C. \quad \text{(B.16)}$$

Since we have equipartition of the energy of the gradient in the constituent phases, i.e.

$$\int_0^t\int_\Omega \left|\nabla T^\epsilon\right|^2 dxds = \int_0^\tau\int_\Omega \chi_{\mathrm{g}}^\epsilon\left|\nabla T^\epsilon\right|^2 dxds + \int_0^\tau\int_\Omega \chi_{\mathrm{s}}^\epsilon\left|\nabla T^\epsilon\right|^2 dxds \quad \text{(B.17)}$$

$$= \int_0^t\int_{\Omega_{\mathrm{g}}^\epsilon} \left|\nabla T^\epsilon\right|^2 dxds + \int_0^\tau\int_{\Omega_{\mathrm{s}}^\epsilon} \left|\nabla T^\epsilon\right|^2 dxds$$

$$= \left\|\nabla T^\epsilon\right\|_{L^2(0,\tau;L^2(\Omega_{\mathrm{g}}^\epsilon))}^2 + \left\|\nabla T^\epsilon\right\|_{L^2(0,\tau;L^2(\Omega_{\mathrm{s}}^\epsilon))}^2 \le C,$$

we deduce by using (B.16), (B.19), and Lemma 4.3.2 that there exists a constant C, not depending on ϵ, such that

$$\sqrt{\epsilon}\,\|T^\epsilon\|_{L^2(0,\tau;L^2(\Gamma^\epsilon))} \le C\,\|T^\epsilon\|_{L^2(0,\tau;H^1(\Omega_g^\epsilon))}\,. \tag{B.18}$$

Thus,

$$\sqrt{\epsilon}\,\|T^\epsilon\|_{L^2(0,\tau;L^2(\Gamma^\epsilon))} \le C. \tag{B.19}$$

□

B.3 Energy estimates for R^ϵ

Proof. We set as test function $\psi = R^\epsilon$ in (4.32) and obtain the following

$$\begin{aligned}
&\epsilon \int_0^t\!\!\int_{\Gamma^\epsilon} \frac{\partial}{\partial s}\,|R^\epsilon|^2\,d\gamma ds = 2\epsilon A \int_0^t\!\!\int_{\Gamma^\epsilon} f(T^\epsilon) C^\epsilon R^\epsilon d\gamma ds \qquad \text{(B.20)}\\
&\le \epsilon C \int_0^t\!\!\int_{\Gamma^\epsilon} (|C^\epsilon|^2 + |R^\epsilon|^2) d\gamma ds\\
&\epsilon \int_{\Gamma^\epsilon} |R(t)^\epsilon|^2\,d\gamma \le C(1 + \epsilon \int_0^t\!\!\int_{\Gamma^\epsilon} |R^\epsilon|^2\,d\gamma ds).
\end{aligned}$$

The first integral on the right hand side of the inequality is bounded by Lemma 4.3.2. Thus, by Gronwall's inequality we have the desired result. Now, testing (4.32) with $\psi = \dfrac{\partial R^\epsilon}{\partial t}$, we obtain

$$\begin{aligned}
&\epsilon \int_0^t\!\!\int_{\Gamma^\epsilon} \left|\frac{\partial R^\epsilon}{\partial s}\right|^2 d\gamma ds = \epsilon A \int_0^t\!\!\int_{\Gamma^\epsilon} f(T^\epsilon) C^\epsilon \frac{\partial R^\epsilon}{\partial s} d\gamma ds \qquad \text{(B.21)}\\
&\le \epsilon A \int_0^t\!\!\int_{\Gamma^\epsilon} (\frac{1}{2\delta}\,|C^\epsilon|^2 + \frac{\delta}{2}\left|\frac{\partial R^\epsilon}{\partial s}\right|^2) d\gamma ds, \text{ and hence}\\
&\epsilon(1 - \frac{A\delta}{2}) \int_0^t\!\!\int_{\Gamma^\epsilon} \left|\frac{\partial R^\epsilon}{\partial s}\right|^2 d\gamma ds \le \epsilon \frac{A}{2\delta} \int_0^t\!\!\int_{\Gamma^\epsilon} |C^\epsilon|^2\,d\gamma ds.
\end{aligned}$$

Choosing δ conveniently and applying Lemma 4.3.2 lead to the desired result. □

Appendix C

Proof of Lemma 4.4.2

C.1 Energy estimate for $\partial_t C^\epsilon$

Proof. For suitable extension of the initial and boundary data of (C^ϵ, T^ϵ), we take in (4.30) a test function $\phi = \dfrac{\partial}{\partial t}(C^\epsilon - C_D)$. We obtain that, after using the boundedness of f and the assumptions on $\boldsymbol{u}^\epsilon$:

$$\begin{aligned}
&\frac{D}{2}\int\limits_{\Omega_{\mathrm{g}}^\epsilon} |\nabla C^\epsilon|^2\, dx + \int\limits_0^t\int\limits_{\Omega_{\mathrm{g}}^\epsilon} \left|\frac{\partial C^\epsilon}{\partial s}\right|^2 dxds \le \int\limits_0^t\int\limits_{\Omega_{\mathrm{g}}^\epsilon} \frac{\partial C^\epsilon}{\partial s}\frac{\partial C_D}{\partial s} dxds \qquad \text{(C.1)}\\
&+D\int\limits_0^t\int\limits_{\Omega_{\mathrm{g}}^\epsilon} \nabla C^\epsilon \frac{\partial}{\partial t}\nabla C_D dxds + \int\limits_0^t\int\limits_{\Omega_{\mathrm{g}}^\epsilon} \boldsymbol{u}^\epsilon \nabla C^\epsilon \frac{\partial C_D}{\partial s} dxds\\
&-\epsilon\int\limits_0^t\int\limits_{\Gamma^\epsilon} C^\epsilon \frac{\partial C^\epsilon}{\partial s} d\gamma ds + \epsilon\int\limits_0^t\int\limits_{\Gamma^\epsilon} C^\epsilon \frac{\partial C_D}{\partial t} d\gamma ds + \frac{D}{2}\int\limits_{\Omega_{\mathrm{g}}^\epsilon} |\nabla C^\epsilon(0)|^2\, dx.
\end{aligned}$$

The boundary terms can be estimated using the trace inequality, i.e.

$$\begin{aligned}
&-\epsilon\int\limits_0^t\int\limits_{\Gamma^\epsilon} \frac{\partial}{\partial s}|C^\epsilon|^2\, d\gamma ds = \epsilon\int\limits_{\Gamma^\epsilon} |C^\epsilon|^2\, d\gamma + \epsilon\int\limits_{\Gamma^\epsilon} |C^\epsilon(0)|^2\, d\gamma \qquad \text{(C.2)}\\
&= -C_1\Big(\|C^\epsilon(t)\|^2_{\Omega_{\mathrm{g}}^\epsilon} + \epsilon^2 \|\nabla C^\epsilon(t)\|^2_{\Omega_{\mathrm{g}}^\epsilon}) + C_2(\|C^\epsilon(0)\|^2_{\Omega_{\mathrm{g}}^\epsilon} + \epsilon^2 \|\nabla C^\epsilon(0)\|^2_{\Omega_{\mathrm{g}}^\epsilon}\Big)
\end{aligned}$$

and

$$\epsilon \int_0^t \int_{\Gamma^\epsilon} C^\epsilon \frac{\partial C_D}{\partial s} d\gamma ds \leq C_1 \int_0^t \int_{\Omega_g^\epsilon} (|C^\epsilon|^2 + \epsilon^2 |\nabla C^\epsilon|^2) dx ds \tag{C.3}$$
$$+ \int_0^t \int_{\Omega_g^\epsilon} \left(\left| \frac{\partial C_D}{\partial s} \right|^2 + \epsilon^2 \left| \nabla \frac{\partial C_D}{\partial s} \right|^2 \right) dx ds$$
$$= C_3 \|C^\epsilon\|^2_{\Omega_g^\epsilon,\tau} + \epsilon^2 C_4 \|\nabla C^\epsilon\|^2_{\Omega_g^\epsilon,\tau} + C_5 \left\| \frac{\partial C_D}{\partial t} \right\|^2_{\Omega_g^\epsilon,\tau} + \epsilon^2 C_6 \left\| \nabla \frac{\partial C_D}{\partial t} \right\|^2_{\Omega_g^\epsilon,\tau}.$$

The remaining integrals can be estimated as follows:

$$\int_0^t \int_{\Omega_g^\epsilon} \left(\frac{\delta}{2} \left| \frac{\partial C^\epsilon}{\partial s} \right|^2 + \frac{1}{2\delta} \left| \frac{\partial C_D}{\partial s} \right|^2 \right) dx ds + \frac{D}{2} \int_0^t \int_{\Omega_g^\epsilon} |\nabla C^\epsilon|^2 dx ds \tag{C.4}$$
$$+ \frac{D}{2} \int_0^t \int_{\Omega_g^\epsilon} \left| \frac{\partial}{\partial s} \nabla C_D \right|^2 dx ds + \frac{\delta M_u}{2} \int_0^t \int_{\Omega_g^\epsilon} |\nabla C^\epsilon|^2 dx ds + \frac{1}{2\delta} \int_0^t \int_{\Omega_g^\epsilon} \left| \frac{\partial C_D}{\partial s} \right|^2 dx ds.$$

Summing all the integral estimates from (C.2)–(C.4) results to

$$(1 - C_1(\delta)) \left\| \frac{\partial C^\epsilon}{\partial t} \right\|^2_{\Omega_g^\epsilon,\tau} + (D + \epsilon^2 C_7) \|\nabla C^\epsilon\|^2_{\Omega_g^\epsilon} \tag{C.5}$$
$$\leq (C_1 - \epsilon^2 C_{12}) \|\nabla C^\epsilon(0)\|^2_{\Omega_g^\epsilon} + C_8 \|C^\epsilon\|^2_{\Omega_g^\epsilon,\tau} + C_{11} \|C^\epsilon(0)\|^2_{\Omega_g^\epsilon}$$
$$+ (C_9 + C_2(\delta) + \epsilon^2 C_{10}) \|\nabla C^\epsilon\|^2_{\Omega_g^\epsilon,\tau} + C_{13} \left\| \frac{\partial C_D}{\partial t} \right\|^2_{\Omega_g^\epsilon,\tau} + (C_{14} + \epsilon^2 C_{15}) \left\| \nabla \frac{\partial C_D}{\partial t} \right\|^2_{\Omega_g^\epsilon,\tau}.$$

Now, by choosing δ and $\epsilon < 1$ conveniently and using the inequalities in Lemma 4.4.1 together with (A4) and (A6), we obtain

$$\left\| \frac{\partial C^\epsilon}{\partial t} \right\|_{L^2(0,\tau;L^2(\Omega_g^\epsilon))} \leq C. \tag{C.6}$$

□

C.2 Energy estimate for $\partial_t T^\epsilon$

Proof. We take $\varphi = \dfrac{\partial}{\partial t}(T^\epsilon - T_D)$ in (4.31) such that after using the boundedness of $f, \mathcal{C}^\epsilon$ and the coercivity of λ^ϵ, and divergence free assumption on $\boldsymbol{u}^\epsilon$, we obtain

$$\begin{aligned}
&\frac{\lambda_0}{2}\int_\Omega |\nabla T^\epsilon|^2\,dx + \mu_1 \int_0^t\int_\Omega \left|\frac{\partial T^\epsilon}{\partial s}\right|^2 dxds \le \lambda_0 \int_0^t\int_\Omega \frac{\partial T^\epsilon}{\partial s}\frac{\partial T_D}{\partial s}dxds \qquad \text{(C.7)}\\
&+\lambda_0 \int_0^t\int_\Omega \nabla T^\epsilon \frac{\partial}{\partial s}\nabla T_D dxds + \lambda_1 \int_0^t\int_\Omega \chi_{\mathrm{g}}^\epsilon \boldsymbol{u}^\epsilon \nabla T^\epsilon \frac{\partial T_D}{\partial s}dxds\\
&+\epsilon Q \int_0^t\int_{\Gamma^\epsilon} C^\epsilon \frac{\partial T^\epsilon}{\partial s}d\gamma ds - \epsilon Q \int_0^t\int_{\Gamma^\epsilon} C^\epsilon \frac{\partial T_D}{\partial s}d\gamma ds + \frac{\lambda_0}{2}\int_\Omega |\nabla T^\epsilon(0)|^2\,dx.
\end{aligned}$$

The boundary integrals can be estimated as follows: integration by parts and application of the Young's inequality yields

$$\begin{aligned}
&\epsilon \int_0^t\int_{\Gamma^\epsilon} C^\epsilon \frac{\partial T^\epsilon}{\partial s}d\gamma ds = -\epsilon \int_0^t\int_{\Gamma^\epsilon} T^\epsilon \frac{\partial C^\epsilon}{\partial s}d\gamma ds + \Big[\epsilon \int_{\Gamma^\epsilon} C^\epsilon(s)T^\epsilon(s)d\gamma\Big]\Big|_{s=0}^{s=t} \qquad \text{(C.8)}\\
&\le \frac{\epsilon}{2}\int_0^t\int_{\Gamma^\epsilon} (|T^\epsilon|^2 + \left|\frac{\partial C^\epsilon}{\partial s}\right|^2)d\gamma ds + \Big[\frac{\epsilon}{2}(\int_{\Gamma^\epsilon} |C^\epsilon|^2 + |T^\epsilon|^2)d\gamma ds\Big]\Big|_{s=0}^{s=t}\\
&= C(1 + \int_0^t\int_{\Omega_{\mathrm{g}}^\epsilon} (\left|\frac{\partial C^\epsilon}{\partial s}\right|^2 + \epsilon^2 \left|\nabla \frac{\partial C^\epsilon}{\partial s}\right|^2)dxds\\
&= C.
\end{aligned}$$

Remark C.2.1. *In* (C.8)*, we have used the boundedness of* C^ϵ *in* (B.9)*, as well as the estimate on its time derivative established in* (C.6)*.*

Furthermore, we have

$$
\begin{aligned}
&-\epsilon \int_0^t \int_{\Gamma^\epsilon} C^\epsilon \frac{\partial T_D}{\partial s} d\gamma ds = \epsilon \int_0^t \int_{\Gamma^\epsilon} T_D \frac{\partial C^\epsilon}{\partial s} d\gamma ds - \left[\epsilon \int_{\Gamma^\epsilon} C^\epsilon(s) T_D(s) d\gamma\right]\Big|_{s=0}^{s=t} \qquad \text{(C.9)}\\
&\leq \frac{\epsilon}{2} \int_0^t \int_{\Gamma^\epsilon} (|T_D|^2 + \left|\frac{\partial C^\epsilon}{\partial s}\right|^2) d\gamma ds + \left[\frac{\epsilon}{2} (\int_{\Gamma^\epsilon} |C^\epsilon|^2 + |T_D|^2) d\gamma ds\right]\Big|_{s=0}^{s=t}\\
&= C_1 \int_0^t \int_{\Omega_g^\epsilon} (\left|\frac{\partial C^\epsilon}{\partial s}\right|^2 + \epsilon^2 \left|\nabla \frac{\partial C^\epsilon}{\partial s}\right|^2) dx ds + C_2 \int_0^\tau \int_\Omega (|T_D|^2 + \epsilon^2 |\nabla T_D|^2) dx ds\\
&+ C_3 \int_\Omega (|T_D(t)|^2 + \epsilon^2 |\nabla T_D(t)|^2) dx - C_4 \int_\Omega (|T_D(0)|^2 + \epsilon^2 |\nabla T_D(0)|^2) dx\\
&= C + C_2(\|T_D\|_{\Omega,\tau}^2 + \epsilon^2 \|\nabla T_D\|_{\Omega,\tau}^2 + C_3(\|T_D(t)\|_\Omega^2 + \epsilon^2 \|\nabla T_D(t)\|_\Omega^2)\\
&- C_4(\|T_D(0)\|_\Omega^2 + \epsilon^2 \|\nabla T_D(0)\|_\Omega^2).
\end{aligned}
$$

(C.8) and (C.9) show that the boundary terms are bounded, which we may simply represent as $\mathcal{K}$. The remaining integrals are estimated as follows:

$$
\begin{aligned}
&\int_0^t \int_\Omega \left(\frac{\delta \mu_1}{2} \left|\frac{\partial T^\epsilon}{\partial s}\right|^2 + \frac{\mu_1}{2\delta} \left|\frac{\partial T_D}{\partial s}\right|^2\right) dx ds + \frac{\lambda_1 \delta}{2} \int_0^t \int_\Omega |\nabla T^\epsilon|^2 dx ds \qquad \text{(C.10)}\\
&+ \frac{\lambda_1}{2\delta} \int_0^t \int_\Omega \left|\frac{\partial}{\partial s} \nabla T_D\right|^2 dx ds + \frac{\delta M_u \mu_1}{2} \int_0^t \int_\Omega |\nabla T^\epsilon|^2 dx ds + \frac{\mu_1}{2\delta} \int_0^t \int_\Omega \left|\frac{\partial T_D}{\partial s}\right|^2 dx ds.
\end{aligned}
$$

Summing up all the integral estimates from (C.8)–(C.10) results to

$$
\begin{aligned}
&\mu_1 (1 - \frac{\delta}{2}) \left\|\frac{\partial T^\epsilon}{\partial t}\right\|_{\Omega,\tau}^2 + \frac{1}{2}(\lambda_0 - \mu_1 \delta M_u) \|\nabla T^\epsilon(t)\|_\Omega^2 \qquad \text{(C.11)}\\
&\leq \frac{\mu_1}{\delta} \left\|\frac{\partial T_D}{\partial t}\right\|_{\Omega,\tau}^2 + \frac{\lambda_1}{2\delta} \left\|\nabla \frac{\partial T_D}{\partial t}\right\|_{\Omega,\tau}^2\\
&+ \frac{\lambda_1 \delta}{2} \|\nabla T^\epsilon\|_{\Omega,\tau}^2 + \frac{\lambda_0}{2} \|\nabla T^\epsilon(0)\|_\Omega^2 + \mathcal{K}.
\end{aligned}
$$

Now, by choosing δ and $\epsilon < 1$ conveniently and using the inequalities in Lemma 4.4.1 together with (A4), we obtain

$$
\left\|\frac{\partial T^\epsilon}{\partial t}\right\|_{L^2(0,\tau;L^2(\Omega))} \leq C. \qquad \text{(C.12)}
$$

□

Bibliography

Adams, R. A. and Fournier, J. J. F. (2003). *Sobolev Spaces*. Academic Press.

Aldushin, A. and Braverman, B. S. (2009). Hydrodynamic instability of filtration combustion wave. In *Doklady Physical Chemistry*, volume 427, pages 125–128. Springer.

Aldushin, A. and Matkowsky, B. (1998). Instabilities, fingering and the Saffman-Taylor problem in filtration combustion. *Combust. Sci. Technol.*, 133(4-6):293–341.

Allaire, G. (1992). Homogenization and two-scale convergence. *SIAM J. Math. Anal.*, 23(6):1482–1518.

Allaire, G., Brizzi, R., Mikelic, A., and Piatnitski, A. (2010). Two-scale expansion with drift approach to the Taylor dispersion for reactive transport through porous media. *Chem. Engrg. Sci.*, 65(7):2292–2300.

Allaire, G., Damlamian, A., and Hornung, U. (1995). Two-scale convergence on periodic surfaces and applications. World Scientific Publishing Co. Pte. Ltd.

Allaire, G. and El Ganaoui, K. (2009). Homogenization of a conductive and radiative heat transfer problem. *Multiscale Modeling and Simulation*, 7(3):1148–1170.

Allaire, G. and Habibi, Z. (2013). Homogenization of a conductive, convective, and radiative heat transfer problem in a heterogeneous domain. *SIAM Journal on Mathematical Analysis*, 45(3):1136–1178.

Allaire, G. and Murat, F. (1993). Homogenization of the Neumann problem with nonisolated holes. *Asymptotic Analysis*, 7:81–95.

Aly, S. L. (1990). Flame structure and reaction kinetics: The effects of the pre-exponential frequency factor, reaction order, and activation energy. *Appl. Energy*, 37:139–150.

Arbogast, T., Douglas, J., and Hornung, U. (1990). Derivation of the double porosity model of single phase flow via homogenization theory. *SIAM J. Math. Anal.*, 21:823–836.

Auriault, J., Boutin, C., and Geindreau, C. (2009). *Homogenization of Coupled Phenomena in Heterogeneous Media*. ISTE Ltd, London.

Auriault, J. L. (1991). Heterogeneous medium. is an equivalent macroscopic description possible? *Int. J. Engng. Sci.*, 29(7):785–795.

Auriault, J. L. and Adler, P. (1995). Taylor dispersion in porous media: Analysis by multiple scale expansions. *Advances in Water Resources*, 18(4):217–226.

Bakhvalov, N. and Panasenko, G. (1989). *Homogenisation: Averaging Processes in Periodic Media*, volume 36 of *Mathematics and its Applications (Soviet Series)*. Kluwer Academic Publishers Group, Dordrecht.

Bensoussan, A., Lions, J. L., and Papanicolaou, G. (1978). *Asymptotic Analysis for Periodic Structures*, volume 5 of *Studies in Mathematics and its Application*. North-Holland.

Britten, J. A. and Kranz, W. B. (1985). Linear stability of planar reverse combustion in porous media. *Combust. Flame*, 60(125).

Buckmaster, J. D. (1985). *The Mathematics of Combustion*. Frontiers in Combustion. Society of Industrial and Applied Mathematics.

Chechkin, G. and Piatnitski, A. (1999). Homogenization of boundary-value-problem in locally periodic perforated domain. *Applicable Anal.*, 71:215–235.

Chen, R.-H., Mitchell, G. B., and Ronney, P. D. (1992). Diffusive-thermal instability and flame extinction in nonpremixed combustion. In *Symposium (International) on Combustion*, volume 24, pages 213–221. Elsevier.

Cheng, P., Bestehorn, M., and Firoozabadi, A. (2012). Effect of permeability anisotropy on buoyancy-driven flow for co2 sequestration in saline aquifers. *Water Resources Research*, 48(9).

Cioranescu, D., Damlamian, A., and Griso, G. (2002). Periodic unfolding and homogenization. *SIAM J. Math. Anal.*, 40(4):1585–1620.

Cioranescu, D. and Donato, P. (1999). *An Introduction to Homogenization*. Oxford University Press, New York.

Cioranescu, D., Donato, P., and Zaki, R. (2006). Periodic unfolding and Robin problems in perforated domains. *C. R. Acad. Sci. Paris*, Ser. I(342):469–474.

Cioranescu, D. and Paulin, J. S. J. (1979). Homogenization in open sets with holes. *J. Math. Anal. Appl.*, 71:590–607.

Cioranescu, D. and Paulin, J. S. J. (1998). *Homogenization of Reticulated Structures*. Springer, New York.

Decker, M. and Schult, D. (2004). Dynamics of smoulder waves near extinction. *Combust. Theory Model.*, 8:491–512.

Di Blasi, C. (1995). Mechanisms of two-dimensional smoldering propagation through packed fuel beds. *Combust. Sci. Technol.*, 106:103–124.

Dinwiddie, R. B., White, M. A., and McElroy, D. L. (2006). *Thermal Conductivity 28*. DEStech Publications. Inc.

Evans, L. C. (1998). *Partial Differential Equations*, volume 19. AMS, Providence, Rhode Island USA.

Fasano, A., Mimura, M., and Primicerio, M. (2009). Modelling a slow smoldering combustion process. *Math. Methods Appl. Sci.*, pages 1–11.

Fatehi, M. and Kaviany, M. (1994). Adiabatic reverse combustion in a packed bed. *Combust. Flame*, 99:1–17.

Fatima, T., Arab, N., Zemskov, E., and Muntean, A. (2011). Homogenization of a reaction-diffusion system modeling sulfate corrosion in locally periodic perforated domains. *J. Eng. Math.*, 69:261–276.

Fatima, T. and Muntean, A. (2014). Sulfate attack in sewer pipes : derivation of a concrete corrosion model via two-scale convergence. *Nonlinear Anal.: Real World Applications*, 15:326–344.

Fatima, T., Muntean, A., and Ptashnyk, M. (2012). Unfolding-based corrector estimates for a reaction-diffusion system predicting concrete corrosion. *Applicable Analysis*, 91(6):1129–1154.

Griso, G. (2004). Error estimate and unfolding for periodic homogenization. *Asymptotic Anal.*, 40:269–286.

Hashin, Z. (1983). Analysis of composite materials. A survey. *J. Appl. Mech.*, 50:483–505.

Hashin, Z. and Shtrikman, S. (1963). A variational approach to the theory of the elastic behaviour of multiphase materials. *J. Mech. Phys. Solids.*, 11:127–140.

Henneke, M. R. and Ellzey, J. L. (1999). Modeling of filtration combustion in a packed bed. *Combust. Flame*, 117(4):832–840.

Hilsenrath, J., Beckett, C. W., Benedict, W. S., Fano, L., Hoge, H. J., Masi, J. F., Nuttall, R. L., Touloukian, Y. S., and Woolley, H. W. (1955). *Tables of Thermal Properties of Gases*. Natl. Bur. Stand. (U.S.), NBS Circular 564.

Hornung, U. (1997). *Homogenization and Porous Media*, volume 6 of *Interdisciplinary Applied Mathematics*. Springer-Verlag, New York.

Hornung, U. and Jäger, W. (1991). Diffusion, convection, adsorption and reaction of chemical in porous media. *J. Diff. Eqs.*, 92:199–225.

Hornung, U. and Showalter, R. E. (1990). Diffusion models for fractured media. *Math. Anal. Appl.*, 147:69–80.

Ijioma, E. R., Muntean, A., and Ogawa, T. (2013). Pattern formation in reverse smouldering combustion: A homogenisation approach. *Combust. Theory and Model.*, 17(2):185–223.

Ikeda, K. and Mimura, M. (2008). Mathematical treatment of a model for smoldering combustion. *Hiroshima Math. J.*, 38:349–361.

Kadowaki, S. (2005). The effects of heat loss on the burning velocity of cellular premixed flames generated by hydrodynamic and diffusive-thermal instabilities. *Combust. Flame*, 143(3):174–182.

Kagan, L. and Sivashinsky, G. (1996). Incomplete combustion in nonadiabatic premixed gas flames. *Physical Review E*, 53:6021–6027.

Kagan, L. and Sivashinsky, G. (2008). Pattern formation in flame spread over thin solid fuels. *Combust. Theory Model.*, 12:269–281.

Kang, S. H., Im, H. G., and Baek, S. W. (2003). A computational study of saffman-taylor instability in premixed flames. *Combust. Theory and Model.*, 7(2):343–363.

Kim, J., Williams, F., and Ronney, P. (1996). Diffusional-thermal instability of diffusion flames. *Journal of Fluid mechanics*, 327(1):273–301.

Leach, S., Rein, G., Ellzey, J., Ezekoye, O., and Torero, J. L. (1990). Kinetic and fuel property effects on forward smoldering combustion. *Combust. Flame*, 120(3):346–358.

Lewandowska, J., Szymkiewicz, A., and Auriault, J. L. (2005). Upscaling of Richards' equation for soils containing highly conductive inclusions. *Adv. Water Res.*, 28:1159–1170.

Lewandowska, J., Szymkiewicz, A., Burzyński, K., and Vauclin, M. (2004). Modeling of unsaturated water flow in double-porosity soils by the homogenization approach. *Adv. Water Res.*, 27:283–296.

Lions, J. L. (1969). *Quelques méthodes de résolution des problemes aux limites nonlinéaires*. Dunod, Paris.

Lu, C. and Yortsos, Y. (2005a). Pattern formation in reverse filtration combustion. *Phys. Rev. E.*, 72:036201(1–16).

Lu, C. and Yortsos, Y. C. (2005b). Dynamics of forward filtration combustion at the pore-network level. *AIChE journal*, 51(4):1279–1296.

Lu, Z., Buckmaster, J., Chen, M., and Massa, L. (2006). Instabilities of reverse smolder waves. *Combust. Theory Model.*, 10:515–534.

Lu, Z. and Dong, Y. (2011). Fingering instability in forward smolder combustion. *Combust. Theory and Model.*, 15(6):795–815.

Matkowsky, B. J. and Sivashinsky, G. I. (1978). Propagation of a pulsating reaction front in solid fuel combustion. *SIAM J. Appl. Math.*, 35(3):465–478.

Meier, S. A. (2008). *Two-scale models for reactive transport and evolving microstructure*. PhD thesis, Universität Bremen, Bremen,Germany.

Monsurro, S. (2003). Homogenization of a two-component composite with interfacial thermal barrier. *Adv. Math. Sci. Appl.*, 13(1):43–63.

Muntean, A. and Noorden, T. L. v. (2013). Corrector estimates for the homogenization of a locally-periodic medium with areas of low and high diffusivity. *European Journal of Applied Mathematics*, 24(5):657–677.

Neuss-Radu, M. (1996). Some extensions of two-scale convergence. *C. R. Acad. Sci. Paris Sér. I Math*, 332:899–904.

Nguestseng, G. (1989). A general convergence result for a functional related to the theory of homogenization. *SIAM J. Math. Anal*, 20:608–623.

Oliveira, A. and Kaviany, M. (2001). Nonequilibrium in the transport of heat and reactants in combustion in porous media. *Progress in Energy and Combustion Science*, 27:523–545.

Olson, S., Baum, H., and Kashiwagi, T. (1998). Finger-like smoldering over thin cellulose sheets in microgravity. *Twenty-Seventh Symposium (International) on Combustion*, pages 2525–2533.

Ozerkovskaya, N., Firsov, A., and Shkadinskii, K. (2010). Emergence of spatial structures during filtration combustion. *Combustion, Explosion, and Shock Waves*, 46(5):515–522.

Pelce, P. and Clavin, P. (1982). Influence of hydrodynamics and diffusion upon the stability limits of laminar premixed flames. *J. Fluid Mech.*, 124:219–237.

Persson, L. E., Persson, L., Svanstedt, N., and Wyller, J. (1993). *The Homogenization Method: An Introduction*. Chartwell-Bratt.

Rein, G. (2005). *Computational model of forward and opposed smoldering combustion with improved chemical kinetics*. PhD thesis, University of California, Berkeley.

Sanchez-Palencia, E. (1980). *Non-Homogeneous Media and Vibration Theory*, volume 127 of *Lecture Notes in Physics*. Springer.

Sanchez-Palencia, E. and Zaoui, A. (1985). *Homogenization Techniques for Composite Media*, volume 272 of *Lecture Notes in Physics*. Springer.

Schult, D., Matkowsky, B., Volpert, V., and Fernandez-Pello, A. (1995). Propagation and extinction of forced opposed smolder waves. *Combust. Flame*, 101:471–490.

Shah, A., Brindley, J., McIntosh, A., and Griffiths, J. (2007). Ignition and combustion of low-exothermicity porous materials by a local hotspot. *Proceedings of the Royal Society A: Mathematical, Physical and Engineering Science*, 463(2081):1287–1305.

Shkadinskii, K. and Firsov, A. (1996). Anisotropy of the characteristics of products behind the front of self-propagating high-temperature synthesis. *Combustion, Explosion and Shock Waves*, 32(6):667–673.

Sivashinsky, G. I. (1983). Instabilities, pattern formation, and turbulence in flames. *Annual Review of Fluid Mechanics*, 15(1):179–199.

Szymkiewicz, A. (2004). *Modeling of unsaturated water flow in highly heterogeneous soils*. PhD thesis, Gdańsk University of Technology, Poland.

Wahle, C., Matkowsky, B., and Aldushin, A. (2003). Effects of gas-solid nonequilibrium in filtration combustion. *Combust. Sci. and Tech.*, 175:1389–1499.

Wall, P. (1997). A comparison of homogenization, Hashin-Shtrikman bounds and the Halpin-Tsai equations. *Applications of Mathematics*, 42(4):245–257.

Wendt, F., Liebowitz, H., and Perrone, N. (1970). *Mechanics of Composite Materials*. Pergamon Press, Oxford.

Whitaker, S. (1999). *The Method of Volume Averaging*. Springer-Verlag, New York.

Yarin, L. P., Hetsroni, G., and Mosyak, A. (2004). *Combustion of Two-Phase Reactive Media*. Heat and Mass Transfer. Springer.

Yuan, F.-p. and Lu, Z.-b. (2013). Structure and stability of non-adiabatic reverse smolder waves. *Applied Mathematics and Mechanics*, pages 1–12.

Zhikov, V., Kozlov, S. M., and Oleĭnik, O. A. (1994). *Homogenization of Differential Operators and Integral Functionals*. Springer-Verlag.

Zik, O. and Moses, E. (1998). Fingering instability in combustion: The characteristic scales of the developed state. *Proceeding of Combustion Institute*, 27:2815–2820.

Zik, O. and Moses, E. (1999). Fingering instability in combustion: An extended view. *The American Phys. Soc.*, 60:518–531.

Zik, O., Olami, Z., and Moses, E. (1998). Fingering instability in combustion. *Phys. Rev. Lett.*, 81:3868–3871.

List of Figures

List of Tables

Nomenclature

Y	reference periodicity cell
Y_{s}	solid part of the periodicity cell
Y_{g}	gas part of the periodicity cell
Y^{ε}	rescaled periodicity cell
n	normal
L_{c}	characteristic length of the system
ℓ_{c}	characteristic length of the pore
y	microscopic variable
x	macroscopic variable
$\mathcal{N}$	vector quantities for cell problems
T_{g}	temperature of gas in the gas part
T_{s}	temperature of solid in the solid part
T	effective temperature
C	oxygen concentration
W	reaction rate
R	surface concentration of the solid product
Q	heat release
D	molecular diffusion coefficient
A	pre-exponential factor
T_{a}	activation temperature
c_{g}	specific heat capacity of gas
c_{s}	specific heat capacity of solid
$\mathcal{T}_{Y,\Gamma}$	unfolding operators
$\mathcal{Q}_Y, \mathcal{U}_\Gamma$	averaging operators

Greek

ϵ	scale parameter
Ω^ε	periodic medium
Γ	interior boundary of a single period
$\Omega_\mathrm{s}^\varepsilon$	ensemble of solid inclusions in Ω^ε
$\Omega_\mathrm{g}^\varepsilon$	matrix of interconnected gas part in Ω^ε
Γ^ε	ensemble of gas/solid boundary of the periodic medium
ϕ	volume porosity
ϕ^s	surface porosity
λ	thermal conductivity
ρ	density
α	thermal diffusivity, $\alpha = \lambda^\mathrm{eff}/C^\mathrm{eff}$

Superscripts

$\sim, *$	nondimensionalised variable
eff	effective
s	surface

Subscripts

c	characteristic quantities
s	solid phase
g	gas phase
u	unburnt or initial values
0	initial values
th	thermal
D	Dirichlet data

Index